Transactions of the ASME®

FLUIDS ENGINEERING DIVISION
Technical Editor
DEMETRI P. TELIONIS (1999)
Assistant to the Editor
J. E. POWELL
Executive Secretary
PAT WHITE (1999)
Calendar Editor
M. F. ACKERSON

Associate Technical Editors
R. E. A. ARNDT (1995)
P. R. BANDYOPADHYAY (1997)
M. GHARIB (1995)
A. F. GHONIEM (1995)
F. GIRALT (1997)
H. HASHIMOTO (1996)
J. A. C. HUMPHREY (1997)
O. C. JONES (1995)
G. E. KARNIADAKIS (1995)
J. H. KIM (1996)
R. W. METCALFE (1995)
L. NELIK (1995)
W.-F. NG (1995)
M. W. REEKS (1996)
W. S. SARIC (1995)
M. M. SINDIR (1997)
D. E. STOCK (1996)
S. P. VANKA (1996)

BOARD ON COMMUNICATIONS
Chairman and Vice-President
R. D. ROCKE

Members-at-Large
T. BARLOW, N. H. CHAO, A. ERDMAN, G. JOHNSON, L. KEER, W. MORGAN, E. M. PATTON, S. PATULSKI, R. E. REDER, S. ROHDE, R. SHAH, F. WHITE, J. WHITEHEAD

OFFICERS OF THE ASME
President,
P. J. TORPEY
Exec. Dir.,
D. L. BELDEN
Treasurer,
R. A. BENNETT

PUBLISHING STAFF
Mng. Dir., Publ.,
CHARLES W. BEARDSLEY
Managing Editor,
CORNELIA MONAHAN
Production Assistant,
MARISOL ANDINO

Transactions of the ASME, Journal of Fluids Engineering (ISSN 0098-2202) is published quarterly (Mar., June, Sept., Dec.) for $150.00 per year by The American Society of Mechanical Engineers, 345 East 47th Street, New York, NY 10017. Second class postage paid at New York, NY and additional mailing offices. POSTMASTER: Send address changes to Transactions of the ASME, Journal of FLuids Engineering, c/o THE AMERICAN SOCIETY OF MECHANICAL ENGINEERS, 22 Law Drive, Box 2300, Fairfield, NJ 07007-2300.
CHANGES OF ADDRESS must be received at Society headquarters seven weeks before they are to be effective. Please send old label and new address.
PRICES: To members, $40.00, annually: to nonmembers, $150.00. Add $30.00 for postage to countries outside the United States and Canada.
STATEMENT from By-Laws. The Society shall not be responsible for statements or opinions advanced in papers or . . . printed in its publications (B7.1, Par. 3).

INDEXED by Applied Mechanics Reviews and Engineering Information, Inc. Canadian Goods & Services Tax Registration #126148048.

Journal of Fluids Engineering

Published Quarterly by The American Society of Mechanical Engineers

VOLUME 117 • NUMBER 2 • JUNE 1995

Technical Briefs

Announcements and Special Notices

(Contents continued on p. 218)

Contents continued)

Journal of Fluids Engineering

Technical Forum

Questions in Fluid Mechanics

Why do Streamwise Vortices Form at the Top and Bottom of a Round Jet Moving Parallel to a Free Surface?

By Dorian Liepmann[1]

Near surface jets are often formed in industrial situations where waste outflows, such as cooling water, are disposed into pools, lakes, or the ocean. Because the environmental and ecological impact of the waste depends strongly on its concentration, the speed at which the waste stream entrains ambient fluid and mixes it with the waste is of critical importance in the design of such systems. In the case of cooling water, a difference of a few degrees can have a profound effect on the response of the local flora and fauna. Therefore, the need to minimize environmental impact demands an understanding of entrainment and mixing by near-surface flows.

In the early development of shear flows, such as jets, primary and secondary vortical structures play a critical role in entrainment and growth. Experimental observations of these structures in submerged jets are numerous including the work of Crow and Champagne (1974), Browand and Laufer (1978), and Yule and co-workers (1974 and 1978). Yule provided the first photographs of secondary instabilities and an explanation of the entrainment process in the near-field ($x/d < 5$, where x is the downstream distance from the nozzle and d is the nozzle diameter). Photographs similar to those of Yule are shown in Figs. 1 and 2. The images show two sequential video images of cross-sections of a round jet in water illuminated using laser induced fluorescence. The Reynolds number of the jet was approximately 6000, the location was 3.25 diameters downstream of the nozzle, and the time difference between the two images was approximately 1/10s. Figure 1 shows the braid region between two primary vortical structures from where the streamwise structures originate. The next figure shows the following primary vortical ring: the ends of the streamwise structures from Fig. 1 are visible distributed around the ring. The streamwise vorticity increases the rate at which the jet entrains ambient

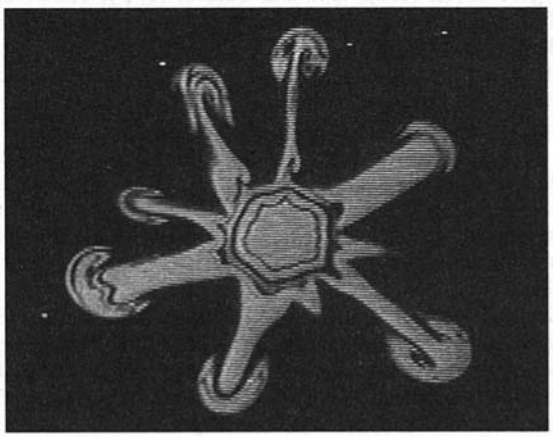

Fig. 2

[1] Department of Mechanical Engineering. University of California, Berkeley, CA 94720.

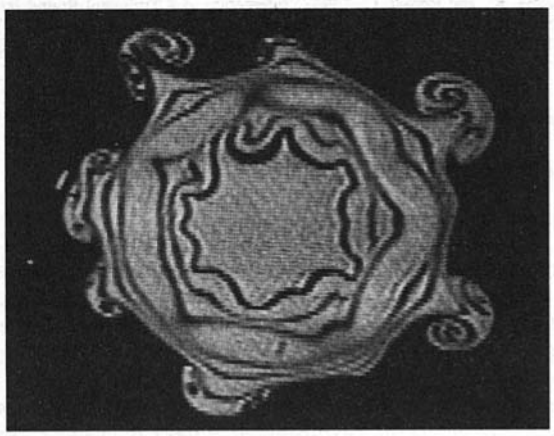

Fig. 1

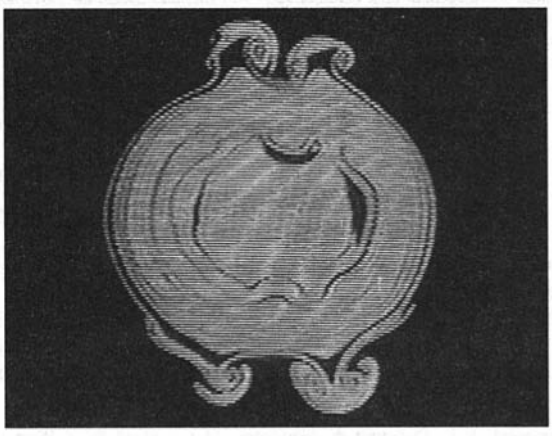

Fig. 3

fluid and grows (Liepmann and Gharib, 1992). The streamwise vorticity may also be important in the actual mixing process as the jet evolves downstream (Broadwell, private communication).

In near-surface jets, these secondary instabilities develop earlier in the dowhstream evolution of the flow and the structures are localized at the top of the jet. Figures 3 and 4 show the same jet positioned one diameter below and parallel to the free-surface at the same conditions as in Figs. 1 and 2. In the early stages of the jet development and at low Froude numbers, the influence of the free-surface on the behavior of the shear flow is much greater than the effect of the flow field on the free surface. The presence of the free-surface makes the entrainment field around the jet no longer radially symmetric. The flow at the top of the jet must move in from the sides and this creates a stagnation region above the flow. The vorticity in at the top of the jet preferentially forms a bump because of the lack of symmetry. The instability induced by the free surface in the braid region of the jet grows into a streamwise vortex structure, like in the submerged case. The formation of strong streamwise structures increases the entainment rate of the near surface jet compared to a submerged jet and causes it to grow faster (Liepmann and Gharib, 1995). The presence of the streamwise structures near the free-surface are clearly evident in the figures.

The reason for the presence of a matching vortex structure at the bottom of the jet is not known. Its effect, coupled with the near-surface vortex structure, is significant however. The two structures fundamentally change the shape of the jet extending it vertically. This shape continues beyond the potential core of the flow and then suddenly widens and spreads out on the surface: Madnia and Bernal (1989, 1994) related this behavior to the axis-switching of an elliptic jet (Gutmark and Ho, 1983).

The two vortical structures also fundamentally change the entrainment patterns around the jet. The digital particle image velocimetry data in Fig. 5 show the time-averaged flow field in a plane normal to the jet two diameters downstream of the nozzle. Although the jet exhibits a slight tilt, the inward flow is much greater from the sides than from below the jet and, in fact, a stagnation line can be seen below the jet core. It is unknown if the flow field generates the streamwise vortical structures at the bottom of the jet or if the steady presence of the structures causes the entrainment pattern around the jet. It is not clear why the influence of the free surface above the jet would have such a major impact on the effectively infinite entrainment field below the jet.

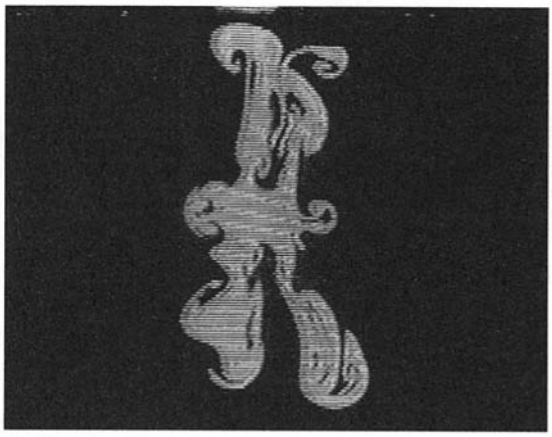

Fig. 4

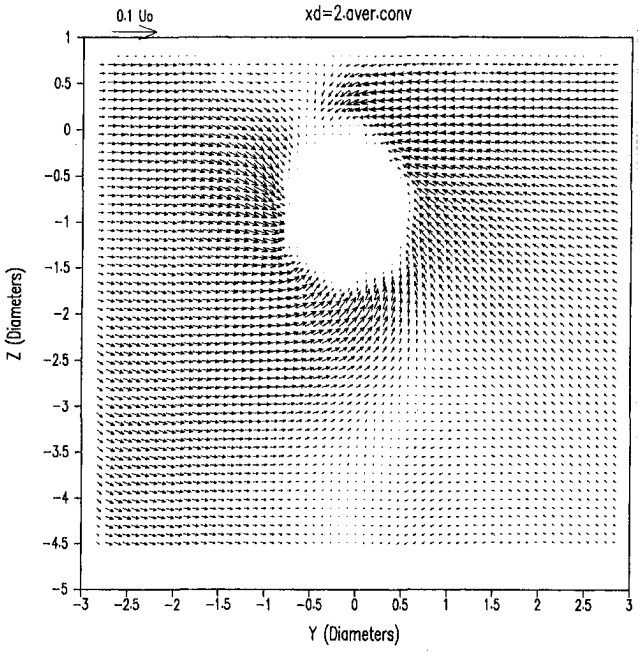

Fig. 5

References

Bowand, F. K., and Laufer, J., 1975 "The Role of Large Scale Structures in the Initial Development of a Circular Jet," *4th Bienniel Symp. on Turbulence in Liquids,* University of Missouri-Rolla.

Crow, S. C., and Champagne, F. H., 1971, "Orderly Structure in Jet Turbulence." *Journal of Fluid Mechanics,* Vol. 48: pp. 547–591.

Liepmann, D., and Gharib, M., 1992, "The Role of Streamwise Vorticity on the Near-Field Entrainment of a Round Jet," *Journal of Fluid Mechanics,* Vol. 245: pp. 643–668.

Liepmann, D., and Gharib, M., 1995, "The Effect of a Free Surface on the Near-Field Dynamics of a Round Jet," Submitted to *The Journal of Fluid Mechanics.*

Madnia, K., 1989, "Interaction of a Turbulent Round Jet with the Free Surface," PhD thesis, University of Michigan.

Madnia, K., and Bernal, L., 1994, "Interaction of a Turbulent Round Jet with the Free Surface," *Journal of Fluid Mechanics,* Vol. 261: pp. 305–332.

Yule, A. J., 1978, "Large-Scale Structure in the Mixing Layer of a Round Jet," *Journal of Fluid Mechanics,* Vol. 89, pp. 413–432.

U. S. Technological Competitiveness: A Fluids Engineers' Viewpoint

Column 7—Postscript

by J. L. Dussourd[1]

Open Forum at the '94 IMECE in Chicago and Membership Response

The Fluids Engineering Division through a special committee lead by its Government Relations function has been investigating the competitiveness problems encountered by U.S. manufacturers of fluid machinery products and what the fluids engineers can do about them. This is the 7th column on this subject to appear in the Journal. In the previous columns, one cause for the problems was traced to our inability to fully marshal the technological resources we already have and an initiative was developed with the promise of helping to remedy these problems. It is based on the establishment of more intensive cooperation between the various sectors working on fluids engineering

[1] President, J. L. Dussourd & Associates, 14 Cleveland Road West, RD2, Princeton, NJ 08540.

fluid and grows (Liepmann and Gharib, 1992). The streamwise vorticity may also be important in the actual mixing process as the jet evolves downstream (Broadwell, private communication).

In near-surface jets, these secondary instabilities develop earlier in the dowhstream evolution of the flow and the structures are localized at the top of the jet. Figures 3 and 4 show the same jet positioned one diameter below and parallel to the free-surface at the same conditions as in Figs. 1 and 2. In the early stages of the jet development and at low Froude numbers, the influence of the free-surface on the behavior of the shear flow is much greater than the effect of the flow field on the free surface. The presence of the free-surface makes the entrainment field around the jet no longer radially symmetric. The flow at the top of the jet must move in from the sides and this creates a stagnation region above the flow. The vorticity in at the top of the jet preferentially forms a bump because of the lack of symmetry. The instability induced by the free surface in the braid region of the jet grows into a streamwise vortex structure, like in the submerged case. The formation of strong streamwise structures increases the entainment rate of the near surface jet compared to a submerged jet and causes it to grow faster (Liepmann and Gharib, 1995). The presence of the streamwise structures near the free-surface are clearly evident in the figures.

The reason for the presence of a matching vortex structure at the bottom of the jet is not known. Its effect, coupled with the near-surface vortex structure, is significant however. The two structures fundamentally change the shape of the jet extending it vertically. This shape continues beyond the potential core of the flow and then suddenly widens and spreads out on the surface: Madnia and Bernal (1989, 1994) related this behavior to the axis-switching of an elliptic jet (Gutmark and Ho, 1983).

The two vortical structures also fundamentally change the entrainment patterns around the jet. The digital particle image velocimetry data in Fig. 5 show the time-averaged flow field in a plane normal to the jet two diameters downstream of the nozzle. Although the jet exhibits a slight tilt, the inward flow is much greater from the sides than from below the jet and, in fact, a stagnation line can be seen below the jet core. It is unknown if the flow field generates the streamwise vortical structures at the bottom of the jet or if the steady presence of the structures causes the entrainment pattern around the jet. It is not clear why the influence of the free surface above the jet would have such a major impact on the effectively infinite entrainment field below the jet.

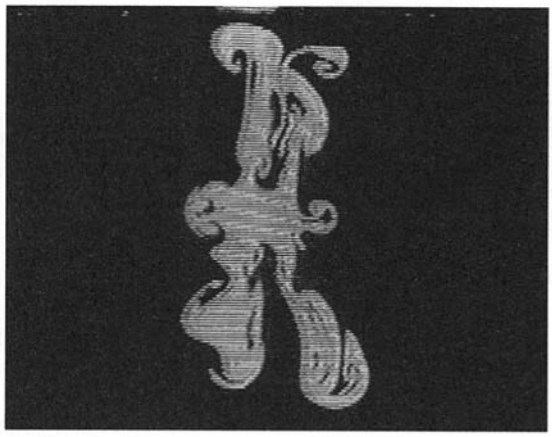

Fig. 4

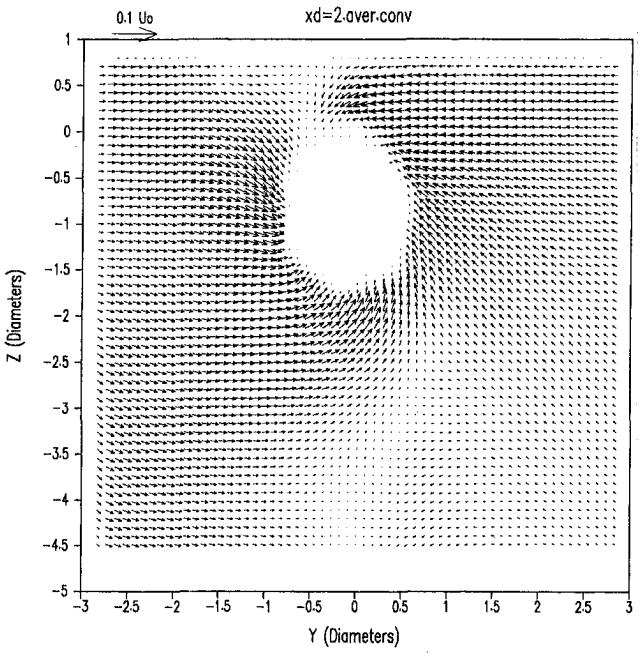

Fig. 5

References

Bowand, F. K., and Laufer, J., 1975 "The Role of Large Scale Structures in the Initial Development of a Circular Jet," *4th Bienniel Symp. on Turbulence in Liquids,* University of Missouri-Rolla.

Crow, S. C., and Champagne, F. H., 1971, "Orderly Structure in Jet Turbulence." *Journal of Fluid Mechanics,* Vol. 48: pp. 547–591.

Liepmann, D., and Gharib, M., 1992, "The Role of Streamwise Vorticity on the Near-Field Entrainment of a Round Jet," *Journal of Fluid Mechanics,* Vol. 245: pp. 643–668.

Liepmann, D., and Gharib, M., 1995, "The Effect of a Free Surface on the Near-Field Dynamics of a Round Jet," Submitted to *The Journal of Fluid Mechanics.*

Madnia, K., 1989, "Interaction of a Turbulent Round Jet with the Free Surface," PhD thesis, University of Michigan.

Madnia, K., and Bernal, L., 1994, "Interaction of a Turbulent Round Jet with the Free Surface," *Journal of Fluid Mechanics,* Vol. 261: pp. 305–332.

Yule, A. J., 1978, "Large-Scale Structure in the Mixing Layer of a Round Jet," *Journal of Fluid Mechanics,* Vol. 89, pp. 413–432.

U. S. Technological Competitiveness: A Fluids Engineers' Viewpoint

Column 7—Postscript

by J. L. Dussourd[1]

Open Forum at the '94 IMECE in Chicago and Membership Response

The Fluids Engineering Division through a special committee lead by its Government Relations function has been investigating the competitiveness problems encountered by U.S. manufacturers of fluid machinery products and what the fluids engineers can do about them. This is the 7th column on this subject to appear in the Journal. In the previous columns, one cause for the problems was traced to our inability to fully marshal the technological resources we already have and an initiative was developed with the promise of helping to remedy these problems. It is based on the establishment of more intensive cooperation between the various sectors working on fluids engineering

[1] President, J. L. Dussourd & Associates, 14 Cleveland Road West, RD2, Princeton, NJ 08540.

problems. Too often, these sectors were seen as preoccupied in the pursuit of their own separate independent agendas.

In an effort to stimulate more vigorous interactions between the fluids engineers from industry and from academia, there were proposed in Column #6 the means for an intensified sharing of their individual skills and technologies in a setting that is mutually profitable and with the ultimate objective of shortening the development lead times of fluid machinery products. It is felt that our competitive strength can greatly benefit from a better utilization of our technologies and that making them more readily available to ourselves should have top priority.

A flow chart for a means of promoting such an interaction is illustrated on the figure. It is an outcome of the committee findings to date and can be explained as follows:

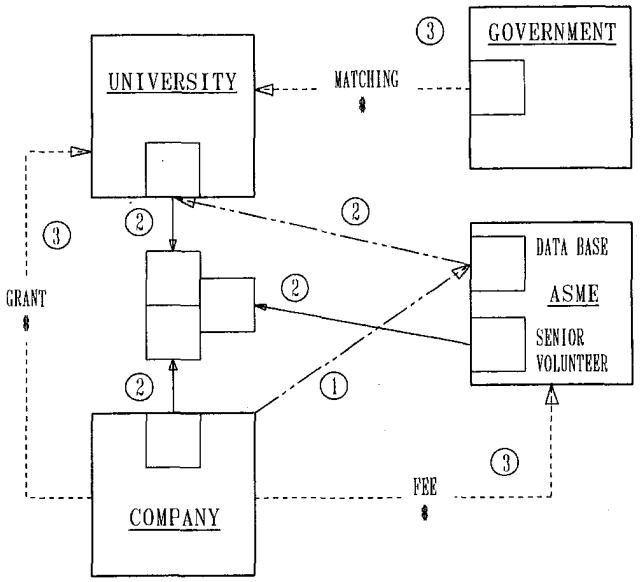

The interactive process begins when a company seeks assistance in improving its analytical design tools and practices or its development capabilities. Following the arrows labeled 1 on the figure, the company can access a data bank compiled by the ASME which lists sources of already existing technologies which can be tapped in the U.S. (and eventually overseas).

If a suitable source can be so located, the company can initiate contacts with or without further help on the part of the ASME. If ASME help is desired, a facilitator can be provided such as a semi-retired ASME member, preferably a specialist in the field of interest. On the figure, these options are identified by cross arrows 2 which lead to meetings between the parties, as depicted by the small boxes at the center of the chart.

A contract is then negotiated, specifying the services to be provided and the renumerations therefor. The latter would be in the forms of grants which the university plows back into its research budget. This research may or may not be related to the problem at hand. In certain instances, the grants may be supplemented with government matching funds (cross arrows 3).

As a result of this process a close rapport is forged between the participants and it is the expectation that it will continue beyond this project and with or without involvement on the part of the ASME.

This essentially is the initiative exposed to the membership at the ASME's 1995 IMECE in Chicago by the committee, with the object of eliciting the reactions of fluids engineers, especially about the benefits of intensified technological exchanges in this fashion, about the feasibility of developing and cultivating long term relationships and about the practicality for the various cultures to work together. In addition, written responses were sought through two survey questionnaires.

The responses from these show certain trends to clearly come through. For example, 80 percent of those in industry expressed the opinion that the availability of better analytical/numerical design software and tools would have speeded up the market introduction of many or at least some of their products. Most reported that their companies already use such tools generated elsewhere and that they feel very comfortable in using them. This indicates that there is much already in use, but perhaps not enough and that questions about confidence in or accountability of those who create them was not really a problem.

Among those who are generators of technologies, mostly from universities, 90 percent would be interested in becoming more involved in solving product engineering problems for industry, alongside their regular duties. Of these, 30 percent are already so engaged, but the others do so rarely or never, with the main reason cited as a lack of opportunities. There are some concerns however with having to deal with a different culture and perhaps with doing work not likely to pay as well as they would like.

Most of the expressed opposition came from the university elite, those already well endowed with government programs. They fear that a diversion to more practical engineering, away from the sciences, would displace some of the projects they have enjoyed throughout their career. Certain others were not really aware that there was a problem with U.S. competitiveness, but if there was, it should be the concern of fluids engineers in industry and not of academicians.

But those whose experience had exposed them to the broader spectrum of engineering practices seemed to be well aware of the endemic condition which separates or even polarizes academia from industry. They support concerted efforts aimed at bringing about an increased sharing of the wisdoms inherent to both.

Included in the survey was a second questionnaire asking the individual fluids engineers to refer this initiative to their management and determine what degree of interest could be found there. As of this date, very few responses have been received. A call is hereby issued to elicit this important feedback from the membership.

These overall reactions were reviewed at the Fluids Engineering Executive committee meeting, with due consideration given to what the next step should be. It was decided that a working proposal be prepared seeking support from the ASME and from NSF in initiating an early implementation of the proposed process and seek further answers to some of the yet not fully answered questions. Most pertinent among these are: 1) The real degree of cooperation to be expected from those in industrial and academic leadership, 2) Whether ASME is the proper agency to broker this process and finally, 3) Whether there really exists in the files of the generators of technologies enough resources to benefit the industrial users. Critically important for this purpose are design tools sufficiently practical and accurate to enhance the analytical design process, to make it possible for the designer to sort out the options he is daily confronted with and to provide him with a better physical understanding of the key constraints limiting him.

The selected strategy to form the basis of the above mentioned proposal to ASME will consist of a pilot operation of the full scale project. It will be restricted to two selected geographical areas only. Simultaneously however it will seek to develop the foundation for the all-important data base in such a way that expansion to its full scope and scale can readily be implemented.

Those fluids engineers who participated in the Chicago Forum are urged again to return their survey forms. Others who did not participate are invited to express their views directly to the author or to the Journal to help provide the needed directions.

Perspective: Selected Benchmarks From Commercial CFD Codes

C. J. Freitas
Computational Mechanics Section,
Southwest Research Institute,
6220 Culebra Rd.,
San Antonio, TX 78228-0510

This paper summarizes the results of a series of five benchmark simulations which were completed using commercial Computational Fluid Dynamics (CFD) codes. These simulations were performed by the vendors themselves, and then reported by them in ASME's CFD Triathlon Forum and CFD Biathlon Forum. The first group of benchmarks consisted of three laminar flow problems. These were the steady, two-dimensional flow over a backward-facing step, the low Reynolds number flow around a circular cylinder, and the unsteady three-dimensional flow in a shear-driven cubical cavity. The second group of benchmarks consisted of two turbulent flow problems. These were the two-dimensional flow around a square cylinder with periodic separated flow phenomena, and the steady, three-dimensional flow in a 180-degree square bend. All simulation results were evaluated against existing experimental data and thereby satisfied item 10 of the Journal's policy statement for numerical accuracy. The objective of this exercise was to provide the engineering and scientific community with a common reference point for the evaluation of commercial CFD codes.

Introduction

The use of Computational Fluid Dynamics (CFD) codes by the engineering community has increased dramatically in the last few years. This rise in interest and use has resulted from improvements in the predictive capabilities of codes, reductions in the cost of workstation technology, and inflation of the costs to perform experiments and to maintain experimental facilities. For a large portion of the engineering community, the primary source of CFD capabilities is through the purchase of a commercial CFD code. Typically, the selection of a commercial CFD code is based on discussions with a vendor's sales or marketing staff and on demonstration of sample simulations (often idealized to highlight features of the code). This is usually done in isolation in which one does not have the opportunity to see several different commercial codes at once, solving the same problem. Therefore, the Coordinating Group for Computational Fluid Dynamics, of the Fluids Engineering Division of ASME, sponsored and organized two unique Forums, allowing for such an evaluation to be made. These forums were; The CFD Triathlon: Three Laminar Flow Simulations by Commercial CFD Codes, held at The Fluids Engineering Conference, Washington D.C., June 20–24, 1993; and, The CFD Biathlon: Two Turbulent Flow Simulations by Commercial CFD Codes, held at The Fluids Engineering Conference, Lake Tahoe, Nevada, June 19–24, 1994. This paper then, summarizes the results of both of these Forums, and attempts to present conclusions in an unbiased form.

These two Forums take their heritage from the Stanford Olympics of 1968 (Kline et al., 1968). However, there the objective was to identify the fundamental predictive capabilities of early CFD codes and turbulence models, as they related to turbulent boundary layer flows. All the codes used in that exercise were research codes. In these Forums, only commercial CFD codes were allowed to participate. The definition of a commercial CFD code used here is that the code is the product, not the consultation resulting from the use of a code, and that there is a marketing and user support staff for the code. Also, both laminar and turbulent flows were chosen here to evaluate the codes.

The objective of the Forums was to provide a common point of reference to the engineering community for the quantitative evaluation of commercial CFD codes. In addition, it was also the intent of the Forums to provide a qualitative evaluation of the insights of and the capabilities that each of the vendors bring to the solution process. This was felt to be important in that a user would more than likely have to rely on the vendor for aid and support sometime during the license period of the code in order to solve highly complex problems. Therefore, the participants were asked to describe in some detail, their method of problem definition, problem solution, and problem analysis.

The Forums were organized through letters of invitation, inviting commercial CFD code vendors to participate. Once a vendor accepted the invitation to participate, a problem definition statement for each problem was sent to them. In the first Forum, the benchmark problems consisted of three different laminar flows; i.e., a steady, two-dimensional laminar flow (low Reynolds number flow over a backward-facing step); an unsteady, two-dimensional laminar flow (low Reynolds number flow around a unit cylinder); and an unsteady, three-dimensional laminar flow (shear-driven cavity flow). In the second Forum, two different turbulent flow problems were defined; i.e., an unsteady, two-dimensional turbulent flow (flow around a square cylinder), and a steady, three-dimensional turbulent flow (spatially-developing flow in a 180-degree bend). Each vendor was then given approximately five months to perform the simulations and write a summary paper. A Forum volume resulted from the CFD Triathlon (Freitas, 1993), however, due to time constraints, no Forum volume was compiled for the CFD Biathlon. Table 1 gives the names of the vendors and codes which participated in one or both of the Forums. Although twenty vendors were invited to participate in these Forums, only five vendors completed each exercise, with only two vendors completing both exercises (with a total of eight vendors participating in these Forums).

In the remainder of this paper the results of both Forum exercises are presented. In the next section, a brief review of the codes which were used to complete the benchmark simulations is given. Then in each of the next five sections the benchmark problems are defined and the results of the simulations

Contributed by the Fluids Engineering Division for publication in the JOURNAL OF FLUIDS ENGINEERING. Manuscript received by the Fluids Engineering Division October 14, 1994; revised manuscript received February 23, 1995. Associate Technical Editor: D. P. Telionis.

Table 1 Vendor and Code names who participated in the Triathlon and Biathlon forums (CFD Triathlon = T, CFD Biathlon = B). The letter legend indicates that that forum excericse was completed

Company or vendor name	Code name
CFD Research Corporation	CFD-ACE-B
Computational Dynamics LTD	STAR-CD-B
Computational Fluids Dynamics Services	CFDS-FLOW3D-T
Engineering Mechanics Research Corporation	NISA/3D-FLUID-T
Flow Science	FLOW-3D-T
Fluent Inc.	FLUENT-T, B
Scientific Services, Inc. (SIMULOG)	N3S-B
Swanson Analysis Systems Inc.	FLOTRAN-T, B

presented and discussed. Finally, in the last section, some lessons learned are given with some general observations concerning the state-of-the-art in commercial CFD codes.

The CFD Codes

A brief review of the capabilities of each of the codes used to complete either the CFD Triathlon simulation series or the CFD Biathlon simulation series are now given. These codes are presented in no specific order, and the reader is to infer nothing by the order of presentation. In the presentation of each code, the header line gives the name of the code, the company name, and the people involved in performing the simulations.

FLOW-3D, Flow Science Inc., J. Sicilian, J. Ditter, C. Bronisz. FLOW-3D is a finite-difference, transient-solution algorithm solving the conventional, conservation equations of fluid dynamics. It consists of three computational modules and an image display program (PLTFSI). The three modules are; a preprocessor (PREP3D), which uses a NAMELIST input data file to create the computational description of the problem; a solver (HYDR3D), which solves the transient flow equations; and a post-processor (FLSCON). FLOW-3D is based on the technology of SOLA-VOF (Hirt and Nichols, 1981). However, it is a completely independent implementation of these techniques. The principal algorithms are SOLA, ICE, VOF, and FAVOR, which are all based on a combination of finite difference and finite volume perspectives. SOLA is a technique for the solution of the time-dependent flow equations in primitive variables, solved on a staggered grid system. The grid used is nonuniform and Cartesian (polar/cylindrical coordinate system is also available) in one, two or three dimensions. With the Cartesian grid as the base for the solution domain, complex geometries are represented by the FAVOR algorithm (**F**ractional **A**rea/**V**olume **R**epresentation) which calculates volume fractions for each mesh cell and area fractions for each face of a mesh cell. These fractions are fully integrated into the conservation equations allowing for the computation of flow through or around complex stationary or moving obstacles. In this method, the shape of a curved surface is represented as a series of linear segments, cutting through a mesh cell at appropriate, but arbitrary orientations (Hirt and Sicilian, 1985). The VOF algorithm (Volume Of Fluid) tracks the movement of fluid by the calculation of fluid fraction for each mesh cell. These fluid fractions are calculated from a conservation equation and represent either the fraction of the mesh cell volume occupied by liquid (for free surface calculations) or the fraction occupied by a specific liquid (for two-fluid calculations). With VOF, surfaces are able to collide with solid bodies, other surfaces, form or destroy bubbles, and to intersect with themselves. FLOW-3D incorporates physical models for porous media flow, conjugate heat transfer, dynamic fluid-interface motion, surface tension, wall adhesion, turbulent flow, incompressible and compressible flow, non-Newtonian fluids, non-inertial reference frames, solidification and melting, thermal buoyancy, and simplified bubble models. FLOW-3D models turbulent flows with either a Prandtl mixing length model, a standard two-equation k-ε model, an RNG model (renormalized group theory model, an extension of the standard k-ε model), or a Large Eddy Simulation model with a Smagorinsky sub-grid scale model. Finally, FLOW-3D uses either a first-order method or a second-order method for space and time derivatives. In all simulations completed with FLOW-3D in the CFD Triathlon exercise, the monotonicity-preserving, second-order spatial-differencing scheme was used to discretize the convection terms.

FLOTRAN, Swanson Analysis Systems, Inc., T. Chopin, D. Ganjoo, E. Underwood. FLOTRAN is a finite-element based, general-purpose algorithm which solves the Navier-Stokes and energy equations using a segregated or sequential solution method. The velocity-pressure formulation uses an equal-order approximation for velocity and pressure, and solves for each variable field in an iterative manner similar to finite volume methods (Schnipke and Rice, 1986). This results in a method which is bandwidth independent and thereby requires significantly less memory than traditional finite-element methods. FLOTRAN uses a monotone streamline upwind technique to discretize the advection terms and has demonstrated improved accuracy over conventional upwind methods for finite elements. The FLOTRAN element library consists of two-dimensional quadrilateral and triangular elements and three-dimensional hexahedral and tetrahedral elements which may be applied to two-dimensional and three-dimensional Cartesian or cylindrical coordinate systems. The effects of periodic boundary conditions, porous media flow, distributed resistances, moving walls, conjugate heat transfer, thermal buoyancy, turbulent flow, incompressible and compressible flow, and rotating reference frames may be simulated. FLOTRAN models turbulent flow with the standard two-equation k-e model. Finally, FLOTRAN is an integrated part of the ANSYS program, or may be a standalone package consisting of FLOTRAN and ANSYS PREP/POST or with an interface to other commercially available pre/post-processors. In the simulations completed with the FLOTRAN code in both the CFD Triathlon and CFD Biathlon exercises, the monotone, streamline upwind method was used to model the convective terms, which has demonstrated greater than second-order accuracy.

STAR-CD, Computational Dynamics LTD, R. Issa, R. Benodekar, R. Sanatian, S. Uslu. STAR-CD is a general purpose, finite-volume algorithm which uses an unstructured grid system to resolve the conservation equations. The unstructured grid allows for a range of optional cell shapes, including hexahedra, tetrahedra, and prisms. These cells may exhibit arbitrary deformation, have sliding internal interfaces, and permit cell insertion and deletion. In addition, local mesh refinement may be utilized to locally enhance accuracy of solutions without encumbering the global solution. Extended versions of the SIMPLE (Patankar and Spalding, 1972) and PISO (Issa, 1983) algorithms are used for steady-state and transient calculations, respectively, solving all variables on a colocated grid system; i.e., all variables are at the cell center, including the Cartesian velocity components. Spatial differencing is second-order and a fully-implicit first-order temporal differencing scheme is used. STAR-CD models turbulent flow using a number of different Reynolds-averaged turbulent models, in particular, the standard two-equation k-ε model, an RNG model, and a two-layer variant of the k-ε model in which the Norris and Reynolds (1975) one-equation, low Reynolds number model is used in the near-wall region. In general, STAR-CD has extensive flow, heat and mass transfer capabilities, including compressible, multiphase and chemical-reacting flows. Finally, STAR-CD has a fully integrated pre/post processing facilities, allowing for mesh generation, visualization of results, and interfacing to external CAD systems. In the simulations completed with the STAR-CD code

in the CFD Biathlon exercise, the self-filtered, second-order spatial differencing scheme was used.

N3S, SIMULOG/Scientific Services, Inc., J. Canu, C. Fletcher, G. Blankenship. N3S was created to address the solution of problems in fluid dynamics with complex, three-dimensional geometries. N3S is based on the finite element method and uses an unstructured grid topology. It solves the time-dependent Navier-Stokes equations and energy equation using a velocity/pressure formulation. Time discretization is performed by an operator splitting method in which the convection step is calculated using a characteristics method (providing a natural upwinding) and the diffusion or Stokes step is calculated by an implicit Euler scheme. Within this technique, first and second-order schemes are implemented. The resulting Stokes problem is discretized in space using triangular elements in two dimensions or tetrahedra in three dimensions and is solved using a preconditioned Uzawa algorithm. A mixed formulation for velocity and pressure is used, providing two element classes, P1-P2 or P1-isoP2. N3S incorporates models for multiphase flow, reacting flow, moving boundaries, and an adaptive meshing routine enhancing solution accuracy locally. N3S models turbulent flow with the standard k-ε model and a variant of it based on the work of Kato and Launder (Launder et al., 1975). N3S uses a variety of grid generation packages and produces output that can be visualized by several visualization packages. The N3S preprocessor does validate the grid and corrects the grid if necessary, plus defines all the conditions necessary to perform a simulation. In the simulations completed with the N3S code in the CFD Biathlon exercise, the second-order form of the solver was used.

CFD-ACE, CFD Research Corporation, R. Avva, Y. Lai, A. Singhal. CFD-ACE is an advanced, general-purpose CFD code with multi-domain solution capabilities. It is based on a strongly conservative finite-volume formulation using nonorthogonal curvilinear coordinate systems with a structured, colocated grid arrangement. A fully-implicit, patched multiblock solution procedure is used which accounts for moving grids, sliding grids, and rotating coordinate systems. The solution algorithms are based on variants of SIMPLEC and PISO, using advanced linear equation solvers including a preconditioned, Conjugate Gradient Squared algorithm and a Symmetric Strongly Implicit procedure. A variety of spatial discretization methods are permitted, i.e., first-order upwind, central, second-order upwind, and a third-order Osher-Chakravarthy TVD scheme. A variety of temporal discretization methods are also permitted, i.e., backward Euler, Crank-Nicholson, and three-point schemes. CFD-ACE has models for incompressible and compressible (subsonic to hypersonic) flows, thermal buoyancy, conjugate heat transfer, radiative heat transfer, variable physical properties, mass transfer with multi-component diffusion, solidification/melting, gaseous combustion, and spray dynamics. CFD-ACE models turbulent flows using a variety of models, in particular, the standard k-ε model, RNG model, and a two-layer k-ε model (Rodi, 1991). Finally, CFD-ACE has a graphical-user-interface which incorporates a grid generation facility and allows for interactive problem definition and solution. Visualization of results is performed with CFD-VIEW. In the simulations completed with the CFD-ACE code in the CFD Biathlon exercise, a second-order central spatial-differencing scheme was used.

FLUENT, Fluent Inc., D. Choudhury, S. Kim, D. Tselepidakis. FLUENT solves the governing conservation equations of fluid dynamics by a finite-volume formulation on a structured, non-orthogonal, curvilinear coordinate grid system using a colocated variable arrangement. Three different spatial discretization schemes may be used; i.e., Power-Law, second-order upwind, and QUICK (Leonard, 1979), a bounded third-order accurate method. Temporal discretization is achieved by a first-order, implicit Euler scheme. Pressure/Velocity coupling is achieved by the SIMPLEC algorithm resulting in a set of algebraic equations which are solved using a line-by-line tridiagonal matrix algorithm, accelerated by an additive-correction type of multigrid method and block-correction. Additional equation solvers are also available to the user. FLUENT models turbulent flows with the standard k-ε model, an RNG model, and a second-moment closure or Reynolds-stress model (RSM). In general, FLUENT includes models for single or multiphase flow, with heat transfer and chemical reactions for incompressible and compressible flows. These features are accessible through a graphical-user-interface permitting problem definition, problem solution, and post-processing. In the simulations completed with the FLUENT code in both the CFD Triathlon and CFD Biathlon Forums, the convective terms were discretized with a bounded, third-order accurate QUICK scheme.

CFDS-FLOW3D, Computational Fluid Dynamics Services, Inc., S. Simcox, H. Pordal, M. Nieburg. CFDS-FLOW3D is also a finite-volume based code using a structured, patched multi-block, nonorthogonal, curvilinear coordinate grid with a colocated variable arrangement. The basic solution algorithm is the SIMPLEC pressure correction scheme which uses a variety of linear equation solvers. Spatial discretization is achieved through the HYBRID scheme, a second-order upwind scheme, and the third-order QUICK scheme. CFDS-FLOW3D has models for multi-phase flow, particle transport, gaseous combustion, chemical species concentration, thermal radiation, compressible and incompressible flows, porous media flow, and conjugate heat transfer. Turbulent flows are modeled with five different closure methods, i.e., the standard k-ε model, a low-Reynolds number k-ε model, an algebraic stress model, a differential Reynolds stress model, and a differential Reynolds flux model. Again, CFDS-FLOW3D utilizes a graphical-user-interface to enhance problem definition, solution, and analysis. In the simulations completed with CFDS-FLOW3D in the CFD Triathlon exercise, a combination of HYBRID differencing and second-order upwind differencing for the convective terms was used. Here, the simulations were usually performed in two steps; i.e., step one consisted of using HYBRID differencing to simulate the development phase of the flow, step two consisted of using the second-order upwind differencing method to continue the simulation to a fully developed state. The third-order QUICK scheme was used to simulate the flow over a backward-facing step.

NISA/3D-FLUID, Engineering Mechanics Research Corporation, K. Bhatia, M. Rahman, B. Agarwal. NISA/3D-FLUID is a finite element based code used to solve the governing conservation equations of fluid dynamics. It uses a Galerkins' approach to discretize the equation system and eliminates pressure through the use of a penalty function. To overcome the stability limits imposed by the convective terms, the SUPG scheme of Brooks and Hughes (1982) is used. First-order backward differencing is used for temporal discretization. The resulting algebraic system is then solved using a frontal solver with wavefront optimization. In general, NISA/3D-FLUID has models for heat transfer, radiation heat transfer, non-Newtonian flows, compressible and incompressible flow, turbulent flows, flow through porous media, rotating reference frames, phase change, free surface flows, chemically reacting flows, fluid-solid interaction, and stress analysis. A large family of isoparametric elements are available to the user, i.e., linear, parabolic, and cubic element types. Again, a fully integrated graphical-user-interface is present to aid in problem definition, solution and analysis. In the simulations completed with the NISA/3D-FLUID code in the CFD Triathlon exercise, linear finite elements were used to resolve the flow fields.

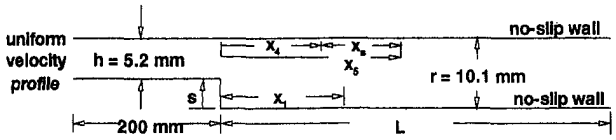

Fig. 1 Definitions for benchmark problem 1. Re = U^*D/ν, where U = average inlet velocity, $D = 2h$, ν = kinematic viscosity of air = 1.5×10^{-5} m^2/s.

Benchmark Problem 1: The Backward-Facing Step Problem

The flow through a straight channel having a sudden asymmetric expansion is called the backward-facing step problem. Separated flows resulting from such changes in geometry are common in industrial, internal flow applications, where the device's performance often depends on the structure of the flow. The flow over a backward-facing step provides an excellent test case for the accuracy of a numerical method because of the dependence of the reattachment lengths on the Reynolds number. Numerical methods which introduce excessive numerical smoothing in favor of stability will result in poor predictions of these reattachment lengths. Only two parameters characterize this flow, i.e., the Reynolds number and the channel step height. In this exercise the experimental configuration and conditions of Armaly et al. (1983) were used and are illustrated in Fig. 1. Here, flow originates in a long inlet channel which then expands into a longer exit channel allowing for a fully developed velocity profile to form. The channel expansion ratio is 1.94. Three different Reynolds numbers were selected for simulation, i.e., 200, 450, and 1000. At a Reynolds number of 200 only the primary recirculation cell develops with a reattachment length of x_1. At a Reynolds number of 450, an additional separation cell forms on the upper wall of the channel. Three characteristic length scales are associated with this additional separation cell; i.e., x_4 is the distance from the step edge to the point of separation, x_s is the reattachment length, x_5 is the sum of x_4 and x_s. Steady, two-dimensional flow develops at both of these Reynolds numbers. At a Reynolds number of 1000, the flow begins to exhibit three-dimensional effects. This final flow condition was selected because Armaly et al. (1983) present experimental data for this flow which exhibits some interesting flow structures, i.e., they report the existence of a secondary recirculation cell on the bottom wall and an imbedded counter-rotating cell in the corner formed by the step face and bottom wall. However, none of the five codes reported the existence of the secondary recirculation cell on the bottom wall at this Reynolds number, and only FLUENT reported resolving in their simulation the imbedded counter-rotating cell in the corner created by the step face and bottom wall.

This benchmark problem was completed by FLOW-3D, FLOTRAN, FLUENT, CFDS-FLOW3D, and NISA/3D-FLUID. All vendors used a uniform inlet velocity profile with an inlet channel of 20 cm, with the exception of FLOW-3D which used an inlet length of 5–10 cm, and FLUENT, which used no inlet channel and prescribed a parabolic velocity profile at the step edge. Table 2 displays the grid resolution used by each vendor and computational resources required for the problem solution. The CPU time per node is calculated as the total CPU time for the solution divided by the number of computational nodes, with the number of solver iterations implicitly included in this time. This normalized CPU time provides an approximate measure of the work units required by each code to provide a converged solution, and does allow for a relative comparison of computational performance. However, this CPU time is strongly affected by the type of boundary conditions, initial conditions, relaxation parameters, and type of algorithm. It should be noted that all the codes solved this problem as a steady state simulation, except FLOW-3D, which solved it as an accelerated transient problem, and thus their computational times tend to be greater than the others. The final row of Table 2 displays a multiplier by which the effects of different computer platforms may be nullified. Following the compiled results of Dongarra (1993), a mflops rating for each of the platforms is obtained based on LINPACK Benchmarks, then each platform used here is scaled against the fastest machine, in this case the IBM RS 6000. This results in a multiplier for which a scaled CPU time may be calculated, i.e., the CPU time per node times the multiplier, however, this calculation is left to the reader.

Table 3 displays the predicted reattachment length, separation length, and recirculation length for the primary and secondary recirculation regions. All values are normalized by the step height s. In general, the maximum deviation of the predicted value of the primary reattachment length varies from the measured value by 8, 15, and 47 percent for the Reynolds numbers of 200, 450, and 1000, respectively. The minimum deviations from this measured length are 0.4, 8, and 20 percent, respectively. The large deviation from the measured value at a Reynolds number of 1000 is not surprising, due to the apparent three-dimensionality and unsteadiness of the measured flow. It has already been documented that this deviation is not due to numerical errors (Kim and Moin, 1985). It is left to the readers to judge whether the 8 percent deviation for a Reynolds number of 450 is accurate enough for their applications. One vendor (CFDS) did perform three different simulations at the same grid resolution, but using three different convective difference schemes (i.e., HYBRID, second-order upwind, and QUICK). At the lower Reynolds numbers of 200 and 450, the QUICK scheme showed less than 10 percent improvement in reattachment length over the HYBRID scheme, indicating that for these flow conditions, the HYBRID scheme was functioning as a second-order central difference scheme. However, at a Reynolds number of 1000, the second-order upwind scheme predicted an improvement to the reattachment length of 113 percent (QUICK results were not reported) to that predicted by the HYBRID method. Clearly this demonstrates the degradation of solution accuracy due to the artificially diffusive nature of first-order upwind methods. In general, none of these results have achieved a grid-convergent solution, nor can it be stated that any code is superior to another, especially at the larger Reynolds number flow conditions.

Benchmark Problem 2: Uniform Flow Past a Circular Cylinder

The second problem investigated in the CFD Triathlon was the uniform flow past a circular cylinder at a low Reynolds number. The Reynolds number selected was 60, based on the diameter of the cylinder and the uniform flow velocity upstream of the cylinder. Several papers were referenced for the participants, i.e., the experimental data of Tritton (1959) and Acrivos et al. (1968), and the computational data by Dennis and Chang (1970) and Takami and Keller (1969). Unfortunately, this problem proved to be the biggest disappointment of the CFD Triathlon exercise, because three of the five simulations performed assumed a symmetry to the flow. It appears that the term "uniform flow" implied to these three participants that the flow was steady throughout the flow domain, and therefore symmetric about the horizontal, radial axis of the cylinder. And certainly in the literature it has been documented that through artificial means, the flow past a circular cylinder can be stable to Reynolds numbers as high as 150. However, with no artificial damping it is commonly accepted that transition to an unsteady wake flow develops at a Reynolds number of 40. Further, in Tritton (1959) a photograph from his experiments clearly show the characteristic vortex shedding phenomena at a Reynolds number of 60, with a well defined vortex street.

FLOW-3D, FLOTRAN, FLUENT, CFDS-FLOW3D, and NISA/3D-FLUID solved this second benchmark problem.

Table 2 Grid resolution and computational resources used in simulations for problem 1

Flow conditions	FLOW-3D	FLOTRAN	FLUENT	CFDS-FLOW3D	NISA/3D-FLUID
Re = 200					
Grid resolution	196 × 50 nodes	7401 nodes	151 × 41 nodes	95 × 30 nodes	3695 nodes
CPU time (s) per node	3.2	5.6	0.2	0.6	0.1
Re = 450					
Grid resolution	195 × 50 nodes	11,561 nodes	151 × 41 nodes	95 × 30 nodes	8358 nodes
CPU time (s) per node	9.5	4.4	0.3	1.3	0.4
Re = 1000					
Grid resolution	196 × 75 nodes	7401 nodes	151 × 41 nodes	95 × 30 nodes	8358 nodes
CPU time (s) per node	13.4	7.5	0.5	2.2	0.6
Computer power	19 mflops RS6000	1.4 mflops SPARC1	9 mflops SPARC 10	4 mflops SPARC 2	10 mflops STARDENT
Power multiplier	1.0	0.07	0.47	0.21	0.53

However, only FLOW-3D and FLUENT solved the asymmetric flow problem. Table 4 summarizes the details of these simulations and the primary results. Based on the work of Tritton (1959) the measured drag coefficient is 1.47, and from Schlichting (1979) the Strouhal number is measured to be 0.14. Both FLOW-3D and FLUENT closely predict the Strouhal frequency, although the authors of FLOW-3D indicate that a vortex street did not fully develop in their simulation. Three of the codes predict the drag coefficient within 10 percent of the measured value. However, the lack of insight brought to bear on this problem by the majority of the vendors is disappointing. In the problem definition statement it was specifically stated that this was a two-dimensional unsteady flow problem and further that the "results of this simulation may be reported in whatever form you feel best describes the flow. However, at a minimum the magnitude of the drag coefficient, surface vorticity, surface shear, and wake length should be provided." The format for the presentation of results was intentionally left vague, but was supplemented by providing the four references cited above, which present a broad range of data and different deduced quantities, plus they cite additional key references. Finally, this author had envisioned that because at this Reynolds number the flow was unsteady in the wake region, that a time dependent simulation would be performed from which the time history of the development of the wake and its developing instability could be presented, assuming the flow began from quiescent initial conditions. Unfortunately, none of the vendors presented results on the time evolution of the flow, nor did any vendor perform a grid sensitivity study.

Benchmark Problem 3: Three-Dimensional Shear-Driven Cavity Flow

The final flow studied in the CFD Triathlon was the flow created by a sustained, constant shear applied to the fluid in a cubic cavity or enclosure. Historically, the shear-driven cavity's geometric simplicity and well defined flow structure in two dimensions and at low Reynolds numbers have allowed for comparative analysis of numerical techniques, and has served as an exceptional benchmark for codes in general. However, experimental results for moderate Reynolds number, three-dimensional shear-driven cavity flow indicated that the physics of this flow was anything but simple (Koseff and Street, 1984). The flow field is unsteady and possesses significant secondary motions in the third dimension; i.e., spanwise direction. The best two-dimensional simulations cannot reproduce the experimental velocity profiles and flow structure variation at these Reynolds numbers due to the absence of a mechanism for energy redistribution in the spanwise direction. However, even three-dimensional simulations were not able to reproduce the complexity of the shear-driven cavity flow until sufficient numerical accuracy was achieved (Koseff, et al., 1983). In 1985 the first successful simulation of the three-dimensional shear-driven cavity flow was reported in Freitas et al., 1985. What makes this flow interesting is the formation of Gortler vortices resulting from a centrifugal instability generated along the curved separation surface between the primary recirculation cell and the largest corner recirculation cell. Gortler vortices are contra-rotating longitudinal vortex pairs which are formed due to the sensitivity of the induced radial pressure gradient to small disturbances which are propagated and amplified in the direct normal to the plane of the primary flow (Freitas and Street, 1988). At a Reynolds number of 3200, based on the shear velocity and cavity width (see Fig. 2), the Gortler vortices exhibit a second-order instability in which the vortex pair is asymmetric and time varying, and tends to meander along their length. Figure 3 is taken from Freitas and Street (1988), and displays particle tracks on a plane which trace the structure of the Gortler vortices.

Table 3 Comparison of reattachment lengths for problem 1

Various Lengths	Armaly et al. data	FLOW-3D	FLOTRAN	FLUENT	CFDS-FLOW3D	NISA/3D-FLUID
Re = 200						
x_1/s	5.0	4.87	4.59	4.98	4.90	4.80
Re = 450						
x_1/s	9.5	8.64	8.12	8.50	8.78	8.08
x_4/s	7.6	7.77	7.62	7.27	n/a	8.31
x_5/s	11.3	10.80	9.32	12.16	n/a	10.27
x_s/s	3.7	3.03	1.70	4.89	2.65	1.96
Re = 1000						
x_1/s	16.3	12.23	8.57	13.08	12.65	12.39
x_4/s	13.5	9.50	6.23	10.33	n/a	9.90
x_5/s	21.7	22.40	16.66	24.70	n/a	22.94
x_s/s	8.2	12.9	10.43	14.37	14.08	13.04

Table 4 Summary of conditions and results for benchmark problem 2

Codes	Distance from lateral boundary to cylinder	Distance from inlet plane to cylinder	Distance from cylinder to exit plane	Downstream boundary condition	Grid resolution	Drag coefficient	Vortex street present?	Strouhal number
FLOW-3D	6.5 D	2.5 D	22 D	Uniform Pressure	198 × 80 Cartesian	1.77	Partial	0.15
FLOTRAN	8 D	~10 D	~20 D	Zero-Gradient	21,498 nodes	1.44	No	N/A
FLUENT	5 D	N/A	20 D	Zero-Gradient	101 × 201 O-H Grid	1.567	Yes	0.15
CFDS-FLOW3D	N/A	3.5 D	9.5 D	Zero-Gradient	3,384 nodes ~125 × 27	0.037	No	N/A
NISA/3D-FLUID	10 D	8 D	20 D	Zero-Gradient	3,603 nodes	1.343	No	N/A

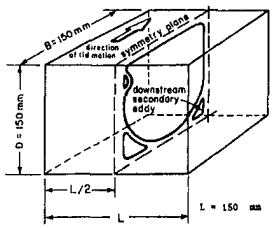

Re = U * B / ν
U = Lid Velocity
B = Lid Width
ν = Kinematic Viscosity of water

Fig. 2 Definitions for benchmark problem 3. Three-dimensional flow in a shear-driven cubical cavity.

In this benchmark exercise the experimental conditions of Prasad and Koseff (1989) are simulated, where the shear-induced flow of water in a cubical cavity at a Re of 3200 is produced. This is a transient simulation which requires sufficient simulated time to develop, requiring a minimum of 6 minutes to setup the primary flow but no more than 20 minutes to resolve all the pertinent flow structures. FLOW-3D, FLUENT, CFDS-FLOW3D and NISA/3D-FLUID were used in this exercise. Each simulation was based on a nonuniform grid with respective resolutions of 32 × 32 × 16, 31 × 31 × 22, 30 × 30 × 15, and 30 × 30 × 10. All four vendors assumed a symmetric flow and imposed a plane of symmetry on the centerline (spanwise direction) of the cavity. The staff using CFDS-FLOW3D solved the steady flow only and did not resolve the transient nature of the flow or the Gortler vortices. The staff using NISA/3D-FLUID solved the transient problem but did not report or apparently resolve the relevant flow structures. The simulation using FLOW-3D did resolve the endwall corner eddy structure and one-half of a Gortler vortex pair, but this single vortex was fixed on the symmetry plane and was constrained from exhibiting a time dependent nature. FLUENT was the only code to fully resolve time evolving pairs of Gortler vortices and coincidentally had the greatest number of grid points in the spanwise direction and used a third-order spatial differencing scheme (QUICK). As indicated above, the accuracy of the spatial and temporal discretizations and the grid distribution are absolutely critical to the successful simulation of this flow. It is worthwhile to note that for the same flow conditions Perng and Street (1989) resolved the flow phenomena on a nonuniform grid of 35 × 35 × 20 and Freitas and Street (1988) for a similar cavity flow (a 1:1:3 aspect ratio cavity), resolved the flow using a 32 × 32 × 45 nonuniform grid resolution. Although these two grid resolutions are comparable to those used by the participants in this exercise, they were both based on QUICK-type spatial schemes with third-order spatial accuracy, and were therefore able to resolve the finer scales of the flow; i.e., time-evolving Gortler vortices. None of the vendors completing this benchmark simulation performed any grid resolution studies in an

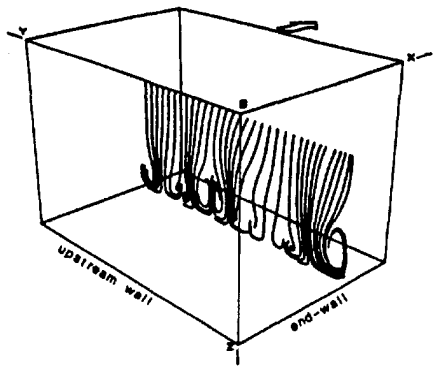

Fig. 3 Particle track field on a plane 45 mm from downstream wall. Duration of particle tracks is 60 s. Velocity field at time of 20 min (Freitas and Street, 1988)

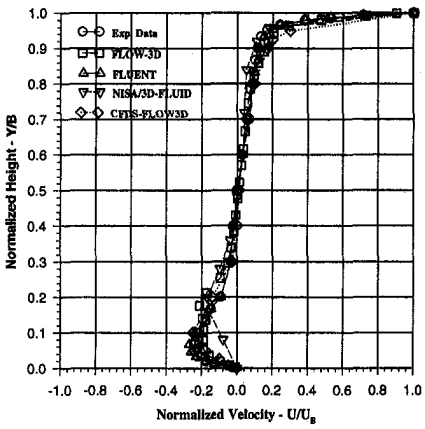

Fig. 4(*a*) Normalized horizontal velocity profile on centerline of symmetry plane

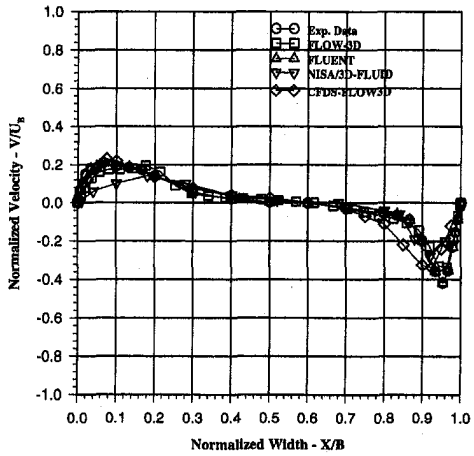

Fig. 4(*b*) Normalized vertical velocity profile on centerline of symmetry plane

attempt to resolve the Gortler vortices. It was not specified in the problem definition what grid resolution to use or that a grid refinement study should be performed, but when a simulation does not predict the presence of a dominant flow structure it would seem reasonable that a finer grid resolution should be run.

Figure 4 displays and compares to the experimental data, the time-averaged (three-minute averages), centerline velocity profiles on the symmetry plane from each of the simulations. All of the simulations were able to reproduce the time-averaged profiles on this plane of the cavity, even the steady-flow simulation of CFDS-FLOW3D predicted some of the trends in these profiles. What this demonstrates is, that on average, the spanwise centerline plane is a symmetry plane for the cavity flow at moderate Reynolds numbers, and that the effect of the Gortler vortices on the symmetry plane flow is nominal. This data, then, is not a true measure of accuracy of the prediction of this flow field. What is a true measure of the accurate simulation of this flow is the presence of the time-evolving Gortler vortices. Without resolving these structures, the balance and distribution of energy throughout the cavity is not predicted (Freitas and Street, 1988). In this flow, as with the next two flows studied, the details of the flow are critical to the overall accuracy of the prediction, and thus, grid resolution and numerical accuracy of discretization in space and time must be carefully evaluated, because mean profiles are no longer sufficient to analyze today's industrial problems.

Benchmark Problem 4: Turbulent Flow Around a Square Cross-Section Cylinder

The first problem studied in the CFD Biathlon was the turbulent flow and wake created by a steady flow, flowing around a cylinder of square cross-section. This flow was experimentally studied by Durao, Heitor, and Pereira (1986 and 1988). The experimental configuration was a horizontal flow in a 120 mm $\times$ 156 mm rectangular water tunnel with a 20 mm $\times$ 20 mm obstacle set across the narrow dimension of the tunnel. The duct extended 1.56 m upstream of the obstacle and 0.44 m downstream of the obstacle. The square cross-section cylinder was centered between the top and bottom walls of the duct. The free-stream reference velocity was 0.68 m/s, and the free-stream turbulence intensity was 6%. The Reynolds number of the flow was 14,000, based on the free-stream reference velocity, the dimension of the bluff body, and water as the working fluid. The resulting flow was verified to be two-dimensional. Further, without the obstacle in the channel, the resulting duct flow was measured, indicating a symmetric flow field with a wall boundary layer thickness at the location of the obstacle of 15 mm. The obstacle imposes a 13 percent blockage to the flow, which is significant and requires that the duct walls be resolved in a numerical simulation.

As indicated by the experimental data, this flow includes regions of recirculating, accelerating, and near uniform velocity. The shear layer surrounding the recirculation bubble is a region of intense velocity fluctuations with the individual turbulent stresses exhibiting anisotropy, in that the vertical-velocity Reynolds stress is greatest close to the rear stagnation point, while the greatest values of the horizontal-velocity Reynolds stress develop along the curved shear layer. However, further analysis of these results show that only 40 percent of the total energy in these regions is due to turbulent fluctuations, the remainder of the energy is associated with local periodic oscillations, which are not turbulent. As demonstrated by Durao et al. (1988) when a filter accounting for mean, periodic, and random velocity components is applied to the measured data, the resulting filtered turbulence profiles of the Reynolds stresses exhibit the same trends of the measured quantities but with significantly reduced magnitudes. The levels of turbulence anisotropy are smaller. The non-turbulent, periodic components of the velocity field account for the additional energy in these regions. Therefore, a numerical simulation must be capable of accurately resolving not only the turbulence field, but the periodic, non-turbulent scales as well, and the interactions between these different scales.

Four codes were used to study this flow, i.e., STAR-CD, CFD-ACE, FLUENT, and N3S. Table 5 summarizes the details and results of these simulations. The measured value of the Strouhal number is 0.138 which corresponds to a fundamental frequency due to vortex shedding of 4.7 Hz. All predicted values of the Strouhal number are within 7 percent of the measured value (except for N3S which is within 16 percent). What is interesting is that depending on the code, the standard k-ε model predicted the Strouhal number to be within 2 to 16 percent of the measured value. This is likely a result of grid resolution and accuracy of the spatial discretization scheme used by each code. In fact, based on Strouhal number alone, the standard k-ε provided the most accurate prediction, indicating, once again, that the Strouhal number is essentially insensitive to the details of the flow. Unfortunately, this trend does not carry over to the mean velocity field or turbulence fields. Clearly shown in Fig. 5, is the poor predictive capability of the standard k-ε model in terms of the details of the wake flow field. Shown in Fig. 5 is the mean horizontal velocity profile along the centerline of the obstacle as predicted by each code using different types of turbulence closure models; i.e., the standard k-ε model (Launder and Spalding, 1974), the Renormalized Group Model (RNG) extension to the k-ε model (Yakhot and Orszag, 1986, Yakhot

Table 5 Summary of conditions and results for benchmark simulation 4 (B = obstacle width, standard = standard k-ε model, K-L model = Kato-Launder model, RNG model = renormalized group model, RSM model = Reynolds stress model, T-L model = two-layer *k-ε* model)

Codes	Domain length upstream of obstacle	Domain length downstream of obstacle	Grid resolution	Turbulence models used	Predicted Strouhal number
STAR-CD	78 B	30 B	17,200 nodes, with local mesh refinement	Standard	0.148
				RNG model	0.148
CFD-ACE	5 B	10 B	120 × 80 nodes	Standard	0.141
				T-L model	0.141
				RNG model	0.132
FLUENT	3 B	10 B	101 × 101 nodes	RNG model	0.1456
				RSM model	0.143
N3S	9 B	20 B	7,530 nodes	Standard	0.16
				K-L model	0.16

and Smith, 1992, and Yakhot et al., 1992), the Kato-Launder *k-ε* model (Launder et al., 1975), the two-layer *k-ε* model (Rodi, 1991), and a Reynolds stress-closure model. The magnitude of the mean, negative horizontal velocity in the wake region of the flow is under-predicted by all closure schemes. The proposed explanation for the poor performance of the standard *k-ε* has been that it over-predicts the turbulent energy upstream of the obstacle, whose influence is then propagated downstream of the obstacle, inhibiting the formation of shed vortices due to excessive turbulent viscosity. It appears that this explanation may hold for enhanced versions of this model as well, albeit to a lesser degree. However, a supplemental explanation for this reduced, predicted, negative horizontal velocity magnitude in the wake region, may be that the non-turbulent component of the periodic oscillation is not fully resolved. Certainly, the results presented by Durao et al. (1988) in which as much as 60 percent of the total energy may be associated with non-turbulent, periodic scales, suggest that the turbulence model alone is not responsible for the under-prediction of the velocity magnitude in the recirculation region. In fact, as the flow moves away from this high-energy recirculating region, the enhanced turbulence models do a good job of predicting the mean velocity profile. Figure 6 displays the time-averaged turbulent kinetic energy along the axial centerline of the obstacle. Again, the turbulence models under-predict the magnitude of turbulent kinetic energy in the near wake region. Finally, all vendors reported results for only one grid resolution. Thus, we can not evaluate from these results the relative importance of grid resolution versus turbulence closure to the solution accuracy.

Benchmark Problem 5: Developing Turbulent Flow in a 180 Degree Bend

The second problem of the CFD Biathlon was the spatially developing flow in a 180-degree bend of square cross-section, which is preceded and followed by sections of straight duct. This flow configuration is directly relevant to many industrial applications and the knowledge of the flow and of its turbulence structure are necessary for understanding the complex flow physics associated with other mechanisms such as particle transport, slurry transport, and heat transfer. This flow was experimentally studied by Humphrey et al. (1982) and Chang et al. (1983). Figure 7 is taken from Chang et al. (1983) and defines the test section dimensions, coordinate system, and velocity components. The cross-sectional dimensions of the square duct were 4.45 cm × 4.45 cm. The flow Reynolds number is 56,700, based on the duct height, a free-stream velocity of 1.28 m/s, and water as the working fluid. The Dean number, which is a function of the Reynolds number and the ratio of the hydraulic diameter to the mean radius of curvature of the duct, is 21,900.

This benchmark problem highlighted the limits of current commercial CFD codes, in that a grid independent solution may be achieved and yet not replicate the physics of the flow due to the limits of the physical models within the code, specifically, the turbulence model. In this flow, the Reynolds stress gradients and pressure gradients combine to create a locally anisotropic flow which exceeds the capabilities of all derivatives of the *k-ε* model. As Humphrey et al. (1982) suggest, modeling at the

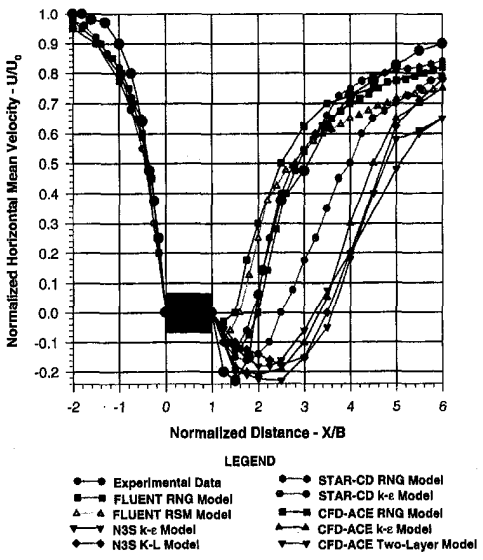

Fig. 5 Centerline mean velocity profiles

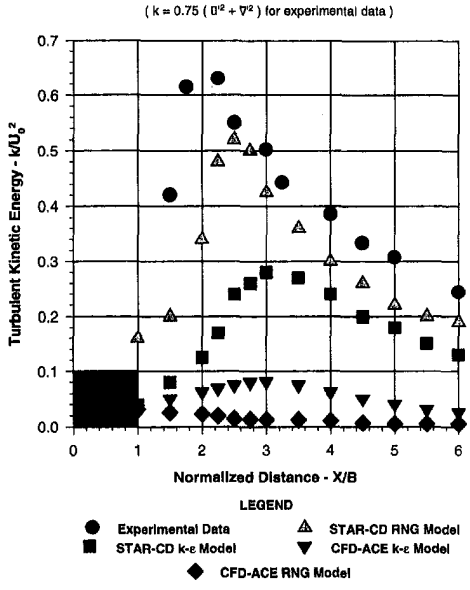

Fig. 6 Centerline mean kinetic energy profile

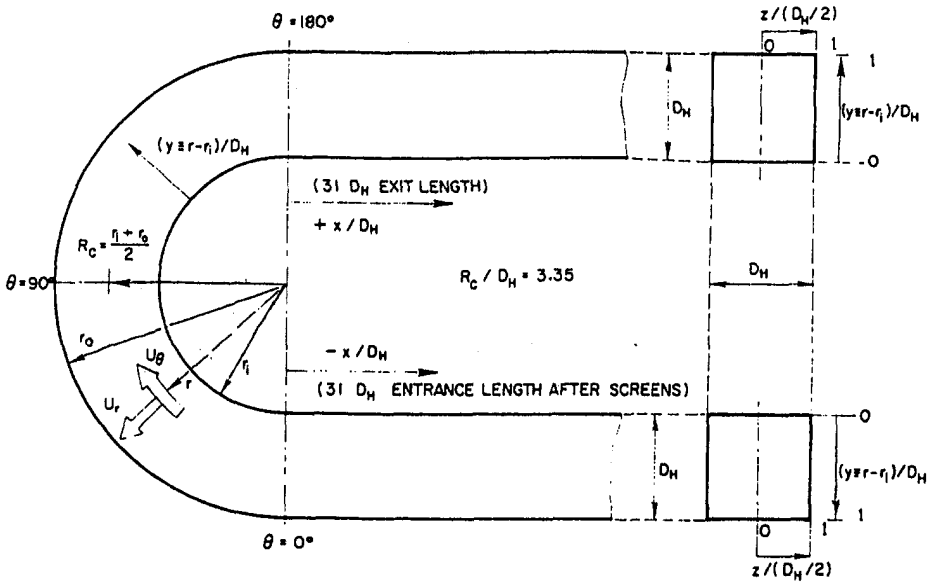

Fig. 7 Definitions for benchmark problem 5. Steady flow in 180-degree bend.

stress-equation closure level will certainly be required to predict wall interactions correctly, including curvature effects. Within this flow, the influence of the bend on the upstream tangent flow is already evident at $X = -5$. Although weak, the combination of Reynolds stress gradients in the cross-stream plane and the favorable pressure gradient at the convex wall in the bend induce a transverse flow at this section. In the first 45-degrees of the bend itself, stabilizing and destabilizing effects of the convex and concave walls, respectively, generate relatively large levels of anisotropy near these boundaries. Measurements of the turbulence characteristics in the region of the bend between 90- and 130-degrees show significant variations in the radial components due to large shearing motions induced by the core flow. As the flow enters the outlet tangent, the secondary motions are rapidly damped due to the opposing effects of the transverse pressure gradient in the bend and the oscillating nature of the secondary motion, maintaining, however, a weak secondary motion well into the downstream tangent.

N3S, FLUENT, FLOTRAN, STAR-CD, and CFD-ACE were used to simulate this flow. Table 6 provides the details of the grid resolutions used and turbulence models implemented. Here, some of the vendors made significant attempts to reproduce the experimental data through refinement of the computational grid and using a suite of turbulence models. One code (STAR-CD) reported achieving a grid convergent solution. Unfortunately, all codes fell short of predicting the measured data in the bend region at angles of 45-degrees and greater. Figure 8 displays the mean axial velocity profiles on a plane at $\theta = 90$-degrees, on the centerline running from the inner-radius wall to the outer-radius wall (i.e., where $z = 0.0$ is the centerline or symmetry plane of the duct). Figure 9 is taken from the FLUENT simulations and highlights the influence of the selection of a turbulence model to the successful simulation of complex turbulent flows. Here, the velocity vector field at a plane of $\theta = 130$-degrees is displayed, where the left and right boundaries are the inside-radial and the outside-radial surfaces of the duct, respectively, and the top boundary is the centerline of the duct. Clearly, the resolved structure of the flow field is significantly different between that generated by the standard k-ε model, the RNG model, and the Reynolds stress model. However, to lay the burden solely on the turbulence model for failing to predict the flow structure in this problem, is not presenting a complete picture of the limitations of today's commercial CFD codes. Although some refinements to the grid were performed, the resolution is still not sufficient to resolve critical scales of the flow and (except for FLUENT) all discretization schemes used in this exercise were second-order at best. Perhaps for flows such as this, higher-order discretization schemes are required.

Table 6 Summary of conditions for the benchmark simulation 5

Code	Grid resolution (Axial × Radial × Spanwise)	Turbulence models used
FLUENT	101 × 47 × 27	Standard k-ε model
	60 nodes in bend	RNG model
		Reynolds Stress model
FLOTRAN	10,240 elements	Standard k-ε model
	21,450 elements	
	52,080 elements	
N3S	26,681 nodes (final grid used)	Standard k-ε model
STAR-CD	167,000 nodes	Standard k-ε model
	250,000 nodes	RNG model
	~500,000 nodes	
CFD-ACE	40 × 40 × 20	Standard k-ε model
	18 nodes in bend	RNG model

Conclusions

A series of five benchmark problems have been simulated by several commercial CFD codes, all simulations performed by the vendors themselves. The first three problems dealt with laminar flows of varying degrees of complexity. In general, the codes that completed the first two simulations, one, a steady two-dimensional laminar flow, and the second, an unsteady two-dimensional laminar flow, gave acceptable results, when the codes were applied to the problems correctly. However, what the author found most discouraging with the solution of these two "simple" problems was the general lack of insight brought to the solution process by some of the vendors. That is, some vendors were satisfied with solutions generated at a single grid resolution, never attempting to demonstrate a grid convergent solution. With the new policy statement on numerical uncertainty that this Journal has invoked (Freitas, 1993), these results would not have been accepted in an archival publication. Further, with the demonstrated sensitivity of these two solutions to the accuracy of the spatial discretization, it was surprising that some vendors used first-order methods in the solution process.

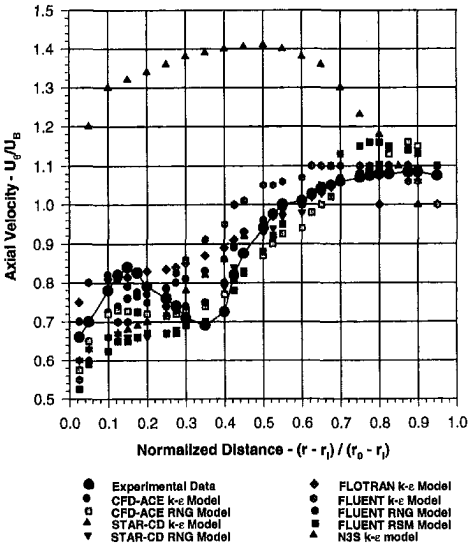

Fig. 8 Axial mean velocity profiles at θ = 90 deg

Again, a prediction based on such first-order methods is no longer considered acceptable for inclusion in this Journal.

The third benchmark problem, the unsteady, three-dimensional flow in a cavity, mandates for a successful solution the use of a spatial discretization scheme that minimizes or eliminates numerical diffusion. With numerical diffusion present, the moderate scale, secondary motions never develop, i.e., the Gortler vortices. This was clearly demonstrated in some of the simulations performed here, where the Gortler vortices were not predicted or sufficiently resolved by the grid. And again, some of the vendors simply did not demonstrate having any insights into the solution of the problem, and no attempts were made to show a grid convergent solution by any of the vendors.

In performing the two turbulent flow benchmark simulations in this exercise, the vendors did demonstrate greater insight to the problem solution and, in some cases, did solve the problems on multiple grids with significantly different resolutions. The two turbulent flow benchmarks used here, the two-dimensional flow around a square cylinder, and the three-dimensional flow in a 180-degree bend, taxed both the numerics of the codes and the turbulence models of the codes. With regard to the turbulence models, the current state-of-the-art in commercial CFD codes are the standard k-ε model and its variants (primarily RNG forms). Unfortunately, many of the problems for which commercial CFD codes are applied to, push the limits and assumptions upon which these models are based. With regard to the discretization methods, the current state-of-the-art is second-order schemes which may prove to still not be accurate enough for some classes of flow; for example, the flow through a 180-degree bend. Historically, it was believed that in spite of the limitations of the models and methods used that a series of simulations would at least resolve the trends as key parameters were varied and certainly for classes of problems this is true. However, as demonstrated in Fig. 9, which simulation is now resolving the correct trends? The mean profiles may be similar, as in Fig. 8, but the details of the flow field may be widely different. The bottomline is that the user of these codes must remember to balance grid resolution and discretization accuracy, and use the appropriate closure model.

In the course of this exercise, it was suggested by some vendors (who selected not to participate in the forum) that these two turbulent flow problems were not appropriate as benchmarks, since they potentially violated the conditions upon which traditional turbulence models are based. However, these commercial CFD codes are being used today by industry, to study similar flows. The author has been at vendor demonstrations in which vendor staff members have claimed the ability to solve these problems. In addition, with some commercial codes using new types of turbulence models such as the RNG extension to the k-ε model and other nonlinear turbulence closures, it is relevant and appropriate to attempt these types of benchmarks. Clearly demonstrated in this exercise, is that further research into more advanced turbulence models for use in commercial CFD codes is required (not a big surprise). And, implementation of higher-order discretization schemes may also be required. These are not unreasonable demands, especially when one considers that both of these turbulent flow problems are essentially, idealizations of typical, industrial flow situations; i.e., one an external flow and the other an internal flow.

Acknowledgments

The author would like to applaud and thank each of the vendors who participated in each Forum, but particularly those vendors that approached this effort with an open and honest attitude. This was especially true for those vendors who participated in the CFD Biathlon Forum. The author recognizes that it is very difficult to report simulation results which do not predict the experimental data within an accepted level of accuracy, especially after making every effort to provide the best solution possible and still falling short. Clearly, for each vendor, the presentation of the simulation results for Benchmark Problem 5 was difficult. But, the author believes that such an exercise provides creditability to this growing CFD industry and will

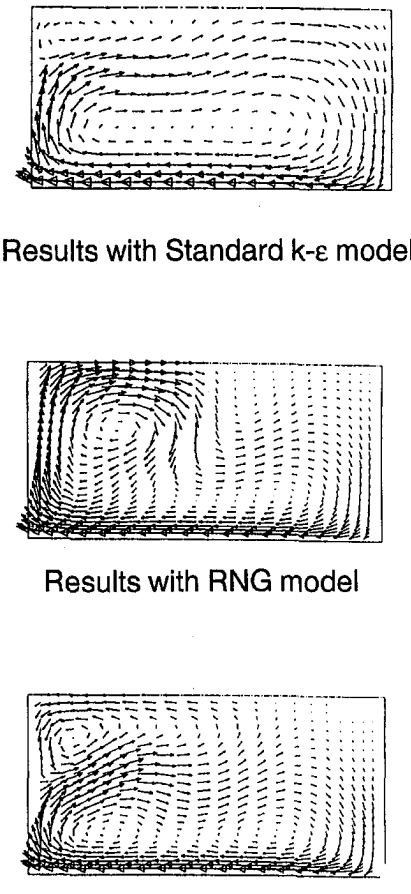

Fig. 9 Velocity vector field predicted by three different turbulence models. Plane displayed is θ = 130 deg. Simulation results from FLUENT.

ultimately serve the interests of the engineering and scientific community.

References

Acrivos, A., Leal, L. G., Snowden, D. D., and Pan, F., 1968, "Further Experiments on Steady Separated Flows Past Bluff Objects," *Journal of Fluid Mechanics,* Vol. 34, Part I, pp. 25–48.

Armaly, B. F., Durst, F., Pereira, J. C. F., and Schonung, B., 1983, "Experimental and Theoretical Investigation of Backward-Facing Step Flow," Journal of Fluid Mechanics, Vol. 127, pp. 473–496.

Chang, S. M., Humphrey, J. A. C., and Modavi, A., 1983, "Turbulent Flow in a Strongly Curved U-Bend and Downstream Tangent of Square Cross-Sections," *Physico-Chemical Hydrodynamics,* Vol. 4, No. 3, pp. 243–269.

Dennis, S. C. R., and Chang, G.-Z., 1970, "Numerical Solutions for Steady Flow Past a Circular Cylinder at Reynolds Numbers up to 100," *Journal of Fluid Mechanics,* Vol. 42, Part 3, pp. 471–489.

Dongarra, J. J., 1993, "Performance of Various Computers Using Standard Linear Equations Software," Computer Science Department, University of Tennessee, Report CS-89-85, January 13.

Durao, D. F. G., Heitor, M. V., and Pereira, J. C. F., 1986, "A Laser Anemometry Study of Separated Flow Around a Squared Obstacle," *Laser Anemometry in Fluid Mechanics III,* Adrian, R. J. et al., eds., Ladoan-IST, Lisbon, Portugal, pp. 227–243.

Durao, D. F. G., Heitor, M. V., and Pereira, J. C. F., 1988, "Measurements of Turbulent and Periodic Flows Around a Square Cross-section Cylinder," *Experiments in Fluids,* Vol. 6, pp. 298–304.

Freitas, C. J., ed., 1993, "The CFD Triathlon: Three Laminar Flow Simulations by Commercial CFD Codes," *Proceedings of the Fluids Engineering Conference,* ASME, FED-Vol. 160.

Freitas, C. J., 1993, "Policy Statement on the Control of Numerical Accuracy," ASME JOURNAL OF FLUIDS ENGINEERING, Vol. 115, No. 3, pp. 339–340.

Freitas, C. J., Street, R. L., Findikakis, A. N., and Koseff, J. R., 1985, "Numerical Simulation of Three-Dimensional Flow in a Cavity," *International Journal for Numerical Methods in Fluids,* Vol. 5, pp. 561–575.

Freitas, C. J., and Street, R. L., 1988, "Non-Linear Transient Phenomena in a Complex Recirculating Flow: A Numerical Investigation," Vol. 8, pp. 769–802.

Hirt, C. W., and Nichols, B. D., 1981, "Volume of Fluid (VOF) Method for the Dynamics of Free Boundaries," *Journal of Computational Physics,* Vol. 39, pp. 201.

Hirt, C. W., and Sicilian, J. M., 1985, "A Porosity Technique for the Definition of Obstacles in Rectangular-Cell Meshes," *Proceedings of the Fourth International Conference on Numerical Ship Hydrodynamics,* National Academy of Science, Washington, D.C., p. 450.

Humphrey, J. A. C., Chang, S. M., and Modavi, A., 1982, "Developing Turbulent Flow in a 180 Degree Bend and Downstream Tangent of Square Cross-Sections," Report No. LBL-14844, Lawrence Berkely Laboratory, University of California, Berkeley.

Issa, R. I., 1983, "Solution of the Implicitly Discretized Fluid Flow Equations by Operator-Splitting," Imperial College of Science and Technology, Report FS/82/15, Sept.

Kim, J., and Moin, P., 1985, "Application of a Fractional-Step Method to Incompressible Navier-Stokes Equations," *Journal of Computational Physics,* Vol. 59, pp. 308–323.

Kline, S. J., Morkovin, M. V., Sovran, G., and Cockrell, D. J., eds., 1968, *Computation of Turbulent Boundary Layers—1968 AFOSR-IFP-Stanford Conference, Volume 1,* Department of Mechanical Engineering, Stanford University.

Koseff, J. R., Street, R. L., Gresho, P. M., Upson, C. D., Humphrey, J. A. C., and To, W.-M., 1983, "A Three-Dimensional Lid-Driven Cavity Flow: Experiment and Simulation," *Proceedings, Third International Conference on Numerical Methods in Laminar and Turbulent Flow,* Seattle, WA. Aug., pp. 564–581.

Koseff, J. R., and Street, R. L., 1984, "Visualization Studies of a Shear Driven Three-Dimensional Recirculating Flow," ASME JOURNAL OF FLUIDS ENGINEERING, Vol. 106, pp. 390–398.

Launder, B. F., Reece, G. J., and Rodi, W., 1975, "Progress in the Development of a Reynolds-stress Turbulence Closure," *Journal of Fluid Mechanics,* Vol. 68, pp. 537–566.

Launder, B. F., and Spalding, D. B., 1974, "The Numerical Computation of Turbulent Flows," *Computer Methods in Applied Mechanics and Engineering,* Vol. 3, pp. 269–289.

Leonard, B. P., 1979, "A Stable and Accurate Convective Modeling Procedure Based on Quadratic Upstream Interpolation," *Computer Methods in Applied Mechanics and Engineering,* Vol. 19, pp. 59–98.

Patankar, S. V., and Spalding, D. B., 1972, "A Calculation Procedure for Heat, Mass and Momentum Transfer in Three-Dimensional Parabolic Flows," *International Journal of Heat and Mass Transfer,* Vol. 15, pp. 1787.

Perng, C.-Y., and Street, R. L., 1989, "Three-Dimensional Unsteady Flow Simulations: Alternative Strategies for a Volume-Averaged Calculation," *International Journal for Numerical Methods in Fluids,* Vol. 9, pp. 341–362.

Prasad, A. K., and Koseff, J. R., 1989, "Reynolds Number and End-wall Effects on a Lid-Driven Cavity Flow," *Physics of Fluids A,* Vol. 1, No. 2, pp. 208–218.

Norris, L. H., and Reynolds, W. C., 1975, "Turbulent Channel Flow with a Moving Wavy Boundary," Stanford University, Report No. FM-10.

Rodi, W., 1991, "Experience with Two-Layer Models Combining the k-ϵ Model with a One-equation Model Near the Wall," AIAA-91-0216.

Schlichting, H., 1979, *Boundary Layer Theory,* McGraw-Hill.

Schnipke, R. J., and Rice, J. G., 1986, "A Streamline Upwind Finite Element Method for Laminar and Turbulent Flow," Department of Mechanical and Aerospace Engineering, University of Virginia, Report No. UVA/643092/MAE86/342.

Takami, H., and Keller, H. B., 1969, "Steady Two-Dimensional Viscous Flow of an Incompressible Fluid Past a Circular Cylinder," *Physics of Fluids Supplement II,* Vol. 12, pp. II-51–II-56.

Tritton, D., 1959, "Experiments on the Flow Past a Circular Cylinder at Low Reynolds Numbers," *Journal of Fluid Mechanics,* Vol. 6, pp 547–567.

Yakhot, V., and Orszag, S. A., 1986, "Renormalization Group Analysis of Turbulence, I. Basic Theory," *Journal of Scientific Computing,* Vol. 1, No. 1, pp. 1–51.

Yakhot, V., and Smith, L. M., 1992, "The Renormalization Group, the ϵ-Expansion and Derivation of Turbulence Models," *Journal of Scientific Computing,* Vol. 7, No. 1, pp. 35–61.

Yakhot, V., Orszag, S. A., Thangam, S., Gatski, T. B., and Speziale, C. G., 1992, "Development of Turbulence Models for Shear Flows by a Double Expansion Technique," *Physics of Fluids A,* Vol. 4, No. 7, pp. 1510–1520.

D. M. Rooney
Associate Professor.

J. Rodichok[1]
Undergraduate Research Assistant.

K. Dolan[2]
Undergraduate Research Assistant.

Department of Engineering,
Hofstra University,
Hempstead, NY 11550

Finite Aspect Ratio Effects on Vortex Shedding Behind Two Cylinders at Angles of Incidence

Wind tunnel tests were undertaken at subcritical Reynolds numbers to determine the vortex shedding characteristics behind a pair of finite circular cylinders at distances from one to six diameters apart and at all angles to one another. In addition, individual finite cylinders with aspect ratios $0.67 \leq L/D \leq 11.33$ were examined to determine the effect of aspect ratio on shedding frequency, and to measure the frequency of the tip vortex when it is present. Aspect ratio was found to be a significant factor in the difference between shedding frequencies of the two cylinders at oblique angles. It was also found that "lock-on" of the two frequencies occurred when longer aspect ratio cylinders were upstream of shorter ones, but not in the reverse case.

1 Introduction

Even though real world instances of circular cylinders interacting with a fluid environment occur over a wide range of length-to-diameter ratios (for example, smokestacks, marine cables, gas tanks, telephone lines), experimenters over the years have devoted by far a preponderant attention to the flow characteristics around a solitary two-dimensional, or infinite cylinder. The variations with Reynolds number of the drag force, vortex shedding frequency, fluctuating lift force, and base pressure have provided sufficient cause to generate research data that, if combined, would fill many journal volumes. But in the last two decades, studies have increasingly focused on the more commonly occurring case of finite length in a circular cylinder, which of course produces a very complex three-dimensional flow pattern in the cylinder wake. In addition, research has been conducted on interference effects between two or more cylinders in relatively close proximity to one another, although vortex shedding studies have been thus far limited to the interaction of infinite length cylinders. It is the purpose of the present paper to look at one feature (the wake vortex shedding frequency) of a flow around two interfering cylinders which are both finite in length, though not necessarily of the same length.

Since this paper represents an incremental advance in a well-trod field of inquiry, it is instructive to review what earlier investigations have already established, as well as where questions or disagreements still remain.

Smoke flow photography and detailed measurements of surface pressure distributions around individual finite length circular cylinders have shown that the flow over the free end greatly affects the wake characteristics, especially as the length-to-diameter (L/D) ratio increases. Okamoto and Yagita (1973) showed, for example, that base pressure coefficients (Cp at 180 deg from the front stagnation point) vary with spanwise distance for up to four diameters from the free end when $L/D \geq 7$, and vary all the way to the fixed end for shorter cylinders. As aspect ratio increases, the value of C_{pb} along the span becomes less negative, with the flow from the free end acting much like that over the tip of a finite wing to decrease the suction pressure. It follows that both the local and the mean drag coefficients also decrease with decreasing aspect ratio. Interestingly, they noted the presence of coherent vortex shedding only for $L/D \geq 7$, and also found that the Strouhal number ($St = fD/U\infty$) increased both with increasing aspect ratio and with increasing Reynolds number. They also found a gradual spanwise decrease in St as the free end of the cylinder was approached. A number of later investigators have presented results that contradict these findings. For example, Vickery (1968), Sakamoto and Arie (1983), Sin and So (1987), Zdravkovich et al. (1989), Szepessy and Bearman (1991), and to some extent Baban et al. (1989), have all measured vortex shedding activity at values of $L/D \leq 7$. Sakamoto and Arie used photographs of smoke patterns to discern what they suggest are two different kinds of vortex shedding: an arch-type or symmetric pair, present when $L/D \leq 2.5$, and the well-known alternating Karman shedding which predominates when $L/D \geq 2.5$. Bearing in mind the fact that their tests were carried out in a turbulent boundary layer (typical of the lower atmosphere), their conclusion that the Strouhal number remained constant over the cylinder span also was at variance with Okamoto and Yagita's results. Kawamura et al. (1984) undertook detailed hot-wire measurements in the wake of various relative length finite cylinders and disputed the existence of the so-called "arch-type" vortex. Rather, they pointed to the presence of three separate systems in longer cylinders: a free end controlled trailing vortex (the analogue of the wing-tip vortex), the Karman vortex, and a "necklace" or horseshoe vortex at the attached end, such as has long been observed in the flow around piers. For shorter cylinders, the central or Karman type is not present. In agreement with Okamoto and Yagita, they could not detect any shedding for $L/D \leq 6$, surmising that the trailing vortex extended to the base and thus suppressed the Karman street. For larger aspect ratios, the free end trailing vortex registered as a periodic signal with a lower Strouhal number than the central Karman street. Farivar (1981) found the same result, though with a greater discontinuity in Strouhal number dividing the regimes. Ayoub and Karamcheti (1982), who conducted the most thorough experimental investigation of end flow patterns, disagreed with Kawamura et al. and Okamoto et al. by proclaiming that vortices must form discrete cells rather than undergo continuous change in the spanwise direction.

Of the studies reviewed that involve multiple cylinders, all employed cylinders spanning the entire width of the wind or water tunnels. (Zdravkovich (1977) provides a very useful summary of earlier studies in this area.) Bearman and Wadcock (1973) looked at the effect on pressure and vortex shedding of increasing separation distance between two cylinders side-by-

[1] Currently, Engineer, H.E.C. Energy and Design Services, Smithtown, NY 11787.

[2] Currently, Engineer, Central Sprinkler Corporation, Lansdale PA 19446.

Contributed by the Fluids Engineering Division for publication in the JOURNAL OF FLUIDS ENGINEERING. Manuscript received by the Fluids Engineering Division August 31, 1992; revised manuscript received October 27, 1994. Associate Technical Editor: R. L. Panton.

side. Base pressures were found to revert to isolated cylinder values at five diameters apart (measured from centerline to centerline), while the Strouhal number jumped from under 0.10 (with cylinders touching) to 0.35 with less than two diameters separation, before dropping to 0.20 at greater than two diameters apart. Williamson (1985) noted the interactions that take place in the wake of such cylinders, producing in some instances a binary vortex street, or anti-phase shedding in others. In particular, he found that for small gap widths the shedding frequency doubles on one side of the cylinder pair. Kiya et al. (1980) placed two cylinders at various angles to one another up to $5\frac{1}{2}$ diameters apart. For side-by-side separation distances less than 1.4 diameters, the pair acted as a single cylinder, while for distances greater than two diameters they behaved as isolated cylinders. In between, one cylinder had a narrower wake and correspondingly higher shedding frequency than the other, as the gap flow was biassed to one side. In a tandem arrangement, no shedding was observed behind the upstream cylinder until the separation distance exceeded three diameters. At other angles, the upstream cylinder always had a smaller wake (and higher Strouhal number) than the downstream cylinder. Bokaian and Geoola's (1984) more fragmentary results only partially agreed with this result. Baxendale et al. (1985) and Barnes et al. (1986) subsequently observed a lock-on effect that occurred when a downstream cylinder was at an angle of 30 deg or less (with respect to the oncoming flow direction) behind the upstream cylinder. Curiously, Kiya et al. did not cite evidence of that phenomenon.

2 Experimental Apparatus and Procedure

A series of tests to determine carefully the effect of aspect ratio on Karman vortex shedding patterns of individual cylinders, and then of two cylinders in close proximity to one another, was undertaken in a subsonic wind tunnel with a circular test section 30.5 cm in diameter. The experimental setup was as follows. Test cylinders of varying aspect ratio, all of diameter 1.9 cm, were fixed on a continuously rotatable circle flush mounted within a smooth flat plate that served as the test section lower surface. The distance from the plate to the test section ceiling was 24.5 cm, and from the cylinder location to the leading edge of the plate at the wind tunnel inlet was 48.3 cm. The test section freestream turbulence intensity was measured at 1.8 percent lower than that of some of the simulated boundary layer flows employed by earlier investigators, but higher than is found in many wind tunnel tests. It was low enough, however, to permit easy detection of vortex activity. It should also be noted that previous studies by Szepessy (1991) have shown very little effect on vortex shedding frequency caused by increasing freestream turbulence levels from .05 to 3.3 percent. (Also Kareem et al. (1989) reported negligible change in shedding in a turbulent boundary layer whether at 7 percent or at 20 percent intensities.) In the present tests, the mean upstream flow was laminar and uniform. Given that the cylinders were placed at a distance from the leading edge of the flat plate, the boundary layer at the surface was turbulent, and was found with the hot-wire instrumentation (to be described below) to be approximately 1.4 cm thick, a value virtually identical with that predicted by the classical turbulent boundary layer solution. The value of 1.4 cm was arrived at by traversing a hot-wire probe upward from the flat plate at the location of the cylinders, and monitoring the signal on an oscilloscope. A marked decrease of fluctuating activity was taken to represent the top of the turbulent boundary layer.

The maximum tunnel blockage produced in the cross-sectional area above the flat plate was 7.8 percent, corresponding to two test cylinders with aspect ratios $L/D = 10.67$ and $L/D = 2.67$. All tunnel velocities were corrected for the test cylinder blockage. A total of 17 cylinder heights were examined, in increments of $\Delta L/D = 0.67$, with the smallest being at $L/D =$ 0.67. When two cylinders were in the test section, readings were taken for every 7.5 deg increment in angle of incidence to one another. The Reynolds number based on cylinder diameter for all tests varied within the range $7.8 \times 10^3 \leq \mathrm{Re} \leq 2 \times 10^4$. Repeated tests showed virtually no change in Strouhal number within these limits. This is in disagreement with a reported result of Okamoto and Yagita (1973), who found that St decreased significantly with decreasing Reynolds number for $\mathrm{Re} < 10^4$, and that the decrease was sharper as L/D decreased. Attempts to reproduce their results for $L/D = 10.67$ over the range $2.3 \times 10^3 \leq \mathrm{Re} \leq 2.4 \times 10^4$ were decidedly negative. (It should be noted that the measurement techniques and spectral representations of Okamoto and Yagita from two decades ago were somewhat wanting in precision.)

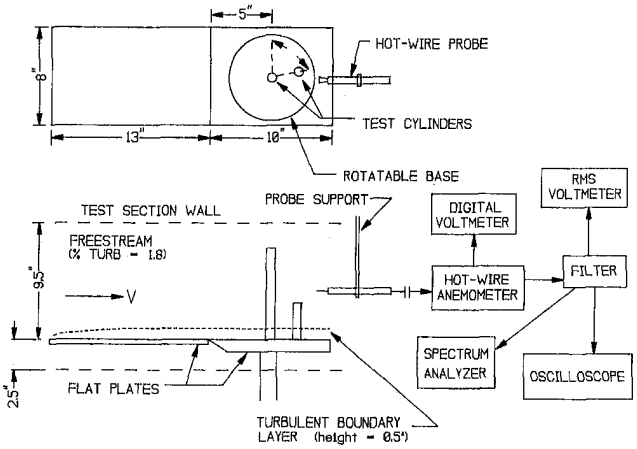

Fig. 1 Experimental test setup

A hot-wire probe connected to a TSI linearizing anemometer traversed the wake behind the cylinders and the signal was then analyzed in a Bruel-Kjaer Spectrum Analyzer. A digital voltmeter, an RMS voltmeter, an oscilloscope, and a filter also formed part of the test equipment. The filter was used to allow a bandwidth of signals between 1 Hz and 1000 Hz through for analysis, thereby cutting down on electronic noise. Controls exterior to the test section allowed positioning of the probe spanwise along the cylinders and across the wake to search for optimum vortex activity. Between tests it could also be relocated in the streamwise direction. Velocities were obtained using a pitot-static tube connected to a digital multimanometer. The test set-up is displayed in Fig. 1. The 95 percent certainty of replication in pressure readings from the digital multimanometer was ± 0.01 in H_2O, and in frequencies determined from the spectrum analyzer $\pm$ 2 Hz over a 100 Hz full range, both being virtually exclusively precision error. The resulting error range for velocity readings was consequently ± 2.4 percent, and in Strouhal number $\pm$ 3.1 percent, yielding a variation in typical Strouhal number of $\pm .0044$.

3 Results and Discussion

Previously published studies, for instance those of Vickery (1968), Okamoto and Yagita (1973), Farivar (1981), and Sakamoto and Arie (1983), have yielded a certain amount of scatter in the data for low aspect ratio finite cylinder shedding frequencies, so the first stage of this investigation consisted of a detailed examination of aspect ratio effects on single cylinder shedding for the specific flow characteristics (turbulence intensity, Reynolds number range, and boundary layer height) of the test setup. The results are plotted in Fig. 2, as Strouhal number versus cylinder aspect ratio L/D. The Strouhal number was taken to be the average value recorded at all spanwise stations over which Karman-type shedding was clearly measured. Typically this meant an average of 15 or more readings taken from

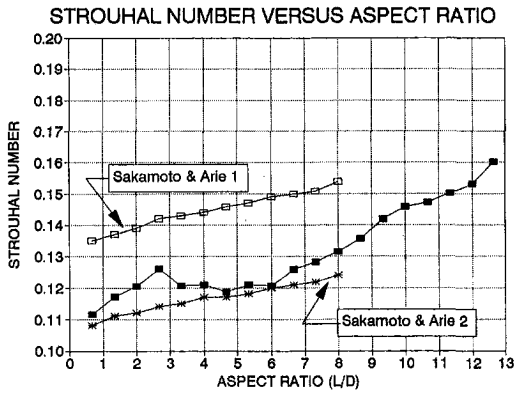

Fig. 2 Variation of spanwise averaged Strouhal number with cylinder aspect ratio

two to five millimeters apart, depending on the length of the cylinder. An average was considered appropriate since the value was not precisely constant along the cylinder span, as will be shown shortly. Two interesting features emerge from the graph of the data. First, the Strouhal number monotonically increases with aspect ratio in the range $5.33 \leq L/D \leq 11.33$, and presumably goes on to approach asymptotically the two dimensional value of St = 0.21. However, in the range $0.67 \leq L/D \leq 5.33$, the value increases at first and then decreases. The values shown are the result of numerous tests which consistently displayed this trend. A review of the actual spectra further yields the fact that in the range $0.67 \leq L/D$ 2.00, the signals were very broad; in the range $2.67 \leq L/D \leq 4.67$, they became much sharper; and then, from $5.33 \leq L/D \leq 7.33$, they became broader again before returning once again to sharply defined frequencies at all higher aspect ratios. Neither the mechanism suggested by Sakamoto and Arie (1983) nor that suggested by Kawamura et al. (1984) seems to fit comfortably with these observations. The former supposed a switch from an arch-type to a Karman-type shedding around $L/D = 2.5$, but the flow is known to be more complicated then their low Reynolds number flow visualization results imply. Their smoke pattern photographs of cylinder wakes, for example, give no indication of the spanwise flow component which Kawamura et al. have clearly shown exists. The latter, however, believe that the downward flow over the free end suppresses the Karman street entirely for aspect ratios less than a critical value dependent on boundary layer thickness, which in their case was $L/D = 6$. The present results showing very strong signals in the range $2.67 \leq L/D \leq 4.67$ are obviously not compatible with their model. It is highly conceivable that in that aspect ratio range the downward end flow serves not to override the Karman street, but causes instead a widening of the wake that results in the lowering of the vortex shedding frequency. Continuing with this supposition, at very low aspect ratios ($L/D \leq 2.00$), the horseshoe vortex is the predominant influence on the Karman street and is reflected in the first rise in Strouhal number with aspect ratio, before the free end flow is strengthened (by the greater three dimensionality that higher aspect ratios produce) and exerts its effect. The horseshoe vortex and indeed the immersion of much of any very low aspect ratio cylinder within the turbulent boundary layer explain the very broad spectra measured. It is interesting to note that Zdravkovich et al. (1989), allowing for the considerable scatter in their data, found a similar downward trend in Strouhal number in the range $2 \leq L/D \leq 8$ in the case of a cylinder with both ends free. While obviously differing from single, free end cases, their set-up nevertheless allows for some comparison because the plane of symmetry at the mid-point of their cylinders acts in some respects like a solid surface.

Also included in Fig. 2 for reference are the upper and lower ranges of values obtained by Sakamoto and Arie for finite cylinders in a turbulent boundary layer. The upper curve corresponds to a case where the cylinder was submerged to 70 percent of its height, and the lower curve to a case where the cylinder was completely submerged, its free end rising only one third the height of the boundary layer. For this second case, the approach velocity is considerably reduced, being less than 80 percent of freestream at the cylinder midpoint. Obviously these lower speeds reduce the vortex shedding frequency. For the upper case, the cylinder midpoint velocity is essentially equal to the freestream flow, but some kind of cellular structure might still be expected for this sheared flow. In any case their flow environment differed sufficiently from that of the present tests to make direct comparisons difficult.

Figure 3 is a plot of Strouhal number as a function of relative spanwise distance along a cylinder for several of the aspect ratio cases examined. The cases shown were chosen to illustrate certain recurring features noticed in the full series of tests. Once again, the decrease in Strouhal number from $L/D = 2$ to $L/D = 4.67$ can be seen, followed by the gradual increase as aspect ratio further rises. But also evident is a slight but perceptible rise in local Strouhal number along the span moving toward the free end in cases where $L/D > 5$. It is possible that the traverse position behind the cylinder is responsible for that shift, since there was no shear flow present, and non-cellular spanwise vortex shedding is not easily justifiable. More importantly, for some cases no frequencies were discerned above a given relative height, and so the data points end at $X/L < 1$. In addition, and even more dramatic, is the sudden drop in vortex shedding frequency that takes place somewhere around midspan of the higher aspect ratio cases. Regardless of the average St in the lower portion of the cylinder, a dominant frequency of about 20 Hz (St = .036) or 40 Hz (St = .072) was registered as the free end was approached. The latter frequency is just the former doubled, presumably representing the probe's picking up both sides of an end-controlled vortex. The signal was too sharp and sustained to be due to a fluctuating cell boundary between the end frequency and the regular Karman frequency. Figure 4 displays the actual power spectral density variations with relative height for the cases $L/D = 2.0$, 7.33 and 9.33. It should be noted that Zdravkovich et al. (1989), have observed that finite cylinders experience, in addition to the Karman vortex street, a periodic shedding similar to that on a delta wing at the free end. The relatively low frequency occurrences noted here, which were very strong on the upper third of the cylinder in a number of the higher aspect ratio cases, indicate the presence of that shedding. Among previous investigators who have measured it, Farivar (1981), who plotted results for cylinders in the range $10 \leq L/D \leq 12.5$, most clearly showed that there is an abrupt changeover from the Karman to free end frequencies.

Figure 5 documents the extent along the cylinder span that the primary vortex street persists. It can be seen that at low

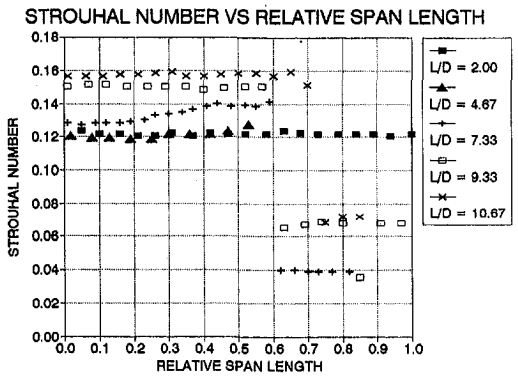

Fig. 3 Spanwise change in local Strouhal number for selected finite cylinder aspect ratios

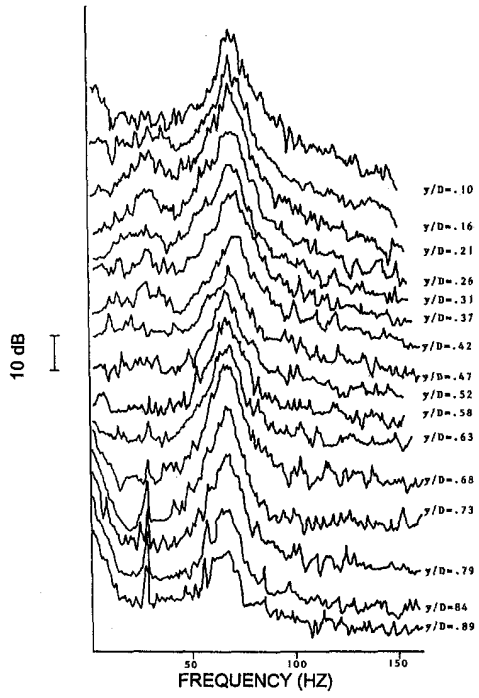

Fig. 4(a)

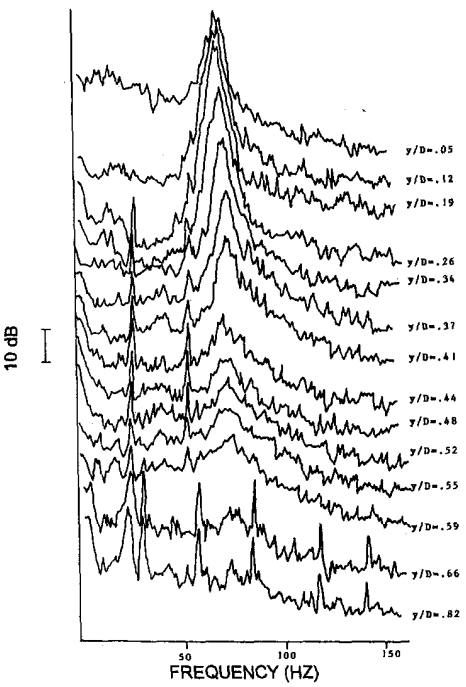

Fig. 4(b)

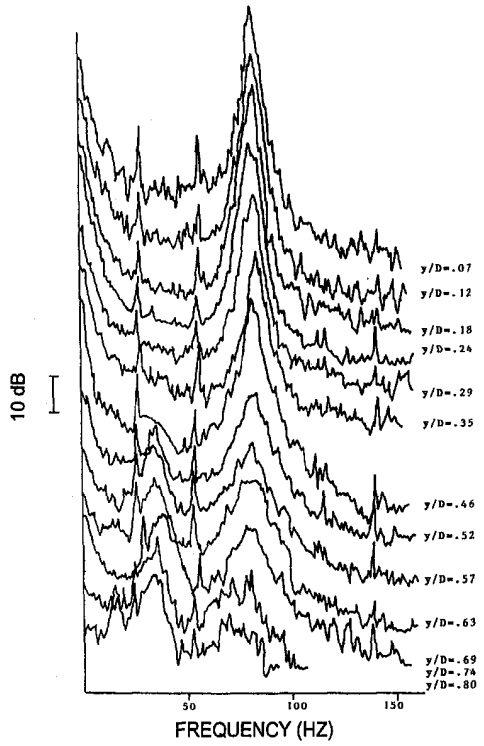

Fig. 4(c)

Fig. 4 Power spectral density of wake velocity at various relative cylinder heights for (*a*) $L/D = 2$, (*b*), $L/D = 7.33$, (*c*) $L/D = 9.33$

aspect ratios the dominant frequency extends almost the entire span, but in the range $4 \leq L/D \leq 8$, it covers only just greater than half the span. As the aspect ratio continues to increase, so does the region experiencing the Karman shedding. As can be seen, the results in the range $2 \leq L/D \leq 6$ compare reasonably well with values found by Sakamoto and Oiwake (1984) for the maximum height for regular shedding. They also found a lower bound that could be as high as 25 percent of the cylinder span, but their measurements were undertaken in a turbulent boundary layer environment.

For examining interference effects, two cylinders with aspect ratios $L/D = 8$ and $L/D = 2.67$ were chosen first. Reference to Fig. 2 reveals that their solitary Strouhal numbers are St = .132 and St = .126, respectively. Placing two cylinders in near proximity to one another drastically affects the flow field around them and the resulting vortex shedding patterns. As a first illus-

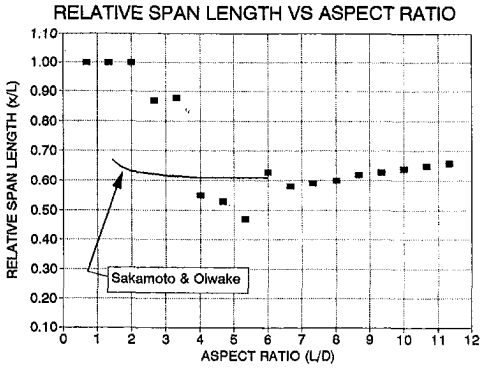

Fig. 5 Fraction of cylinder span over which Karman shedding exists versus cylinder aspect ratio

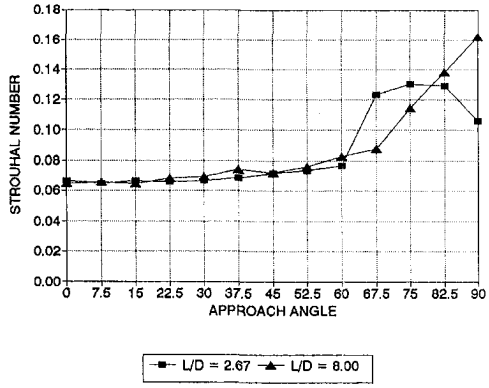

Fig. 7 Variation in Strouhal number with approach angle for two cylinders (L/D = 8 and L/D = 2.67) at one diameter spacing

tration of this fact, Fig. 6 shows actual vortex shedding frequencies measured along the two cylinders at Re = 1.38×10^4 with the cylinders placed in a line perpendicular to the oncoming flow, while the spacing between their spanwise axes increases from one to six diameters. At one diameter separation the cylinders act as a unit with twice the diameter of a single cylinder; hence the shedding frequency of 38 Hz over the lower portion. A small region of high frequency 93.5 Hz vortices appeared around midspan of the larger cylinder, and was then displaced by the free end controlled 22.5 Hz signal over the upper half. At two diameters apart, the flow is even more complicated, with broad band signals suggesting multiple frequencies (or unstable boundaries) at certain heights. Nevertheless over the small cylinder, two distinct regions emerged, with 93.5 Hz shedding giving way to 73.5 Hz shedding about midway up the cylinder, while the 73.5 Hz signal dominated less than one third of the larger cylinder's length. Kiya et al. (1980) had also found multiple frequencies at similar spacings. The divergence in the measured shedding frequency is a consequence of the gap flow being deflected to one side. For their infinite cylinders, they also found a reversion to solitary cylinder Strouhal numbers, with a threshold separation distance of only two diameters. In the present set of experiments, when finite cylinders were three diameters apart, the shedding had begun to approach the isolated case for the longer cylinder, although the shorter one appeared locked into the longer one's frequency. When the distance increased to four, five, and six diameters, the independent shedding frequencies of the two aspect ratios were gradually approached. Conversion of the frequencies at six diameters apart gives Strouhal numbers of .135 for the larger and .125 for the smaller cylinder.

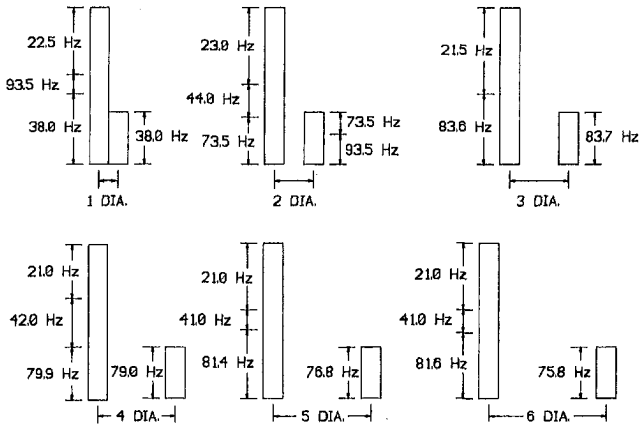

Fig. 6 Vortex shedding frequencies measured behind two side-by-side cylinders (L/D = 8 and L/D = 2.67) at spacings from one to six diameters

Figure 7 illustrates the variation in Strouhal number with the two cylinders side by side, but varying the angle α they make with the oncoming flow from 0 deg (side by side) to 90 deg (front and back). For this test measurements were taken at a height 1.8 cm above the cylinder bases. With the longer cylinder in front, the Strouhal number increased slowly with α at first, and then rapidly as the short cylinder in the back narrowed the wake, with a maximum St = .162 reached when the cylinders were in line with the flow. When the short cylinder was placed in front of the longer one, the maximum Strouhal number attained was only St = .130, and it actually decreased to St = .105 when the cylinders were in line. Clearly a different wake structure existed (even though the cross-sectional geometry at probe height was unchanged in the two cases) because of the different conditions present at higher stations in this strongly three dimensional flow. Again, a comparison with infinite cylinder results is called for. Kiya et al. (1980) measured St = .08 for α = 0 deg, rising slowly to St = .11 at α = 75 deg, and then dramatically increasing to St = .29 at α = 90 deg. With both cylinders spanning the test section, the wake is more streamlined when they are in tandem (α = 90 deg) than with the finite cylinders in tandem.

Figure 8 presents graphs of the Strouhal number measured at the same probe height as in the previous test, for both the L/D = 8 and L/D = 2.67 cylinders as a function of approach angle α and relative distances from three diameters to six diameters apart. No graph is presented for the two diameter separation distance because the peak frequencies were too broad band to pick out a dominant value, again emphasizing the particular complexity of flow interactions at that distance apart. Some of those broad signals, however, were at frequencies approximately double the values found more distinctly at three or greater diameters apart. These signals are again consistent with values found by Kiya et al. (1980) for their infinite cylinders, and are explicable in light of the results reported by Williamson (1985). He noted the existence of a second harmonic mode of vortex shedding at close side by side spacing, the result of vortex pairs in the gap being amalgamated with the outer vortices to one side of the cylinder pair. At larger gap widths this phenomenon no longer occurs.

Referring again to Fig. 8, corresponding to the case of the longer cylinder upstream of the shorter one, it can be vividly seen that the shorter cylinder's vortex shedding is captured or locked into the longer cylinder's when it falls within a region of influence given by α = 60 deg or higher. This capturing is most pronounced in the three diameter test, where the Strouhal number of the rear, shorter cylinder jumped from St = .111 to St = .161 as it moved from 60 to 67.5 deg behind the longer cylinder. Also evident from the graphs is that the divergence between the frequencies of the two cylinders reached a maximum as relative distance decreased and at angles just before

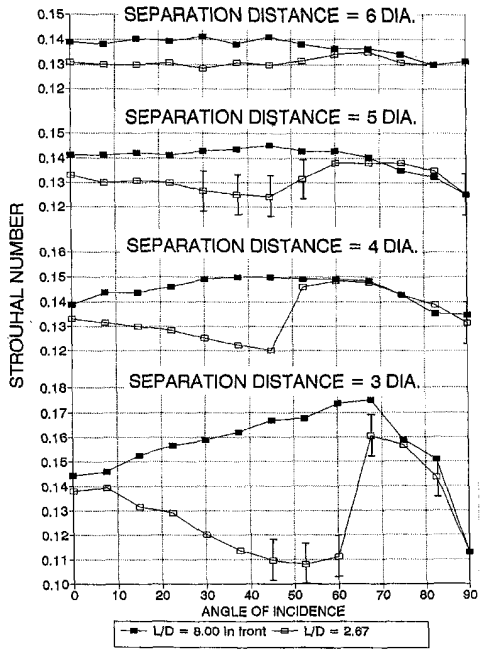

Fig. 8 Strouhal number for two cylinders (L/D = 8 in front of L/D = 2.67) as a function of approach angle at spacings of (*a*) three diameters, (*b*) four diameters, (*c*) five diameters, (*d*) six diameters

lock-on occurred. On this and succeeding graphs, a response width bar indicates when the measured frequency was broad-banded.

There are, of course, two factors responsible for the divergence in the Strouhal numbers. The first is their difference in aspect ratio, and the second is the biassed gap flow between the two cylinders which becomes more pronounced the closer the spacing between them. A comparison between Figs. 8 and 9 elucidates the relative importance of those factors, since the second case shows results obtained with the shorter cylinder in the upstream position. At relatively close spacings, positioning the shorter cylinder in front (Fig. 9(a)) produces a similar result as when the longer one is in the forward position (Fig. 8(a)). The maximum gap between Strouhal numbers is somewhat smaller, as would be expected from the effect of aspect ratio on solitary shedding frequencies. Instead of a ΔSt_{max} = .063, one finds ΔSt_{max} = .040. In addition, the frequencies actually lock on only when the cylinders are almost in tandem. Barnes et al. (1986) and Baxendale et al. (1985) were the first to report the lock-on phenomenon with infinite cylinders. In fact the latter's results, plotted in the range 40 deg $\leq \alpha \leq$ 90 deg for a separation distance of three diameters, showed the upstream cylinder at St = .214 and the downstream one at St = .199 at α = 40 deg, with lock-on occurring at α = 65 deg at St = .192, and the joint value dropping to St. = .175 at α = 90 deg. Their divergence was therefore not as extreme as in the present case, but the angle of lock-on was virtually identical.

It is obvious from the series of results plotted in Fig. 8 that the frequency measured behind the upstream cylinder increases up to the lock-on angle. As Zdravkovich (1977) has pointed out, the gap flow produces a narrowing of the streamlines flowing between the cylinders, thereby compressing the wake of the forward cylinder, in a process which is called a "wake displacement." Then, once the lock-on angle is exceeded, there is a decrease in Strouhal number that is magnified as the tandem arrangement is approached. This trend was present in all the cases investigated, and correlates well with Kiya et al.'s (1980) results for infinite cylinders at similar spacings. There is, of course, no gap flow in the tandem arrangement, and hence no narrowing of the wake behind either cylinder. The rear cylinder is now fully immersed in the wake of the forward one, so its shedding frequency decreases proportionally with increasing velocity defect in the oncoming flow caused by the forward cylinder wake.

When the separation distance between the cylinders is increased to four diameters, the divergence between the front and back cylinder shedding frequencies diminishes accordingly, with the longer cylinder in the forward position (Fig. 8(b)). Nevertheless a distinct lock-on occurs at α = 52.5 deg, and this process continues as the spacing increases to five and six diameters, with a weaker lock-on being evident around α = 60 deg (Figs. 8(c) and 8(d). Obviously as the spacing increases at low angles of incidence, there is less and less of a biassed gap flow. The largest spacing examined corresponds to the limit at which Williamson (1985) suggested any vortex shedding synchronization occurs.

On the other hand, when the shorter cylinder was placed in front four diameters apart (Fig. 9(b)), no abrupt lock-on could be discerned because the two frequencies are close to one another throughout the range of angles. At low angles of incidence, the longer cylinder exhibits a markedly greater shedding frequency, but as it passes through the wake of the shorter cylinder, both frequencies drop. As the spacing increases (Figs. 9(c) and 9(d)), the shedding from each cylinder becomes increasingly distinct. There may be some lock-on around α = 80 deg and higher, but for the most part there is a reversion toward isolated cylinder behavior. At six diameters a comparison of Figs. 8(d) and 9(d) shows that the divergence is greater when the short cylinder is in front than when it is at the rear.

One further set of results is included in Figs. 10 and 11 to show the effect of increasing the difference in the cylinder heights. With the front cylinder lengthened to L/D = 10.67, the maximum divergence between shedding frequencies increased to ΔSt = .068 for a spacing of three diameters at α = 52.5 deg, as can be seen in Fig. 10(a). At all spacings the lock-on effect was much more dramatic than in Fig. 8. It very clearly occurred at α = 67.5 deg at the three and four diameter spacings (Figs. 10(a) and 10(b), and at α = 75 deg for the five and six diameter spacings (Figs. 10(c) and 10(d)). With the long and short cylinders reversed (Fig. 11) no lock-on occurred at

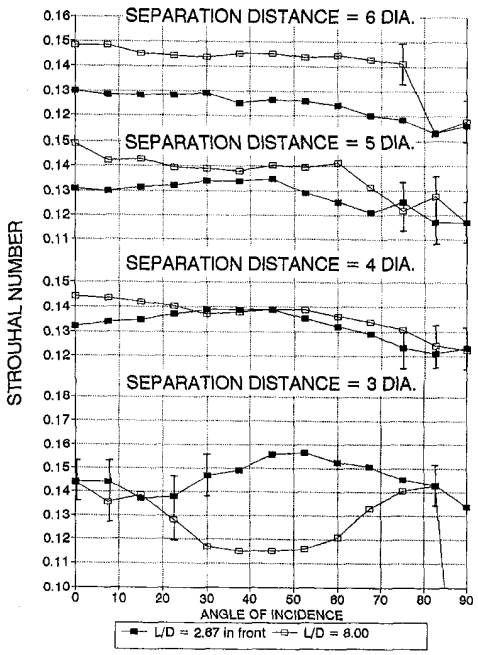

Fig. 9 Strouhal number for two cylinders (L/D = 2.67 in front of L/D = 8) as a function of approach angle at spacings of (*a*) three diameters, (*b*) four diameters, (*c*) five diameters, (*d*) six diameters

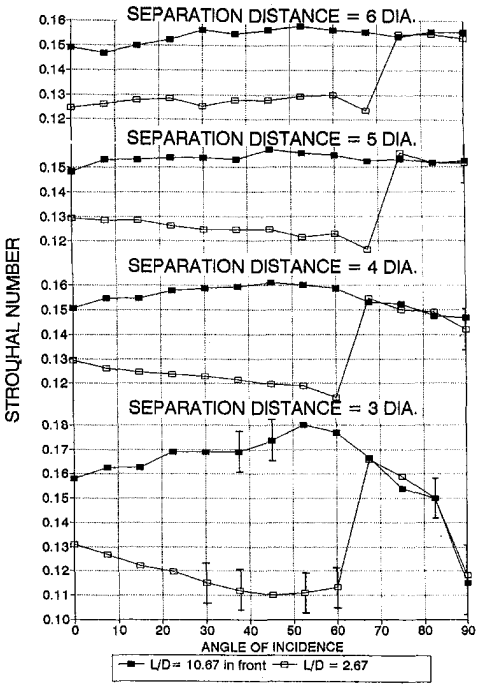

Fig. 10 Strouhal number for two cylinders (L/D = 10.67 in front of L/D = 2.67) as a function of approach angle at spacings of (*a*) three diameters, (*b*) four diameters, (*c*) five diameters, (*d*) six diameters

any spacing. At three diameters the short cylinder exhibited a higher shedding frequency only in the range 35 deg $\leq \alpha \leq$ 70 deg, while Fig. 9(a) shows that from 20 deg $\leq \alpha \leq$ 80 deg it generated that biassed gap flow effect. The shorter cylinder has virtually no effect on the longer one at a distance of four diameters (Fig. 11(b)), whereas in Fig. 9, some effect is seen to persist up to five diameters away.

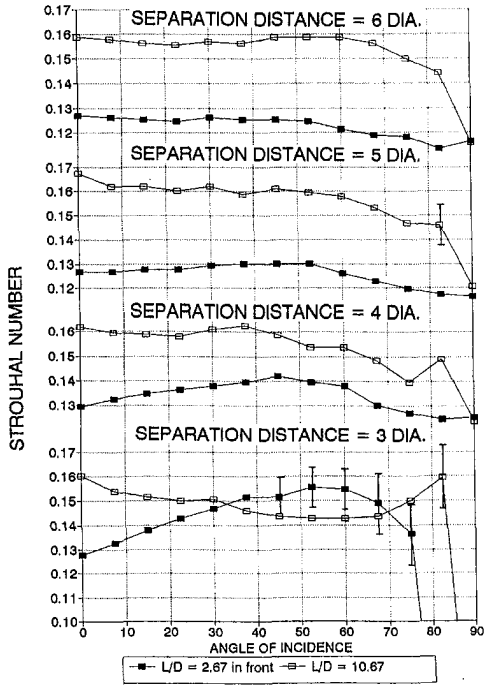

Fig. 11 Strouhal number for two cylinders (L/D = 2.67 in front of L/D = 10.67) as a function of approach angle at spacings of (*a*) three diameters, (*b*) four diameters, (*c*) five diameters, (*d*) six diameters

4 Conclusion

The series of experiments described above has focussed on the effect of finite cylinder size on interference between two cylinders at all angles to one another within a six diameter spacing. A number of conclusions can be arrived at based on these results:

1. Solitary finite cylinders exhibit some organized vortex shedding at aspect ratios even below $L/D = 1$. The three dimensional structure of the wake flow appears to change between $2.67 \leq L/D \leq 4.67$, probably due to the downward end flow interfering in the wake flow in that range, while at lower aspect ratios the base horseshoe vortex controls the wake size.
2. A very identifiable low frequency tip vortex is measurable for aspect ratios greater than 6, and the frequency remains constant regardless of aspect ratio. For most aspect ratios the Karman vortex street extends about 60 percent up the cylinder span.
3. The greater the divergence in aspect ratios of two cylinders, the greater the maximum difference in their shedding frequencies, which occurs around α = 60 deg, just before lock-on. The variation in Strouhal number with angle and relative distance is consistent with the supposition that a "wake displacement" is taking place in the flow between the cylinders.
4. An identifiable lock-on region occurs when a longer finite cylinder is upstream of a shorter one; when their relative positions are reversed, no lock-on occurs.

References

Ayoub, A., and Karamcheti, K., 1982, "An Experiment on the Flow past a Finite Circular Cylinder at High Subcritical and Supercritical Reynolds Numbers," *Journal of Fluid Mechanics,* Vol. 118, pp. 1–26.

Baban, F., So, R. M. C., and Otugen, M. V., 1989, "Unsteady Forces on Circular Cylinders in a Cross-Flow," *Experiments in Fluids,* Vol. 7, pp. 293–302.

Barnes, F. H., Baxendale, A. J., and Grant, I., 1986, "A Lock-In Effect in the Flow Ever Two Cylinders," *Aeronautical Journal,* Vol. 90, Apr., pp. 128–138.

Baxendale, A. J., Grant, I., and Barnes, F. H., 1985, "The Flow Past Two Cylinders Having Different Diameters," *Aeronautical Journal,* Vol. 89, Apr., pp. 125–134.

Bearman, P. W., and Wadcock, A. J., 1973, "The Interaction Between a Pair of Circular Cylinders Normal to a Stream," *Journal of Fluid Mechanics,* Vol. 61, Part 3, pp. 499–511.

Bokaian, A. and Geoola, F., 1984, "Vortex Shedding from Two Interfering Circular Cylinders," *ASCE Journal of Engineering Mechanics,* Vol. 110, No. 4, Apr., pp. 623–628.

Farivar, D., 1981, "Turbulent Uniform Flow Around Cylinders of Finite Length," *AIAA Journal,* Vol. 19, No. 3, Mar., pp. 275–281.

Kareem, A., Cheng, C. M., and Lu, P. D., 1989, "Pressure and Force Fluctuations on Isolated Circular Cylinders of Finite Height in Boundary Layer Flows," *Journal of Fluids and Structures,* Vol. 3, pp. 481–508.

Kawamura, T., Hiwada, M., Hibino, T., Mabuchi, I., and Kumada, M., 1984, "Flow Around a Finite Circular Cylinder on a Flat Plate," *Bulletin of JSME,* Vol. 27, No. 232, Oct., pp. 2142–2151.

Kiya, M., Arie, M., Tamura, H., and Mori, H., 1980, "Vortex Shedding from Two Circular Cylinders in Staggered Arrangement," ASME JOURNAL OF FLUIDS ENGINEERING, Vol. 102, June, pp. 166–173.

Okamoto, T., and Yagita, M., 1973, "The Experimental Investigation on the Flow Past a Circular Cylinder of Finite Length Placed Normal to the Plane Surface in a Uniform Stream," *Bulletin of JSME,* Vol. 16, No. 95, May, pp. 805–814.

Sakamoto, H., and Arie, M., 1983, "Vortex Shedding From a Rectangular Prism and a Circular Cylinder Placed Vertically in a Turbulent Boundary Layer," *Journal of Fluid Mechanics,* Vol. 126, pp. 147–165.

Sakamoto, H., and Oiwake, S., 1984, "Fluctuating Forces on a Rectangular Prism and a Circular Cylinder Placed Vertically in a Turbulent Boundary Layer," ASME JOURNAL OF FLUIDS ENGINEERING, Vol. 106, June, pp. 160–166.

Sin, V. K., and So, R. M. C., 1987, "Local Force Measurements on Finite-Span Cylinders in a Cross-Flow," ASME JOURNAL OF FLUIDS ENGINEERING, Vol. 109, June, pp. 136–143.

Szepessy, S., 1991, "The Effect of Free Stream Turbulence on a Circular Cylinder for Various Aspect Ratios," Paper II in Szepessy, S., "On the three-dimensionality of vortex shedding from a circular cylinder," Ph.D. thesis, Dept. of Thermo and Fluid Dynamics, Chalmers University of Technology, Goteborg, Sweden.

Szepessy, S., and Bearman, P. W., 1991, "Aspect Ratio and End Plate Effects on Vortex Shedding from a Circular Cylinder," Paper I in Szepessy, S., "On the three dimensionality of vortex shedding from a circular cylinder," Ph.D. thesis,

Dept. of Thermo and Fluid Dynamics, Chalmers University of Technology, Goteborg, Sweden.

Vickery, B. J., 1968, "Load Fluctuations in Turbulent Flow," *ASCE Journal of Engineering Mechanics,* EM 1, pp. 31–46.

Williamson, C. H. K., 1985, "Evolution of a Single Wake Behind a Pair of Bluff Bodies," *Journal of Fluid Mechanics,* Vol. 159, pp. 1–18.

Zdravkovich, M. M., 1977, "Review of Flow Interference Between Two Circular Cylinders in Various Arrangements," ASME JOURNAL OF FLUIDS ENGINEERING, Vol. 99, No. 4, Dec., pp. 618–633.

Zdravkovich, M. M., Brand, V. P., Mathew G., and Weston, A., 1989, "Flow Past Short Circular Cylinders with Two Free Ends," *Journal of Fluid Mechanics,* Vol. 203, pp. 557–575.

Computation of Vortex Lock-In in the Laminar Wake of a Circular Cylinder Using Unsteady Monopole Sources

Dartzi Pan
Associate Professor.

Yu-Chi Chin
Graduate Student.

Chih-Hao Chang
Graduate Student.

Institute of Aeronautics and Astronautics,
National Cheng Kung University,
Tainan, Taiwan,
Republic of China

The vortex lock-in in the laminar wake behind a circular cylinder induced by the unsteady monopole source is numerically simulated in this paper. The artificial compressibility method is employed to solve the incompressible Navier-Stokes equations. A high-order accurate upwind flux-difference finite-volume scheme is used to discretize the flow field. The unsteady monopole source is simulated by a pulsating volume flux through the cylinder surface at a prescribed forcing frequency and amplitude. The forcing amplitude is set to a fixed value while the frequency is varied to search for the lock-in region. The flow field of the periodic lock-in state is examined in detail. Finally, the effects of a higher amplitude and a different source location are briefly investigated.

Introduction

It is well known that Karman vortex streets are formed in the wake behind a circular cylinder when the Reynolds number is above 60. When the flow is under some form of unsteady disturbances, e.g., when a periodic component is superimposed upon the incident mean flow, or when the cylinder is vibrating or rotating, the vortex shedding frequency may be modified or shifted from its natural shedding frequency to the forcing frequency of the disturbances. This phenomenon of vortex shedding resonance, or lock-in, is the subject of many past studies, e.g., see Bearman (1984) and Griffin and Hall (1991) for references. It provides a potential means for active control of the bluff body wake flow, which has numerous practical engineering applications.

The application of sound field is also capable of achieving vortex lock-in. However, there are very few reported studies of the effect of sound. Blevins (1985) demonstrated the vortex lock-in in the turbulent wake behind a circular cylinder using sound field generated by the loudspeakers mounted on the wind tunnel wall. He observed that the vortex lock-in was induced by the velocity fluctuation rather than the pressure fluctuation. Hsiao and Shyu (1991) applied the sound wave emanating from a slot on the cylinder surface to influence the flow field. They observed that the vortex shedding frequency is shifted when the forcing frequency matches the shear-layer instability frequency. They also concluded that the most effective forcing location is around the separation point. As for the numerical simulation, there is no reported study of vortex lock-in by acoustic excitation known to the authors. Numerical studies on vortex lock-in using other forms of excitation are also very rare. One example is by Karniadakis and Triantafyllou (1989), who numerically applied a small spatially and temporally varying periodic disturbance into the near-wake of the cylinder. The disturbance is analogous to a vibrating wire with the appropriate frequency and amplitude. Another example is by Chang and Sa (1992), who computed the vortex shedding patterns from a circular cylinder oscillating in streamwise direction.

Mathematically, the monopole type acoustic source can be modelled by a localized volumetric pulsation that drives the fluid around it. Numerically, this can be achieved by specifying the volume flux through the computational cell face at a prescribed frequency and amplitude. The pressure fluctuation, or acoustic radiation, from the source is a consequence of the change in velocity field dictated by the volume flux. In this study, this type of monopole source is numerically simulated and applied to achieve the vortex lock-in in the laminar wake of a circular cylinder. The incompressible Navier-Stokes equations are solved by the artificial compressibility method (Chorin, 1967) and a high-order accurate upwind finite-volume discretization (Pan and Chakravarthy, 1989; Pan and Chang, 1993). The divergence-free condition, and hence the time accurate solution is assured by subiterations at every time step. The transpired wall boundary condition with a specified normal volume flux is used to simulate the monopole source placed on the wall. The wall pressure is then solved from the momentum equation normal to the wall. To validate this modeling of monopole source, the monopole radiation over a finite flat plate in an incompressible flow is computed and compared with the analytical solution (Lu and Huang, 1992). Then the monopole source is placed on a circular cylinder and applied to influence the laminar vortex shedding at a Reynolds number of 100. The forcing frequency is varied from half to twice the

Contributed by the Fluids Engineering Division for publication in the JOURNAL OF FLUIDS ENGINEERING. Manuscript received by the Fluids Engineering Division August 10, 1993; revised manuscript received May 11, 1994. Associate Technical Editor: G. Karniadakis.

natural vortex shedding frequency, while the amplitude is kept constant and the location fixed. The data are recorded and processed by the Fast Fourier Transformation (FFT) to analyze the frequency response. The flow field of the periodic lock-in state is examined in detail. Finally, the effects of a higher amplitude and a different source location are investigated briefly.

Governing Equations and Finite-Volume Discretization

The integral form of conservation laws can be written as:

$$\frac{\partial}{\partial \tau}\int\int_{\Omega} Q d\Omega + \oint_S \mathbf{F}\cdot\hat{\mathbf{n}}\, dS = 0 \tag{1}$$

where τ is the nondimensional time; Ω is the domain of interest; S is the boundary surrounding Ω; $\hat{\mathbf{n}}$ is the unit normal of S in outward direction; Q is the vector of conserved variables, and $\mathbf{F}$ is the vector of flux functions through S. With the aid of artificial compressibility, the incompressible Q and $\mathbf{F}$ are given as:

$$\mathbf{F} = \mathbf{F}^I - \frac{1}{\mathrm{Re}}\mathbf{F}^V = \left(f^I - \frac{1}{\mathrm{Re}}f^V\right)\hat{\mathbf{i}} + \left(g^I - \frac{1}{\mathrm{Re}}g^V\right)\hat{\mathbf{j}}$$

$$Q = \begin{bmatrix} p \\ u \\ v \end{bmatrix}, \quad f^I = \begin{bmatrix} \beta u \\ uu + p \\ uv \end{bmatrix}, \quad g^I = \begin{bmatrix} \beta v \\ uv \\ vv + p \end{bmatrix}, \quad f^V = \begin{bmatrix} 0 \\ u_x \\ v_x \end{bmatrix}, \quad g^V = \begin{bmatrix} 0 \\ u_y \\ v_y \end{bmatrix} \tag{2}$$

where the superscripts I and V denote the inviscid and viscous fluxes; $\hat{\mathbf{i}}$ and $\hat{\mathbf{j}}$ are the unit vectors in x and y direction; u and v are the velocity components normalized by reference speed U_{ref}; p is the pressure normalized as $(p - p_{\mathrm{ref}})/(\rho_{\mathrm{ref}}U_{\mathrm{ref}}^2)$; Re is the Reynolds number; β is the artificial compressibility; u_x, u_y, v_x, and v_y are the first derivatives of the velocity components. The semi-discrete form of Eq. (1) on a structured mesh can be written as:

$$\frac{\partial}{\partial \tau}(Q_{j,k}V_{j,k}) = -(\Delta_j F^N + \Delta_k F^N) = -RH_{j,k}$$

$$\Delta_j(\cdot) = (\cdot)_{j+1/2,k} - (\cdot)_{j-1/2,k}, \quad \Delta_k(\cdot) = (\cdot)_{j,k+1/2} - (\cdot)_{j,k-1/2}$$

$$F^N_{j,k+1/2} = (\mathbf{F}\cdot\hat{\mathbf{n}}\Delta S)_{j,k+1/2} \tag{3}$$

where j and k are the indices denoting the cell center of the computational cell; $j \pm 1/2$ and $k \pm 1/2$ denote the cell faces of cell (j, k); $Q_{j,k}$ is the averaged conserved variables stored at the cell center; $V_{j,k}$ is the cell volume; and $F^N_{j,k+1/2}$ is the numerical fluxes through the cell-face $\Delta S_{j,k+1/2}$.

The inviscid numerical fluxes at a cell-face $m + 1/2$ is given by an upwind flux-difference formulation based on Roe's approximate Riemann solver (Roe, 1981):

$$F^I_{m+1/2} = 1/2\,[F^I(Q^+_{m+1/2}) + F^I(Q^-_{m+1/2}) - |\bar{A}|\,(Q^+_{m+1/2} - Q^-_{m+1/2})]$$

$$|\bar{A}| = R|\Lambda|L \tag{4}$$

where $Q^+_{m+1/2}$ and $Q^-_{m+1/2}$ are the reconstructed right and left states of cell-face $m + 1/2$; $\bar{A}$ is the flux Jacobian evaluated by Roe's average state; R, L and Λ are the eigenvector matrices and eigenvalue matrix of $\bar{A}$. It is known that for incompressible flows, Roe's average state is just the simple average of Q^+ and Q^-. A special reconstruction formulation for Q^+ and Q^- (Chakravarthy and Osher, 1985) is chosen in this paper which yields a third-order accurate scheme for the linear model problems. To prevent the possible numerical oscillation caused by the application of monopole sources, a total variation diminishing (TVD) slope limiter is applied to the reconstructed Q^+ and Q^- whenever necessary.

To evaluate the viscous numerical fluxes, it is necessary to compute the velocity gradient at the cell face. This can be done using Gauss theorem:

$$\nabla Q = \frac{1}{A_\Omega}\oint_{\partial A} Q\hat{\mathbf{n}}\, dS \tag{5}$$

where ∂A is a chosen integration path and A_Ω is the area enclosed by ∂A. For each cell face, two triangular integration paths containing the cell face can be made by connecting the two end vertices and the two neighboring cell centers. The variable values at the end vertices can be obtained by a distance-weighted interpolation of the surrounding cell-center values. Each triangular integration path can then be used to estimate a velocity gradient using Eq. (5). Finally the velocity gradient at the middle of the cell face can be obtained by an area-weighted average of the two gradients just estimated. Assuming accurate variable values at the end vertices, the above procedure yields a second-order accurate gradient estimation on a parallelogram mesh, but is only first-order on a general mesh.

Time Discretization

Neglecting the index (j,k) for simplicity, an implicit time discretization of Eq. (3) can be written as:

$$\left\{\frac{V}{\Delta\tau} + I_\alpha\frac{\partial RH}{\partial Q}\right\}(Q^{s+1} - Q^s) = -\left\{\frac{I_d(Q^s - Q^n)V}{\Delta\tau} + I_\alpha RH^s + (I - I_\alpha)RH^n\right\} = RHS,$$

$$I_d = \mathrm{diag}\,(0, 1, 1), \quad I_\alpha = \mathrm{diag}\,(1, \alpha, \alpha) \tag{6}$$

where $\Delta\tau$ is the time step; n is the time index; s is the subiteration index; I is the identity matrix; I_d is a diagonal matrix that is necessary to obtain divergence free condition at each time step; I_α is a diagonal matrix that specifies the time integration method; and α determines the order of time accuracy. It is the first-order Euler implicit method for $\alpha = 1$, and second-order Trapezoidal rule for $\alpha = 1/2$. When the RHS is subiterated to zero, Q^{s+1} approaches the time accurate Q^{n+1}. Equation (6) is to be inverted by various relaxation methods. The diagonal form of the Approximate Factorization scheme (Pulliam and Chaussee, 1981) is used in this study.

Boundary Conditions

The characteristic boundary treatment is natural for the far field open boundaries. When the contravariant velocity U relative to the boundary face is positive, there are two positive eigenvalues, U and $U + c$, where c is the artificial speed of sound, carrying information from upstream. There is one negative eigenvalue, $U - c$, carrying information from downstream. In matrix form, the linearized characteristic-like equation for this boundary can be written as

$$\begin{bmatrix} l_{11}l_{12}l_{13} \\ l_{21}l_{22}l_{23} \\ l_{31}l_{32}l_{33} \end{bmatrix}\begin{bmatrix} p \\ u \\ v \end{bmatrix}_{BC} = \begin{bmatrix} (l_{11}p + l_{12}u + l_{13}v)_{\mathrm{downstream}} \\ (l_{21}p + l_{22}u + l_{23}v)_{\mathrm{upstream}} \\ (l_{31}p + l_{32}u + l_{33}v)_{\mathrm{upstream}} \end{bmatrix} \tag{7}$$

where l's are the elements of the left eigenvector matrix whose eigenvalues are arranged in ascending order, that is, $U - c$, U and $U + c$. A similar equation can be formulated for the boundary face where the contravariant velocity is negative. Equations (7) provides satisfactory nonreflecting treatment for the far field boundaries (Pan and Chakravarthy, 1989; Pan and Chang, 1993).

For a viscous wall, the no-slip condition is applied. With a monopole source on the wall, the tangential velocity v_t is ex-

trapolated from flow interior while the normal velocity v_n is set by the volume flux $\dot{Q}$ of the source as

$$v_n = \begin{cases} 0, & \text{no source} \\ \dot{Q}/\Delta S, & \text{with monopole} \end{cases} \tag{8}$$

where ΔS is the surface area of the source cell. An unsteady monopole source is given by

$$\dot{Q} = Q_c \sin(f_e \tau) \tag{9}$$

where τ is the nondimensional time, f_e the forcing frequency and Q_c the forcing amplitude. In practice, Q_c is smoothly distributed over several cells to reduce the theoretical singularity at the center of the source. The velocity component on the wall can then be obtained by

$$\begin{bmatrix} u \\ v \end{bmatrix} = \begin{bmatrix} n_x & n_y \\ n_y & -n_x \end{bmatrix}^{-1} \begin{bmatrix} v_n \\ v_t \end{bmatrix} \tag{10}$$

where n_x and n_y are the components of the wall unit normal. After knowing the velocity, the wall pressure is solved from the momentum equation normal to the wall. Specifically, the following equation is applied to the first cell above the wall:

$$\hat{\mathbf{n}}_{j,1/2} \cdot \left\{ \frac{\partial (\mathbf{v}V)_{j,1}}{\partial \tau} + \sum_{(j-1/2,1),(j,1/2)}^{(j+1/2,1),(j,3/2)} \left[\mathbf{v}(\mathbf{v} \cdot \hat{\mathbf{n}} S) + p \hat{\mathbf{n}} S - \frac{1}{\mathrm{Re}} \nabla(\mathbf{v}) \cdot \hat{\mathbf{n}} S \right] = 0 \right\} \tag{11}$$

where $k = 1/2$ represents the wall. The summation operation is done over the four cell faces of the boundary cell. Using the last pass values for variables with $k \neq 1/2$, and the wall velocity components just obtained, the above equation can be solved explicitly for the pressure at wall $P_{j,1/2}$. The time accuracy of Eq. (11) is only first order.

Computational Results

I Monopole Radiation Over a Finite Flat Plate in an Incompressible Flow. This is a test problem for the simulation of monopole acoustic source placed at the center on the upper surface of a finite flat plate in an inviscid incompressible flow. The analytical solution is obtained by Lu and Huang (1992). The plate is located at $-1 \leq x \leq 1$, $y = 0$, and the computational domain is $-5 \leq x \leq 20$, $-5 \leq y \leq -5$. A 110 $\times$ 60 grid with clustering near both plate ends and the center is used for the computation. The volume flow rate is chosen with $Q_c = 2 \times 10^{-3}$ and $f_e = 1.05$. Here Q_c is distributed over four cells covering $-0.032 \leq x \leq 0.032$ with weighting 1/6, 1/3, 1/3, and 1/6. The artificial compressibility coefficient β is set to 10. The first-order Euler implicit method is used for time integration and about 410 time steps is taken for one cycle of radiation. Five to six subiterations are needed to drop the residual at each time step to less than 5×10^{-5} in single precision. Figures 1(*a*) and 1(*b*) show the computed lift and moment coefficient, respectively. Excellent agreement with the analytical solution is obtained. The vorticity integral at position x in the wake is defined as

$$\gamma(x) = \int \nabla \times \mathbf{v}\, dy \tag{12}$$

where the integration is done over the entire y axis. Figure 1(*c*) shows the computed distribution of $\gamma(x)$ along the wake. The comparison with analytical solution is satisfactory with some deterioration in the far wake. Analytically, the generation of vorticity in this irrotational flow is caused by the enforcement of the artificial Kutta condition at the trailing edge. The present numerical simulation, however, solves the incompressible Euler equations which does not explicitly enforce the Kutta condition. These test results clearly validated the modelling of the unsteady monopole source used in this study.

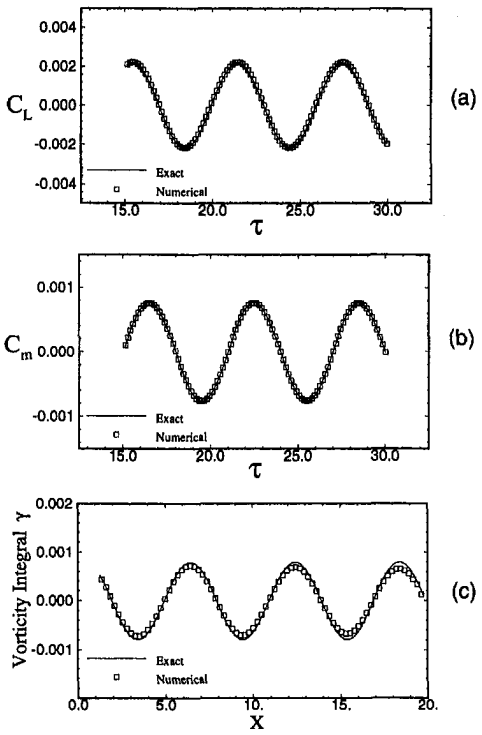

Fig. 1 Time history of (*a*) lift coefficient C_L and (*b*) moment coefficient C_m, (*c*) distribution of vorticity integral γ along the wake, inviscid incompressible flow over a flat plate with monopole radiation at the center of the upper surface, symbols: computed, lines: analytical (Lu and Huang, 1992)

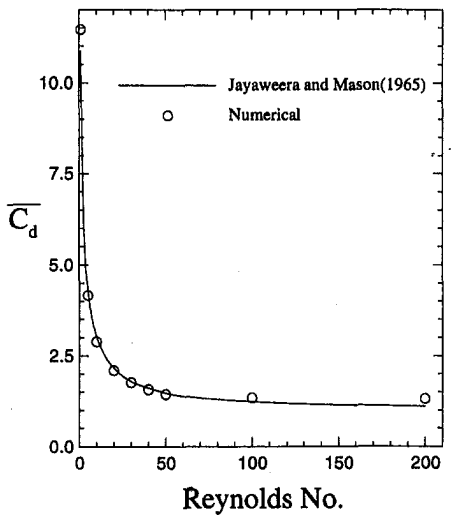

Fig. 2 Time mean drag coefficient at various Reynolds numbers, flow over a circular cylinder, Re = 100, symbols: computed, line: experiment (Jayaweera and Mason, 1965)

II Laminar Flow Over a Stationary Circular Cylinder. A two-zone grid is used to compute the laminar flow over a circular cylinder. The first zone grid wraps around the cylinder using 83 points and extends 10 diameters radially using 60 points. The 36 $\times$ 25 second zone patches the downstream side of the outer boundary of the first zone and extends another 10 diameters downstream to capture the wake flow better. The artificial compressibility coefficient β is set to 10. The Reynolds number based on the diameter and the free stream conditions is varied from 1 to 200. Figure 2 shows the computed time mean drag coefficient at various Reynolds number.

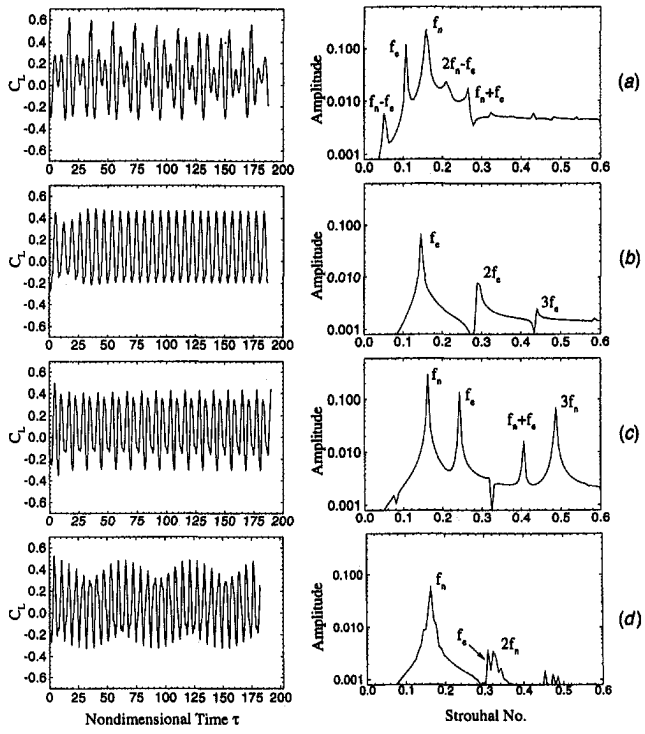

Fig. 3 Time curves of the lift coefficient C_L and their FFT spectrums, flow over a circular cylinder excited by monopole sources on the surface, Re = 100, (a) $f_e = 0.67\ f_n$, (b) $f_e = 0.9\ f_n$, (c) $f_e = 1.5\ f_n$, (d) $f_e = 1.9\ f_n$

The comparison with the experiment by Jayaweera and Mason (1965) is satisfactory.

For the case of Reynolds number 100, the first-order Euler implicit method is used for time integration and 570 steps is taken for one cycle of vortex shedding. The reduced frequency of the vortex shedding f_n, or Strouhal number, estimated from the lift coefficient is 0.162. This compares well with Williamson (1989) that gives $f_n = 0.161$ at Reynolds number 101. The computed lift coefficient C_L oscillates around zero with an amplitude ΔC_L of 0.64. The time mean drag coefficient $\bar{C}_d$ is 1.356. The separation point on the upper shoulder of the cylinder oscillates between $114.5 \leq \Psi \leq 119.4$ deg. To examine the time accuracy of the solution, the second-order Trapezoidal rule is also used. With Trapezoidal rule, ΔC_L is 0.68, $\bar{C}_d$ is 1.38, Strouhal number is 0.163 and the separation point on the upper shoulder of the cylinder oscillates between $114.3 \leq \Psi \leq 120.2$ deg. Since the main interest of this study is the frequency response of the flow, the less expensive Euler implicit method is chosen for the rest of this study.

III Effects of Monopole Source Placed on the Cylinder Surface. For the case of Reynolds number 100, a arbitrary instant in the periodic solution just computed is taken as the initial condition. The unsteady monopole source described by Eq. (9) is applied thereafter to influence the vortex shedding of the laminar wake. The transpired wall boundary condition is enforced on the cylinder for $108.7 \leq \Psi \leq 123.4$ deg which covers the region of separation point of the unforced case. The volume flux is distributed over the five-cell source with weighting 0.105, 0.22, 0.35, 0.22 and 0.105. The amplitude is set to $Q_c = 6.4 \times 10^{-2}$ and the forcing frequency f_e is varied. The goal is to see whether the application of unsteady monopole sources can induce vortex lock-in. No attempt is made to identify the exact lock-in boundaries.

Figure 3 shows the lift curves and their FFT spectrums in log scale for $f_e/f_n = 2/3$, 0.9, 3/2 and 1.9. For $f_e = 0.9 f_n$, one dominant peak at f_e and two weak peaks at the multiples of f_e are seen, indicating that the vortex shedding frequency is

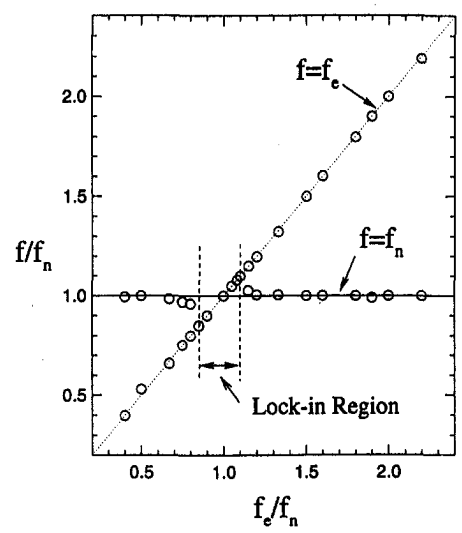

Fig. 4 Occurrences of f_e and f_n in FFT spectrum at different forcing frequencies, flow over a circular cylinder excited by monopole sources on the surface, Re = 100

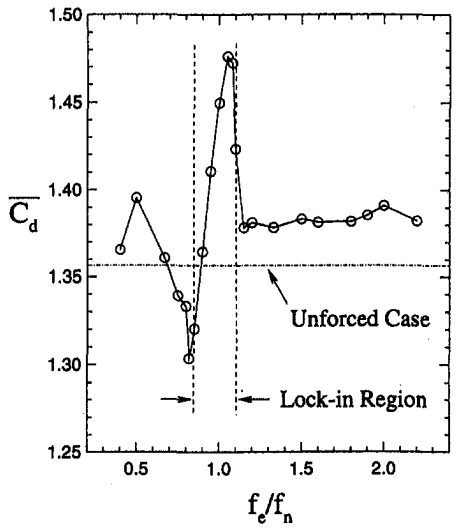

Fig. 5 Time mean drag coefficient $\bar{C}_d$ verses forcing frequency f_e, flow over a circular cylinder excited by monopole sources on the surface, Re = 100

shifted to the forcing frequency. This is the characteristic of a periodic lock-in state. For the other three cases, the FFT spectrum contains a dominant peak at f_n, a weak peak at f_e and those peaks due to the nonlinear wave interactions between f_n and f_e. For these cases, the vortex shedding remains its natural shedding frequency, indicating non-lock-in states. Figure 4 summarizes the occurrences of f_e and f_n in the FFT spectrum at different forcing frequencies. Roughly for $0.85 f_n \leq f_e \leq 1.10\ f_n$, only one major peak is seen at f_e, and no peak at f_n is recorded. This roughly estimated lock-in region is indicated by the dashed lines. Outside this region, the peak at f_n becomes dominant and coexists with the minor peak at f_e. The peak at f_e becomes relatively weaker as it is moved further away from f_n.

Figure 5 shows the computed time mean drag coefficient at various forcing frequencies. The average drag has a local maximum inside the lock-in region, and a local minimum outside. Note that the drag is generally higher than the unforced case for $f_e/f_n \geq 1$. Figure 6 shows the time mean surface pressure coefficient $\bar{C}_p$ distributions for the unforced case and three lock-in frequencies, namely, $f_e/f_n = 0.9$, 1.0 and 1.08. For the two

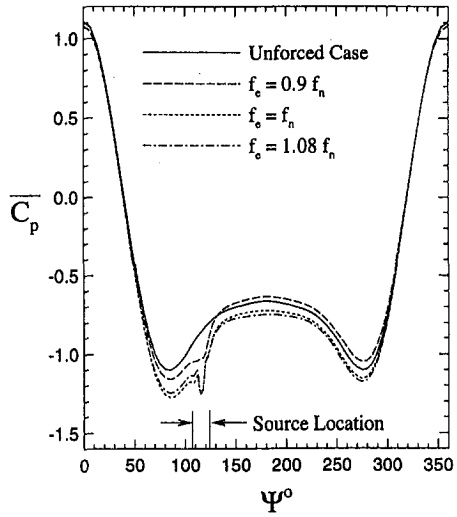

Fig. 6 Time mean surface pressure coefficient $\bar{C}_p$ for three lock-in frequencies, flow over a circular cylinder excited by monopole sources on the surface, Re = 100

higher forcing frequencies, the surface pressure is lower than the unforced case on the entire downstream half of the cylinder. For $f_e = 0.9f_n$, the surface pressure is lower than the unforced case only in the region upstream of and on the source cells. The sound pressure level (SPL) in dB is defined by SPL $= 20 \log(p_{rms}/p_{ref})$ where p_{rms} is the root mean square of the fluctuating pressure and $p_{ref} = 2 \times 10^{-5}$ N/m^2. For all the cases shown in Fig. 5, the highest SPL measured on the cylinder surface locates at the middle of source cells, and is always lower than 100 dB.

Figure 7 shows the variation in Ψ of the location of zero stress points on the cylinder surface for the same three lock-in frequencies. They are compared with the period of the monopole volume flux Q. The point of zero stress can be either a separation point or an attachment point. The diamond symbols represent the attachment point oscillating around the downstream tip of the cylinder. The triangle symbols close to $\Psi = 240$ deg indicate the separation point on the lower half of the cylinder. The triangle symbols just upstream and downstream of the source location appear only when the volume flow is positive. In other words, streamlines close to the source cells lift off when the source is blowing into the flow. Note that the center of the source cells is also a point of zero stress, but it is not shown in Fig. 7.

Although it is hard to identify the precise moment of the genesis and the shedding of the separation vortex, a rough description of the vortex shedding period is still possible. Referring to Fig. 7, as the attachment point moves away from its minimum Ψ position, the upper separation vortex grows bigger. As the attachment point reaches the maximum Ψ position and reverses its direction, the upper separation vortex sheds from the surface and moves downstream. In the mean time the separation vortex on the lower surface starts to grow. Similarly, as the attachment point moves away its maximum Ψ position, the lower separation vortex grows bigger. As the attachment point reaches its minimum Ψ position and reverses its direction, the lower separation vortex sheds from the surface and moves downstream. In the mean time the upper separation vortex starts to grow. This completes the vortex shedding process. The process is not symmetric when there is asymmetric excitation, as can be seen from Fig. 7.

Figure 7 also indicates that in the lock-in region, the phase of the vortex shedding process with respect to the period of the monopole is a function of the forcing frequency. For $f_e = 0.9f_n$, the attachment point reaches its maximum Ψ position when Q is negative. This means that the upper separation vortex sheds off when the source is in its suction stage. For $f_e = 1.08f_n$, on the other hand, the attachment point reaches it maximum Ψ position when Q is positive. This means that the upper separation vortex sheds off when the source is blowing into the stream. For $f_e = f_n$, the phase of the vortex shedding is roughly between the other two frequencies. To examine more about this phase relationship, two different initial conditions are arbitrarily chosen from the periodic solution computed in Section II, and the $f_e = 0.9f_n$ forcing is applied. Figure 8 shows the computed drag coefficients. The two drag curves coincide after a transient period, indicating that the final lock-in state is independent of the initial conditions.

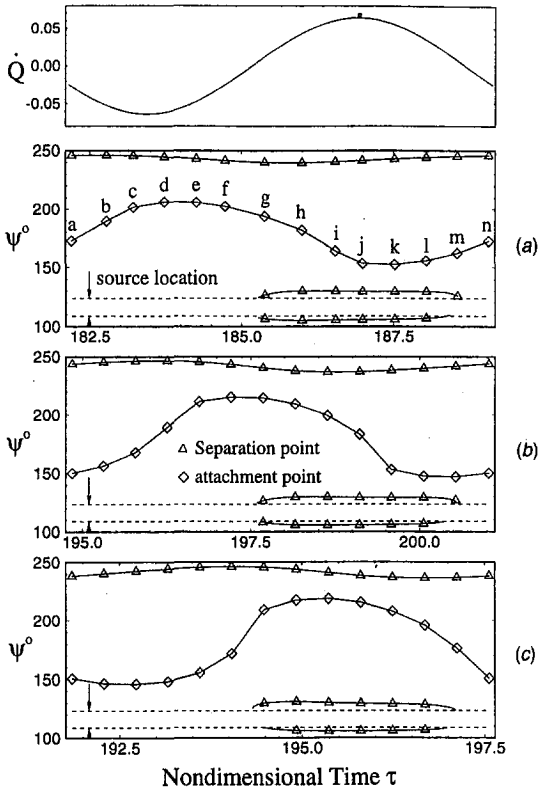

Fig. 7 The angle Ψ of zero stress points measured from the upstream tip of the cylinder and compared with the forcing period, flow over a circular cylinder excited by monopole sources on the surface, Re = 100, (a) $f_e = 0.9\ f_n$, (b) $f_e = 1.0\ f_n$ and (c) $f_e = 1.08\ f_n$; diamonds: attachment point, triangles: separation point

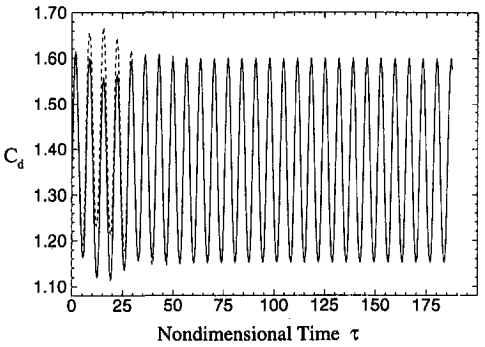

Fig. 8 Time curves of the drag coefficient C_d under two different initial conditions, flow over a circular cylinder excited by monopole sources on the surface, Re = 100, $f_e = 0.9\ f_n$

Figure 9 shows for $f_e = 0.9f_n$ the instantaneous stream function contours and the surface C_p distributions at 7 instants marked in Fig. 7. It is seen that the pressure fluctuation is more pronounced upstream of and on the source cells. At some

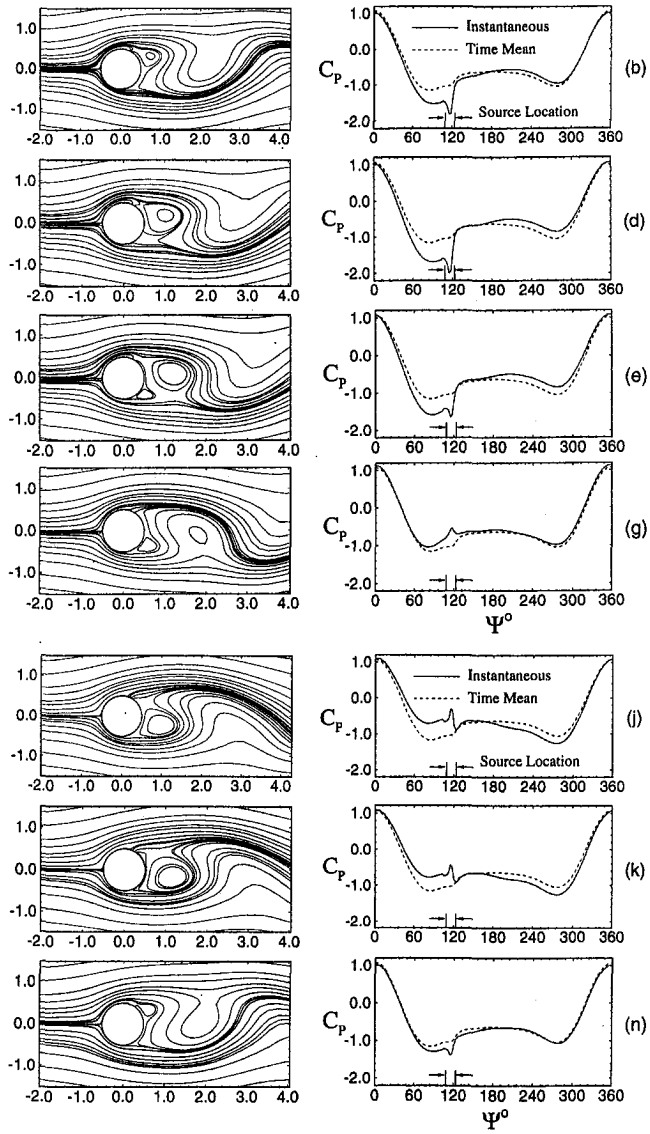

Fig. 9 Instantaneous stream function contours and surface C_p distributions at 7 instants (marked in Fig. 7) in one forcing period, flow over a circular cylinder excited by monopole sources on the surface, Re = 100, $f_e = 0.9\ f_n$; line: instantaneous value, dashes: time mean value

instant between Figs. 9(*d*) and 9(*e*) the attachment point of the upper separation vortex reaches its maximum Ψ position and the lower separation starts to grow. At some instant between Figs. 9(*j*) and 9(*k*), the attachment point of the lower separation vortex reaches its maximum Ψ position and the upper separation starts to grow. This is consistent with the previous description of the vortex shedding period.

To investigate the effect of a higher amplitude, sample calculations are done with Q_c increased to 1.5 times its original value. It is found that the lock-in state develops at $f_e = 0.8f_n$. This confirms the known fact that the lock-in region widens when the forcing amplitude is increased. To show the effect of a different source location, calculations are done with original Q_c and $f_e = 0.9f_n$ for source cells located at (*a*) $120.0 \leq \Psi \leq 137.14$ deg and (*b*) $137.14 \leq \Psi \leq 154.29$ deg. Note that due to the grid density variation, the actual angle $\Delta\Psi$ covered by the source cells has increased to 17.1 deg. Figure 10 shows the lift coefficients and their FFT spectrums. The lock-in state develops in Fig. 10(*a*) but not in 10(*b*). Remember that the separation point of the unforced case covers $114.5 \leq \Psi \leq 119.4$ deg. It is evident that for a fixed amplitude, the applied forcing is less effective and may be ineffective to generate lock-in when it is placed further away from the separation

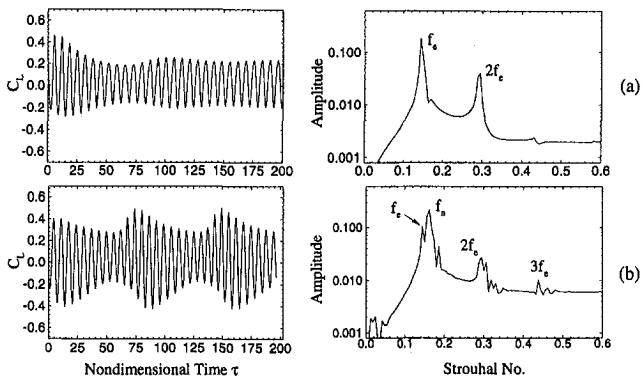

Fig. 10 Time curves of the lift coefficient C_L and their FFT spectrums for different source locations, flow over a circular cylinder excited by monopole sources on the surface, Re = 100, $f_e = 0.9\ f_n$, (*a*) $120.0 \leq \Psi \leq 137.14$ deg and (*b*) $137.14 \leq \Psi \leq 154.29$ deg

point. This is similar to the conclusion indicated by Hsiao and Shyu (1991), who applied the internal acoustic excitation to influence the cylinder wake flow and concluded that the most effective forcing location is around the separation point. A more detailed investigation of the effects of the source amplitude, the source location and Reynolds number is currently in progress.

Conclusions

The vortex lock-in in the laminar wake behind a circular cylinder induced by unsteady monopole sources is numerically simulated in this paper. The incompressible Navier-Stokes equations are solved by the artificial compressibility method and an upwind finite volume discretization. The transpired wall boundary condition is used to model the unsteady monopole source placed on the wall. The technique is validated by the computation of the monopole radiation over a finite flat plate in an inviscid incompressible flow. Then the monopole sources are placed on the circular cylinder at a Reynolds number of 100. With a fixed amplitude, lock-in states are obtained for a range of forcing frequencies which brackets the natural shedding frequency. In this lock-in region, the phase of the vortex shedding about the period of the monopole source is a function of the forcing frequency, and is independent of the initial condition. This lock-in region widens when the forcing amplitude is increased. It is also demonstrated that for a fixed amplitude, the applied forcing is less effective and may be ineffective to generate lock-in when it is placed further away from the separation point.

Acknowledgment

This work was partially supported by the National Science Council under grant NSC-83-0424-E006-023.

References

Bearman, P. W., 1984, "Vortex Shedding From Oscillating Bluff Bodies," *Annual Review of Fluid Mechanics*, Vol. 16, pp. 195–222.

Blevins, R. D., 1985, "The Effect of Sound on Vortex Shedding From Cylinders," *Journal of Fluid Mechanics*, Vol. 161, pp. 217–237.

Chang, K. S., and Sa, Jong. Y., 1992, "Patterns of Vortex Shedding From an Oscillating Circular Cylinder," *AIAA Journal*, Vol. 30, No. 5, pp. 1331–1336.

Chakravarthy, S. R. and Osher, S., 1985, "Computing with High Resolution Upwind Schemes for Hyperbolic Equations," *Lecture in Applied Mathematics*, Vol. 22, pp. 57–86.

Chorin, A. J., 1967, "A Numerical Method for Solving Incompressible Viscous Flow Problems," *Journal of Computational Physics*, Vol. 2, pp. 12–26.

Griffin, O. M., and Hall, M. S., 1991, "Review-Vortex Shedding Lock-in

and Flow Control in Bluff Body Wakes," ASME JOURNAL OF FLUIDS ENGINEERING, Vol. 113, pp. 526–537.

Hsiao, F. B., and Shyu, J. Y., 1991, "Influence of Internal Acoustic Excitation upon Flow Passing a Circular Cylinder," *Journal of Fluid & Structure*, Vol. 5, pp. 427–442.

Jayaweera, K. L. L. F., and Mason, B. J., 1965, "The Behavior of Freely Falling Cylinders and Cones in a Viscous Fluid," *Journal of Fluid Mechanics*, Vol. 22, Part 4, pp. 709–720.

Karniadakis, G. E., and Triantafyllou, G. S., 1989, "Frequency Selection and Asymptotic States in Laminar Wakes," *Journal of Fluid Mechanics*, Vol. 199, pp. 441–469.

Lu, P. J., and Huang, L. J., 1992, "Flutter Suppression of Thin Airfoils Using Active Acoustic Excitations," *AIAA Journal*, Vol. 30, No. 12, pp. 2873–2881.

Pan, D., and Chakravarthy, S. R., 1989, "Unified Formulation For Incompressible Flows," AIAA paper 89-0122.

Pan, D., and Chang, C. H., 1994, "Upwind Finite-Volume Method for Natural and Forced Convections," *Numerical Heat Transfer*, Part B, Vol. 25, pp. 177–191.

Pulliam, T. H., and Chaussee, D. S., 1981, "A Diagonal Form of an Implicit Approximate Factorization Algorithm," *Journal of Computational Physics*, Vol. 39, pp. 347–363.

Roe, P. L., 1981, "Approximate Riemann Solvers, Parameter Vectors and Difference Schemes," *Journal of Computational Physics*, Vol. 43, pp. 357–372.

Williamson, C. H. K., 1989, "Oblique and Parallel Modes of Vortex Shedding In The Wake of A Circular Cylinder At Low Reynolds Numbers," *Journal of Fluid Mechanics*, Vol. 206, pp. 579–627.

Application of Turbulence Models to Separated Flow Over Rough Surfaces

V. C. Patel
University of Iowa Foundation
Distinguished
Professor of Mechanical Engineering,
and Director.
Fellow ASME

J. Y. Yoon
Postdoctoral Research Associate.

Iowa Institute of Hydraulic Research.
The University of Iowa, Iowa City,
Iowa 52242-1585

Principal results of classical experiments on the effects of sandgrain roughness are briefly reviewed, along with various models that have been proposed to account for these effects in numerical solutions of the fluid-flow equations. Two models that resolve the near-wall flow are applied to the flow in a two-dimensional, rough-wall channel. Comparisons with analytical results embodied in the well-known Moody diagram show that the k-ω model of Wilcox performs remarkably well over a wide range of roughness values, while a modified two-layer k-ε based model requires further refinement. The k-ω model is applied to water flow over a fixed sand dune for which extensive experimental data are available. The solutions are found to be in agreement with data, including the flow in the separation eddy and its recovery after reattachment. The results suggest that this modeling approach may be extended to other types of surface roughness, and to more complex flows.

1 Introduction

Fluid flow over a rough surface occurs in diverse situations, including atmospheric wind over terrain of varying roughness and water flow over a river bed in the natural environment, and flow past man-made surfaces, such as those of airplanes, ships, turbomachinery, heat exchangers, and piping systems, to name only a few. Surface roughness affects, in addition to the flow itself, the transport of heat and mass in the atmosphere, and transport of sediment in rivers. In other applications, it affects resistance (or drag) and heat transfer. In all cases, the principal effect of roughness is a change in the velocity and turbulence distributions near the surface. As the type and relative size of roughness varies widely from one application to another, it might be expected that the problem of determining the effect of roughness in these diverse fields of fluids engineering would be treated in different ways. While a cursory review of the literature in each of these fields might suggest just such a situation, in reality, all of these fields rely on an empirical framework and a rather narrow database, both of which were established from observations in what are now regarded as classical experiments in pipes and boundary layers. Subsequent experiments and correlations have sought to relate different types of roughness in different fields to the results of these classical experiments. Thus, for example, there is considerable work which attempts to relate the regular roughness geometries used for heat-transfer enhancement, and similarly, corrosion and fouling roughness encountered in ships, to sandgrain roughness employed in the classical experiments. Similar efforts have been made with respect to terrain roughness in atmospheric boundary layers, and bed-form and gravel roughness in hydraulics.

In spite of the advances made in recent years to calculate very complex flows by methods of computational fluid dynamics (CFD), little progress has been made in the modeling of flow near rough surfaces. With few exceptions, surface roughness is treated by the so-called wall-function method in which numerical solution of the flow near the wall is avoided altogether by assuming that the local velocity distribution is given by the classical semi-logarithmic law of the wall for rough surfaces. Recent work on smooth walls, on the other hand, leads to the conclusion that the wall-function approach must be abandoned in favor of near-wall turbulence models because the law of the wall does not apply in flows with strong pressure gradients and separation (see, for example, the recent study of the flow in a channel with a smooth sinusoidally wavy wall by Patel et al., 1991). This paper is concerned with alternatives to the wall-functions approach for flow over rough surfaces. These alternatives involve modifications or extensions of existing turbulence models to describe the flow near a rough surface.

In this paper, the various approaches to modeling the effect of roughness are briefly reviewed. This suggested that, at the present time, the most promising approach to model the flow in the neighborhood of rough walls lies in extension of the so-called two-equation turbulence models that have found extensive applications in flows over smooth surfaces. Two such models, namely, the two-layer k-ε model of Chen and Patel (1988) and the k-ω model of Wilcox (1993), are applied to the flow in a two-dimensional, rough-wall channel. Comparisons with analytical results embodied in the well-known Moody diagrams revealed that the k-ω model of Wilcox performs remarkably well over a wide range of roughness values while the k-ε based model requires further refinement. The k-ω model is applied to water flow over a sand dune for which extensive experimental data have been obtained by Mierlo and de Ruiter (1988). The solutions are found to be in agreement with the data in most important respects.

2 Some Classical Results

The early work of Nikuradse (1933) with densely-packed uniform sandgrain roughness, Schlichting (1936) with distributed roughness elements, Hama (1954), aided by Sarpkaya, with wire-mesh roughness, and Moore (1951) with regularly spaced transverse ribs, established experimental results that are described in most fluid mechanics textbooks and are still in use today. The principal result, obtained from experiments in pipes, and closed and open channels, is that the velocity distribution near a rough wall, when plotted in the semi-logarithmic form of the law of the wall, has the same slope (giving the same Karman constant, κ) as on a smooth wall, but different intercepts (additive constant, B):

$$u^+ = \frac{1}{\kappa} \ln y^+ + B - \Delta B \qquad (1)$$

where $u^+ = U/u_\tau$, $y^+ = u_\tau y/\nu$, the wall, and u_τ is the friction

Contributed by the Fluids Engineering Division for publication in the JOURNAL OF FLUIDS ENGINEERING. Manuscript received by the Fluids Engineering Division August 16, 1993; revised manuscript received November 14, 1994. Associate Technical Editor: R.W. Metcalfe.

velocity. The dependence of the shift ΔB, also called the *roughness function,* on the type and size of roughness is a subject of considerable research and much uncertainty, as is the definition of the effective location of the wall, from which the distance y is measured and where the average velocity is zero.

For sandgrain roughness, ΔB is found to be a function of k_s^+ $(=u_\tau k_s/\nu)$, where k_s is the height of the sandgrain. For nonuniform sand, such as that on a river bed, k_s is often taken as the median diameter (D_{50}), although somewhat larger values are also used. The observed variation of ΔB with k_s^+ has led to classification of rough surfaces as follows: hydrodynamically smooth surface ($k_s^+ < 5$), transitional roughness ($5 < k_s^+ < 70$), and fully-rough surface ($k_s^+ > 70$). Cebeci and Bradshaw (1977) suggest the following correlation of Nikuradse's data

$$\Delta B = \left[B - 8.5 + \frac{1}{\kappa} \ln k_s^+ \right] \times \sin \{0.4258(\ln k_s^+ - 0.811)\} \quad (2)$$

for $2.25 \leq k_s^+ < 90$, with $B = 5.2$ and $\kappa = 0.42$. The formula of Nikuradse, without the sin term, is employed for $k_s^+ > 90$. Tani (1987) provides a very cogent review of boundary layers on rough surfaces, including a re-analysis of the data of Nikuradse and others.

For roughness other than sandgrain, ΔB depends on parameters that describe the roughness and, to a lesser extent, on the flow geometry. There is, at present, no theoretical way to predict ΔB for any particular roughness configuration. This is the so-called *roughness characterization* problem. There have been numerous experiments conducted to determine ΔB, and the so-called *equivalent sandgrain roughness,* for different types of roughness. For a given roughness type, however, a single length-scale parameter is usually not sufficient to characterize the roughness effect.

3 Modeling of Flow Over Rough Surfaces

There are several different levels at which models of roughness are made, apart from the classical analysis in which Eq. (1) is integrated to derive friction formulas for pipes (the Moody diagram), channels and flat plates. Here, we summarize the various approaches.

Rotta (1962) proposed a simple modification to the well known van Driest (1956) formula for mixing length to account for roughness:

$$l^+ = \kappa(y^+ + \Delta y^+)\left\{1 - \exp\left[-\frac{y^+ + \Delta y^+}{A^+}\right]\right\} \quad (3)$$

in which the shift in the wall coordinate, Δy^+, was expressed as a function of the equivalent sandgrain roughness parameter k_s^+

$$\Delta y^+ = 0.9\left[\sqrt{k_s^+} - k_s^+ \exp\left(-\frac{k_s^+}{6}\right)\right] \quad (4)$$

Cebeci and Chang (1978) used this model with A^+ as a function of pressure gradient. Equation (4) is a curve fit to the correlation of Rotta, and is valid for $4.535 < k_s^+ < 2000$, with the lower limit corresponding to the upper bound of hydraulically-smooth surfaces. The model of Rotta, along with several other that have been suggested, were reviewed by Granville (1985) to relate the damping function A^+, and the distributions of mixing length and eddy viscosity, to the roughness function ΔB of Eq. (1). In a later paper, Granville (1988) extended this analysis of the wall region to flat-plate boundary layers on smooth and rough surfaces. The earlier work of Cebeci and Chang (1978) may, in some respects, be regarded as an application of Granville's version of the van Driest-Rotta mixing-length model. In a recent paper, Krogstad (1991) has suggested yet another version of the mixing-length model for sandgrain roughness. The various mixing-length models differ in the manner in which the effect of roughness is introduced, ranging from a shift in the wall distance (effectively specifying a nonzero mixing length at the wall) to introduction of roughness dependent damping functions in formulas of the van Driest type. Once the mixing-length distribution is prescribed, the Reynolds stress in the momentum equation is known in terms of the mean velocity and that equation can be solved, along with continuity, to determine the flow development. However, these models cannot be generalized to apply to flows involving separation, and to three-dimensional flows.

The second approach to modeling wall roughness is to account for it indirectly by recognizing its effect on the flow at some distance from the wall. This is the so-called *wall-function approach.* In this approach, the equations of continuity and momentum, along with turbulence-model equations are solved only in the region $y^+ > y_m^+$, and all boundary conditions are specified at a point y_m^+, usually chosen to lie in the logarithmic region, where Eq. (1) applies. The boundary conditions needed to solve the equations depend on the turbulence model that is employed. In the k-ε model, for example, it is necessary to prescribe, in addition to the velocity components, the values of k and ε at y_m^+. Following the practice for smooth surfaces, these are deduced by assuming that the turbulence is in local equilibrium. The wall functions most commonly used are

$$u^+ = \frac{1}{\kappa} \ln (Ey^+); \quad k = \frac{u_\tau^2}{\sqrt{C_\mu}}; \quad \varepsilon = \frac{u_\tau^3}{\kappa y} \quad (5)$$

where $E = \exp\{\kappa(B - \Delta B)\}$ and ΔB depends on k_s^+. As the wall-function approach relies on the law of the wall (1), it is also not suitable for separated flows and it cannot be readily extended to three-dimensional flows without further assumptions.

Yet another way to account for surface roughness, especially roughness introduced by a regular array of discrete three-dimensional elements, such as cones or spheres, is to introduce a form drag term into the momentum equation and take into account the blockage effect of the roughness elements on the flow. Among such approaches are those of Christoph and Pletcher (1983), who added a sink term to the momentum equation for the form drag and employed a variant of the mixing-length model including roughness effect to investigate the influence of discrete roughness elements on skin friction and heat transfer in compressible flows, and Taylor et al. (1985), who modified the continuity and momentum equations to account for the blockage effect of the roughness array, added a form drag term to the momentum equations, and employed the standard smooth-wall mixing-length formula of van Driest. An advantage of the discrete element model is that it attempts to make a direct connection between the roughness geometry (size, shape, distribution, etc.) and roughness effect, and does not rely on a single length scale (such as the equivalent sandgrain size k_s^+) to characterize roughness. Such models are not immediately applicable to sandgrain or similar roughness.

The last level of modeling considered involves modification of smooth-wall turbulence-model equations to treat rough walls. Mixing-length and eddy-viscosity models discussed in the previous section also could be included in this category to the extent that they are sometimes used in combination with turbulence-model equations, as in the k-ε model. On a somewhat different level, however, are models that explicitly account for roughness effects through additional terms in the turbulence-model equations, or modifications in model constants or functions.

A model that falls in this category is the k-ω model of Wilcox (1993), in which the same equations are employed for smooth and rough surfaces but the effect of roughness is accounted for through the boundary conditions at the wall. In this model, the

Reynolds stresses, $-\overline{u_i u_j}$, are related to the mean rates of strain via

$$-\overline{u_i u_j} = \nu_t\left(\frac{\partial U_i}{\partial x_j} + \frac{\partial U_j}{\partial x_i}\right) - \frac{2}{3}k\delta_{ij} \quad (6)$$

and the eddy viscosity ν_t is related to the turbulent kinetic energy k and specific dissipation rate ω by $\nu_t = \gamma^* k/\omega$, where γ^* is a constant, U_i and u_i are, respectively, the mean and fluctuating velocity components, and δ_{ij} is the Kronecker delta. The quantities k and ω are determined from the model equations:

$$\frac{\partial k}{\partial t} + U_j\frac{\partial k}{\partial x_j} = \frac{\partial}{\partial x_j}\left[(\nu + \sigma^*\nu_t)\frac{\partial k}{\partial x_j}\right] - \overline{u_i u_j}\frac{\partial U_i}{\partial x_j} - \beta^* k\omega \quad (7)$$

$$\frac{\partial \omega}{\partial t} + U_j\frac{\partial \omega}{\partial x_j} = \frac{\partial}{\partial x_j}\left[(\nu + \sigma\nu_t)\frac{\partial \omega}{\partial x_j}\right] + \gamma\frac{\omega}{k}\left(-\overline{u_i u_j}\frac{\partial U_i}{\partial x_j}\right) - \beta\omega^2 \quad (8)$$

where t is time, and the values of the various model constants are $\beta = 3/40$, $\beta^* = 0.09$, $\gamma = 5/9$, $\gamma^* = 1$, and $\sigma = \sigma^* = 0.5$.

From an analysis of these equations in the near-wall region, Wilcox showed that, for rough surfaces, the wall boundary condition for the specific dissipation rate is $\omega = u_\tau^2 S_R/\nu$, in which S_R depends on k_s^+ such that velocity distribution conforms with Eq. (1). For sandgrain roughness, he proposed

$$S_R = \begin{cases} (50/k_s^+)^2 & k_s^+ < 25 \\ 100/k_s^+ & 25 \le k_s^+ \le 400 \end{cases} \quad (9)$$

In the k-ε model, Eq. (6) is retained but the eddy viscosity is related to the turbulence kinetic energy k and its rate of dissipation ε by $\nu_t = C_\mu k^2/\varepsilon$, and k and ε are determined from the model equations

$$\frac{\partial k}{\partial t} + U_j\frac{\partial k}{\partial x_j} = \frac{\partial}{\partial x_j}\left[\left(\nu + \frac{\nu_t}{\sigma_k}\right)\frac{\partial k}{\partial x_j}\right] - \overline{u_i u_j}\frac{\partial U_i}{\partial x_j} - \varepsilon \quad (10)$$

$$\frac{\partial \varepsilon}{\partial t} + U_j\frac{\partial \varepsilon}{\partial x_j} = \frac{\partial}{\partial x_j}\left[\left(\nu + \frac{\nu_t}{\sigma_\varepsilon}\right)\frac{\partial \varepsilon}{\partial x_j}\right] + C_{\varepsilon 1}\frac{\varepsilon}{k}\left(-\overline{u_i u_j}\frac{\partial U_i}{\partial x_j}\right) - C_{\varepsilon 2}\frac{\varepsilon^2}{k} \quad (11)$$

in which the constants take the values $C_\mu = 0.09$, $\sigma_k = 1.0$, $\sigma_\varepsilon = 1.3$, $C_{\varepsilon 1} = 1.44$, and $C_{\varepsilon 2} = 1.92$. Comparison of Eqs. (7) and (10) shows that $\omega = \varepsilon/\beta^* k$ and, therefore, it is possible to transform the ω-equation into one for ε, and vice versa. The resulting model equations are, of course, different.

To the authors' knowledge, almost all applications of the more familiar k-ε model to rough walls have employed the wall-functions approach outlined above. On the other hand, a great deal of effort has been devoted to abandon the wall functions for smooth walls by using the so-called low-Reynolds-number or near-wall models, in which the model constants are replaced by functions, and additional terms are introduced in the ε-equation. Patel et al. (1985) reviewed the various approaches and concluded that none was really suitable for describing the flow near a smooth wall. A few more near-wall models have appeared since that review but none has considered the possibility of including surface roughness.

An alternative to the near-wall extensions of the k-ε model is to use a two-layer approach in which the near-wall flow is resolved by a one-equation model and the flow beyond the wall layer by the standard two-equation model. In one such model, proposed by Chen and Patel (1988), ε in the near-wall region is specified by $\varepsilon = k^{3/2}/l_\varepsilon$, the eddy viscosity is obtained from $\nu_t = C_\mu k^{1/2} l_\mu$, and the length scales l_μ and l_ε are prescribed to model the wall-damping effects in terms of the turbulence Reynolds number R_y $(=\sqrt{k}y/\nu)$. This approach offers a very direct way to extend the k-ε model to rough walls by modification of the two prescribed length scales as follows:

$$l_\mu = C_l(y + \Delta y)[1 - \exp - (R_y + \Delta R_y)/A_\mu] \quad (12)$$

$$l_\varepsilon = C_l(y + \Delta y)[1 - \exp - (R_y + \Delta R_y)/A_\varepsilon] \quad (13)$$

where $C_l = \kappa C_\mu^{-3/4}$, $A_\varepsilon = 2C_l$, $A_\mu = 70$, $\kappa = 0.418$, and $\Delta R_y = k^{1/2}\Delta y/\nu$. The dependence of Δy on roughness is given by Eq. (4). The boundary between the two layers is placed in the usual logarithmic region, where the eddy viscosity is much larger than the molecular viscosity, and the eddy viscosity is matched at that location.

To summarize this section, it is noted that modeling of the flow near a rough surface, and particularly that between the logarithmic layer, for which empirical correlations exist, and the effective location of the wall, where the no-slip condition applies in some average sense, presents considerable difficulties. Such modeling has not received much attention particularly in the context of their application to complex flows with separation and reattachment, where the logarithmic law and the associated wall-function approach loses its validity. In the selection of a turbulence model for rough surfaces, two factors are critical: (*a*) the model should be capable of describing the three roughness regimes, and (*b*) it should be possible to apply the model to describe separated flows. In the following, we assess the k-ω model and the extended two-layer k-ε model outlined above. For the present, discussion is restricted to sandgrain roughness for which the classical correlations based on the experiments of Nikuradse apply.

4 Use of Rough-Wall Turbulence Models in Reynolds-Averaged Navier-Stokes Equations

In principle, the turbulence models outlined in the last section may be employed in any numerical method that solves the Reynolds-averaged Navier-Stokes equations, or some reduced forms of those equations appropriate for specific applications. The full equations are required, however, for a general treatment of flows with separation.

The numerical method used here is a derivative of that described in detail by Chen and Patel (1988), and employed by Richmond and Patel (1991). This method solves the full Reynolds-averaged Navier-Stokes equations in generalized, nonorthogonal coordinates. The momentum and turbulence transport equations are discretized using analytic solutions of the linearized equations. This approach does not lend itself to the usual order-of-accuracy analysis that is common to traditional finite-difference methods based on Taylor expansions. However, a recent comparative study made by Sotiropoulos et al. (1994) for three-dimensional flows suggests that the accuracy of the finite-analytic method is comparable with that of a second-order finite-difference method although the former tends to become first-order in the limit of infinite mesh aspect ratio. The pressure-velocity coupling is made through the continuity equation using the well-known SIMPLER algorithm. Although the numerical method solves the unsteady-flow equations in a time-marching scheme, the present work is confined to steady flows where time is used simply as an iteration parameter to seek the steady-state solution.

The numerical method described in the references cited above was employed by Patel et al. (1991) to study the flow over smooth wavy walls, where the wave amplitude was varied to include flows with separation and reattachment. The grid-dependency of the method was extensively tested during the course of that study. Thus, the present work may be regarded as a natural extension of that study.

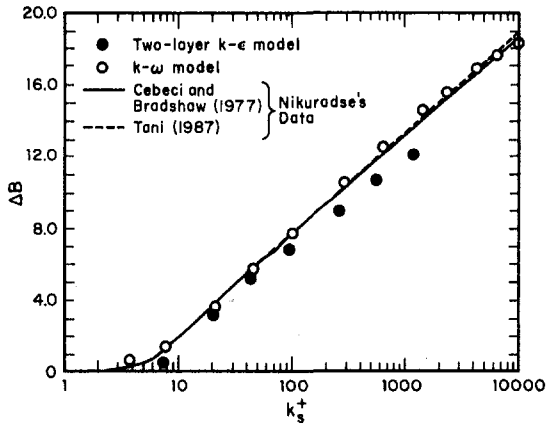

Fig. 1 Roughness function ΔB

For the present study, the version of the numerical method employed by Patel et al. (1991) was further modified to apply space-periodic boundary conditions which are appropriate for fully-developed flows that are invariant in the streamwise direction, or flows that are periodic in space. This resulted in a considerable saving of computer time and enabled a high grid concentration to be used in the solution domain. During the application of the method to rough walls, however, it was found that further grid refinement was needed in the near-wall region to obtain convergence and grid-independent solutions. This is presumably due to the increasing near-wall gradients of mean-velocity components and turbulence parameters with increasing roughness.

5 Flow in a Straight Rough-Wall Channel: The Moody Diagram

Analysis of fully-developed turbulent flow in long, straight, round pipes and two-dimensional channels can be found in most fluid mechanics textbooks. In particular, integration of Eq. (1) leads to well-known logarithmic friction formulas that are embodied in the so-called Moody diagram. Numerical solutions of such simple flows are readily obtained with periodic boundary conditions applied in the streamwise direction. As a preliminary test of the two rough-wall turbulence models, calculations were made for a two-dimensional channel at a Reynolds number of 10^6, based on channel height H. For the highest roughness considered, as many as 159 grid points across one-half of the channel, with the first grid point placed at a distance of 10^{-8} channel heights from the wall, were required to obtain converged and grid-independent solutions. To achieve convergence of the maximum residuals of pressure, velocity components, and turbulence parameters to with 10^{-5}, with a constant time step of 0.1, some 750 steps or iterations were required. This took about 95 minutes of CPU time on a Apollo DN10000 computer. The grid density quoted above may be compared with that used in the previous smooth-wall calculations of Patel et al. (1991), where only 49 points, with the first point at about 10^{-5}, were required to obtain similar level of convergence.

It was found that, with the k-ω model solutions could be obtained for values of k_s^+ much higher than the upper limit of 400 originally suggested by Wilcox in Eq. (9). In case of the two-layer model, roughness heights in the range $4.535 < k_s^+ < 2000$ were considered because Eq. (4) was designed for that range.

The predictions with the two turbulence models were compared in several ways. The roughness function ΔB determined from the calculated velocity profiles is shown in Fig. 1 along with the correlation of Cebeci and Bradshaw (1977) of Nikuradse's data, and Tani's (1987) re-evaluation of the same data. It is found that the k-ω model gives an almost perfect match with the empirical correlation for k_s^+ as large as 10^4, much larger than the limit of 400 imposed by Wilcox. The two-layer k-ε model, while providing the correct trends, underestimates the roughness effect, and the discrepancy appears to grow with increasing roughness. Not surprisingly, these observations were confirmed by comparison of the calculated friction coefficients with the analytically derived values. The friction coefficient predicted with the k-ω model was only 1.8 percent lower in the smooth channel, and 3.6 percent lower at the highest roughness, which, at the chosen Reynolds number corresponds to $k_s/H = 0.1$, the largest value shown in most Moody diagrams. While the two-layer k-ε model yielded an almost identical result for the smooth channel, it predicted a friction coefficient that was almost 31 percent lower at the highest roughness tested ($k_s^+ = 1205$, $k_s/H = 0.02$). As expected, these results were also reflected in the predicted eddy-viscosity and turbulence-energy profiles, the two-layer model yielding much lower values than those predicted by the k-ω model.

While the channel flow considered here is a rather simple case insofar as the numerical method is concerned, it is a very stringent and direct test of the underlying turbulence models especially because there are few, if any, uncertainties related to the numerical solutions. The results for this case suggest that the k-ω model reproduces, with quite remarkable accuracy, the well known effects of sandgrain roughness over a wide range of roughness size. The modifications made in the two-layer k-ε model, on the other hand, predict trends that are only qualitatively correct. It appears that this model would require additional tuning to bring it to the same level of performance as the k-ω model. In view of this, only the k-ω model is employed in the next example.

6 Flow Over a Sand Dune: Flow With Separation and Reattachment

Consider clear water (without sediment) turbulent flow over a train of fixed, two-dimensional dunes, identical in size and shape. The channel is open and the flow is uniform (i.e., the bed slope is adjusted to achieve a constant water depth). This somewhat idealized arrangement enables direct application of the present numerical method to a single dune, with periodic boundary conditions, and comparisons with the recent experiments of Mierlo and de Ruiter (1988), briefly described below.

The experiments were performed in a 55-m long, 1.5-m wide water flume. Some 33 identical, sand-plastered concrete dunes, of wavelength $\lambda = 1.6$ m and height $h = 0.08$ m, were installed on the flume bottom. The dune profile is shown in Fig. 2. A layer of sandgrains of nearly uniform size (mean diameter, $D_{50} = 1.6$ mm, and standard deviation of 1.1) was glued over the concrete dunes.

Experiments were performed with two water depths; the one with the higher depth ($d = 0.292$ m, designated as case T6) was chosen for the present calculations. For the present two-dimensional flow calculations, the reference bulk velocity U_0 was determined by integration of the measured velocity profile. The measurements were made with a two-component LDV some distance off the channel centerplane at 16 streamwise sections along the 17th dune. The data include the longitudinal and vertical components of mean velocity (U, V) and the three Reynolds stresses ($\overline{u^2}$, $\overline{v^2}$, $\overline{uv}$) associated with the velocity fluctuations in these directions. The friction velocity (u_τ) and the wall shear stress ($\tau_w = \rho u_\tau^2/2$) were recalculated at each measurement location along the dune following a procedure similar to Mierlo and de Ruiter, in which Eq. (1), with $k_s = D_{50}$, was fitted to the measured velocity distribution in the near-wall region. As this method involves considerable uncertainty, the results will be shown with an error bar. The reanalysis was abandoned in regions where the uncertainty became unacceptable. The recalculated experimental values gave k_s^+ less than

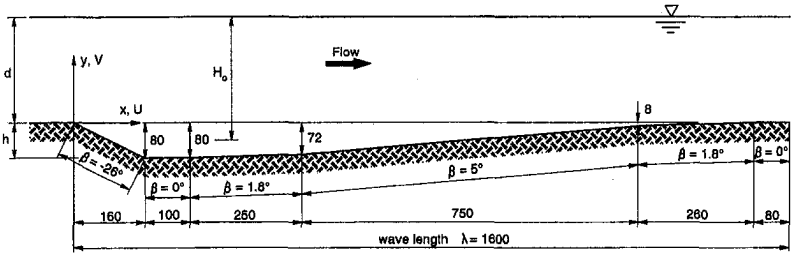

Fig. 2 Dune profile of Mierlo and de Ruiter (1988) (all dimensions in mm, β is local slope)

70 indicating a transitional roughness regime over the entire dune. The eddy viscosity (ν_t) was computed from its usual definition for two-dimensional flow: $\nu_t = -\overline{uv}/(\partial U/\partial y)$, which involves differentiation of the measured velocity data. These procedures need to be kept in mind when the experimental data are compared with the numerical solutions.

6.1 Numerical Simulation. Calculations were performed for the dune geometry of Fig. 2 using only the k-ω model. The grid consisted of 82 streamwise points and 69 cross-stream points, with the first grid point from the bed at a distance of 10^{-6} (normalized by d) and that from the free surface at 10^{-2}. This distribution was determined on the basis of the calculations which were carried out for the channel flow over a range of roughness sizes. To apply the periodic boundary conditions on the upstream and downstream boundaries of the dune, it was extremely important to ensure that all coordinates, and the associated grid-generation functions, were properly matched at the upstream and downstream stations. The free surface was assumed to be flat and treated as a plane of symmetry. In other words, the calculations were made for one-half of a closed channel. The pressure distribution along the center of this channel was then converted to a free-surface elevation assuming hydrostatic pressure variation in the normal direction. Along the dune bed, the usual no-slip conditions were applied to the velocity components and turbulent kinetic energy, and the value of ω was prescribed by Eq. (9). Finally, in the time-marching numerical method, the solution was started from a simple parabolic mean velocity profile throughout, and iterated to a converged steady state. The manner in which these computations were performed make them completely predictive, i.e., only the boundary geometry, roughness and the Reynolds number are prescribed, with no reference made to the experimental data.

The Reynolds number based on the bulk velocity ($U_0 = 0.633$ m/s) and inlet depth ($d = 0.292$ m) for water at 18°C is 174,640. The calculations were made with the actual roughness $k_s = D_{50}$ ($k_s/d = 0.0055$). Calculations were also performed with other roughness heights but they are not of interest in the present context.

6.2 Results: Pressure and Friction Distributions. An overview of the flow in the dune-bed channel in provided by Fig. 3. Figure 3(a) shows the locations of the 16 streamwise stations where LDV measurements were made, the calculated mean streamlines, the points of separation and reattachment, and the eddy containing the recirculating flow. The pressure and friction coefficients, defined by

$$C_{p0} = \frac{p - p_{\text{ref}}}{\frac{1}{2}\rho U_0^2}; \quad C_{f0} = \frac{\tau_w}{\frac{1}{2}\rho U_0^2} \tag{14}$$

where p_{ref} is the reference pressure at the downstream boundary, are shown in Fig. 3(b). The points of separation and reattachment can be readily identified from the friction distribution. The calculated friction distribution is in reasonable agreement with that determined from Eq. (1) and the measured velocity profiles, in spite of the uncertainties involved. The bed pressure distribution shows that there is a steep pressure rise between stations 4 and 9, on either side of the reattachment point, a favorable pressure gradient from station 9 to about station 15, and nearly constant pressure over the top of the dune and in the upstream part of the separation eddy.

As noted above, the pressure variation along the assumed flat free surface can be converted into a free-surface elevation assuming hydrostatic variation with depth. These free surface elevations are shown in Fig. 3(c). The bed roughness has a rather small effect on the free surface, but the effect of the bed shape and the separation eddy is evident from the distortion of the free surface. It is observed that the free surface is depressed over the crest of the dune and elevated some distance downstream of the reattachment point. This coupling between dune shape, the separation eddy, and the free surface is, of course, of considerable interest as it would vary with Froude number (flow depth).

6.3 Velocity and Turbulence Distributions. The calculated distributions, with distance from the bed (y), of the mean velocity components (U, V), the Reynolds stress ($-\overline{uv}$), and the eddy viscosity (ν_t), all made dimensionless by d and U_0, as appropriate, are compared with the experimental

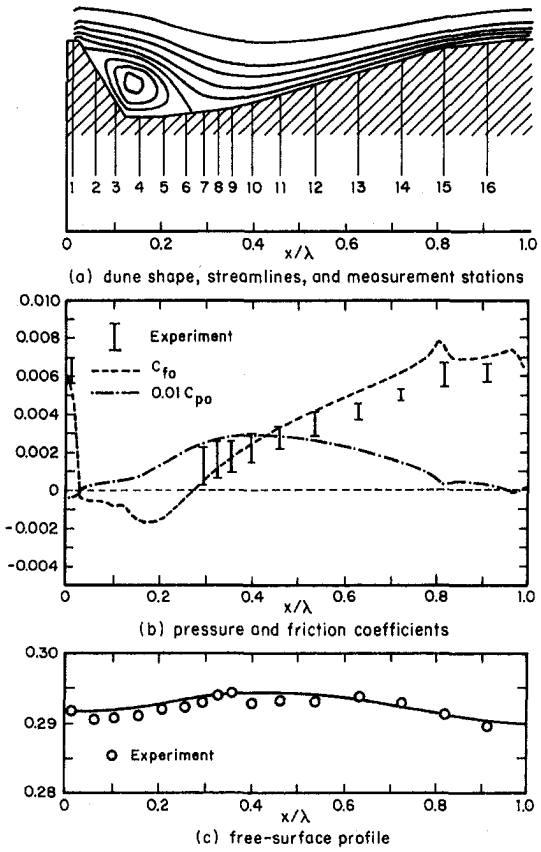

Fig. 3 Overview of the flow in dune-bed channel

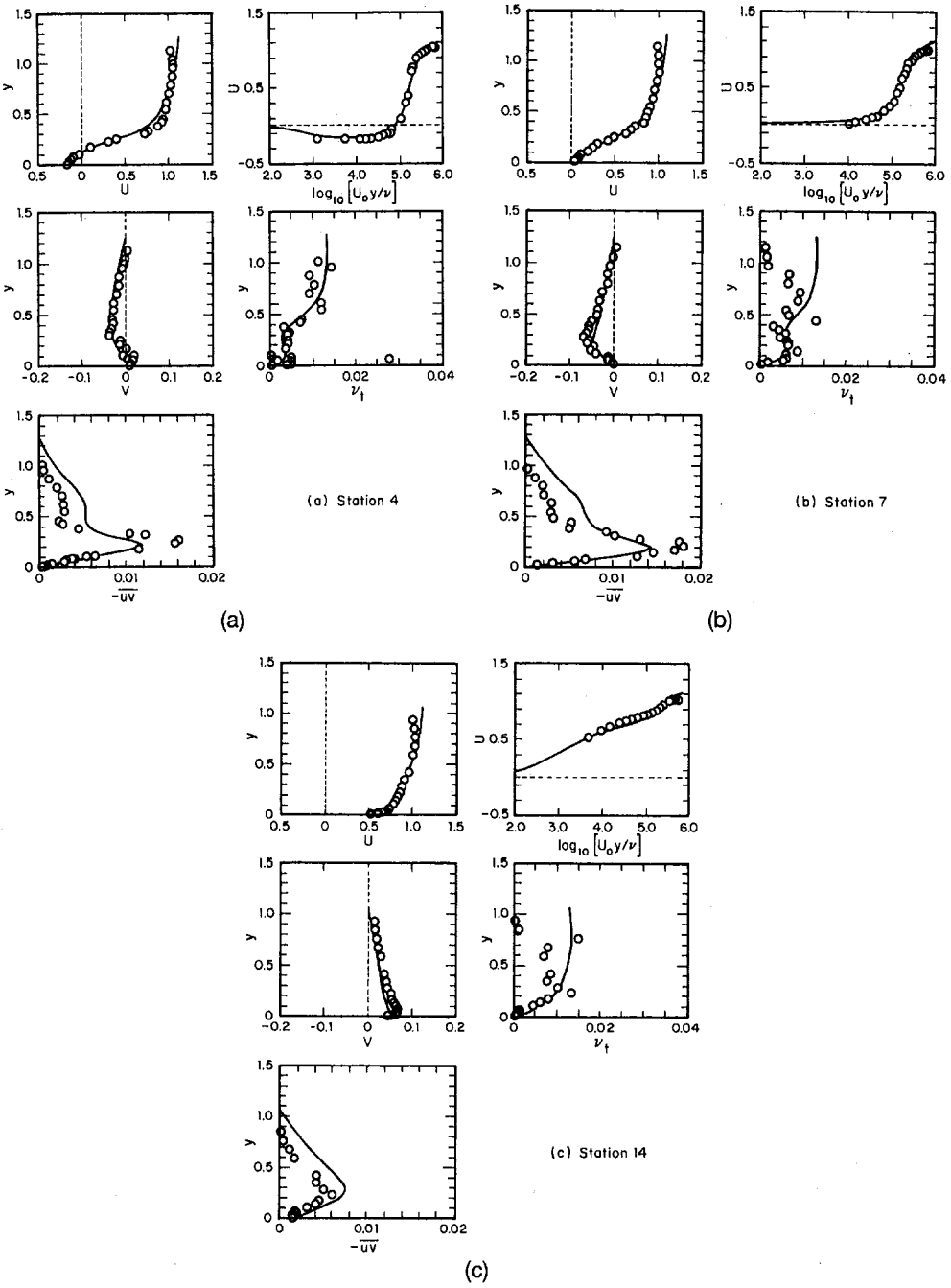

Fig. 4 Velocity and turbulence profiles at three sections along the dune

data in Fig. 4. In addition, the distribution of the streamwise velocity is shown in logarithmic coordinates (U versus $\log_{10} U_0 y/\nu$), to examine the possible validity of the law of the wall. Although measurements were made at 16 stations, comparisons are made with the calculations at only three representative stations, namely, stations 4, 7 and 14, marked in Fig. 3(a).

With reference to Fig. 3(a), it is convenient to consider the flow over the dune in three segments: stations 2 to 6, which lie in the separated zone; stations 7 to 9, which are in the region where the flow recovers following reattachment; and stations 10 to 16 and station 1, where the flow may be regarded as well developed. The boundaries of these regions are, of course, not precisely defined.

In the first region, Fig. 4(a) for station 4 indicates a layer of flow reversal ($U < 0$) near the wall, in the linear as well as the logarithmic plots. The latter reveals general agreement in the shape of the measured and calculated velocity distributions in the near-wall region but the calculated velocity is somewhat lower and the height of the reverse flow region is slightly underestimated. The lack of a clearly defined logarithmic region in the measured and calculated velocity profiles indicates that use of the law of the wall to infer the friction velocity from measured data, or to apply wall functions in calculations, is clearly unjustified. Figure 4(a) also indicates that the k-ω turbulence model performs remarkably well in predicting the overall features of the velocity components, the Reynolds stress, and the eddy viscosity distributions although the magnitudes are not precisely captured in some parts of the flow. Locally high values of the Reynolds stress are observed in the shear layer above the separation eddy in the experiments but they are not reproduced by the calculations.

The disagreement between the data and the calculations near the free surface, particularly in the longitudinal velocity and eddy viscosity, is observed at all stations, and is related, to some extent, to lack of any special free-surface treatment (to account for damping of the vertical velocity fluctuations and consequent changes in the eddy viscosity and shear stress) in the turbulence model. More specifically, the measurements reveal a velocity maximum below the free surface while the calculations have a maximum at the free surface (which is treated as a plane of symmetry). Also, in spite of the errors that are inherent in the determination of the eddy viscosity from measurements, the data indicate a consistent drop near the free surface while the calculations reach a constant high value. However, it should be pointed out that this effect may not be entirely due to turbulence as the experiments also contain the effects of secondary motions that are not accounted for in the calculations. Be that as it may, it would be of interest to explore the possibility of incorporating some modification in the k-ω model for the free surface effect.

At station 7, shown in Fig. 4(b), where the flow is recovering after reattachment, the calculated mean velocity components are in excellent agreement with the data, except near the free surface. A logarithmic segment in the velocity profile is evident, and therefore use of the law of the wall in the determination of the wall shear stress and in wall functions would be justified in this case. With respect to the two turbulence quantities, it is found that agreement between the calculations and experimental data is similar to that at the previous station. The layer of high Reynolds stress persists at some distance from the wall.

In the third and final region, extending from station 10 to 16, and including station 1, which lies just ahead of the dune crest, the measured Reynolds stress did not show the characteristic peaks observed in the two upstream regions suggesting that the shear layer resulting from the separation has mixed with the ambient flow. At station 14, shown in Fig. 4(c), it is found that the predicted streamwise velocity tends to be somewhat lower, and the Reynolds stress to be somewhat higher, than the data. As smooth-wall calculations also showed the same tendency, this discrepancy could not be attributed to the treatment of roughness in the turbulence model. Instead, the overestimation of the Reynolds stress at this station, and in the outer layers at the previous two stations, appears to be a general feature of the basic k-ω model.

7 Discussion and Conclusions

The well-known results of classical experiments with sandgrain roughness were reviewed together with four different approaches to model surface roughness in numerical solutions of fluid flow equations. Algebraically prescribed mixing-length (or, equivalently, eddy-viscosity) models, and the so-called wall-functions approach, are the two most common ways to allow for surface roughness. As in smooth-wall flows, both are restricted to relatively simple flows where the underlying correlations are valid. These models cannot be used in more complex flows, including separation, without further intervention. The discrete element approach, on the other hand, has been applied to regular roughness with some success but it is unlikely to be practical in complex flows. The fourth approach, involving modifications in turbulence-model equations and/or boundary conditions for these equations, appears, at the present time, to be the most promising one for extension of the increasingly powerful methods of computational fluid mechanics to rough surfaces. In view of this, two alternatives in this category were further examined, namely, the k-ω model of Wilcox (1993), and an extension of the two-layer k-ε model of Chen and Patel (1988).

The calculations presented here indicate that the k-ω turbulence model provides quite accurate predictions of the effects of sandgrain roughness for the classical case of fully-developed turbulent flow in a two-dimensional channel. In fact, the present calculations suggest that the well known Moody diagram of friction factor in smooth and rough pipes can be constructed over the entire roughness and Reynolds-number range of interest. This may not be a worthwhile exercise, however, as each point requires a complete numerical solution and considerable computing time. The power of the numerical approach and the turbulence model lies, instead, in the fact that it can be applied to much more complicated wall geometries because it has been validated against this standard.

Extension of the two-layer k-ε model is quite straightforward, but the results presented here suggest that further modifications are needed for this model to achieve the same level of performance as the k-ω model. There are a number of ways in which improvements may be made, including adjustments of the constants and damping functions in the length-scale equations, and judging by the success of the k-ω model, by explicitly including a roughness dependence in the length scale at the wall. In the absence of appropriate turbulence data or other guidance, numerical experiments are needed to establish such modifications. This course of action was not pursued here largely because of the success of the k-ω model.

Turbulent flow in a channel with a fixed sand-dune bed was used as a vehicle to study the performance of the k-ω model in separated flow over a sandgrain roughened surface. Comparisons with the experiments of Mierlo and de Ruiter (1988) provided some degree of validation of the model as most of the important flow features were captured in the numerical solutions. Prediction of resistance of dune-bed channels is an important problem in hydraulic engineering. The solution procedure employed here provides a very basic way to re-examine the various empirical friction formulas in current use in that field.

While the k-ω model is not completely satisfactory with respect to the details of the predicted velocity and turbulence distributions, it is perhaps the only model that can be employed to extend the applicability of modern computational codes to rough surfaces as it is not, in principle, restricted to simple attached flows. The fact that the model equations remain the same in the near-wall region is an additional advantage.

Finally, it should be noted that the present work was principally concerned with sandgrain roughness. The same approach to turbulence modeling can be applied to other types of roughness once an equivalent sandgrain roughness is established.

Acknowledgment

This research was supported by the National Science Foundation under grant no. CTS-90-267.

References

Cebeci, T., and Bradshaw, P., 1977, *Momentum Transfer in Boundary Layers,* Hemisphere Publishing Corporation.

Cebeci, T., and Chang, K. C., 1978, "Calculation of Incompressible Rough-Wall Boundary-Layer Flows," *AIAA Journal,* Vol. 16, pp. 730–735.

Chen, H. C., and Patel, V. C., 1988, "Near-Wall Turbulence Models for Complex Flows Including Separation," *AIAA Journal,* Vol. 26, pp. 641–648.

Christoph, G. H., and Pletcher, R. H., 1983, "Prediction of Rough-Wall Skin Friction and Heat Transfer," *AIAA Journal,* Vol. 21, pp. 509–515.

Granville, P. S., 1985, "Mixing-Length Formulations for Turbulent Boundary Layers over Arbitrarily Rough Surfaces," *Journal of Ship Research,* Vol. 29, pp. 223–233.

Granville, P. S., 1988, "Eddy Viscosities and Mixing Lengths for Turbulent Boundary Layers on Flat Plates, Smooth or Rough," *Journal of Ship Research,* Vol. 32, pp. 229–237.

Hama, F. R., 1954, "Boundary Layer Characteristics for Smooth and Rough Surfaces," *Transactions of the Society of Naval Architects & Marine Engineers,* Vol. 62, pp. 333–358.

Krogstad, P., 1991, "Modification of the van Driest Damping Function to Include the Effects of Surface Roughness," *AIAA Journal,* Vol. 29, pp. 888–894.

Mierlo, M. C. L. M., and de Ruiter, J. C. C., 1988, "Turbulence Measurements above Artificial Dunes," Delft Hydraulics Lab., Delft, The Netherlands, Report Q789.

Moore, W. F., 1951, "An Experimental Investigation of the Boundary-Layer Development along a Rough Surface," Ph.D. dissertation, University of Iowa, Iowa City, IA.

Nikuradse, J., 1950, "Laws of Flow in Rough Pipes," National Advisory Committee for Aeronautics, NACA TM 1292 (Translation from VDI-Forschungsheft 361, 1933).

Patel, V. C., Chon, J. T., and Yoon, J. Y., 1991, "Turbulent Flow in a Channel with a Wavy Wall," ASME JOURNAL OF FLUIDS ENGINEERING, Vol. 113, pp. 579–586.

Patel, V. C., Rodi, W., and Scheuerer, G., 1985, "Turbulence Models for Near-Wall and Low Reynolds Number Flows: A Review," *AIAA Journal,* Vol. 23, pp. 1308–1319.

Richmond, M. C., and Patel, V. C., 1991, "Convex and Concave Curvature Effects in Wall-Bounded Turbulent Flows," *AIAA Journal,* Vol. 29, pp. 895–902.

Rotta, J., 1962, "Turbulent Boundary Layers in Incompressible Flow," *Progress in Aerospace Science,* Oxford, UK, Vol. 2, pp. 73–82.

Schlichting, H., 1936, "Experimentelle Untersuchungen zum Rauhigkeitsproblem," *Ingenieur-Archiv.,* Vol. 7, pp. 1–34; also, NACA TM 823 (1937).

Sotiropoulos, F., Kim, W. J., and Patel, V. C., 1994, "A Computational Comparison of Two Incompressible Navier-Stokes Solvers in Three-Dimensional Laminar Flows," *Computers & Fluids,* to appear.

Tani, I., 1987, "Turbulent Boundary Layer Development over Rough Surfaces," *Perspectives in Turbulence Studies,* H. U. Meier and P. Bradshaw, eds. Springer.

Taylor, R. P., Coleman, H. W., and Hodge, B. K., 1985, "Prediction of Turbulent Rough-Wall Skin Friction Using a Discrete Element Approach," ASME JOURNAL OF FLUIDS ENGINEERING, Vol. 107, pp. 251–257.

van Driest, E. R., 1956, "On Turbulent Flow Near a Wall," *Journal of Aeronautical Sciences,* Vol. 23, pp. 1007–1011, 1036.

Wilcox, D. C., 1993, "Turbulence Modeling for CFD," DCW Industries Inc., La Canada, CA.

The Effect of Torsion on the Bifurcation Structure of Laminar Flow in a Helical Square Duct

C. J. Bolinder
Division of Heat Transfer,
Lund Institute of Technology,
Box 118, 221 00 Lund, Sweden

The laminar fully developed flow problem in a helical square duct with a finite pitch is solved numerically using the finite-volume method with the SIMPLEC algorithm. h^2-extrapolation is used to locate the limit points of the stable solution branches. Results for the friction factor are presented. For helical ducts of small pitch, or torsion, it is verified that all investigated flow properties are very similar to those for a toroidal duct with the same dimensionless curvature. A new correlation is proposed for the friction factor ratio.

Introduction

Flow in curved ducts is often considered from an analytical/numerical or experimental point of view, see e.g. the review articles by Berger et al. (1983), Nanadakumar and Masliyah (1986), Ito (1987), and Berger (1991). The curved geometry is important from both an industrial and an academic standpoint. The curvature κ and the torsion τ of the centerline of the duct characterize the particular kind of a duct. For example, for a toroidal duct κ is constant and τ is zero, and for a helical duct both κ and τ are constant and nonzero. The torsion gives rise to the so-called pitch of the duct, $2\pi K$ in Fig. 1. A finite torsion also makes the coordinate system nonorthogonal. This complicates the analysis, and might be a reason why relatively few articles concern the effect of a finite pitch. In fact, most analytical/numerical studies concentrate on the toroidal duct, while many experimental studies concern helical ducts. The use of nonorthogonal coordinates makes the choice of velocity components ambiguous. Often the contravariant velocity components are used. They are obtained when the velocity vector is expanded in the so-called natural basis of the coordinate system (see below). However, this is not convenient if the natural basis is nonorthogonal (i.e., the coordinate system is nonorthogonal). It is preferable to use a physical, that is an orthonormal basis, since then the physical velocity components are obtained as the projections of the velocity vector on the respective physical base vectors. For curved ducts there exists an obvious choice of physical basis, viz. the tangent $\mathbf{t}$, the normal $\mathbf{n}$, and the binormal $\mathbf{b}$ of the centerline of the duct. Thus, we expand $\mathbf{v}$ as follows

$$\mathbf{v} = w\mathbf{t} + u\mathbf{n} + v\mathbf{b}. \tag{1}$$

The axial flow component w is then obtained as the projection of the velocity on the tangent $\mathbf{t}$, and the secondary flow components u and v are obtained as the projection of the velocity on the cross-plane vectors, the normal $\mathbf{n}$ and the binormal $\mathbf{b}$. Note that Eq. (1) generalizes the definition of the secondary flow components for a toroidal duct to the helical duct. As will be shown in the following, one may for a fully developed flow in a helical duct define a function Ψ, which has properties similar to those of a stream function. Ψ satisfies the continuity equation, but for nonzero torsion, the curves Ψ = constant do not define secondary flow streamlines in the $\mathbf{n}$, $\mathbf{b}$-plane. Thus, to depict the secondary flow with contours of Ψ for a duct with nonzero torsion is deceptive. A true picture of the secondary flow can only be obtained from a vector plot.

Previous theoretical investigations on the effect of a finite pitch have mainly concerned ducts of circular cross-section, viz. Murata et al. (1981), Wang (1981), Germano (1982), Kao (1987), Tuttle (1990), Xie (1990), Chen and Jan (1992), and Liu and Masliyah (1993). Ducts of elliptical cross-section have been studied by Germano (1989) and Tuttle (1990), annular cross-section by Yang and Ebadian (1993) and square cross-section by Chen and Jan (1993). A more detailed review of some of the above-mentioned papers can be found in Bolinder (1993). Notably, the author does not agree with Tuttle's (1990) discussion about different frames of reference of the observer. For example, from "elementary kinematics" Tuttle obtains his Eq. (27), which reads (with our notations)

$$\mathbf{v} = w\mathbf{t} + u\mathbf{n} + v\mathbf{b}$$
$$= w\mathbf{t} + (v^x\mathbf{n} + v^y\mathbf{b}) + \frac{\tau}{1 - \kappa x} w(-y\mathbf{n} + x\mathbf{b}), \tag{2}$$

where v^x and v^y are contravariant velocity components (denoted by u and v in Tuttle). The physical and the contravariant velocity components are related by

$$\left.\begin{aligned} w &= (1 - \kappa x)\, v^s, \\ u &= v^x - \tau y v^s, \\ v &= v^y + \tau x v^s. \end{aligned}\right\} \tag{3}$$

Contributed by the Fluids Engineering Division for publication in the JOURNAL OF FLUIDS ENGINEERING. Manuscript received by the Fluids Engineering Division February 8, 1994; revised manuscript received August 4, 1994. Associate Technical Editor: G. Karniadakis.

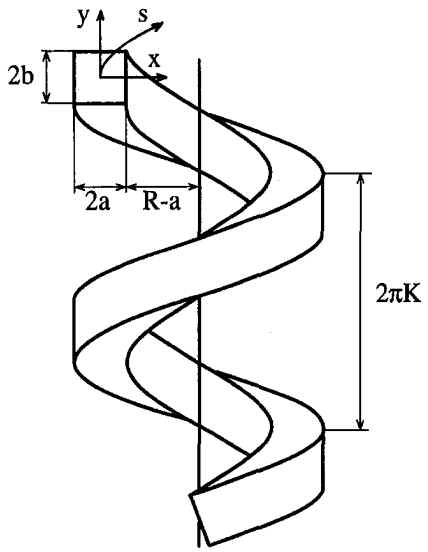

Fig. 1 Helical square duct

Thus Eq. (2) is obtained simply by expressing the physical velocity components u and v in terms of v^x, v^y and w. Note that $\mathbf{n}'$ and $\mathbf{b}'$ in Tuttle are identical to $\mathbf{n}$ and $\mathbf{b}$, they do not rotate with respect to each other. By introducing an "angular velocity" $\omega = \tau w\mathbf{t}/(1 - \kappa x)$, Tuttle rewrites the last term in Eq. (2) as $\omega \times (x\mathbf{n} + y\mathbf{b})$, and he interprets this term as "a rotational velocity caused by the rotation of $\mathbf{n}$ and $\mathbf{b}$ about the tangent vector $\mathbf{t}$." This rotational velocity should, according to Tuttle, relate a fixed observer to an observer "travelling along the pipe axis and rotating with the Frenet triad." In this author's opinion, $\omega \times (x\mathbf{n} + y\mathbf{b})$ is merely a part of the secondary flow, which accidentally may be written as a cross product. For ω to actually represent an angular velocity, relating two observers, ω must in particular not vary over the cross-section of the duct. Tuttle suggests the physical velocity component w to be used for the axial flow, and to use the contravariant velocity components v^x and v^y for the secondary flow, which justifies the use of a stream function Ψ for the secondary flow. Liu and Masliyah (1993) accept the arguments put forward by Tuttle and recommend the use of a stream function Ψ to represent the secondary flow.

Chen and Jan (1993) use polar coordinates in the $\mathbf{n}$, $\mathbf{b}$-plane and a finite-element technique to study the flow in a helical square duct. They derive the governing equations in terms of physical contravariant velocity components, i.e. the velocity is expanded in the normalized natural basis. The results are however presented in terms of our physical components. Chen and Jan conclude that the so-called Dean's instability, which occurs in a toroidal square duct, can be avoided due to the effect of torsion. This result is contrary to the findings of the present investigation.

Previous numerical work on toroidal ducts is much more extensive. Here is only referred to a few studies concerning the rectangular cross-section. Joseph et al. (1975) and Cheng et al. (1976) performed fully developed flow calculations for a toroidal square duct. When the Dean number, $\mathrm{De} = \mathrm{Re}\sqrt{\kappa d_h}$, was raised above a critical value of about 100, the secondary flow abruptly changed from the familiar two-vortex structure to a four-vortex structure, with two extra vortices near the outer wall of the duct. This behavior is now sometimes referred to as Dean's instability. Later Winters (1987) performed an accurate determination of the solution structure for toroidal rectangular ducts. He discovered several solution branches, some of which were found to be unstable. The findings of Joseph et al. and Cheng et al. could now be explained as follows: the abrupt change of flow structure at the critical Dean number was due to a jump from the primary S_1 branch to the S_3 branch (see Fig. 3). Solutions of the S_3 branch are however unstable to perturbations breaking the symmetry of the cross-section. Thus to be able to detect the S_3 branch with a transient solution procedure, symmetry must be assumed. Other references to the fully developed flow case are Daskopoulos and Lenhoff (1989) and Kao (1992). Developing flow in toroidal rectangular ducts is considered for example by Sankar et al. (1988) and Bara et al. (1992). The related problem of flow through straight twisted rectangular ducts has been treated by Masliyah and Nandakumar (1981), Nandakumar and Masliyah (1983) and Kheshgi (1993).

In this investigation, the stable solution branches are determined for fully developed flow in helical square ducts. The curvature is held constant, while the torsion is increased from zero. In this way we can study how the stable solution branches for a toroidal duct develop, as the duct is provided with an increasing torsion or pitch. Of particular interest is to determine the end points or the "limit points" of the solution branches. A limit point, or a "one-sided bifurcation point," marks the upper *or* the lower limit of two connected solution branches, where at least one of these branches is unstable. Therefore, since the present numerical method is transient and no unstable solutions can be found, at most one branch (the stable one) can be detected above or below a limit point.

Governing Equations

To save space, only a brief description of the method for deriving the governing equations is given here. For more de-

Nomenclature

a = half width of duct
b = half height of duct
$\mathbf{b}$ = binormal of centerline, $\mathbf{t} \times \mathbf{n}$
d_h = hydraulic diameter, $4ab/(a + b)$
De = Dean number, $\mathrm{Re}\sqrt{\kappa d_h}$
f = friction factor, $gd_h/(2\rho\bar{w}^2)$
g = $-\partial p/\partial s$
h = grid spacing
$2\pi K$ = pitch of helical duct, $2\pi\tau/(\kappa^2 + \tau^2)$
L_1, L_2, L_3, L_8 = limit points
$\mathbf{n}$ = normal of centerline, $\mathbf{r}_c''/\kappa$
p = generalized pressure
$\mathbf{r}$ = position vector of point in duct, Eq. (5)
$\mathbf{r}_c$ = position vector of centerline
R = radius of helical duct, $\kappa/(\kappa^2 + \tau^2)$
Re = Reynolds number, $\bar{w}d_h/\nu$
s = arc length of centerline, streamwise coordinate
S_1, S_3, S_5 = solution branches
$\mathbf{t}$ = tangent of centerline, $\mathbf{r}_c'$
u, v = secondary flow components, $\mathbf{v}\cdot\mathbf{n}$ and $\mathbf{v}\cdot\mathbf{b}$
U, V = dimensionless secondary flow components, $(u, v)d_h/\nu$
v^s, v^x, v^y = contravariant velocity components
$\mathbf{v}$ = velocity vector
w = axial flow component, $\mathbf{v}\cdot\mathbf{t}$
$\bar{w}$ = mean axial flow
x, y = coordinates along $\mathbf{n}$ and $\mathbf{b}$
ϵ = dimensionless curvature, κd_h
η = dimensionless torsion, τd_h
κ = curvature of centerline, $R/(R^2 + K^2)$
ν = kinematic viscosity
ρ = density
τ = torsion of centerline, $K/(R^2 + K^2)$
Ψ = stream function, Eq. (6)

Superscript

$'$ = derivative with respect to s

tails, and the actual equations, the reader is referred to Bolinder (1993). The position vector of the centerline of the duct is denoted by $\mathbf{r}_c(s)$. The parameter s is the arc length, which is used as a coordinate along the duct. The curvature κ and the torsion τ of $\mathbf{r}_c$ may for a circular helix be written

$$\kappa = \frac{R}{R^2 + K^2}, \quad \tau = \frac{K}{R^2 + K^2}. \tag{4}$$

R is the radius of the cylinder on to which the helix is coiled, and $2\pi K$ is the pitch of the helix, see Fig. 1. For a toroidal duct the pitch is zero, which implies that $\tau = 0$ and $\kappa = 1/R$. A straight twisted duct is obtained if $R = 0$, which implies that $\kappa = 0$ and $\tau = 1/\mathrm{K}$. Let x be a coordinate along the normal $\mathbf{n}$ and y a coordinate along the binormal $\mathbf{b}$, according to Fig. 1. Then the position vector can be represented as

$$\mathbf{r}(s, x, y) = \mathbf{r}_c(s) + x\mathbf{n}(s) + y\mathbf{b}(s). \tag{5}$$

The so-called natural base vectors of the coordinate system (s, x, y) are obtained as the partial derivatives of $\mathbf{r}$ with respect to the coordinates, they are thus tangents to the coordinate curves. One finds that the natural base vectors are nonorthogonal for points off the centerline, except for a toroidal duct (with $\tau = 0$). By expanding the velocity vector in the natural basis, the contravariant velocity components v^s, v^x, and v^y are obtained. However, as discussed in the introduction, if the natural basis is nonorthogonal, it is better to expand the velocity in the physical basis ($\mathbf{t}$, $\mathbf{n}$, $\mathbf{b}$) according to Eq. (1). Essentially two methods have been used in the past to derive the governing equations. The method employed, for example by Germano (1982, 1989) utilizes the fact that an orthogonal coordinate system is obtained if the x and y coordinate axes are rotated with respect to $\mathbf{n}$ and $\mathbf{b}$ in a prescribed manner along the duct. The orthogonality makes it easier to derive the governing equations, but then the coordinates must be transformed to undo the rotation. The other method to obtain the governing equations utilizes standard tensor analysis (e.g., Sokolnikoff, 1964) to derive the equations in terms of contravariant velocity components. To obtain the physical velocity components, the transformation given by Eq. (3) must then be employed. Note that the above two methods yield the same final result. Thus the method of Germano (1982, 1989) makes no simplifying assumptions as claimed by some authors, e.g., Xie (1990) and Chen and Jan (1992, 1993). By using basic vector and tensor analysis one may derive the governing equations directly in terms of the coordinates s, x, and y and the physical velocity components w, u, and v. This method was used by the present author, see Bolinder (1993) for the final result.

The governing equations, i.e., the continuity and the Navier-Stokes equations, are simplified by assuming a steady, incompressible and fully developed flow. The assumption of a fully developed flow means that all s-derivatives are set to zero, except for the pressure derivative $g = -\partial p/\partial s$, which is assumed to be constant. This constant is used as an input to the computations. The Reynolds number and the Dean number are then calculated from the converged solution. At the boundary, the usual no-slip condition is assumed.

A stream function $\Psi = \Psi(x, y)$, which automatically satisfies the continuity equation, may be defined according to

$$\left.\begin{aligned} \frac{\partial \Psi}{\partial y} &= (1 - \kappa x)\, u + \tau y w, \\ -\frac{\partial \Psi}{\partial x} &= (1 - \kappa x)\, v - \tau x w. \end{aligned}\right\} \tag{6}$$

$\Psi(x, y)$ = constant defines a three-dimensional surface, and $\nabla\Psi$ is normal to this surface. For a given s, $\Psi(x, y)$ = constant defines a curve in the $\mathbf{n}$, $\mathbf{b}$-plane, and $\nabla\Psi$ is orthogonal to the tangent of this curve. One can show that

$$\nabla\Psi \cdot (u\mathbf{n} + v\mathbf{b}) = \tau w(xu + yv),$$

which means that, unless $\tau = 0$, so that the above expression is zero, the curves Ψ = constant do *not* define streamlines for the secondary flow ($u\mathbf{n} + v\mathbf{b}$). However, one finds that

$$\nabla\Psi \cdot \mathbf{v} = 0,$$

which proves that the velocity is tangent to the *surfaces* Ψ = constant. That is, these surfaces define streamtubes for the velocity field.

Numerical Procedure

The governing equations are discretized and solved according to the well-known finite-volume method, with a staggered grid, cf. Patankar (1980). To assure stability of the numerical procedure, the hybrid difference scheme is employed, which implies that central differences are used for the convection and diffusion terms when the absolute grid Peclet number is less than two, and for other Peclet numbers upwind differences are used for the convection terms, whereas the diffusion terms are ignored. All source terms are discretized using central differences. Since the upwind scheme is only first-order accurate, it is desirable to keep the grid Peclet number small enough, so that only central differences are used in the hybrid scheme. This is accomplished by a sufficient number of grid points. For the square cross-section, a grid of 41 × 41 was found to be acceptable. Upwind was used only for a limited number of grid points, for the highest flow rates considered. Also to remain as close as possible to second-order accuracy, a uniform grid is employed. The velocity-pressure coupling was in most cases handled by use of the SIMPLEC algorithm of Van Doormaal and Raithby (1984). Their recommended accelerated TDMA-solver was also found to be very effective. A θ-value of 1.9 was used for both the momentum and the pressure-correction equations. Under-relaxation factors of 0.6, 0.6 and 0.8 were used for the u, v, and w momentum equations, respectively. The pressure was under-relaxed by a factor of 0.9. The accelerated TDMA-solver was used together with an ADI-technique: one sweep in each direction for the momentum equations, and ten sweeps for the pressure-correction equation. Concerning the derivation of the pressure-correction equation, it was found that the "extra" pressure-derivative terms $\tau y \partial p/\partial x - \tau x \partial p/\partial y$ in the axial momentum equation (see Bolinder, 1993), could be neglected for ducts of moderate torsion. Only for the highest torsions considered, retaining the extra terms improved convergence.

To be able to determine the limit points accurately, it is necessary to have a sharp enough convergence criterion. For the present numerical method, the convergence is extremely slow close to the limit points. In fact, the limit point is characterized by an infinitely slow rate of convergence, and it separates an interval of convergence from an interval of nonconvergence. The nonconvergence intervals are not characterized by an unlimited growth of the residuals. Instead the residuals oscillate in a regular manner between a lower and an upper limit. The velocity and the pressure also oscillate regularly. Therefore, if the convergence criterion is not sharp enough, convergence will be detected in the nonconvergence intervals. The following convergence criterion was used: with u^n and v^n the secondary flow components at a grid point near the outer wall at iteration number n, it was required that

$$\frac{|u^n - u^{n-1}|}{\sqrt{(u^n)^2 + (v^n)^2}} < \delta \quad \text{and} \quad \frac{|v^n - v^{n-1}|}{\sqrt{(u^n)^2 + (v^n)^2}} < \delta$$

for up to 500 consecutive iterations. A typical value of δ was 10^{-5}. It was verified that close to convergence the velocity change from one iteration to the next was greatest in an area near to the outer wall. The procedure to detect a limit point was as follows: starting with a converged solution, the negative pressure gradient was raised or lowered (depending on the search direction) by a small amount Δg. In the case of con-

Table 1 Dean numbers at the limit points for a toroidal square duct with $\epsilon = 0.04$

	De_1	De_2	De_3	De_{12}	De_{23}	Winters (1987)
L_1	111.76	112.44	112.69	113.00	113.01	113.35
L_2	128.21	129.56	130.08	130.66	130.76	131.13
L_3	212.55	216.64	218.27	220.00	220.42	190.78
L_8	309.73	326.40	331.70	340.14	338.65	

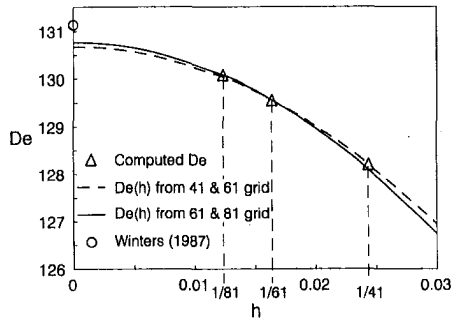

Fig. 2 Dean number at L_2 as a function of the grid spacing h for a toroidal square duct with $\epsilon = 0.04$

vergence, the search was continued with the same increment Δg. If convergence was not detected, Δg was halved and a new computation was initiated. When Δg was reduced below a given value, the process was stopped, and the latest obtained converged solution was defined as the limit point. The smallest relative increment $\Delta g/g$ used was about 0.1 percent for all cases.

Test of Accuracy by Use of h^2-Extrapolation

For a toroidal square duct of dimensionless curvature $\epsilon = \kappa d_h = 0.04$, Winters (1987) has determined the limit points of some solution branches. Winters used a "direct", as opposed to a transient, solution procedure, and he was thus able to detect unstable solution branches as well. The limit points were located by solving an extended system of equations, quite different from the present cruder method. For a toroidal square duct, three solution branches were detected in the present investigation, denoted by S_1, S_3, and S_5 following Winters. They are depicted in a state or bifurcation diagram, Fig. 3, showing a component of the secondary flow at one grid point as a function of the Dean number $De = Re\sqrt{\epsilon}$. The limit points determined were L_1—the lower limit of S_3, L_2—the upper limit of S_1, L_3 and L_8—the lower and upper limits of S_5, respectively. Winters did not consider high enough Dean numbers to be able to determine L_8. Since the present numerical method is practically second-order accurate, we may adopt h^2—or Richardson extrapolation to obtain fourth-order accuracy. For a sufficiently small grid spacing h, any computed flow property P may be expressed

$$P(h) = P_0 + ch^2 + O(h^4). \quad (7)$$

Thus, knowing $P(h_1)$ and $P(h_2)$ for two grid sizes h_1 and h_2, and neglecting the $O(h^4)$ terms, we may eliminate the leading error term ch^2, and determine P_0, which then is a correct approximation of P to the fourth order in the (coarsest) grid spacing. Three grids are used in this investigation, a 41 × 41, a 61 × 61, and an 81 × 81 grid. The properties computed on the respective grids are denoted by indices 1, 2, and 3, respectively. Extrapolated properties using the 41 × 41 and the 61 × 61 grid are denoted by the index 12, and extrapolated properties using the 61 × 61 and the 81 × 81 grid are denoted by the index 23. Table 1 shows the Dean number at the determined limit points, for the duct considered by Winters (1987). In Fig. 2 is plotted the function De(h) for the limit point L_2.

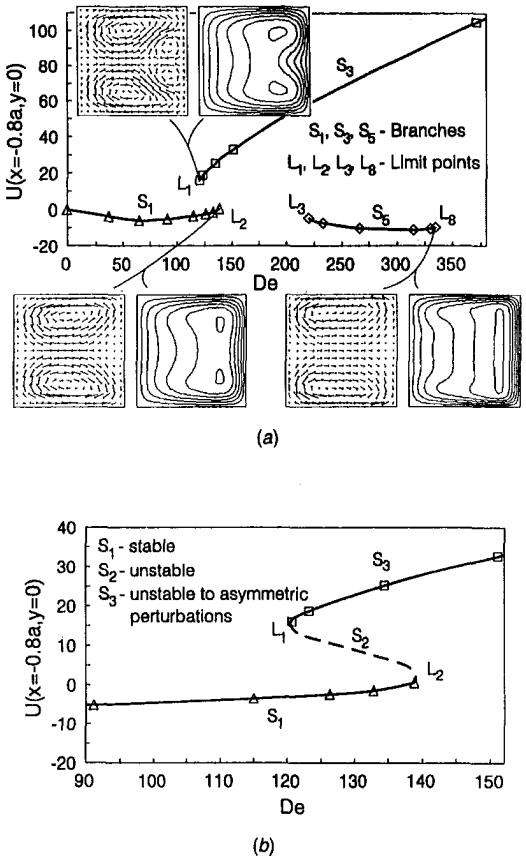

Fig. 3 State diagram for toroidal square duct with $\epsilon = 0.2$. (a) S_1, S_3 and S_5 branches. (b) Enlargement in region of limit points L_1 and L_2.

Table 2 Dean numbers at the limit points for a toroidal square duct with $\epsilon = 0.2$

	De_1	De_2	De_3	De_{12}	De_{23}
L_1	120.27	121.04	121.30	121.67	121.65
L_2	139.05	140.83	141.43	142.29	142.21
L_3	220.04	225.30	227.34	229.64	230.02
L_8	334.77	348.73	354.58	360.23	362.26

The fact that De_{12} and De_{23} differ at most by 0.4 percent (for L_8), indicates that the primary solutions obtained on the respective grids are of second-order accuracy, and that the expansion in Eq. (7) is valid for the limit points. The extrapolated values lie close to those obtained by Winters for the limit points L_1 and L_2. However, for L_3 there is a significant difference. The reason for this discrepancy is not clear, but it might be that different limit points have been considered.

Results and Discussion

Toroidal Square Duct. Figure 3 shows a state diagram for a toroidal square duct with $\epsilon = 0.2$. Vector plots of the secondary flow and contours of the axial flow are also shown at the limit points L_1, L_2, and L_8. In these plots the outer wall is to the right. Table 2 shows the Dean number at the limit points, together with the extrapolated values. In comparison with the duct of $\epsilon = 0.04$, we see that the Dean numbers at the limit points are slightly higher for the duct with $\epsilon = 0.2$. The S_1 branch is unconditionally stable, and it is characterized by the secondary flow having two symmetric counter-rotating vortices. Close to L_2, two extra very weak vortices start to develop near the outside wall. They can hardly be distinguished in the vector plot. The two extra counter-rotating vortices have reached a fully developed state on the S_3 branch,

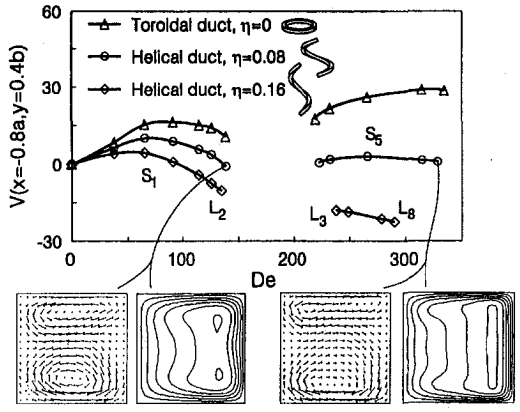

Fig. 4 State diagram for helical square ducts with $\epsilon = 0.2$, showing the S_1 and S_5 branches for three values of η

and where these occur the axial velocity shows a "dip." Converged solutions of the S_3 branch were obtained up to a Dean number of about 550. For this high flow rate, the hybrid scheme to a large extent chooses the upwind scheme, so no attempt was made to determine the possible upper limit of the S_3 branch. In fact, no author has reported an upper limit of S_3. According to Winters (1987) solutions of the S_3 branch are unstable to asymmetric perturbations. This is confirmed in the present study, since the four-vortex solutions could only be obtained if symmetry was imposed in the computations. As indicated in Fig. 3(*b*), the S_1 and the S_3 branches are connected by the genuinely unstable S_2 branch, which could not be detected in the present study. If one retains the unsteady terms in the governing equations and performs truly transient computations without assuming symmetry, one finds for Dean numbers between L_2 and L_3, and above L_8, that the flow oscillates between a two-vortex and a four-vortex structure. A similar behavior is reported by Sankar et al. (1988) and Bara et al. (1992) in their computations of developing flow in a toroidal square duct; for Dean numbers between L_2 and L_3, spatial oscillations develop, alternating between a two-vortex and a four-vortex structure. Obviously there is an analogy between their parabolic solution method, where the solution is advanced in space along the duct, and our transient method, where the solution is advanced in time. The S_5 branch is unconditionally stable, and has a two-vortex structure like the S_1 branch. As mentioned above, Winters (1987) did not determine the upper limit of S_5. Daskopoulos and Lenhoff (1989) however report an upper limit of their corresponding branch, labelled "*e*." Daskopoulos and Lenhoff assume a dimensionless curvature ϵ much less than one. They also assume symmetric solutions, which implies that the S_3 branch (their *c* branch), is found to be stable. It was decided, after an examination of the bifurcation diagram of Daskopoulos and Lenhoff, to denote the upper limit point of the S_5 branch by L_8.

Helical Square Duct. For a curved square duct with a finite pitch no symmetric solutions can be expected. Thus, with no possibility to impose symmetry, we are not likely to find stable solutions of the S_3 branch. Solutions of the S_1 and S_5 branches might however be possible to detect. We use the same labels for the branches and for the limit points in the finite pitch case as in the toroidal case. Figure 4 is a state diagram for ducts of moderate pitches. Note the different velocity components on the vertical axis in Figs. 3 and 4. Up to a dimensionless torsion η of 0.16, solutions of both the S_1 and S_5 branches were obtained, and for higher torsion, only solutions of the S_1 branch. Figure 5 shows the extent of the S_1 and S_5 branches for increasing torsion. For ducts of small torsion, $\eta \leq 0.08$, the extent is essentially unaltered, and for higher torsion the extent decreases. For very high torsion, $\eta > 0.7$, the S_1 branch extends to higher Dean numbers again. Grid refinements and h^2-extrapolation were done for three helical ducts with $\eta = 0.08$, 0.6 and 1. The results are shown in Tables 3 and 4. Note the relatively small differences between the helical duct with $\eta = 0.08$ and the toroidal duct with $\eta = 0$ (Table 2). Note also that the h^2-extrapolation failed for $\eta = 1$. For this case, the finer grids predicted a lower Dean number at L_2, and it seems to be a linear relationship between De and the grid spacing h. The author has no good explanation for this behaviour. A characteristic feature of increasing torsion, is that the lower vortex of the secondary flow grows at the expense of the upper vortex. This is seen in the vector plots in Figs. 4 and 5. The same behavior is reported by Kao (1987) for a helical circular pipe. For the highest torsion, no sign of the upper vortex can be seen; the lower vortex has moved upwards, and covers the whole cross-section. The disappearance of the upper vortex might have a stabilizing effect on the flow, and thus explain why L_2 moves to a higher Dean number. The effect of torsion on the axial flow is minor for ducts of low and moderate pitches, see Fig. 4. The maximum axial flow shifts slightly to the upper half of the cross-section. If the torsion is increased further, the location of the maximum axial flow moves from the upper outside corner to the upper inside corner, and then downwards along the inside, see Fig. 5.

Table 3 Dean numbers at the limit points for a helical square duct with $\epsilon = 0.2$ and $\eta = 0.08$

	De_1	De_2	De_3	De_{12}	De_{23}
L_2	138.99	140.87	141.57	142.42	142.50
L_3	223.04	226.71	228.11	229.73	229.95
L_8	327.19	340.06	344.99	350.67	351.44

Table 4 Dean numbers at L_2 for helical square ducts with $\epsilon = 0.2$

	De_1	De_2	De_3	De_{12}	De_{23}
$\eta = 0.6$	90.97	91.40	91.59	91.75	91.84
$\eta = 1.0$	139.72	137.37	135.04	—	—

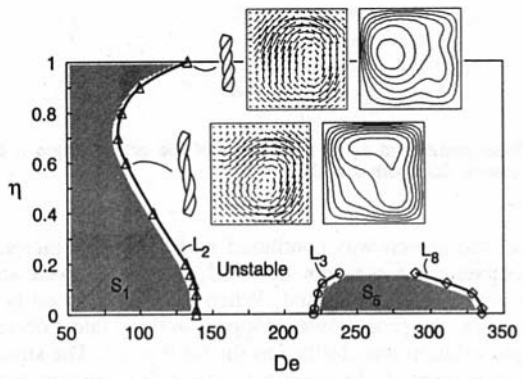

Fig. 5 Dean numbers at L_2, L_3, and L_8 for helical square ducts with $\epsilon = 0.2$ and varying η

Friction Factor Results. Figure 6 shows the friction factor ratio $f\mathrm{Re}/(f\mathrm{Re})_s$ for a toroidal square duct. By definition, the Fanning friction factor $f = gd_h/(2\rho\bar{w}^2)$. The index s refers to a straight square duct, for which $(f\mathrm{Re})_s = 14.22$. Note that the four-vortex solutions of the S_3 branch have a slightly higher friction factor than the two-vortex solutions of the S_1 and S_5 branches. In Fig. 6 is also plotted a few correlations found in

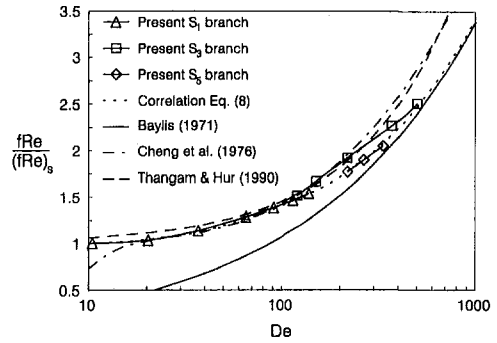

Fig. 6 Friction factor ratio as a function of Dean number for a toroidal square duct

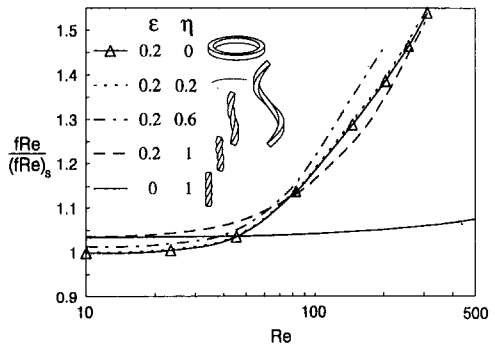

Fig. 7 Friction factor ratio as a function of Reynolds number for the S_1 branch of some ducts

the literature. The agreement is generally good, despite that different curvatures are considered, i.e., the curvature effect seems to be well captured by the Dean number alone. To obtain a quantitative check of the effect of curvature, the friction factor ratio was computed for two additional ducts with $\epsilon = 0.04$ and $\epsilon = 0.47$, respectively. Compared to the duct with $\epsilon = 0.2$, $f\mathrm{Re}/(f\mathrm{Re})_s$ was about 3 percent lower for $\epsilon = 0.04$ and about 4 percent higher for $\epsilon = 0.47$, for Dean numbers between 100 and 300. For lower Dean numbers the difference approaches zero. Thus, the curvature effect starts to become significant for $\epsilon > 0.2$. For smaller curvature, the explicit effect of ϵ is virtually negligible. These results are expected, since for loosely coiled ducts (with $\epsilon \ll 1$) the Dean number is the single controlling similarity parameter, see e.g. Berger et al. (1983).

The correlations by Baylis (1971) and by Cheng et al. (1976) indicate that $f\mathrm{Re}/(f\mathrm{Re})_s$ is proportional to the square root of the Dean number. This was also found by Mori et al. (1971) in their boundary layer analysis of flow in a curved square duct. The boundary layer method is assumed to be valid for Dean numbers in the upper laminar regime. A square root relationship has also been confirmed for a curved duct of circular cross-section, see Liu et al. (1994). Assuming that Baylis' (1971) correlation is valid for $\mathrm{De} > 500$, the following new correlation is proposed

$$\frac{f\mathrm{Re}}{(f\mathrm{Re})_s} = (1 + 0.288\mathrm{De} + 8.8 \cdot 10^{-8}\,\mathrm{De}^4)^{-0.3} + 0.107\sqrt{\mathrm{De}}, \quad \mathrm{De} < 1500, \quad \epsilon < 0.4, \quad \frac{\eta}{\epsilon} \le 1. \quad (8)$$

Equation (8) gives correct values in both the limits of high and low Dean numbers, and for $\epsilon = 0.2$ it deviates by less than 2 percent from the computed values of the two-vortex branches, see Fig. 6. For $0.05 < \mathrm{De} < 2.4$ however, the formula overpredicts the friction factor ratio by up to 3.6 percent, and for $\mathrm{De} < 6$ it is recommended to use $f\mathrm{Re}/(f\mathrm{Re})_s = 1$. Equation (8) presumes a laminar flow, and the upper Dean number limit is set to 1500. Baylis (1971) gives an upper limit of 70,000 in his correlation, which is based on experiments where mercury was driven electromagnetically in a toroidal square duct. As remarked by Baylis, the electromagnetic force is assumed to have a stabilizing effect on the flow, and for more "normal" conditions, the flow will be turbulent at a much lower Dean number than 70,000. For example, Mori et al. (1971) in their experiments detected transition at $\mathrm{De} = 850$, and for $\mathrm{De} > 2500$ the flow was fully turbulent. The values of $f\mathrm{Re}/(f\mathrm{Re})_s$ for turbulent flow measured by Mori et al. were higher than the predicted values from their boundary layer analysis.

For helical ducts of small and moderate torsion, the friction factor of both the S_1 and S_5 branches is almost identical to the friction factor for a toroidal duct with the same dimensionless curvature ϵ. For the S_1 branch this is seen in Fig. 7, where the friction factor ratio is plotted for a few helical ducts. At least for $\eta/\epsilon \le 1$, Eq. (8) could be used for the friction factor ratio with a negligible error. Even for ducts of higher torsion, the friction factor is hardly affected by the torsion. In Fig. 7 is also plotted the friction factor ratio for a straight twisted square duct with $\epsilon = 0$ and $\eta = 1$. For small Reynolds numbers, the friction factor is similar to the friction factor for the helical duct with $\eta = 1$. But for an increasing Re, the finite curvature of the helical duct rapidly increases the flow resistance.

Conclusions

Fully developed flow solutions have been obtained for helical square ducts of varying pitch or torsion. The finite-volume method together with the SIMPLEC algorithm has been found effective in this highly non-linear problem. As in the case of a toroidal duct, stable solutions are only obtained for limited Dean number intervals. By using h^2-extrapolation the end points or limit points of these intervals were located accurately. It was found that for helical ducts of small torsion, the stability structure is scarcely affected by the torsion. The effect of a finite pitch is to distort the symmetry of the flow; the "lower vortex" of the secondary flow is enlarged at the expense of the upper vortex, and the maximum of the axial flow is shifted to the upper half of the cross-section. However, for ducts of small pitch the effect is minor. It was also found that the friction factor for a helical duct is almost identical to the friction factor for a toroidal duct with the same dimensionless curvature ϵ.

To be able to find unstable solutions, and thus to be able to determine a more complete bifurcation structure, a "direct" numerical method is necessary, as used for example by Winters (1987) and Daskopoulos and Lenhoff (1989) for a toroidal duct. Another issue that needs consideration in the future, concerns the validity of the assumption of a steady and fully developed flow. Clearly, if no symmetry assumption is made, there are no stable solutions for certain Dean number intervals in the laminar regime. At these intervals the flow seems to oscillate between a two-vortex and a four-vortex structure. If unsteady computations are performed with the assumption of a fully developed flow, the oscillations are found to be temporal. If instead steady and parabolic computations are performed on a developing flow, the oscillations are found to be spatial (Sankar et al., 1988 and Bara et al., 1992). To reveal a more exact nature of the oscillations, it might be necessary to perform unsteady and fully elliptic computations of developing flow. However, the choice of inlet and outlet conditions and the way disturbances or perturbations are introduced, will probably have a significant impact on the solution. It is likely that the real three-dimensional flow problem in a curved rectangular duct possesses some sort of convective instability, which means that imposed perturbations will be convected downstream, while they grow or develop in some way, cf. Bottaro (1993).

References

Bara, B., Nandakumar, K., and Masliyah, J. H., 1992, "An Experimental and Numerical Study of the Dean Problem: Flow Development Towards Two-Dimensional Multiple Solutions," *Journal of Fluid Mechanics*, Vol. 244, pp. 339–376.

Baylis, J. A., 1971, "Experiments on Laminar Flow in Curved Channels of Square Section", *Journal of Fluid Mechanics*, Vol. 48, pp. 417–422.

Berger, S. A., 1991, "Flow and Heat Transfer in Curved Pipes and Tubes" Paper no. AIAA 91-0030 of the 29th Aerospace Sciences Meeting, Reno, Nevada.

Berger, S. A., Talbot, L., and Yao, L.-S., 1983, "Flow in Curved Pipes," *Annual Review of Fluid Mechanics*, Vol. 15, pp. 461–512.

Bolinder, C. J., 1993, "Numerical Visualization of the Flow in a Helical Duct of Rectangular Cross-Section" ASME FED-Vol. 172, presented at the *Third Symposium on Experimental and Numerical Flow Visualization*, New Orleans, pp. 329–338.

Bottaro, A., 1993, "On Longitudinal Vortices in Curved Channel Flow," *Journal of Fluid Mechanics*, Vol. 251, pp. 627–660.

Chen, W.-H., and Jan, R., 1992, "The Characteristics of Laminar Flow in a Helical Circular Pipe," *Journal of Fluid Mechanics*, Vol. 244, pp. 241–256.

Chen, W.-H., and Jan, R., 1993, "The Torsion Effect on Fully Developed Laminar Flow in Helical Square Ducts", ASME JOURNAL OF FLUIDS ENGINEERING, Vol. 115, pp. 292–301.

Cheng, K. C., Lin, R.-C., and Ou, J.-W., 1976, "Fully Developed Laminar Flow in Curved Rectangular Channels," ASME JOURNAL OF FLUIDS ENGINEERING, Vol. 98, pp. 41–48.

Daskopoulos, P., and Lenhoff, A. M., 1989, "Flow in Curved Ducts: Bifurcation Structure for Stationary Ducts," *Journal of Fluid Mechanics*, Vol. 203, pp. 125–148.

Germano, M., 1982, "On the Effect of Torsion on a Helical Pipe Flow," *Journal of Fluid Mechanics*, Vol. 125, pp. 1–8.

Germano, M., 1989, "The Dean Equations Extended to a Helical Pipe Flow," *Journal of Fluid Mechanics*, Vol. 203, pp. 289–305.

Ito, H., 1987, "Flow in Curved Pipes," *JSME International Journal*, Vol. 30, pp. 543–552.

Joseph, B., Smith E. P., and Adler, R. J., 1975, "Numerical Treatment of Laminar Flow in Helically Coiled Tubes of Square Cross Section," *AIChE Journal*, Vol. 21, pp. 965–974.

Kao, H. C., 1987, "Torsion Effect on Fully Developed Flow in a Helical Pipe," *Journal of Fluid Mechanics*, Vol. 184, pp. 335–356.

Kao, H. C., 1992, "Some Aspects of Bifurcation Structure of Laminar Flow in Curved Ducts," *Journal of Fluid Mechanics*, Vol. 243, pp. 519–539.

Kheshgi, H. S., 1993, "Laminar Flow in Twisted Ducts," *Physics of Fluids A*, Vol. 5, No. 11, pp. 2669–2681.

Liu, S., and Masliyah, J. H., 1993, "Axially Invariant Laminar Flow in Helical Pipes with a Finite Pitch," *Journal of Fluid Mechanics*, Vol. 251, pp. 315–353.

Liu, S., Afacan, A., Nasr-El-Din, H. A., and Masliyah, J. H., 1994, "An Experimental Study of Pressure Drop in Helical Pipes," *Proceedings of the Royal Society of London*, Series A, Vol. 444, pp. 307–316.

Masliyah, J. H., and Nandakumar, K., 1981, "Steady Laminar Flow Through Twisted Pipes," ASME *Journal of Heat Transfer*, Vol. 103, pp. 785–796.

Mori, Y., Uchida, Y., and Ukon, T., 1971, "Forced Convective Heat Transfer in a Curved Channel with a Square Cross Section," *International Journal of Heat and Mass Transfer*, Vol. 14, pp. 1787–1805.

Murata, S., Miyake, Y., Inaba, T., and Ogata, H., 1981, "Laminar Flow in a Helically Coiled Pipe," *Bulletin of the JSME*, Vol. 24, pp. 355–362.

Nandakumar, K. and Masliyah, J. H., 1983, "Steady Laminar Flow Through Twisted Pipes: Fluid Flow and Heat Transfer in Rectangular Tubes," *Chemical Engineering Communications*, Vol. 21, pp. 151–173.

Nandakumar, K. and Masliyah, J. H., 1986, "Swirling Flow and Heat Transfer in Coiled and Twisted Pipes," *Advances in Transport Processes*, Vol. IV, Mujumdar, A. S. and Mashelkar, R. A., eds., Wiley, pp. 49–112.

Patankar, S. V., 1980, *Numerical Heat Transfer and Fluid Flow*, McGraw-Hill, NY.

Sankar, S. R., Nandakumar, K., and Masliyah, J. H., 1988, "Oscillatory Flows in Coiled Square Ducts," *Physics of Fluids*, Vol. 31, pp. 1348–1359.

Sokolnikoff, I. S., 1964, *Tensor Analysis*, Wiley.

Thangam, S., and Hur, N., 1990, "Laminar Secondary Flows in Curved Rectangular Ducts," *Journal of Fluid Mechanics*, Vol. 217, pp. 421–440.

Tuttle, E. R., 1990, "Laminar Flow in Twisted Pipes," *Journal of Fluid Mechanics*, Vol. 219, pp. 545–570.

Van Doormaal, J. P., and Raithby, G. D., 1984, "Enhancements of the SIMPLE Method for Predicting Incompressible Fluid Flows," *Numerical Heat Transfer*, Vol. 7, pp. 147–163.

Wang, C. Y., 1981, "On the low-Reynolds-Number Flow in a Helical Pipe," *Journal of Fluid Mechanics*, Vol. 108, pp. 185–194.

Winters, K. H., 1987, "A Bifurcation Study of Laminar Flow in a Curved Tube of Rectangular Cross-Section," *Journal of Fluid Mechanics*, Vol. 180, pp. 343–369.

Xie, D. G., 1990, "Torsion Effect on Secondary Flow in a Helical Pipe," *International Journal of Heat and Fluid Flow*, Vol. 11, pp. 114–119.

Yang, G., and Ebadian, M. A., 1993, "The Effect of Torsion on Flow in the Curved Annular Sector Duct," ASME FED-Vol. 170, *Contributed Papers in Fluids Engineering*, pp. 11–18.

A Calculation Method for Developing Turbulent Flow in Rectangular Ducts of Arbitrary Aspect Ratio

M. Naimi
Senior Specialist Engineer,
Boeing Commercial Airplane Group,
The Boeing Company,
Seattle, WA 98124

F. B. Gessner
Professor,
Department of Mechanical Engineering,
University of Washington,
Seattle, WA 98195

This paper describes a full Reynolds stress transport equation model for predicting developing turbulent flow in rectangular ducts. The pressure-strain component of the model is based on a modified form of the Launder, Reece and Rodi pressure-strain model and the use of a linear wall damping function. Predictions based on this model are compared with predictions referred to high Reynolds number and low Reynolds number $k - \epsilon$ transport equation models and with experimental data taken in square and rectangular ducts. The results indicate that the proposed model yields improved predictions of primary flow development and Reynolds stress behavior in a square duct. The proposed model also yields Reynolds stress anisotropy and secondary flow levels that are compatible and agree well with experiment, without recourse to a quadratic damping function to model near-wall pressure-strain behavior.

Introduction

Turbulent flow in straight ducts of rectangular cross section is characterized by the presence of secondary flows superimposed upon the primary flow. In order to predict secondary flow, Reynolds normal and shear stress components acting in the cross plane must be modeled accurately. Within the framework of two-equation type turbulence models (e.g., $k - \epsilon$ transport equation models), Reynolds stress components must be modeled by means of an anisotropic (as opposed to Boussinesq type) eddy viscosity model. Models in this category include the high Reynolds number, $k - \epsilon$ models proposed by Naot and Rodi (1981), Nakayama et al. (1983), Demuren and Rodi (1984), and Speziale et al. (1993), and the low Reynolds number versions utilized by Nisizima (1990), Myong (1991), and Myong and Kobayashi (1991). In the high Reynolds number models, wall functions are used to model the behavior of U, k, and ϵ in the cross plane along the first mesh line adjacent to the wall, either via relationships that have been developed for two-dimensional boundary layer flows or via relationships which purportedly account for corner effects in their formulation. Gessner et al. (1991) have shown, however, that previously proposed wall functions for k and ϵ are not wholly adequate for predicting streamwise corner flows, and that alternate wall functions should be specified in order to model observed near-wall flow behavior more accurately.

In the high Reynolds number forms of the $k - \epsilon$ model that have been applied to rectangular duct flows to date and, indeed, in a recent paper in which full Reynolds stress transport equation closure was employed (Demuren, 1990), the coefficient c_μ which appears in the Prandtl-Kolmogoroff expression for the eddy viscosity, namely $\nu_t = c_\mu k^2/\epsilon$, is specified as 0.09 (a constant). In the low Reynolds number versions of the $k - \epsilon$ model, c_μ is replaced by $c_\mu f_\mu$, where f_μ is a damping coefficient that is typically specified as a function of y^+ and Re_t (cf. Myong and Kasagi, 1990 and Speziale et al., 1992). In a recent paper Gessner et al. (1993) have shown that specifying c_μ as 0.09 is not compatible with experimentally observed damping coefficient behavior in the near-wall region of fully developed square duct flow. Their results also indicate that f_μ varies in a complex manner as a corner is approached, so that sensitivity of f_μ to both y^+ and z^+ is required in any analytical formulation for f_μ. The problem can be circumvented by effecting closure to the system of equations via a Reynolds stress model that does not require *apriori* specification of c_μ (or $c_\mu f_\mu$) in its application. One example of this approach is the full Reynolds stress transport equation model recently proposed by Launder and Li (1993). Their predictions of fully developed square duct flow, although limited in scope, agree reasonably well with experimental data. Another example is the nonlinear Reynolds stress model based on Renormalization Group (RNG) theory proposed by Barton et al. (1991) which does not require empirical adjustment of constants or special treatment for the near-wall region.

Alternate models which require empiricism in the near-wall region include the large eddy simulation (LES) models for square duct flow proposed by Madabhushi and Vanka (1991), Balaras and Benocci (1992), Kajishima and Miyake (1992), and Su and Friedrich (1994). Predictions based on this approach generally agree well with experimental data, although the computational time required for a converged solution can be relatively long, even for simulation of fully developed square duct flow. The computational cost is even higher, of course, for DNS-type calculations, which have now been performed for low Reynolds number, fully developed square duct flow (cf. results presented by Gavrilakis, 1992; Madabhushi and Vanka, 1993; and Huser and Biringen, 1993). In the study by Madabhushi and Vanka, for example, 180 CPU hours on a CRAY-2 computer were required for a converged solution at a bulk Reynolds number of 3850.

The above-referenced RNG, LES, and DNS studies indicate that recent advances have been made in developing techniques for predicting streamwise corner flows with a minimum amount of empirical input. From the standpoint of available computer capability, these advanced techniques are presently limited to computing relatively low Reynolds number, rectangular duct flows under fully developed flow conditions. The need still exists, therefore, for a computationally efficient method that can be used to predict developing rectangular duct flows at high Reynolds number with good accuracy. The $k - \epsilon$ transport

Contributed by the Fluids Engineering Division for publication in the JOURNAL OF FLUIDS ENGINEERING. Manuscript received by the Fluids Engineering Division December 26, 1993; revised manuscript received January 13, 1995. Associate Technical Editor: G. Karniadakis.

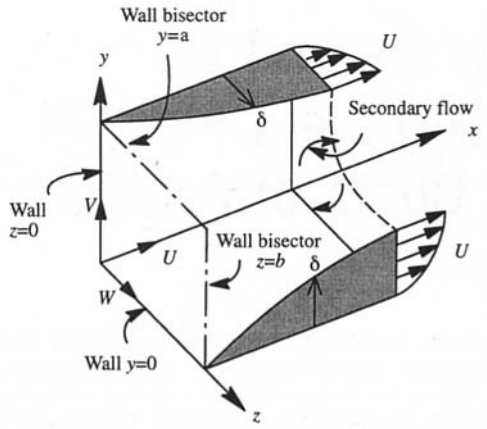

Fig. 1 Velocity components and coordinate system for rectangular duct flow

equation models fulfill this objective to some extent, but not completely, because the numerical value for c_μ, the analytical forms for f_μ, and the wall functions prescribed in previous studies do not model experimentally observed behavior in the near-wall region. In the present paper, a full Reynolds stress transport equation model is proposed which obviates the need for specifying the behavior of c_μ and f_μ as empirical input. The only wall function that is utilized is the law-of-the-wall on the first computational meshline, which, on the basis of experimental results presented by Gessner et al. (1991, 1993), is a valid assumption. In the discussion that follows, the constitutive components of the overall model are briefly summarized. For a detailed discussion of the physical arguments leading to its development, the reader is referred to the thesis by Naimi (1993).

Mathematical Formulation

Equations of Motion. In reference to Fig. 1, let U, V, W and u, v, w denote the mean and fluctuating velocity components, respectively, referred to the xyz coordinate system shown in this figure. After the boundary layer approximations are applied to the equations of motion, the Reynolds-averaged forms of these equations for steady, incompressible flow with constant properties can be written as:

Continuity Equation:

$$\frac{\partial U}{\partial x} + \frac{\partial V}{\partial y} + \frac{\partial W}{\partial z} = 0 \tag{1}$$

Reynolds Equations:

$$U\frac{\partial U}{\partial x} + V\frac{\partial U}{\partial y} + W\frac{\partial U}{\partial z} = -\frac{1}{\varrho}\frac{d\bar{P}}{dx} + \nu\left(\frac{\partial^2 U}{\partial y^2} + \frac{\partial^2 U}{\partial z^2}\right) - \frac{\partial \overline{uv}}{\partial y} - \frac{\partial \overline{uw}}{\partial z} \tag{2}$$

$$U\frac{\partial V}{\partial x} + V\frac{\partial V}{\partial y} + W\frac{\partial V}{\partial z} = -\frac{1}{\varrho}\frac{\partial p}{\partial y} + \nu\left(\frac{\partial^2 V}{\partial y^2} + \frac{\partial^2 V}{\partial z^2}\right) - \frac{\partial \overline{v^2}}{\partial y} - \frac{\partial \overline{vw}}{\partial z} \tag{3}$$

$$U\frac{\partial W}{\partial x} + V\frac{\partial W}{\partial y} + W\frac{\partial W}{\partial z} = -\frac{1}{\varrho}\frac{\partial p}{\partial z} + \nu\left(\frac{\partial^2 W}{\partial y^2} + \frac{\partial^2 W}{\partial z^2}\right) - \frac{\partial \overline{vw}}{\partial y} - \frac{\partial \overline{w^2}}{\partial z} \tag{4}$$

where, following Patankar and Spalding (1972), the mean static pressure has been modeled as $P = \bar{P}(x) + p(y, z)$, with $\bar{P}(x)$ defined as the cross-sectional averaged pressure and $p(y, z)$ as the perturbation pressure about $\bar{P}(x)$ caused by transverse momentum exchange.

Reynolds Stress Transport Equation Model. In general, the Reynolds stress transport equations for steady, incompressible flow can be written as:

$$U_k\frac{\partial \overline{u_i u_j}}{\partial x_k} = P_{ij} + \Phi_{ij} + D_{ij} - \epsilon_{ij} \tag{5}$$

where P_{ij} is the mean-strain generation, Φ_{ij} is the pressure-strain

Nomenclature

a = duct half width
a' = diagonal duct half width
b = duct half height
c_1, c_2, γ = primary pressure-strain coefficients
c_1', c_2', γ' = wall correction pressure-strain coefficients
$c_{\epsilon 1}$, $c_{\epsilon 2}$ = coefficients, Eq. (29)
c_μ^* = coefficient, Eq. (12)
D_h = hydraulic diameter
f_l = linear wall damping function
f_μ = eddy viscosity damping function
k = turbulence kinetic energy, $k = \frac{1}{2}(\overline{u^2} + \overline{v^2} + \overline{w^2})$
l_p = Prandtl's mixing length, Eq. (27)
p = cross-sectional perturbation pressure
$\bar{P}$ = cross-sectional average pressure
$\mathcal{P}$ = turbulence kinetic energy production rate, Eq. (10)
Re_b = bulk Reynolds number, $\mathrm{Re}_b = U_b D_h/\nu$
Re_t = turbulent Reynolds number, $\mathrm{Re}_t = k^2/(\nu\epsilon)$
$\langle s \rangle$ = linear average wall distance, Eq. (28)
u, v, w = fluctuating velocity components in x, y, z directions, respectively
U, V, W = mean velocity components in x, y, z directions, respectively
U_b = bulk (cross-sectional averaged) velocity
U_c = centerline velocity
U_τ = local friction velocity, $U_\tau = \sqrt{\tau_w/\varrho}$
V' = resultant secondary flow velocity, $V' = \sqrt{V^2 + W^2}$
x, y, z = cartesian coordinates, Fig. (1)
y' = diagonal coordinate
y^+ = dimensionless coordinate, $y^+ = yU_\tau/\nu$
z^+ = dimensionless coordinate, $z^+ = zU_\tau/\nu$
α_{CD} = coefficient, Eq. (9)
δ = boundary layer thickness
ϵ = isotropic dissipation rate of k
$\varkappa$ = von Karman's constant
ν = kinematic viscosity
ν_t = eddy viscosity
ξ_p = ratio of turbulence kinetic energy production to its dissipation rate, Eq. (13)
ϱ = fluid density
σ_k, σ_ϵ = diffusion coefficients
τ_w = local wall shear stress
ψ = dimensionless stream function defined by Hoagland (1960)

Special Notation

$\overline{(\ )}$ = Reynolds averaged quantity

effect, D_{ij} is diffusive transport, and ϵ_{ij} is the viscous dissipation. If $CD(\overline{u_iu_j})$ is defined as the convection minus diffusion effect, and $ASM(\overline{u_iu_j})$ is defined as the combined effect of mean-strain generation, the pressure-strain effect, and viscous dissipation, then, on the basis of Eq. (5),

$$CD(\overline{u_iu_j}) = ASM(\overline{u_iu_j}) \tag{6}$$

where

$$CD(\overline{u_iu_j}) = U_k \frac{\partial \overline{u_iu_j}}{\partial x_k} - D_{ij} \tag{7}$$

and

$$ASM(\overline{u_iu_j}) = P_{ij} + \Phi_{ij} - \epsilon_{ij} \tag{8}$$

In the present work, $CD(\overline{u_iu_j})$ was modeled by means of a composite model proposed by Eppich (1987), namely:

$$CD(\overline{u_iu_j}) = \alpha_{CD}\left\{ U_k \frac{\partial \overline{u_iu_j}}{\partial x_k} - \frac{\partial}{\partial x_k}\left[\left(\nu + \frac{\nu_t}{\sigma_k}\right)\frac{\partial \overline{u_iu_j}}{\partial x_k}\right]\right\} + (1 - \alpha_{CD})\tfrac{2}{3}\delta_{ij}(\mathcal{P} - \epsilon) \tag{9}$$

where all terms are retained in the expanded form of Eq. (9) and the turbulent kinetic energy production rate, $\mathcal{P}$, is equivalent to

$$\mathcal{P} = -\overline{u^2}\frac{\partial U}{\partial x} - \overline{v^2}\frac{\partial V}{\partial y} - \overline{w^2}\frac{\partial W}{\partial z} - \overline{uv}\frac{\partial U}{\partial y} - \overline{uw}\frac{\partial U}{\partial z} - \overline{vw}\left(\frac{\partial V}{\partial z} + \frac{\partial W}{\partial y}\right) \tag{10}$$

In Eq. (9) the turbulent eddy viscosity, ν_t, is related to the turbulence kinetic energy, k, and the isotropic dissipation rate, ϵ, by

$$\nu_t = c_\mu^* \frac{k^2}{\epsilon} \tag{11}$$

with

$$c_\mu^* = [\tfrac{2}{3}(c_1^* - 1)\Omega^* - \gamma^* c_1^* - (2\beta^*\Omega^* + 4\Lambda^*\Pi^*)\xi_p]/(c_1^*)^2 \tag{12}$$

and

$$\xi_p = -\frac{k}{\epsilon}\left(\frac{\overline{uv}}{k}\frac{\partial U}{\partial y} + \frac{\overline{uw}}{k}\frac{\partial U}{\partial z}\right) \tag{13}$$

where α_{CD}, σ_k, c_1^*, γ^*, β^*, Λ^*, Ω^*, and Π^* are coefficients to be defined shortly. The analytical form for c_μ^* given by Eq. (12) is a derived result obtained by formal manipulation of Eq. (8) with $ASM(\overline{u_iu_j})$ set equal to zero and with the secondary flow terms neglected in the expanded form of Φ_{ij}.

Equation (9) simplifies to an expression based on actual convection rates and a gradient diffusion model for D_{ij} when $\alpha_{CD} = 1$, and to an expression corresponding to the convection minus diffusion model proposed by Mellor and Yamada (1974) when $\alpha_{CD} = 0$. The need for this type of composite model is discussed briefly by Eppich (1987), who notes that $k - \epsilon$ transport equation predictions based on the former model ($\alpha_{CD} = 1$) yield a value for u^2/k on the centerline of plane channel flow which is too high (1.2) compared to the experimentally observed value (1.0) for high Reynolds number operating conditions, and that the latter model ($\alpha_{CD} = 0$) yields a value for u^2/k which is too low (0.67). According to Eppich, when α_{CD} is set equal to 0.75, the correct numerical value for u^2/k is predicted (1.0). This observation, in conjunction with behavior observed in the present study, namely that numerical instabilities can occur when α_{CD} is specified as unity for predicting developing flow in a square duct with non-uniform wall roughness, led to α_{CD} being specified as 0.75. This course of action is admittedly pragmatic, inasmuch as the convective term in Eq. (9) now becomes a modeled effect.

In order to develop working expressions for $ASM(\overline{u_iu_j})$, Φ_{ij} in Eq. (8) was modeled by means of a modified form of the Launder, Reece, and Rodi (1975) pressure-strain model, as proposed by Eppich (1987). Terms involving streamwise gradients of the V and W velocity components and streamwise diffusion of the Reynolds stresses were neglected in the development. Consistent with the approach taken in modeling $CD(\overline{u_iu_j})$, the dissipation rate tensor was modeled in terms of the isotropic dissipation rate ϵ. The final working forms of $ASM(\overline{u_iu_j})$ for the individual Reynolds stress components can be written as:

$$ASM(\overline{u^2}) = -c_1^*\frac{\epsilon}{k}\overline{u^2} + \frac{2}{3}\epsilon(c_1^* - 1) + 2\overline{uv}\frac{\partial U}{\partial y}(\beta^* - \Pi^*) + 2\overline{uw}\frac{\partial U}{\partial z}(\beta^* - \Pi^*) + S_{11} \tag{14}$$

$$ASM(\overline{v^2}) = -c_1^*\frac{\epsilon}{k}\overline{v^2} + \frac{2}{3}\epsilon(c_1^* - 1) + 2\overline{uv}\frac{\partial U}{\partial y}(\beta^* + \Lambda^*) + 2\beta^*\overline{uw}\frac{\partial U}{\partial z} + S_{22} \tag{15}$$

$$ASM(\overline{w^2}) = -c_1^*\frac{\epsilon}{k}\overline{w^2} + \frac{2}{3}\epsilon(c_1^* - 1) + 2\overline{uw}\frac{\partial U}{\partial z}(\beta^* + \Lambda^*) + 2\beta^*\overline{uv}\frac{\partial U}{\partial y} + S_{33} \tag{16}$$

$$ASM(\overline{uv}) = -c_1^*\frac{\epsilon}{k}\overline{uv} + (\Lambda^*\overline{u^2} - \Pi^*\overline{v^2} + \gamma^* k)\frac{\partial U}{\partial y} - \Pi^*\overline{vw}\frac{\partial U}{\partial z} + S_{12} \tag{17}$$

$$ASM(\overline{uw}) = -c_1^*\frac{\epsilon}{k}\overline{uw} + (\Lambda^*\overline{u^2} - \Pi^*\overline{w^2} + \gamma^* k)\frac{\partial U}{\partial z} - \Pi^*\overline{vw}\frac{\partial U}{\partial y} + S_{13} \tag{18}$$

$$ASM(\overline{vw}) = -c_1^*\frac{\epsilon}{k}\overline{vw} + \Lambda^*\overline{uv}\frac{\partial U}{\partial z} + \Lambda^*\overline{uw}\frac{\partial U}{\partial y} + S_{23} \tag{19}$$

where S_{ij} are defined by:

$$S_{11} = 2\beta^*\left[\overline{v^2}\frac{\partial V}{\partial y} + \overline{vw}\frac{\partial V}{\partial z} + \overline{vw}\frac{\partial W}{\partial y} + \overline{w^2}\frac{\partial W}{\partial z}\right] + 2\gamma^* k\frac{\partial U}{\partial x} + 2\overline{u^2}\frac{\partial U}{\partial x}(\beta^* - \Omega^*) \tag{20}$$

$$S_{22} = 2\overline{v^2}\frac{\partial V}{\partial y}(\beta^* - \Omega^*) + 2\gamma^* k\frac{\partial V}{\partial y} + 2\overline{vw}\frac{\partial V}{\partial z}(\beta^* - \Pi^*) + 2\overline{vw}\frac{\partial W}{\partial y}(\beta^* + \Lambda^*) + 2\beta^*\left(\overline{u^2}\frac{\partial U}{\partial x} + \overline{w^2}\frac{\partial W}{\partial z}\right) \tag{21}$$

$$S_{33} = 2\overline{w^2}\frac{\partial W}{\partial z}(\beta^* - \Omega^*) + 2\gamma^* k\frac{\partial W}{\partial z}$$

$$+ 2\overline{vw}\frac{\partial W}{\partial y}(\beta^* - \Pi^*) + 2\overline{vw}\frac{\partial V}{\partial z}(\beta^* + \Lambda^*) + 2\beta^*\left(\overline{u^2}\frac{\partial U}{\partial x} + \overline{v^2}\frac{\partial V}{\partial y}\right) \quad (22)$$

$$S_{12} = \Omega^*\overline{uv}\frac{\partial W}{\partial z} + \overline{uw}\left(\Lambda^*\frac{\partial W}{\partial y} - \Pi^*\frac{\partial V}{\partial z}\right) \quad (23)$$

$$S_{13} = \Omega^*\overline{uw}\frac{\partial V}{\partial y} + \overline{uv}\left(\Lambda^*\frac{\partial V}{\partial z} - \Pi^*\frac{\partial W}{\partial y}\right) \quad (24)$$

$$S_{23} = \overline{v^2}\left(\Lambda^*\frac{\partial V}{\partial z} - \Pi^*\frac{\partial W}{\partial y}\right) + \overline{w^2}\left(\Lambda^*\frac{\partial W}{\partial y} - \Pi^*\frac{\partial V}{\partial z}\right) - \Omega^*\overline{vw}\left(\frac{\partial W}{\partial z} + \frac{\partial V}{\partial y}\right) + \gamma^* k\left(\frac{\partial V}{\partial z} + \frac{\partial W}{\partial y}\right) \quad (25)$$

The coefficients which appear in Eqs. (14)–(25) are as follows:

$$c_1^* = c_1 + c_1' f_l \qquad \beta^* = -(2 + 3c_2^*)/11$$
$$c_2^* = c_2 + c_2' f_l \qquad \Lambda^* = \beta^* + c_2^*$$
$$\gamma^* = \gamma + \gamma' f_l \qquad \Omega^* = 1 - \alpha^* - 2\beta^* - c_2^*$$
$$\alpha^* = (10 + 4c_2^*)/11 \qquad \Pi^* = \Omega^* + \Lambda^*$$

where c_1, c_2, and γ correspond to primary pressure-strain coefficients, c_1', c_2', and γ' correspond to wall correction coefficients, and f_l is a linear wall damping function. In the present study these coefficients were set equal to the numerical values recommended by Eppich (1987), who determined values for c_1, c_2, and γ on the basis of comparisons with plane homogeneous shear flow data taken by Champagne et al. (1970) and Harris et al. (1977). Numerical values for c_1', c_2', and γ' were selected by examining near-wall Reynolds stress levels measured in fully developed pipe flow and plane channel flow. The values for these coefficients are summarized below:

$$c_1 = 1.4 \qquad c_2 = 0.385 \qquad \gamma = -0.12$$
$$c_1' = -0.76 \qquad c_2' = -0.043 \qquad \gamma' = -0.066$$

In contrast to the quadratic wall damping function specified by others as a means of modeling near-wall effects on pressure-strain behavior (Demuren and Rodi, 1984; Demuren, 1990), the use of a linear wall damping function, f_l, as proposed by Gessner and Eppich (1981), was found to be entirely adequate in the present study. The adopted form for f_l is based on Buleev's (1963) length scale model for rectangular duct flows and can be written as:

$$f_l = \frac{l_p}{\varkappa\langle s\rangle} \quad (26)$$

where

$$l_p = \frac{(c_\mu^*\xi_p)^{3/4}k^{3/2}}{\epsilon} \quad (27)$$

and

$$\frac{1}{\langle s\rangle} = \frac{1}{2}\left[\frac{\sqrt{y^2 + z^2}}{yz} + \frac{\sqrt{(2a - y)^2 + z^2}}{(2a - y)z} + \frac{\sqrt{y^2 + (2b - z)^2}}{y(2b - z)}\right] + \frac{\sqrt{(2a - y)^2 + (2b - z)^2}}{(2a - y)(2b - z)} \quad (28)$$

In order to close the system of equations, the high Reynolds number form of the transport equation for ϵ appropriate for developing rectangular duct flows was employed, namely (cf. Demuren and Rodi, 1984):

$$U\frac{\partial \epsilon}{\partial x} + V\frac{\partial \epsilon}{\partial y} + W\frac{\partial \epsilon}{\partial z} = \frac{\partial}{\partial y}\left[\left(\nu + \frac{\nu_t}{\sigma_\epsilon}\right)\frac{\partial \epsilon}{\partial y}\right] + \frac{\partial}{\partial z}\left[\left(\nu + \frac{\nu_t}{\sigma_\epsilon}\right)\frac{\partial \epsilon}{\partial z}\right] + c_{\epsilon 1}\frac{\epsilon}{k}\mathcal{P} - c_{\epsilon 2}\frac{\epsilon^2}{k} \quad (29)$$

The remaining empirical coefficients that appear in Eqs. (9)–(29), namely σ_k, σ_ϵ, $c_{\epsilon 1}$, and $c_{\epsilon 2}$ were assigned the following numerical values:

$$\sigma_k = 1.0 \quad c_{\epsilon 1} = 1.44$$
$$\sigma_\epsilon = 1.2 \quad c_{\epsilon 2} = 1.92$$

The value for σ_k is the same as the one originally specified by Launder and Spalding (1974), whereas the dissipation coefficient σ_ϵ was assigned a value of 1.2, which is slightly less than Launder and Spalding's value (1.3), but close to the value selected by Bo et al. (1991) in their numerical simulation of turbulent flow in a rotating square duct (1.22). The values chosen for $c_{\epsilon 1}$ and $c_{\epsilon 2}$ (1.44 and 1.92, respectively) are standard values specified in the high Reynolds number form of the dissipation rate transport equation (cf. Naot and Rodi, 1981; Nakayama et al., 1983; Demuren and Rodi, 1984).

Wall Function and Boundary Condition Specification. The proposed differential Reynolds stress model given by Eqs. (6)–(29), hereafter designated as the DS model, is not applicable in the immediate vicinity of a wall and therefore wall functions must be specified on the first computational mesh line adjacent to the wall. In all of the simulations described in this paper, the first mesh line was always positioned at a y^+ location within the interval $30 \leqslant y^+ \leqslant 100$, so that the law-of-the-wall could be applied as the wall function for U on that line. The velocity component normal to the wall was set equal to zero on the wall, whereas the binormal velocity component was specified on the first mesh line following the procedure outlined by Tatchell (1975). In order to simulate the behavior of the individual Reynolds stresses in the near-wall region, the convective and diffusive terms in the Reynolds stress transport equations were initially omitted, which resulted in a set of algebraic expressions that served as a near-wall boundary condition for the Reynolds stress field. This procedure, although attractive, was not successful because calculations based on this approximation were numerically unstable. As an alternative, convection and diffusion effects were retained in the Reynolds stress transport equations in the near-wall region and a zero gradient condition was applied to each Reynolds stress component at the wall. This alternate treatment eliminated the numerical instabilities noted earlier. Inasmuch as rectangular ducts of different aspect ratio were considered in the present work, computations were performed over a full quadrant of the duct. In reference to Fig. 1, the assigned wall boundary conditions for the Reynolds stresses were: for the solid wall defined by $y = 0$, $\partial(\overline{u_i u_j})/\partial y|_w = 0$, $i, j = 1, 2, 3$ and for the solid wall defined by $z = 0$, $\partial(\overline{u_i u_j})/\partial z|_w = 0$, $i, j = 1, 2, 3$. These boundary conditions were actually applied between the wall and the first grid line parallel to the wall. Along the first mesh line adjacent to each wall it was assumed that the dissipation rate, ϵ, is equal to the turbulence kinetic energy production rate, $\mathcal{P}$, as evaluated from Eq. (10). The dependent variables identically zero on planes of symmetry (e.g., along the wall bisectors $y = a$ and $z = b$ in Fig. 1) were set equal to zero and a zero gradient condition was applied on each bisector to variables symmetric about the bisector.

Solution Procedure. In order to solve the system of equations, a revised version of the staggered cell, three-dimensional, streamwise-marching SIMPLER algorithm of Patankar (1980) was employed. For purposes of comparison the $k - \epsilon$ transport equation model proposed by Demuren and Rodi (1984), henceforth designated as the DR model, was also coded. In square duct flow calculations utilizing either the DR or DS model, a 20×20 clustered grid in one quadrant of the duct was used, because computations referred to 30×30 and 40×40 clustered grids yielded essentially the same results. More specifically, diminished differences occurred with grid refinement which indicated that a grid invariant solution had been reached. Additional computations referred to a 3:1 aspect ratio duct were performed using a 60×20 clustered grid. At the duct inlet ($x/D_h = 0$), a low turbulence level, uniform mean flow was assumed ($U = U_b$, $V = W = 0$), and k and ϵ were assigned small values, so that the turbulent eddy viscosity was several times larger than the kinematic viscosity. At this location, the Reynolds shear stress components were set equal to zero and each Reynolds normal stress component was set equal to $(2/3)k$.

Starting with these initial conditions, the system of equations was solved over a development length that extended from $x/D_h = 0$ to $x/D_h = 84$ for comparisons with square duct flow data obtained by Gessner and his co-workers (1981, 1982, 1993), to $x/D_h = 90$ for comparisons with data obtained by Fujita (1978), and to $x/D_h = 75$ for comparisons with data obtained by Hoagland (1960) in a 3:1 aspect ratio duct. The initial forward step size was typically $0.0025D_h$. For the DR model, the forward step size was progressively increased from $0.0025D_h$ to $0.025D_h$. This model became susceptible to numerical instabilities, however, as the step size was increased to values above $0.025D_h$. In contrast, the DS model was quite stable, even when a maximum forward step size of $0.05D_h$ was used. For the range of forward step sizes considered, results based on the DR and DS models were found to be nearly independent of step size when a converged solution could be obtained. Furthermore, in comparison to the DR model, the DS model required less iteration cycles in the cross plane to meet the same convergence criteria. The convergence criteria included a residual check on all of the flow properties, together with a check on local (individual cell) mass flow and global (duct cross section) mass flow conservation. The local and global mass flow criteria were 1×10^{-10} and 1×10^{-15}, respectively, when normalized by the bulk mass flow rate. The fewer number of cross plane iterations, together with the larger axial step size, enabled the DS model computations for a given run to be completed in roughly the same amount of computer time as that required for the DR model. Thus, the computational time required to implement the DS model, which consists of seven transport equations for the turbulence-related variables, was essentially the same as that associated with implementation of the two transport equation DR model. The runs were performed on an APOLLO series 10000 workstation. Each square duct run took about three hours to complete, which is roughly equivalent to 12 minutes of CPU time on a CRAY type computer.

Results and Discussion

Developing Flow in a Square Duct. The streamwise development of axial mean velocity in a square duct at $Re_b = 250{,}000$ is shown in Fig. 2. The distributions apply at fixed distances from the wall along the wall bisector (Fig. 2(a)) and corner bisector (Fig. 2(b)) of the duct, where y' and a' in Fig. 2(b) correspond, respectively, to the diagonal distance from the corner and the diagonal half width of the duct. In this figure data reported by Gessner (1982) are compared with predictions referred to the DR and DS models, and with predictions presented by Myong and Kobayashi (1991), which are based on the low Reynolds number, $k - \epsilon$ transport equation model developed by Myong (1988), henceforth designated as the MY

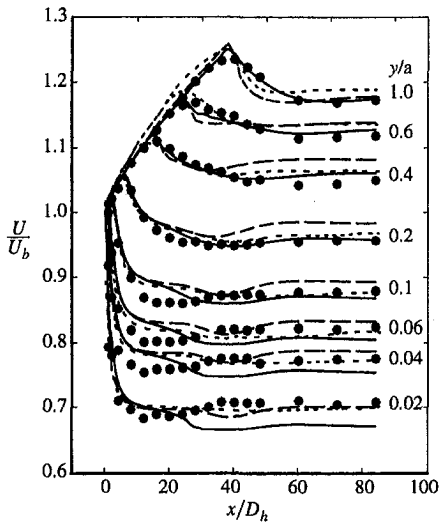

Fig. 2(*a*) Wall bisector

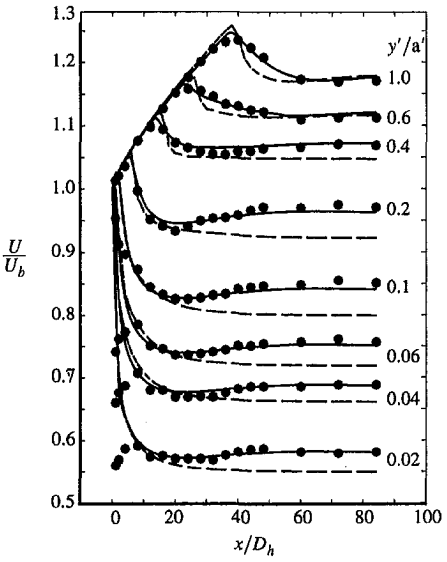

Fig. 2(*b*) Corner bisector

Fig. 2 Predicted and measured axial mean velocity distributions at fixed distances from the wall of a square duct, $Re_b = 250{,}000$. Data: ●, Gessner (1982); – – –, DR model; -----, MY model; ——, DS model.

model. In reference to Fig. 2(a), it can be seen that all three models perform reasonably well for predicting local flow development along the wall bisector. There are, however, some systematic differences between predictions and experiment. Along the axial centerline of the duct ($y/a = 1.0$), the MY model predicts too rapid an increase in U/U_b values downstream of the duct inlet before peaking occurs. Along this same traverse, the DS model predictions agree well with experiment, whereas predictions based on the DR and MY models decay too rapidly beyond the U/U_b peak near $x/D_h = 38$. In this context it should be noted that the observed peaking on the axial centerline is not a secondary flow effect, but the result of shear layer interactions which occur as the boundary layers on opposite walls of the duct merge. In reference to Fig. 2(b), it can be seen that DS model outperforms the DR model on the corner bisector over the entire flow development region. The differences between predictions and experiment in the near corner region just downstream of the duct inlet (cf. the distributions of $y'/a' = 0.02$, 0.04, and 0.06 between $x/D_h = 0$ and 5) are not attributable to

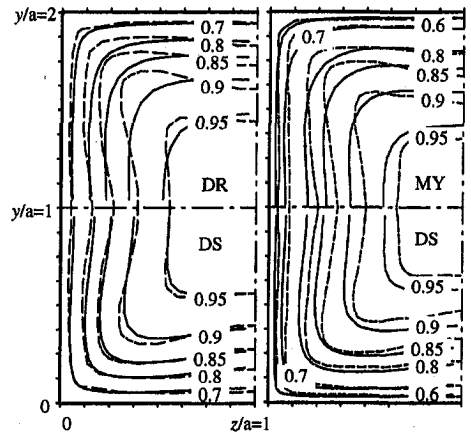

(a) x/D_h = 84, Re_b = 250,000 (b) x/D_h = 90, Re = 65,000

Fig. 3 Predicted and measured U/U_c contours for square duct flow. Data: - - -, Gessner (1982), Re_b = 250,000; Fujita (1978), Re_b = 65,000; ——, Predictions.

model deficiencies, but are the result of delayed transition in the corner region of the experimental flow. As a result, for a short distance along the duct, an outwardly directed transverse flow was present in the corner region which convected low momentum fluid away from the corner, resulting in the relatively low experimental U/U_b values seen in Fig. 2(*b*).

The ability of the DS model to predict primary flow behavior can be demonstrated further by referring to the results in Fig. 3, which shows predicted and measured isovelocity contours in the cross plane of a square duct for fully developed flow conditions. In reference to predictions based on the DR and MY models, it can be seen that predicted contours do not penetrate as deeply into the corner region as their experimental counterparts. This lack of penetration is typical of results referred to previously proposed methods of closure based on the use of two transport equations (i.e., $k-\epsilon$, $k-l$, $k-\omega$, or $k-\tau$ models). For closure at the full Reynolds stress transport equation level, Fig. 3 shows that proper penetration and improved agreement is possible when the DS model is employed.

Local wall shear stress distributions corresponding to the results in Fig. 3 are shown in Fig. 4. In this figure, local wall shear stress values are normalized by the bulk dynamic pressure, rather than the spanwise-averaged wall shear stress, in order to illustrate more clearly the predictive capabilities of each model. In reference to the lower set of distributions, the DR and MY models outperform the DS model in the immediate vicinity of

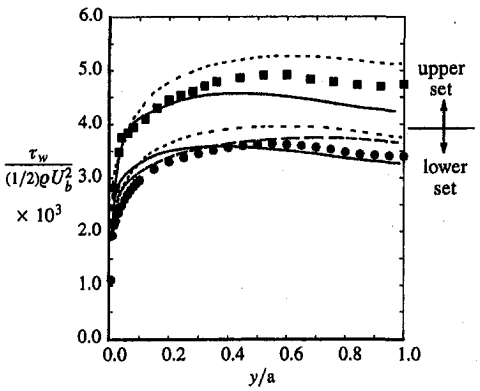

Fig. 4 Predicted and measured local wall shear stress distributions for fully developed square duct flow. Data: ●, Lund (1977), Re_b = 250,000; ■, Fujita (1978), Re_b = 65,000; - - -, DR model; -----, MY model; ——, DS model.

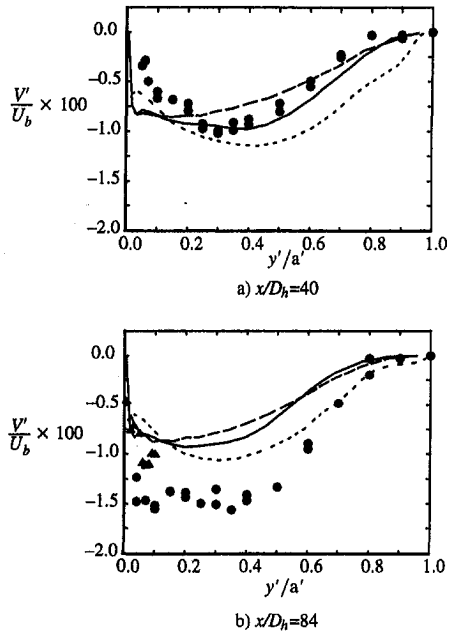

Fig. 5 Secondary flow velocity component profiles along the corner bisector at x/D_h = 40 and 84 for square duct flow, Re_b = 250,000. Data: ●, Gessner and Emery (1981); ▲, Lund (1977); - - -, DR model; -----, MY model; ——, DS model.

the corner ($0 < y/a < 0.1$), but that the DS model performs best as the wall bisector is approached ($y/a \to 1.0$). In reference to the upper set of distributions, the DS model outperforms the MY model in the near corner again, but elsewhere the MY and DS models respectively overpredict and underpredict the experimental distribution by similar amounts. On balance, all three models perform reasonably well, but with systematic differences between predictions and experiment, which implies that further work on model development is needed in order to realize improved agreement.

This same comment applies to predictions of secondary flow in a square duct, as indicated by the results in Fig. 5, which shows predicted and measured secondary flow velocity distributions along the corner bisector of a square duct at two streamwise locations (x/D_h = 40 and 84) for Re_b = 250,000. Figure 5(*a*) indicates that the DS model is the best overall performer at x/D_h = 40 relative to performance by the DR and MY models, which, respectively, underpredict and overpredict secondary flow levels along a portion of the bisector. At x/D_h = 84, Fig. 5(*b*) shows that predictions based on the MY model agree best with the data reported by Gessner and Emery (1981). This figure also shows that predictions by the DR and DS models are quite similar at x/D_h = 84, although primary flow isovelocity contours predicted at this same location are quite different (refer to Fig. 3(*a*)). In order to examine this apparent anomaly more closely, predictions referred to both models were compared with secondary flow data obtained by Lund (1977) in the near-wall region of a square duct at x/D_h = 84 and Re_b = 250,000. These results, which are shown in Fig. 6, indicate that secondary flow profiles predicted by both models agree relatively well with the experimental profiles, which satisfy continuity in the cross plane to the extent that cross flow directed toward the corner at each z/a location agrees to within 20 percent with cross flow directed away from the corner. The irregularities that appear in the DR model predicted secondary flow (Fig. 6(*a*)) are due to the Reynolds stress gradient source terms, which varied considerably between the first and second computational cells away from a wall when the DR model was employed. The secondary flow velocities measured by Lund on the corner bisector, when superimposed on the results shown in Fig. 5(*b*), indicate that

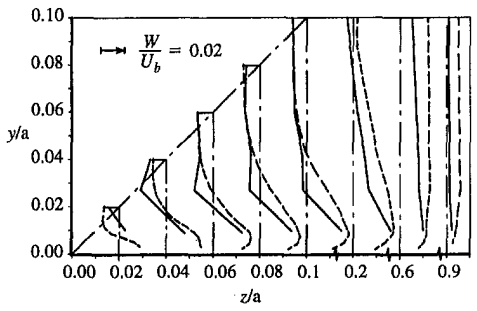

Fig. 6(a) DR model

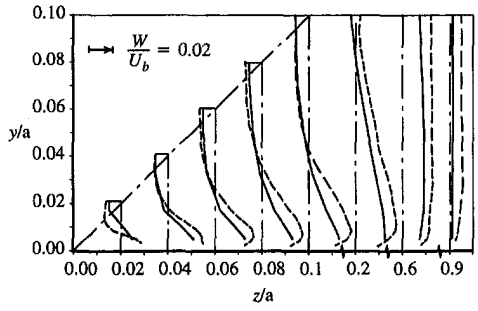

Fig. 6(b) DS model

Fig. 6 Secondary flow velocity component profiles in the near-wall region of a square duct, $x/D_h = 84$, $Re_b = 250{,}000$. Data: - - -, Gessner et al. (1993); ——, Predictions.

the earlier data, as reported by Gessner and Emery (1981), are somewhat high. Predictions referred to all three models agree better with Lund's data in the near corner region, which implies that all three models may be performing properly. If this is true and secondary flow predictions by the MY, DR, and DS models are, in fact, all relatively accurate in the entire cross section at $x/D_h = 84$, then differences among the three models with respect to predicting the primary flow are not due primarily to inaccurate prediction of the secondary flow.

As Fig. 3 indicates, the DS model correctly predicts experimentally observed isovelocity penetration into the corner region whereas the MY and DR models do not. Aside from differences in wall function and/or boundary condition specification, one of the major differences among these models is that the DS model employs transport equations for v^2 and w^2, whereas the MY and DR models utilize algebraic expressions for these stress components. Accordingly, the DS model accounts directly for convective and diffusive transport effects on v^2 and w^2 and, more importantly, on the anisotropy between these two stress components, namely $v^2 - w^2$. Inasmuch as gradients of $v^2 - w^2$ act as a secondary flow source term in the axial vorticity equation, one would anticipate that more accurate modeling of $v^2 - w^2$ would lead to more accurate simultaneous prediction of the primary and secondary flow velocity fields. If one assumes that secondary flow predictions by the MY, DR, and DS models are all relatively accurate at $x/D_h = 84$ (as they appear to be at $x/D_h = 40$; refer to Fig. 5(*a*), then the neglect of convective and diffusive transport effects on $\overline{v^2}$ and $\overline{w^2}$ in the MY and DR models may be responsible for the inability of these models to predict experimentally observed isovelocity contour penetration into the corner region, as indicated by the results shown in Fig. 3.

In order to explore this point further, additional computations were performed using the high Reynolds number, $k - \epsilon$ transport equation model proposed by Eppich (1987). This model employs the same coefficient values as those prescribed in the DS model and is derivable from the DS model when the equations which simulate convective and diffusive transport effects on the Reynolds stress components are replaced by the algebraic relationships proposed by Eppich. This model, when applied by Eppich to plane channel flow, yielded very good agreement between predictions and experiment for the primary flow and the individual Reynolds stresses, and outperformed the DR model for this limiting case. In the present study, when Eppich's $k - \epsilon$ model was used to predict developing flow in a square duct at $Re_b = 250{,}000$, the secondary flow was significantly underpredicted, and predicted isovelocity contours did not penetrate into the corner region. These results demonstrate that it is important to include convective and diffusive transport effects on $v^2 - w^2$ in the overall model and that these effects must be simulated accurately.

The importance of accurately modeling the anisotropy between v^2 and w^2 can also be demonstrated by referring to Fig. 7, which shows predicted and measured distributions of $(\overline{v^2} - \overline{w^2})/U_b^2$ in the near-wall region of a square duct. The operating conditions for these data are the same as those shown in Fig. 6 ($x/D_h = 84$, $Re_b = 250{,}000$), and therefore direct comparisons can be made between the results shown in each figure. In reference to Fig. 7, it can be seen that the DR model overpredicts the anisotropy between v^2 and w^2 along the traverses $y/a = 0.02$ and 0.03. This behavior is the direct result of the wall correction coefficients specified by Launder et al. (1975) in their pressure-strain model, as adopted by Demuren and Rodi, which yield an anisotropy level $-(v^2 - w^2)/k = 0.33$ in the near-wall region. This value is well above the consensus value established by Eppich (1987) for fully developed pipe flow (0.24) and plane channel flow (0.20). In contrast, the wall correction coefficients employed in the DS model yield a more reasonable anisotropy level in the near-wall region, namely $-(v^2 - w^2)/k = 0.21$, which is close to the consensus value for square duct flow established by Eppich (0.20). As a result, predictions based on the DS model in Fig. 7 are in good agreement with anisotropy levels measured in the immediate vicinity of the wall, whereas predictions based on the DR model are too high. Demuren and Rodi compensate for this behavior by specifying a quadratic wall damping function in their pressure-strain model. This maneuver is relatively successful in maintaining secondary flow at acceptable levels, as indicated by the DR model predictions shown in Fig. 6*a*. This is accomplished, however, by artificially damping anisotropy levels that are too high. In contrast, the DS model yields anisotropy and secondary flow levels that agree well with experiment (refer to Figs. 6(*b*) and 7), which implies that the linear wall damping

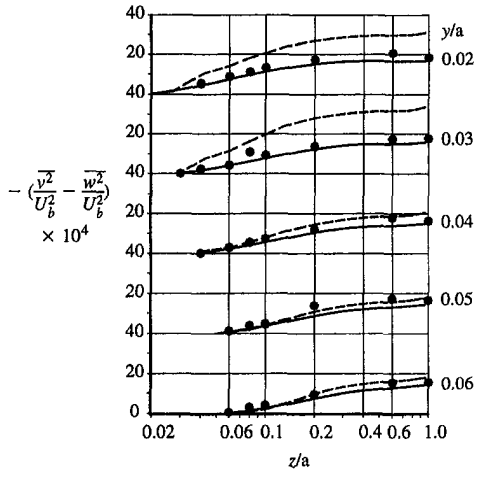

Fig. 7 Predicted and measured anisotropy between $\overline{v^2}$ and $\overline{w^2}$ in the near-wall region of a square duct, $x/D_h = 84$, $Re_b = 250{,}000$. Data: ●, Eppich (1982); - - -, DR model; ——, DS model.

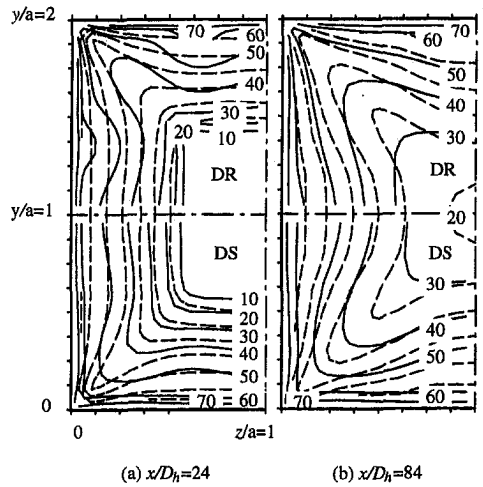

Fig. 8 Predicted and measured $(k/U_b^2) \times 10^4$ contours for square duct flow, Re_b = 250,000. Data: - - -, Gessner (1982); ——, Predictions.

function, as prescribed by Eqs. (26) – (28), is performing properly.

The discussion thus far has centered on similarities and differences among the DS, DR, and MY models as they pertain to primary and secondary flow predictions in a square duct. The relative capabilities of each model for predicting Reynolds stress behavior is also of interest. Figure 8 shows turbulence kinetic energy contours predicted by the DR and DS models at two streamwise locations (x/D_h = 24 and 84) for Re_b = 250,000. Corresponding contours of the primary shear stress component $\overline{uw}$ are shown in Fig. 9. For purposes of comparison experimental contours reported by Gessner (1982) are included in both figures. In the developing flow region (at x/D_h = 24) Figs. 8(a) and 9(a) show that the DR model predicts bulges in k and $\overline{uw}$ contours near the wall z = 0 at $y/a \simeq 1.4$ which are not present in the experimental flow. This occurs because secondary flow levels are apparently overpredicted by the DR model in this region, a region where experimental data are not available for purposes of comparison. In contrast, the DS model appears to predict secondary flow levels correctly at x/D_h = 24, because predicted and measured turbulence kinetic energy and Reynolds shear stress contours agree relatively well at this location. In the fully developed flow region (at x/D_h = 84), Figs. 8(b) and 9(b) show that both models perform reasonably well in predicting experimentally observed behavior. Again,

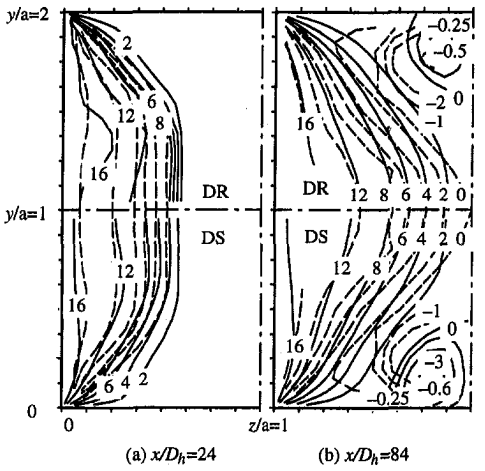

Fig. 9 Predicted and measured $-(\overline{uw}/U_b^2) \times 10^4$ contours for square duct flow, Re_b = 250,000. Data: - - -, Gessner (1982); ——, Predictions.

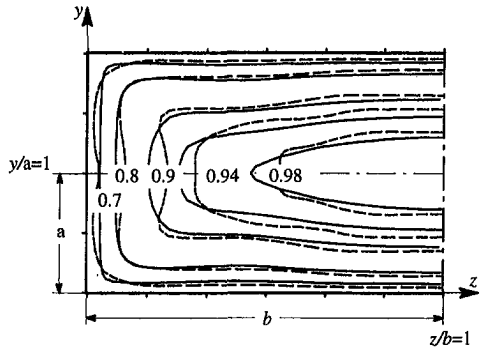

Fig. 10 Predicted and measured U/U_c contours for fully developed flow in a 3:1 aspect ratio rectangular duct, Re_b = 60,000. Data: - - -, Hoagland (1960); ——, DS model.

however, there are systematic differences between predictions and experiment, namely lesser penetration of predicted k contours into the corner region, which indicates that further work on model development is still needed. In this context, it should be noted that when the calculations were repeated using the DS model with α_{CD} = 1 (convection exact; refer to Eq. (9)), better overall agreement was obtained between predictions and experiment, as evidenced by greater penetration of predicted k contours into the corner region.

Fully Developed Flow in a Rectangular Duct

The DS model was also used to predict fully developed flow in a 3:1 aspect ratio, rectangular duct for comparison with Hoagland's data at Re_b = 60,000. Predicted and measured primary flow isovelocity contours are shown in Fig. 10; the corresponding predicted and measured secondary flow patterns are shown in Fig. 11. The level of agreement between predictions and experiment in Fig. 11 is similar to that observed by Speziale et al. (1993), who compared secondary flow predictions based on two levels of closure ($k - \epsilon$ and full transport equation model predictions) with Hoagland's data. Figure 11 shows that secondary flow stream function contours predicted by the DS model agree very well with contours evaluated from Hoagland's secondary flow measurements. The predicted and measured isovelocity contours in Fig. 10 also agree well, except for a region near the wall bisector y/a = 1.0. More specifically, near y/a = 1.0, the predicted U/U_c = 0.9 contour is relatively undistorted, whereas the experimental U/U_c = 0.9 contour is outwardly distorted in a manner indicative of secondary flow directed away from the wall z = 0. Close comparison with Hoagland's secondary flow results in Fig. 11 shows that this outward distortion occurs at a location where the measured secondary flow is actually directed toward the wall z = 0. It appears, therefore,

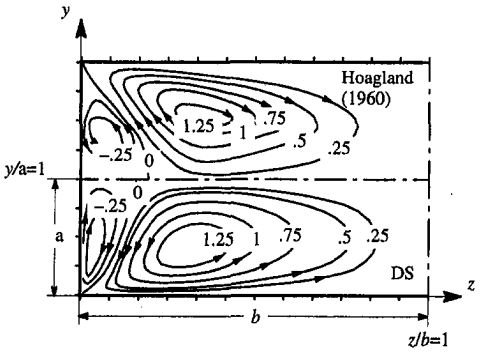

Fig. 11 Predicted and measured $\psi \times 10^{-3}$ contours for fully developed flow in a 3:1 aspect ratio rectangular duct, Re_b = 60,000

that the lack of agreement between predicted and measured isovelocity contours in Fig. 10 near $y/a = 1.0$ may be due primarily to inaccuracies in the measured contours, rather than to deficiencies in the predictive capability of the DS model.

Concluding Remarks

A full Reynolds stress transport equation model has been presented in this paper which can be used to predict developing turbulent flow in rectangular ducts of arbitrary aspect ratio. The pressure-strain component of the model employs primary and wall correction coefficients which are derived wholly from comparisons with pipe flow and plane channel flow data. The convection minus diffusion effect is modeled by means of a modified version of the model originally proposed by Mellor and Yamada (1974). Predictions based on the overall model have been compared with predictions referred to the $k - \epsilon$ transport equation models proposed by Myong (1988) and by Demuren and Rodi (1984). The results indicate that the proposed model outperforms these models with respect to predicting primary flow behavior in a square duct. The proposed model also yields improved Reynolds stress predictions in the developing flow region of a square duct in comparison to predictions based on the Demuren and Rodi model. Secondary flow predictions referred to all three models are comparable at, and beyond, a streamwise location where the wall boundary layers first merge and are in relatively good agreement with experimental data. Local wall shear stress predictions show slight, but systematic, deviations from experimental results for all three models. The proposed model is self-consistent in that predicted $\overline{v^2} - \overline{w^2}$ anisotropy levels in the near-wall region of a square duct agree well with experiment. As a result, secondary flow levels are predicted with good accuracy using a linear wall damping function in the pressure-strain component of the model. This is not possible if the pressure-strain wall correction coefficients proposed by Launder et al. (1975) are adopted, as was done by Demuren and Rodi, which lead to relatively high predicted $\overline{v^2} - \overline{w^2}$ anisotropy levels in the near-wall region. Under these conditions, secondary flow levels cannot be predicted with reasonable accuracy unless a quadratic wall damping function is used, as was specified by Demuren and Rodi in their model. This paper has shown that improved predictions are possible when convective and diffusive transport effects on $\overline{v^2}$ and $\overline{w^2}$ are included in the overall model. The low Reynolds number and high Reynolds number forms of the $k - \epsilon$ model all utilize algebraic relationships to model the behavior of $\overline{v^2}$ and $\overline{w^2}$. As a consequence, further model modifications at this level of closure are not likely to lead to significant improved agreement between predictions and experiment.

References

Balaras, E., and Benocci, C., 1992, "Large Eddy Simulation of Flow in a Square Duct," *Proceedings of the 13th Symposium on Turbulence,* Department of Chemical Engineering, University of Missouri-Rolla, pp. A33-1–A33-8.

Barton, J. M., Rubinstein, R., and Kirtley, K. R., 1991, "Non-linear Reynolds Stress Model for Turbulent Shear Flows," *AIAA* Paper 91-0609.

Bo, T., Iacovides, H., Launder, B. E., 1991, "The Prediction of Convective Heat Transfer in a Rotating Square Duct," *Proceedings of the Eighth Symposium on Turbulent Shear Flows,* Technical University of Munich, Sept. 9–11, pp. 24–4.1–24.4.6.

Buleev, N. J., 1963, "Theoretical Model of the Mechanism of Turbulent Exchange in Fluid Flows," *AERE Translation 957,* Atomic Energy Research Establishment, Howell, England.

Champagne, F. H., Harris, V. G., and Corrsin, S., 1970, "Experiments on Nearly Homogeneous Turbulent Shear Flow," *Journal of Fluid Mechanics,* Vol. 41, Part 1, pp. 81–139.

Demuren, A. O., 1990, "Calculation of Turbulent Flow in Complex Geometries With a Second-Moment Closure Model," *Forum on Turbulent Flows,* W. M. Bower, M. J. Morris, and M. Samimy, eds., FED-Vol. 94, pp. 163–167, ASME, New York.

Demuren, A. O., and Rodi, W., 1984, "Calculation of Turbulence-Driven Secondary Motion in Non-Circular Ducts," *Journal of Fluid Mechanics,* Vol. 140, pp. 189–222.

Eppich, H. M., 1987, "The Development and Preliminary Testing of a Constitutive Model for Turbulent Flow Along a Streamwise Corner," Ph.D. dissertation, Department of Mechanical Engineering, University of Washington.

Fujita, H., 1978, "Turbulent Flows in Square Ducts Consisting of Smooth and Rough Planes," *Research Reports of the Faculty of Engineering, Mie University,* Vol. 3, pp. 11–25.

Gavrilakis, S., 1992, "Numerical Simulation of Low-Reynolds-Number Turbulent Flow Through a Straight Square Duct," *Journal of Fluid Mechanics,* Vol. 244, pp. 101–129.

Gessner, F. B., 1982, "Corner Flow Data Evaluation," *Proceedings of the 1980–81 AFOSR-HTTM-Stanford Conference on Complex Turbulent Flows,* Vol. III, pp. 182–204, Stanford University.

Gessner, F. B., and Emery, A. F., 1981, "The Numerical Prediction of Developing Turbulent Flow in Rectangular Ducts," ASME JOURNAL OF FLUIDS ENGINEERING, Vol. 103, pp. 445–454.

Gessner, F. B., and Eppich, H. M., 1981, "A Near-Wall Pressure-Strain Model for Turbulent Corner Flows," *Proceedings of the Third Symposium on Turbulent Shear Flows,* University of California, Davis, Sept. 9–11.

Gessner, F. B., Eppich, H. M., and Lund, E. G., 1991, "The Near-Wall Structure of Turbulent Flow Along a Streamwise Corner," *Proceedings of the Eighth Symposium on Turbulent Shear Flows,* Technical University of Munich, Sept. 9–11.

Gessner, F. B., Eppich, H. M., and Lund, E. G., 1993, "Reynolds Number Effects on the Near-Wall Structure of Turbulent Flow Along a Streamwise Corner," *Proceedings of the International Conference on Near-Wall Turbulent Flows,* Tempe, Arizona, Mar. 15–17, pp. 965–975.

Harris, V. G., Graham, J. A. H., and Corrsin, S., 1977, "Further Experiments in Nearly Homogeneous Shear Flow," *Journal of Fluid Mechanics,* Vol. 81, Part 4, pp. 657–687.

Hoagland, L. C., 1960, "Fully Developed Turbulent Flow in Straight Rectangular Ducts—Secondary Flow, Its Cause and Effect on the Primary Flow," Ph.D. dissertation, Mechanical Engineering Department, MIT.

Huser, A., and Biringen, S., 1993, "Direct Numerical Simulation of Turbulent Flow in a Square Duct," *Journal of Fluid Mechanics,* Vol. 287, pp. 65–95.

Kajishima, T., and Miyake, Y., 1992, "A Discussion on Eddy Viscosity Models on the Basis of the Large Eddy Simulation of Turbulent Flow in a Square Duct," *Computers and Fluids,* Vol. 21, No. 2, pp. 151–161.

Launder, B. E., and Li, S.-P., 1993, "On the Prediction of Flow Over Riblets Via 2nd-Moment Closure," *Proceedings of the International Conference on Near-Wall Turbulent Flows,* Tempe, Arizona, Mar. 15–17, pp. 739–748.

Launder, B. E., Reece, G. J., and Rodi, W., 1975, "Progress in the Development of a Reynolds-Stress Turbulence Closure," *Journal of Fluid Mechanics,* Vol. 68, Part 2, pp. 537–566.

Launder, B. E., and Spalding, D. B., 1974, "The Numerical Computation of Turbulent Flows," *Computer Methods in Applied Mechanics and Engineering,* Vol. 3, pp. 269–289.

Lund, E. G., 1977, "Mean Flow and Turbulence Characteristics in the Near Corner Region of a Square Duct," MS thesis, Department of Mechanical Engineering, University of Washington.

Madabhushi, R. K., and Vanka, S. P., 1991, "Large Eddy Simulation of Turbulence-Driven Secondary Flow in a Square Duct," Computational Fluid Dynamics Laboratory, Report No. CFD-91-03, Department of Mechanical and Industrial Engineering, University of Illinois at Urbana-Champaign.

Madabhushi, R. K., and Vanka, S. P., 1993, "Direct Numerical Simulation of Turbulent Flow in a Square Duct at Low Reynolds Number," *Proceedings of the International Conference on Near-Wall Turbulent Flows,* Tempe, Arizona, Mar. 15–17, pp. 297–306.

Mellor, G. L., and Yamada, T., 1974, "A Hierarchy of Turbulence Closure Models for Planetary Boundary Layers," *Journal of Atmospheric Sciences,* Vol. 31, pp. 1791–1806.

Myong, H. K., 1988, "Fundamental Studies on Two-Equation Turbulence Model for Wall-Bounded Shear Flow And Heat Transfer," Doctor of Engineering Thesis, Department of Mechanical Engineering, University of Tokyo.

Myong, H. K., 1991, "Numerical Investigation of Fully Developed Turbulent Fluid Flow and Heat Transfer in a Square Duct," *International Journal of Heat and Fluid Flow,* Vol. 12, pp. 344–352.

Myong, H. K., and Kasagi, N., 1990, "Prediction of Anisotropy in the Near-Wall Turbulence with an Anisotropic Low-Reynolds-Number $k - \epsilon$ Turbulence Model," ASME JOURNAL OF FLUIDS ENGINEERING, Vol. 112, pp. 521–524.

Myong, H. K., and Kobayashi, T., 1991, "Prediction of Three-Dimensional Developing Turbulent Flow in a Square Duct With an Anisotropic Low-Reynolds-Number $k - \epsilon$ Model," ASME JOURNAL OF FLUIDS ENGINEERING, Vol. 113, pp. 608–615.

Naimi, M., 1993, "Numerical Simulation of Turbulence-Induced Secondary Flow in Rectangular Ducts," Ph.D. dissertation, Department of Mechanical Engineering, University of Washington.

Nakayama, A., Chow, W. L., and Sharma, D., 1983, "Calculation of Fully Developed Turbulent Flows in Ducts of Arbitrary Cross-Section," *Journal of Fluid Mechanics,* Vol. 128, pp. 199–217.

Naot, D., and Rodi, W., 1981, "Numerical Simulation of Secondary Currents in Open Channel Flow with an Algebraic Stress Turbulence Model," SFB 80/T/187, Sonderforschungsbereich 80, University of Karlsruhe. (see also *Journal of Hydraulics Division, Proceedings of ASCE,* Vol. 108, HY8, 1982, pp. 948–968.)

Nisizima, S., 1990, "A Numerical Study of Turbulent Square Duct Flow Using an Anisotropic $k - \epsilon$ Model," *Theoretical and Computational Fluid Dynamics,* Vol. 2, No. 1, pp. 61–71.

Patankar, S. V., 1980, *Numerical Heat Transfer and Fluid Flow,* McGraw-Hill, New York.

Patankar, S. V., and Spalding, D. B., 1972, "A Calculation Procedure for Heat, Mass and Momentum Transfer in 3-D Parabolic Flows," *International Journal of Heat and Mass Transfer,* Vol. 15, pp. 1787–1806.

Po, J. K., 1975, "Developing Turbulent Flow in the Entrance Region of a Square Duct," MS thesis, Department of Mechanical Engineering, University of Washington.

Speziale, C. G., Abid, R., and Anderson, E. C., 1992, "Critical Evaluation of Two-Equation Models for Near-Wall Turbulence," *AIAA Journal,* Vol. 30, No. 2, pp. 324–331.

Speziale, C. G., So, R. M. C., and Younis, B. A., 1993, "On the Prediction of Turbulent Secondary Flows," *Proceedings of the International Conference on Near-Wall Turbulent Flows,* Tempe, Arizona, Mar. 15–17, pp. 105–114.

Su, M. D., and Friedrich, R., 1994, "Investigation of Fully-Developed Turbulent Flow in a Straight Duct with Large Eddy Simulation," ASME JOURNAL OF FLUIDS ENGINEERING, Vol. 116, No. 4, pp. 677–684.

Tatchell, D. G., 1975, "Convection Processes in Confined, Three Dimensional Boundary Layers," Ph.D. dissertation, Mechanical Engineering Department, Imperial College, London.

The Effect of Rotary Arms on Corotating Disk Flow

John Girard

Scott Abrahamson

Kevin Uznanski

Aerospace Engineering and Mechanics,
University of Minnesota,
110 Union St., S.E.,
Minneapolis, MN 55455

This investigation studied the impact of rotary style arms on the flow between corotating disks contained by a stationary cylindrical enclosure. Both ventilated and nonventilated hub configurations were considered. The particular geometry used represents a simplified model for common disk drives. Flow visualizations were performed over the Reynolds number range of 3.4×10^4 to 3.4×10^5. The arms were observed to dramatically alter the flow field and to produce an azimuthal pressure gradient throughout the flow field. The dominant feature of the flow between two disks was the arm wake. Moreover, an exchange of fluid across the shroud opening, which provided arm access, was observed. Arm effects became stronger as the arm tips were positioned closer to the hub. The combination of arms and radial through flow was studied over a similar Reynolds number range. In this case, the flow field remained dominated by arm effects, although some effects arising from the radial flow were observed.

Introduction

This investigation builds upon the current understanding of the flow structure associated with a disk drive geometry. Both particle transport and heat transfer effects are influenced by the physical constraints of various geometric components inside a disk drive. To date, flow studies have been performed in configurations having varying degrees of geometric simplification relative to production disk drives. This study focuses on the flow structure effects arising from two common elements found in disk drives: rotary arms and a ventilated hub. Hence, the objectives to this study are to explore the influence of a rotary arm obstruction on the global flow structure and to study the interaction between arm induced effects and those arising from radial flow through the ventilated hub. The radial through flow is driven by the pumping action of the rotating disks.

The simplest geometry relevant to disk drive flows consists of a rotating assembly of disks enshrouded by a stationary circular cylinder. This flow has been studied by several investigators and is summarized by Abrahamson et al. (1989) and Schuler et al. (1990). As characterized by Abrahamson et al. the flow structure consists of three distinct regions, each of which represents domination by different terms in the equations of motion. Flow in the inner region, which extends from the hub to approximately 75 percent of the disk radius, is dominated by the effects of rotation. The resulting flow rotates in solid body motion, exhibiting little or no motion relative to the spinning disks. In contrast the Shroud Boundary Layer region, extending from the shroud inward to approximately 90 percent of the disk radius, is dominated by viscous forces due to the no-slip condition on the wall. An outer region occupies the space between these two regions and represents a mixture of rotational and viscous effects. This interaction results in a circumferentially-periodic train of large, axially-aligned vortices, which are nearly uniform in size, approximately span the radial extent of the outer region, and rotate contrary to disk rotation. These vortical structures force the boundary separating the inner and outer regions to take the shape of a polygon.

The introduction of an arm between two disks modifies the flow field. Inside disk drives, the arm supports the read/write heads. The effects due to radially oriented arms has been investigated by Tzeng and Humphrey (1989), Abrahamson et al. (1989), and Usry et al. (1990). However, many manufacturers use a rotary style arm, which generates fewer wear particles. This investigation focuses on the effects due to rotary arms.

Ventilation (or perforation) of the hub assembly has been used in production disk drives with the objective of improving particulate filtration by enhancing global mixing. Ventilation permits radial flow through the rotating assembly in an effort to transport contaminants away from the region between the disks. Owen and Pincombe (1980), Abrahamson et al. (1991), and Humphrey et al. (1992), all used an external pump to drive the radial flow to study ventilation effects. In production disk drives, this flow is typically driven by the self-pumping action of the rotating disks. This configuration has been studied by Girard and Abrahamson (1993).

A study by Gor et al. (1993) measured the combined effects of hub ventilation and obstruction by a radially inserted arm using laser Doppler anemometry. Data were reported for various azimuthal locations.

Experimental Facility

A clear acrylic tank was used for this study. The rotating assembly consists of four glass disks and three spacer rings as shown in Fig. 1. The three spacer rings were either all solid or all perforated as described in Girard and Abrahamson (1993). A transparent cylindrical shroud enclosed the disk assembly.

Contributed by the Fluids Engineering Division for publication in the JOURNAL OF FLUIDS ENGINEERING. Manuscript received by the Fluids Engineering Division November 8, 1993; revised manuscript received January 10, 1994. Associate Technical Editor: J.A.C. Humphrey.

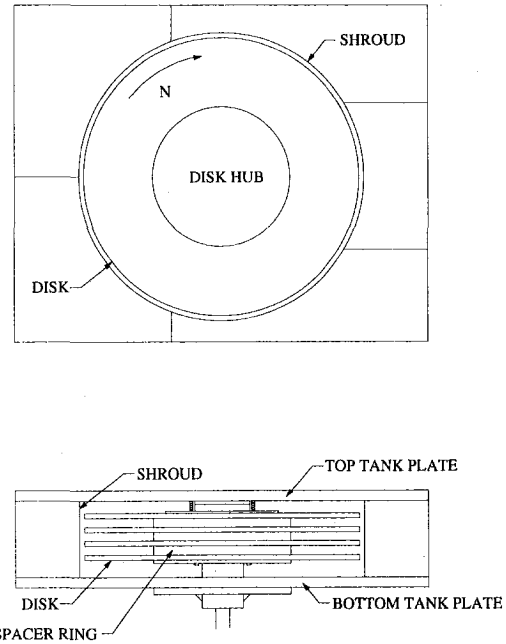

Fig. 1 Experimental apparatus

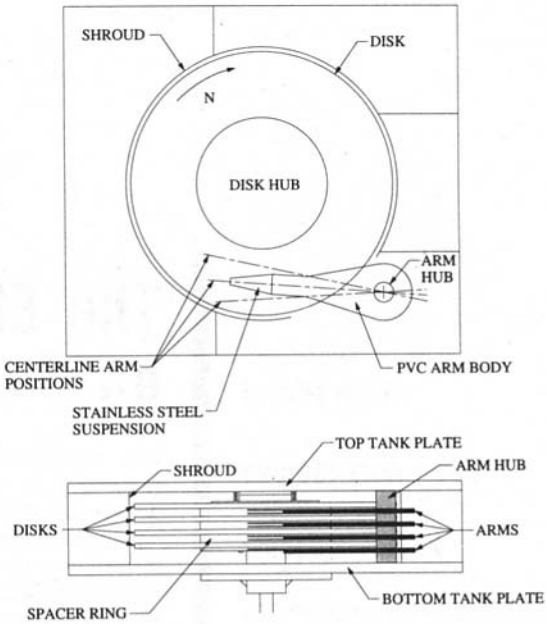

Fig. 2 Arm position and placement

Using the disk radius (254 mm) as a length scale, the hub radius is 0.5, the disk spacing is 0.0625 and the shroud radius is 1.031. Water is the working fluid.

The principle dimensionless parameter governing the fluid mechanics in a disk drive is the Reynolds number. The Reynolds number is $\mathrm{Re} = \Omega R^2/\nu$, where Ω is the rotational speed, R is the disk radius, and ν is the kinematic viscosity. For comparison, the Re for a production drive operating at approximately 25°C may be expressed in industry standard units as $\mathrm{Re} = 1.07ND^2$, where N is the rotational rate in rpm and D is the disk diameter in inches. A cylindrical coordinate system (r, θ, z) is used where r and z represent the radial and disk spin axis-aligned coordinates, respectively.

Two flow visualization studies were completed. A detailed explanation of the dye technique, which incorporates the pH indicator bromothymol blue, can be found in Abrahamson et al. (1989). The flow field motions were recorded on video tape.

The first study explored the effect of arms modeled after the rotary actuated arms found in many current disk drives. The body of each arm was made of PVC while the head suspensions were thin stainless steel plate. The suspensions modeled the fluid dynamic blockage of production suspensions, not the actual slider/suspension dynamics. Other arm attachments found in actual disk drives, such as the signal leads from the heads, were not modeled. To provide access for the arm assembly, the circular shroud has an opening of approximately 45 deg as shown in Fig. 2. The arm assembly consisted of four arms, one arm inserted into each interior disk gap and the fourth fit below the bottom disk. The axial blockage due to an arm was approximately 52 percent of the disk-to-disk spacing. The Re for this study ranged from 3.4×10^4 to 3.4×10^5.

A second study combined the effects of the arms and ventilation flow. The solid spacer rings were replaced with perforated rings to allow the disks to pump fluid through the rotating assembly. For this study, the Re ranged from 2.69×10^4 to 1.34×10^5.

Results and Discussion

The discussion below focuses on the impact of arms on the flow field with and without ventilation. Moreover, the arguments expand upon the description of the flow field by Abrahamson et al. (1989). A sketch of the resulting flow with rotary arms and no ventilation is shown in Fig. 3 and a frame from a flow visualization video recording is shown in Fig. 4. In general, arm effects become more pronounced with increased rotational rate (Re) and arm penetration toward the hub. Additionally, the visual periodicity observed in the simplified, axisymmetric configuration is no longer present.

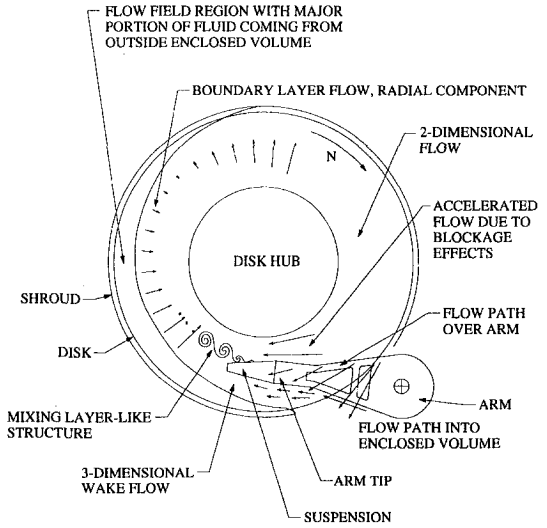

Fig. 3 Flow characteristics induced by rotary arm

As a consequence of the arm blockage, two regions in the flow field were observed to support coherent vortical structures where none were observed in the axisymmetric case. In the near hub region, vortices were observed infrequently, usually less than one structure present at any instant. In this region, a structure formed downstream of the arm tip, adjacent to the hub and rotated with the same sense as the disks. The structure became distorted or destroyed when accelerated through the converging channel formed between the arm and the hub (see Fig. 3). Video recordings revealed tangential slip of fluid relative to the disk surfaces in this region with the slowest flow upstream of the arms and the fastest flow between the arm tip and hub. The dependence of tangential velocity on θ indicated

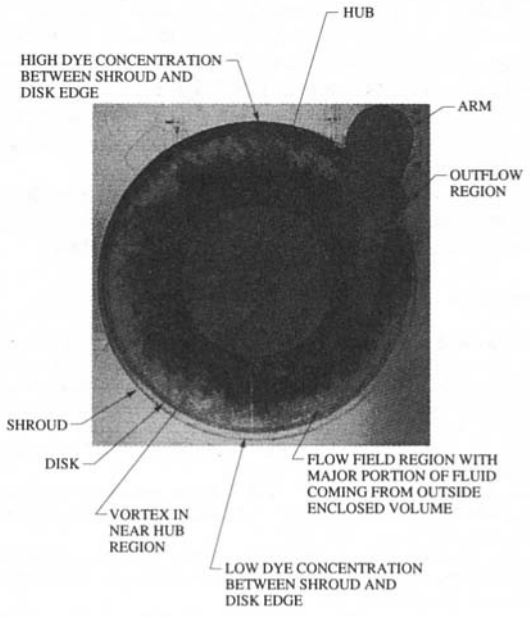

Fig. 4 Video frame of flow field at Re = 101000

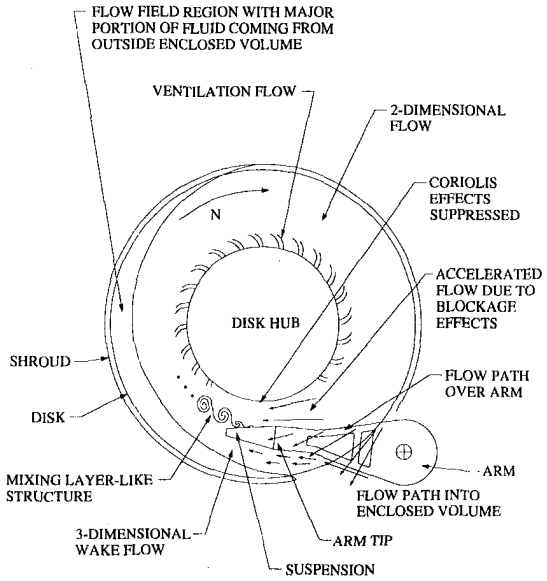

Fig. 5 Flow characteristics for combination of rotary arm and hub ventilation

an azimuthal pressure gradient existed. Furthermore, flow visualizations indicated arm blockage produced an azimuthal pressure gradient throughout the flow field with the highest pressure on the upstream side of the arm at large r.

The azimuthal pressure gradient caused a strong shear at the arm tip. Visually, a continuous train of vortices were observed emanating from the arm tip with vortex axes aligned with the disk spin axis. These structures rotated contrary to both disk rotation and near hub vortices. Physically, the large dynamic head at the outer radii in conjunction with the inclination of the arm axis relative to a radial line (see Fig. 2) provided a favorable pressure gradient along the upstream face of the arm. From the convergence of streamlines in the gap between the arm and hub, fluid was observed to accelerate toward the arm tip as depicted in Fig. 3. Along the downstream face of the arm, the flow was retarded due to blockage effects. The higher speed flow was observed to separate from the sharp corner at the tip, forming a separation line which rolled up into a mixing layer-like structure as shown in Fig. 3. The vortices grew in size and were observable downstream for approximately 150 deg before becoming indistinguishable from the arm wake. In contrast, fluid acceleration towards the tip was less pronounced for radially oriented arms (Abrahamson et al., 1991).

The previously described hub vortices were observed to form between sequential mixing layer vortices, so it is likely that the mixing layer vortices and their images inside the hub contribute to the formation of the hub vortices.

The outer region vortices observed in the axisymmetric, solid hub geometry were not observed when the arms were present. Indeed, the flow at radii previously described as the outer region was substantially different with arms present. The flow between the relatively low turbulence region near the hub and the shroud boundary layer region was dominated by the three-dimensional arm wake.

Since only a portion of the approaching flow to the arm gets diverted into the converging channel flow, the remaining portion travels between the arm and disk. The high pressure upstream and the low pressure downstream of the arm necessarily allowed this fluid to acquire significant momentum. Depending upon radius, the flow appeared to take one of two paths, with the dividing point not discernible. The portion nearer the hub forms the arm wake while the remainder was observed to leave the enclosed volume through the arm access port as shown in Fig. 4. To conserve mass, undyed fluid must enter the enshrouded volume. This fluid was observed to remain in the near shroud region as shown in Fig. 4. The character of the near shroud flow remained different for approximately 180 deg downstream of the arm access port. This makeup flow was complicated, but visualizations indicated the arms permitted considerable axial variation not observed in the axisymmetric case. If the axial gradients of the velocity outside the boundary layer were small, boundary layer theory (Lance and Rogers, 1962, Benton, 1966) would predict outward radial transport in the disk boundary layers. No dyed fluid from the wake was observed to enter the near shroud flow downstream of the arms. Therefore, radial transport in the disk boundary layers was concluded to be directed inward in this region, which suggested that near the disks the tangential velocity of the fluid must exceed local disk speed. In contrast, beyond the 180 deg point, dye reappeared in the near shroud region, which indicated a reversal in direction of the boundary layer radial flow. For disk drive manufacturers utilizing a peripheral filter located within 180 deg downstream of the arm access port, the above flow conditions would imply that fluid which enters the filter comes from outside the shroud and not from between the disks.

The wake of the arm was the principal cause of increased turbulence in the flow field. With arms present, the turbulence levels throughout the space between the disks were elevated in comparison to those observed in the axisymmetric geometry with either the solid or ventilated hub. The increased number of coherent vortical structures present in the flow field contributed less to the higher levels of turbulence. The rise in turbulence was observed through increased rates of dye neutralization. If the arm behaved as a bluff body, the wake flow would contain strong radial vorticity and form a trailing vortex street. None was observed. However, immediately downstream of the arm the wake flow exhibited three dimensional, turbulent characteristics. As the wake advanced, the three dimensional flow decayed toward a two dimensional flow due to rotational effects. Typically, this transition occurred by the time the wake entered into the last quarter sector upstream of the arm.

When the spacer rings at the hub are perforated, the flow in the axisymmetric geometry is modified. In the study of Girard and Abrahamson (1993), the radial flow through the hub

was driven into the interior disk gap by the pumping action of the disks. The flow field remained periodic. The ventilated flow dominated the region extending from the hub to approximately 70 percent of the disk radius. Tangential slip in this region required the ventilated flow to be entrained into the disk boundary layers and transported away from the region. The low turbulence fluid of the Inner region in the solid hub case was displaced radially outward beyond the region dominated by ventilated flow. The displaced Inner region remained a low turbulence region. Vortical structures were present in the outer region, but the number of structures increased relative to the solid hub flow at otherwise similar conditions. The radial extent of the outer region was reduced due to the displacement of the inner region.

The flow field which resulted from combining the rotary arms with hub ventilation was dominated by the effects due to the arms and is shown in Fig. 5. Many of the characteristics described above for the arms alone remained. Moreover, the arms influenced the ventilation flow. The distribution of the flow through the holes in the spacer ring was azimuthally nonuniform. In the region where arm blockage accelerated fluid in the flow field, no fluid was observed to enter the interior disk gap from the hub (see Fig. 5). Presumably, the elevated pressure caused by the arm overpowered the exiting ventilation flow. At all θ, the ventilation flow was insufficient to displace the comparatively low turbulence region adjacent to the hub.

Conclusions

The introduction of model arms between the disks significantly modifies the flow structure relative to that found in the axisymmetric geometry. The global flow structure between the corotating disks takes on a pronounced asymmetry and bears little resemblance to the inner and outer regions described by Abrahamson et al. (1989). The flow field turbulence levels are increased, largely due to the strong azimuthal pressure gradient across the arm. Arm position determined the extent of arm effects, with stronger flow field modifications observed as the arm tip is located closer to the hub. An important consequence of non-radially oriented arms is the modification to the direction of radial transport in the disk boundary layers. The boundary layer flow is no longer radially outward at all locations. Finally, fluid was observed leaving the enshrouded volume through the arm access port. The incoming flow through the same port formed into a region that remained adjacent to the shroud and which extended beyond the typical location of a peripheral filter.

Hub ventilation does not appear to influence the flow field effects attributed to the arms. On the contrary, arm effects suppressed ventilation flow in the vicinity of the arms.

References

Abrahamson, S., Koga D., and Eaton J., 1989, "The Flow Between Corotating Shrouded Disks," *Physics of Fluids A*, Vol. 1, No. 2, pp. 241–251.

Abrahamson, S., Chiang C., and Eaton J., 1991, "Flow Structure in Head-Disk Assemblies and Implications for Design," *Advances in Information Storage Systems*, Vol. 1, pp. 111–132.

Benton, E., 1966, "On the Flow Due to a Rotating Disk," *Journal of Fluid Mechanics*, Vol. 24, Part 4, pp. 781–800.

Girard, J., and Abrahamson, S., 1993, "On the Flow Structure Due to Corotating Disks With a Ventilated Hub," ASME JOURNAL OF FLUIDS ENGINEERING, Vol. 115, No. 3, pp. 408–410.

Gor, D., Humphrey, J., and Greif, R., 1993, "Ventilated Flow Between Corotating Disks with Large Obstructions," *Proceedings of ASME Winter Annual Meeting*, New Orleans, LA.

Humphrey, J., Schuler, C., and Iglesias, I., 1992, "Analysis of Viscous Dissipation in Disk Storage Systems and Similar Flow Configurations," *Physics of Fluids A*, Vol. 4, No. 7, pp. 1415–1427.

Lance, G. and Rogers, M., 1962, "The Axially Symmetric Flow of a Viscous Fluid Between Two Infinite Rotating Disks," *Proceedings of the Royal Society A*, Vol. 266, pp. 109–121.

Owen, J., 1988, "Air-Cooled Gas-Turbine Discs: A Review of Recent Research," *International Journal of Heat and Fluid Flow*, Vol. 9, No. 4, pp. 354–365.

Owen, J., and Pincombe, J., (1980), "Velocity measurements inside a rotating cavity with a radial outflow of fluid," *Journal of Fluid Mechanics*, Vol. 99, No. 1, pp. 111–127.

Schuler, C., Usry, W., Weber, B., Humphrey, J., and Greif, R., 1990, "On the flow in the unobstructed space between shrouded corotating disks," *Physics of Fluids A*, Vol. 2, No. 10, pp. 1760–1770.

Tzeng, H., and Humphrey, J., 1989, "Corotating disk flow in an axisymmetric enclosure with and without a bluff body," *Seventh Symposium on Turbulent Shear Flows*, Reynolds, W.C., ed., Stanford University, Stanford, CA.

Usry, W., Schuler, C., Humphrey, J. and Greif, R., 1990, "Unsteady Flow Between Corotating Disks in an Enclosure with an Obstruction," *Proceedings of the 5th International Symposium on Application of Laser Techniques to Fluid Mechanics*, Lisbon, Portugal.

Reinvestigation of Hot-Wire Anemometry Applicable to Subsonic Compressible Flows Using Fluctuation Diagrams

P. C. Stainback[1]
Senior Research Engineer,
Analytical Services and Materials, Inc.,
Hampton, VA 23666

K. A. Nagabushana[2]
Research Engineer,
ViGYAN, Inc.,
Hampton, VA 23666

Much has been written about the improbability and impossibility of obtaining solutions to the mean square equation for constant current anemometry in subsonic slip and transonic flows. For these flow conditions, the voltage across a heated wire mounted normal to the flow is a function of velocity, density, and total temperature. In principal, the fluctuations of these quantities can be measured; however, to date there are no known acceptable solutions to the mean square equation in these flow regimes. In this study, data presented in the 1950's by Spangenberg were used to compute the sensitivities of a heated wire to changes in velocity, density, and total temperature. These results indicated that there was a large region in the Nusselt number-Reynolds number or Nusselt number-Knudsen number regimes where the velocity and density sensitivities were different, a condition required for solutions to the mean square equation. A second necessary condition for a solution was also noted. The possible existence of a solution to the mean square equation was based on the evaluation of the condition number of the sensitivity matrix. The condition numbers obtained from Spangenberg's data were very large and near perfect data would be required to obtain accurate measurements of the fluctuations.

Introduction

Constant current anemometry (CCA) has been extensively used to measure fluctuations in incompressible and compressible flows (Stainback and Nagabushana, 1993; Laufer, 1961; Wagner and Weinstein, 1974). In compressible flow the heated wire is, in general, sensitive to changes in velocity, density, and total temperature and in principal the fluctuations of these quantities can be measured (Morkovin, 1956). In supersonic flow it was found experimentally that the mean voltage measured across a heated wire is only a function of changes in mass flow and total temperature (Kovasznay, 1950). Using this result for supersonic flow, Kovasznay developed a graphical technique for determining fluctuations of mass flow, total temperature, and their correlation (Kovasznay, 1953). Very few attempts have been made to measure fluctuations in subsonic compressible flow using a CCA because of the complexity that exists when the heat transfer from the wire is a function of three independent variables.

Some efforts were made to measure fluctuations in subsonic compressible flow using a constant temperature anemometer (CTA). For these investigations, a three-wire probe was used and the voltages across the wires were digitized. A system of three equations was solved to obtain the instantaneous changes in velocity, density, and total temperature as a function of time. Statistical techniques were then used to obtain fluctuations and correlations of interest (Jones and Stainback, 1988).

For compressible flow, where the wire is sensitive to velocity, density, and total temperature, equations for CCA are usually derived using mean square values. This results in a single equation with six unknowns. Much has been written about the improbability (Morkovin, 1956) and impossibility (Demetriades, 1978) of obtaining solutions to this mean square equation. Solution to this equation requires that the velocity and density sensitivities of the heated wire be sufficiently different. In this report, data published by Spangenberg (1955) were used to show that there exist a large region in the Nusselt number-Reynolds number or Nusselt number-Knudsen number regimes where the velocity and density sensitivities appeared to be sufficiently different to permit suitable solutions to the mean square equation. It was further shown that solutions were possible only when the velocity and density sensitivities were nonlinearly related in a specific manner. Again Spangenberg's data were used to show that this second condition can often be satisfied, further indicating that solutions to the mean square equation are possible. In the final analysis, the condition numbers for the sensitivity matrix were used to further evaluate the possible existence of solutions to the mean square equation.

Spangenberg's Data

Spangenberg's data were presented in terms of $\mathrm{Nu}_\infty = f(\mathrm{M}, \rho, \tau_w)$ for T_0 = constant. Data were presented for several wire diameters and wire lengths. The data considered herein were obtained using a Pt-10 percent Rh wire of diameter 0.00015 in. and a length of 2.80 mm. Data were limited to the following conditions:

$$0.05 < \mathrm{M} < 0.95$$

$$0.0004 < \rho, \mathrm{gm/cm^3} < 0.0012$$

$$0.221 < \tau_w < 2.192$$

The Nusselt numbers presented were corrected for heat loss to the supports of the wire. This corrected Nusselt number, Nu_∞, is suitable for comparing heat transfer results from different experiments using different wire materials and different ratios of l/d. For computing fluctuations, the sensitivities of the wire

[1] Currently Distinguished Research Associate, NASA Langley Research Center, Hampton, VA 23681.

[2] Currently Research Associate, Old Dominion University Research Foundation, Norfolk, VA 23508.

Contributed by the Fluids Engineering Division for publication in the JOURNAL OF FLUIDS ENGINEERING. Manuscript received by the Fluids Engineering Division September 25, 1993; revised manuscript received August 30, 1994. Associate Technical Editor: D. Stock.

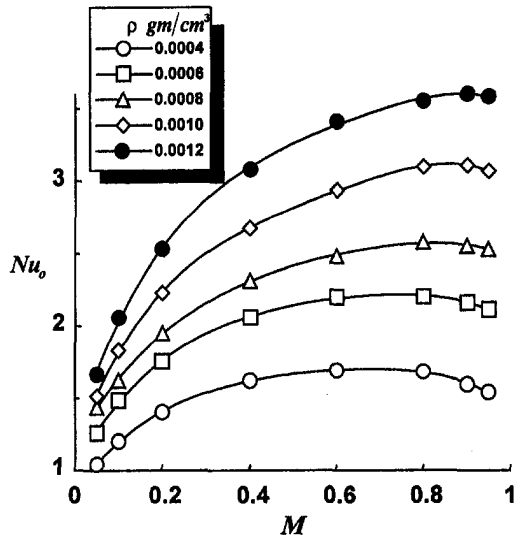

Fig. 1 Example of Spangenberg's data; Nu_0 versus M for $\tau_w = 1.696$

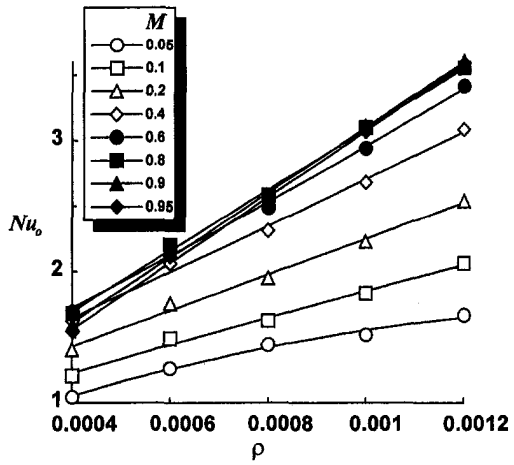

Fig. 2 Example of Spangenberg's data; Nu_0 versus ρ for $\tau_w = 1.696$

must be obtained using the uncorrected Nusselt number, Nu_0. For the results presented herein, Nu_∞ values were converted to Nu_0 values using the inverse of the method presented by Spangenberg.

Examples of Spangenberg's data are presented in Figs. 1–3. In Fig. 1 the uncorrected Nusselt number is presented as a function of Mach number for various values of density for a given value of τ_w. The Nusselt number increased rapidly with Mach number at very low values. The slopes of the curves decreased somewhat as the Mach number increased. At the higher Mach numbers ($0.6 < M < 0.95$) the Nusselt number often reached a peak prior to decreasing. This variation of Nu_0 with M at the higher Mach numbers often resulted in zero or negative slopes. The Mach numbers at which the slopes of the curves reach zero increased with increasing density. This variation was also observed in the data presented by Baldwin (1958) and Nagabushana et al. (1994). Polynomials were used to fit curves to the data from which the required derivatives were obtained. A fourth degree equation was required to obtain "good" fits. The variation of Nu_0 with ρ, shown in Fig. 2, is monotonically increasing with increasing density. A second degree equation was used to fit curves to the Nu_0 versus ρ data.

The variation of Nusselt number with respect to τ_w is presented in Fig. 3 and this variation of Nu_0 is rather complex and nonlinear. The Nusselt number often increased then decreased with increasing values of τ_w. A closer look at Nu_0 versus τ_w data revealed that, for most of the data, the values of Nu_0 decreased from $0.629 \leq \tau_w \leq 1.629$ but most often increased or tended to increase from $1.629 \leq \tau_w \leq 2.192$. This variation of

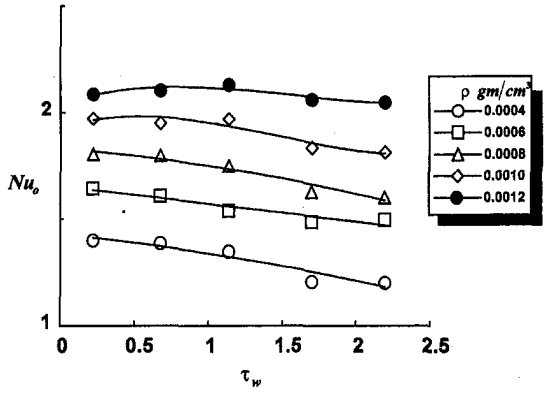

Fig. 3 Example of Spangenberg's data; Nu_0 versus τ_w for M = 0.1

Nomenclature

a, b, c, and d = constants in Eq. (A-4)
A = quantity given by Eq. (5)
c_p = specific heat at constant pressure
c_v = specific heat at constant volume
d = wire diameter
e' = fluctuating voltage across the sensor
E_w = mean voltage across sensor
f, g, h = constants in Eq. (A-4)
I_w = current through the wire
$K = \partial \log T_w / \partial \log R_w$
Kn = Knudsen number
l = wire length
M = Mach number
Nu_∞ = Nusselt number based on free stream temperature
Nu_0 = Nusselt number based on 0°C
q = sensitivity ratio = S_u/S_{T_0}
Re = Reynolds number
R_w = resistance of wire
s = sensitivity ratio = S_ρ/S_{T_0}
S_u = velocity sensitivity
S_ρ = density sensitivity
S_{T_0} = total temperature sensitivity
T = temperature
T_0 = total temperature
u = velocity
$\epsilon = -(\partial \log I_w / \partial \log R_w)$
$\alpha = \left(1 + \frac{\gamma - 1}{2} M^2\right)^{-1}$
η = recovery temperature ratio, T_{adw}/T_0
θ = temperature parameter, T_w/T_0
γ = specific heat ratio, c_p/c_v
ρ = density
τ_w = temperature loading parameter, $(T_w - T_{adw})/T_0$
ϕ' = normalized fluctuation voltage ratio = $(e'/E_w)/S_{T_0}$

Subscript and Superscript

adw = adiabatic wall condition
w = wire condition
∞ = free stream or static condition
$'$ = instantaneous value
$\bar{(\ )}$ = mean value

Nu_0 over this later interval of τ_w was present in about 80 percent of the data and had a profound effect on the relationship between the velocity and density sensitivities. It is not known if this variation can be supported by the limited amount of data available. If third degree curves were fitted to the data, there were significant changes in the derivatives for most of the data at the higher values of τ_w. Because of these changes, the values of Nu_0 were fitted to values of τ_w using both second and third degree equations. The results obtained using these two curve fits on the variation of the velocity and density sensitivities will be presented subsequently.

Data presented by Baldwin also showed a similar variation of the Nusselt number with τ_w. This complex and nonlinear variation of Nusselt number with τ_w or overheat is probably the reason that solutions to the mean square equation for CCA might exist.

In general, the scatter in the values of Nu_0 with respect to M and ρ were acceptably small; the apparent scatter of Nu_0 with respect to τ_w was somewhat larger. This was probably due to the relatively small change in Nu_0 with respect to τ_w or the limited number of values of τ_w that were available.

Theoretical Considerations

Because of the manner in which Spangenberg presented his data, equations must be derived for the change in voltage across the wire in terms of the sensitivity of the wire to changes in velocity, density, and total temperature. For the present case the sensitivities can be obtained using the method described by Anders (1974) and the independent variables used by Spangenberg. For CCA they are given by:

$$\frac{e'}{E_w} = S_u \frac{u'}{u} + S_\rho \frac{\rho'}{\rho} - S_{T_0} \frac{T_0'}{T_0} \tag{1}$$

$$S_u = \frac{A}{\alpha}\left[\frac{\partial \log Nu_0}{\partial \log M} - \frac{\eta}{\tau_w}\frac{\partial \log \eta}{\partial \log M}\left(\frac{\partial \log Nu_0}{\partial \log \tau_w} + 1\right)\right] \tag{2}$$

$$S_\rho = A\left[\frac{\partial \log Nu_0}{\partial \log \rho} - \frac{\eta}{\tau_w}\frac{\partial \log \eta}{\partial \log \rho}\left(\frac{\partial \log Nu_0}{\partial \log \tau_w} + 1\right)\right] \tag{3}$$

$$S_{T_0} = A\left[-\frac{1}{2\alpha}\frac{\partial \log Nu_0}{\partial \log M} + \frac{\eta}{\tau_w}\left(\frac{\partial \log Nu_0}{\partial \log \tau_w} + 1\right) \times \left(\frac{1}{2\alpha}\frac{\partial \log \eta}{\partial \log M} - 1\right) - \frac{\partial \log Nu_0}{\partial \log \tau_w}\right] \tag{4}$$

where

$$A = \frac{(1-\epsilon)}{\left[(1-2\epsilon) - \dfrac{\theta K}{\tau_w}\left(\dfrac{\partial \log Nu_0}{\partial \log \tau_w} + 1\right)\right]} \tag{5}$$

For Spangenberg's data η varied with M and plots of η versus M were presented in his report. The values for first and second degree temperature – resistance coefficient for the wire material were also presented. Therefore, after the partial derivatives in Eqs. (2)–(5) were determined the sensitivities to changes in u, ρ, and T_0 could be calculated.

The Partial Derivatives and Sensitivities

Spangenberg's data were measured and tabulated in a form that is necessary to obtain the partial derivatives of the dependent variable with respect to one independent variable while holding the remaining independent variables constant. These are the only data known to the authors where measurements were obtained in this necessary manner. For the present report, polynomials were used to fit the data to obtain the desired derivatives of Nu_0 with respect to the independent variables.

Table 1 Possible solutions to mean square equation for CCA

$$\overline{\phi'^2} = q^2\overline{\left(\frac{u'}{u}\right)^2} + [f(q)]^2\overline{\left(\frac{\rho'}{\rho}\right)^2} + \overline{\left(\frac{T_0'}{T_0}\right)^2} + 2qf(q)\frac{\overline{u'\rho'}}{u\rho} - 2q\frac{\overline{u'T_0'}}{uT_0} - 2f(q)\frac{\overline{\rho'T_0'}}{\rho T_0}$$

$$s = f(q) = a + bq^f + cq^g + dq^h$$

f	g	h	Terms in q	
f	1	0	$q^{2f}; q^{f+1}; q^f; q^2; q^1; q^0$	$f = 3, 4, 5, \ldots$ $f = -2, -3, -4, \ldots$
f	0	0	$q^{2f}; q^{f+1}; q^f; q^2; q^1; q^0$	$f = 3, 4, 5, \ldots$ $f = -2, -3, -4, \ldots$
f	1	0	$q^{2f}; q^{f+1}; q^f; q^2; q^1; q^0$	f = noninteger values $1 < f$
f	0	0	$q^{2f}; q^{f+1}; q^f; q^2; q^1; q^0$	f = noninteger values $1 < f$
f	1	0	$q^{2f}; q^{f+1}; q^f; q^2; q^1; q^0$	$0 < f < 1$ $f \neq 0.5$
f	0	0	$q^{2f}; q^{f+1}; q^f; q^2; q^1; q^0$.	$0 < f < 1$ $f \neq 0.5$

The degree of the polynomial was chosen to give the "best fit" to the data.

After the partial deviates were determined, the sensitivities were obtained using Eqs. (2)–(5). In general,

$$S_u : S_\rho : S_{T_0} = f(M, \rho, \tau_w) \tag{6}$$

Plots of the sensitivities are not presented since it will be shown subsequently that the ratios S_u/S_{T_0} and S_u/S_{T_0} are the important parameters for the present study.

The Mean Square Equation

In the past hot wire data, using a CCA, were obtained from mean square values. Following Kovasznay, squaring Eq. (1), dividing by $S_{T_0}^2$, and taking the mean gives:

$$\overline{\phi'^2} = q^2\overline{\left(\frac{u'}{u}\right)^2} + s^2\overline{\left(\frac{\rho'}{\rho}\right)^2} + \overline{\left(\frac{T_0'}{T_0}\right)^2} + 2qs\frac{\overline{u'\rho'}}{u\rho} - 2q\frac{\overline{u'T_0'}}{uT_0} - 2s\frac{\overline{\rho'T_0'}}{\rho T_0} \tag{7}$$

The above equation is an equation for an elliptic hyperboloid and, following Kovasznay fluctuation diagram technique, the fluctuation diagram exists on the surface of the hyperboloid. Equation (7) is a single equation in six unknowns, (i.e., $\tilde{u}/u$, $\tilde{\rho}/\rho$, $\tilde{T}_0/T_0$, $(\overline{u'\rho'/u\rho})$, $(\overline{u'T_0'/uT_0})$, $(\overline{\rho'T_0'/\rho T_0})$). Since ϕ'^2, q and s are functions of the overheat of the wire, one can, in principal, operate a single wire at six overheats and solve a system of six equations for the fluctuations and their correlations. The unsuccessful attempts that were made in the past to obtain solutions in this manner were thought to be due to the mean flow calibrations not being accurate enough or the sensitivities not being sufficiently different to permit accurate solutions (Morkovin). Demetriades stated that no solutions to Eq. (7) are possible unless the independent variable occurs at least to the fifth power. It is shown in the Appendix that if s is assumed to be a function of q, solutions to Eq. (7) are possible if, after substituting the functional relationship for s into the equation, the resulting equation has six terms. This result requires that values for s have very restrictive, nonlinear variations with respect to q as the overheat of the wire is changed. Table 1 presents conditions where solutions to Eq. (7) exist based on s being a simple, finite, power series of q.

Figure 4 is presented to show to what extent $q \neq s$ for $\tau_w = 2.192$. From the figure it can be seen that both q and s are negative and $|s|$ is, in general, greater than $|q|$. The difference can be large since q can often approach zero at higher values of M. This is due to $\partial \log \mathrm{Nu}_0/\partial \log \mathrm{M}$ being equal to zero or negative at the higher Mach number and for these conditions it is possible for $S_u = 0$ where the wire is not sensitive to changes in velocity. At higher values of M the sign of q could change and positive values are not presented in the figure.

Morkovin gave the following equation for the Knudsen number:

$$\mathrm{Kn} = \frac{7.75 \times 10^{-9}}{\rho d} \tag{8}$$

where ρ is in gm/cm^3 and d is in cm. Using this equation, the value for the Knudsen number for the present data ranged from 0.017 to 0.051. Stadler et al. (1951) suggest that continuum flow occurs for $\mathrm{Kn} < 0.001$ and slip flow occurs for $0.001 \leq \mathrm{Kn} \leq 2$. Other references suggest that continuum flow occurs for $\mathrm{Kn} < 0.01$. These quoted boundaries are not sharply defined, and if it is assumed that slip flow occurs for $\mathrm{Kn} > 0.01$, all of Spangenberg's data considered herein is in the slip flow regime where $S_u \neq S_\rho$. This result is in agreement with the data presented in Fig. 4 where $S_u/S_{T_0} \neq S_\rho/S_{T_0}$. However, a few data points do approach $S_u/S_{T_0} = S_\rho/S_{T_0}$.

Calibration data for several wires were obtained in a small calibration facility at the Langley Research Center (Nagabushana et al., 1994) using a constant temperature anemometer. These data were used to compare the wire sensitivities over a flow range similar to the one investigated by Spangenberg. Results from this study is presented in Fig. 5 and reveal that for a range of flow conditions $|s| > |q|$. Even though there is little one-to-one comparison that can be made between these data and Spangenberg's results, the general results are in good agreement.

Solution to Mean Square Equation

Solutions to Eq. (7) can be obtained by using the method of least squares. Applying this method results in the following matrix equation:

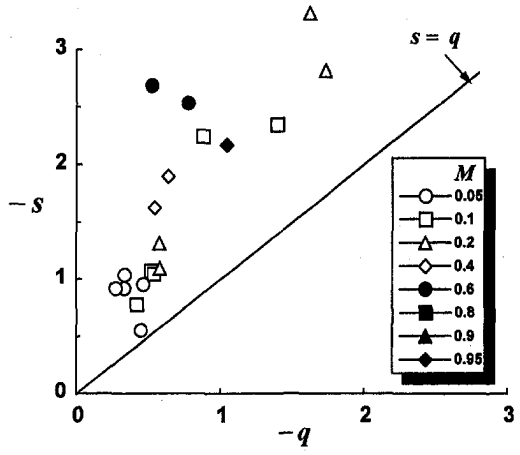

Fig. 4 Density sensitivity ratio, s versus velocity sensitivity ratio, q for $\tau_w = 2.192$; (Spangenberg's data)

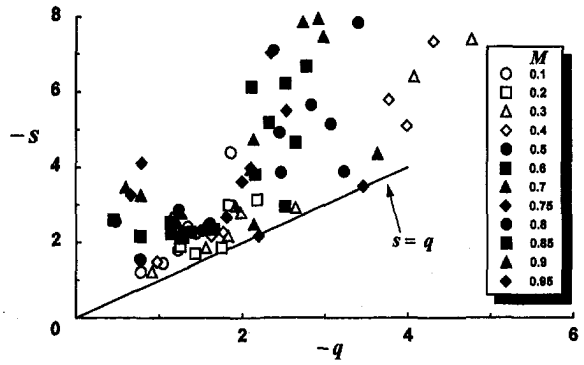

Fig. 5 Density sensitivity ratio, s versus velocity sensitivity ratio, q for $T_0 = 80°\mathrm{F}$; (Nagabushana et al. data)

$$\begin{vmatrix} \sum q^4 & \sum q^2 s^2 & \sum q^2 & \sum sq^3 & \sum q^3 & \sum q^2 s \\ & \sum s^4 & \sum s^2 & \sum qs^3 & \sum qs^2 & \sum s^3 \\ & & n & \sum qs & \sum q & \sum s \\ & & & \sum q^2 s^2 & \sum q^2 s & \sum qs^2 \\ & & & & \sum q^2 & \sum sq \\ & & & & & \sum s^2 \end{vmatrix} \times \begin{vmatrix} \overline{(u'/u)^2} \\ \overline{(\rho'/\rho)^2} \\ \overline{(T_0'/T_0)^2} \\ 2\overline{\frac{u'}{u}\frac{\rho'}{\rho}} \\ -2\overline{\frac{T_0'}{T_0}\frac{u'}{u}} \\ -2\overline{\frac{\rho'}{\rho}\frac{T_0'}{T_0}} \end{vmatrix} = \begin{vmatrix} \sum q^2\overline{\phi'^2} \\ \sum s^2\overline{\phi'^2} \\ \sum \overline{\phi'^2} \\ \sum qs\overline{\phi'^2} \\ \sum q\overline{\phi'^2} \\ \sum s\overline{\phi'^2} \end{vmatrix} \tag{9}$$

In Eq. (9) q, s, and $\overline{\phi'^2}$ are functions of the overheat parameter, τ_w. Solutions to Eq. (9) can be obtained as follows. Obtain a set of values for q, s, and $\overline{\phi}$ for a suitable number of τ_w values, say 10 or 12. Fit suitable curves to q and ϕ'^2 versus τ_w. Also obtain curve fits for $s = f(q)$ that satisfies the requirements noted in the Appendix to determine if a solution to Eq. (9) is possible. The "best curve fit" to these data can be used to relate s to q and ultimately s and τ_w. Using the equations obtained for q, s, and ϕ'^2 versus τ_w, compute a set of values, say 20, to be used in Eq. (9) to obtain the fluctuations and their correlations.

An additional datum point can be obtained for s and q by using the limiting values for these variables. These equations are:

$$q = -\frac{1}{\alpha}\frac{\dfrac{\partial \log \eta}{\partial \log \mathrm{M}}}{\left(\dfrac{1}{2\alpha}\dfrac{\partial \log \eta}{\partial \log \mathrm{M}} - 1\right)}; \quad \tau_w = 0 \tag{10}$$

$$s = -\frac{\dfrac{\partial \log \eta}{\partial \log \rho}}{\left(\dfrac{1}{2\alpha}\dfrac{\partial \log \eta}{\partial \log \mathrm{M}} - 1\right)}; \quad \tau_w = 0 \tag{11}$$

No fluctuating voltages were presented by Spangenberg, therefore, no fluctuating quantities could be calculated. His data were used to obtain relationships between q and s, to calculate the elements of the matrix in Eq. (9), and to obtain the condition

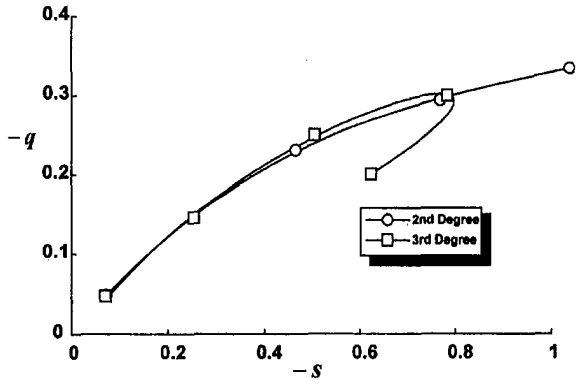

Fig. 6 Example of s versus q for M = 0.05 and ρ = 0.0004 gm/cm³ for variable τ_w; (Spangenberg's data)

numbers for these matrices. An indication of the accuracy and suitability of results expected from solution to Eq. (9) were obtained by computing the condition number (Strang, 1976) for the 6 × 6 matrix. Higher accuracy can be expected from calculated results if the condition numbers are small.

Examples of the variation of s with q obtained from Spangenberg's data for variable τ_w are presented in Fig. 6. The case where the Nusselt number was assumed to be a cubic relationship with respect to τ_w most often resulted in a hairpin like variation of s with q. This type of variation does not appear reasonable. A curve is also presented in the figure where Nu_0 was assumed to be given by a second degree equation. This assumption resulted in a more reasonable variation of s with q. It must be noted that the behavior obtained with the cubic curve fit might be due to the limited amount of data available.

There were several sets of data where Nu_0 could be fitted with a cubic equation with respect to τ_w without the derivative of Nu_0 increasing at the higher values of τ_w. Examples of data for these cases are presented in Fig. 7. The powers of q presented in Table 1 was used to fit the $s - q$ data, and the powers that gave the "best curve fit" to the data are presented in the Table 2. Most of the curves fitted to the data appear to be good based on the R^2 values except for the case M = 0.60. The equations with these powers were used to relate s to q and in turn to τ_w. Twenty values for q were selected, the values for s computed, and the elements for the 6 × 6 matrix in Eq. (9) calculated. Using the elements of the matrix, the condition numbers for the cases presented in Fig. 7 were determined and these results are presented in the Table 2. These large condition numbers indicate that the 6 × 6 matrix in Eq. (9) is very ill conditioned. It is not known if these results are general or limited to the cases investigated which has a limited number of overheats. Thus, it

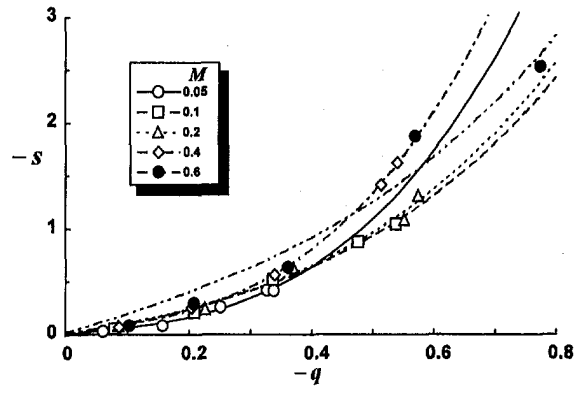

Fig. 7 s versus q for various Mach numbers and ρ = 0.0012 gm/cm³ for variable τ_w; (Spangenberg's data)

Table 2 Possible solutions to mean square equation for CCA based on Spangenberg's data

M	ρ gm/cm³	f	g	h	R^2	$q_{min} \le q \le q_{max}$ condition number
0.05	0.0012	3.0	1	0	0.9936	1.97×10^7
0.10	0.0012	3.0	1	0	0.9966	2.92×10^8
0.20	0.0012	3.0	1	0	0.9933	1.92×10^8
0.40	0.0012	3.0	1	0	0.9997	1.09×10^7
0.60	0.0012	3.0	1	0	0.9718	6.54×10^8

appeared that the necessary condition for a solution to the mean square equation has been established i.e., $S_u \neq S_\rho$ and the required variation of s with respect to q could be obtained. However, the large condition numbers of the matrix indicated that even with near perfect data, large error would occur for any measurement of the fluctuations.

There are several possible reasons for the large condition numbers. Equations (10) and (11) show that s and q, in general, cannot be zero at the same time. This means that the condition required to obtain the total temperature fluctuations do not lie on the curve defined by $s = f(q)$. Therefore, the total temperature fluctuations must be obtained by extrapolation to the condition where $q = s = 0$. This condition is not determined by the accuracy of the mean flow calibration data but by the relationships used to obtain Eq. (7). This problem is not limited to the subsonic compressible flow case, but could also exist in supersonic flow if $\partial \log \eta / \partial \log \mathrm{Re} \neq 0$. In supersonic flow an extrapolation would be required in two-dimensional space, whereas in subsonic flow the extrapolation must be in three-dimensional space. Extrapolation of nonlinear functions in three-dimensional space could result in highly inaccurate solutions.

In subsonic slip and transonic flows, the values of s are, in general, larger in absolute magnitude than those for q. Both of these quantities approach small limiting values as the overheat of the wire approaches zero. However, except for very low densities, the limiting values for s are smaller in magnitude than those for q as the overheat approaches zero. Because of this, there is a range of overheats in the vicinity of zero where q and s are approximately equal and the locus of points for q and s in the $q - s$ plane crosses the $q = s$ line. Thus, the mean square equation reduces from the case of a single equation with six unknowns to a single equation with three unknowns. In other words, as the overheat is reduced, the mean square equation degenerates from a three-dimensional to a two-dimensional problem. This could result in an inability of the equation to give accurate results.

After the wire is calibrated, sensitivities are obtained, and the RMS and mean voltage measured across the wire, the search for a possible solution to the mean square equation becomes one of geometry. The values for q, s, and the corresponding values of ϕ in three-dimensional space must be used to define the hyperboloid from which the fluctuations and their correlations must be determined since the fluctuation diagram lies on its surface. In general, hot-wire anemometry can obtain values for q and s in only one quadrant of the $q - s$ plane as the overheat of the wire is changed, and the hyperboloid must be determined from this limited amount of data. Table 2 shows that attempts to do this resulted in matrices with large condition numbers indicating that even with near perfect data any fluctuations obtained would be subject to large errors. These errors might be reduced if additional information could be obtained.

Is there a reasonable method that can be developed to supply additional information to define more accurately the hyperboloid, thereby producing more accurate solutions to the mean square equation? The mean square equation is the general equation for an hyperboloid which means that the hyperboloid is

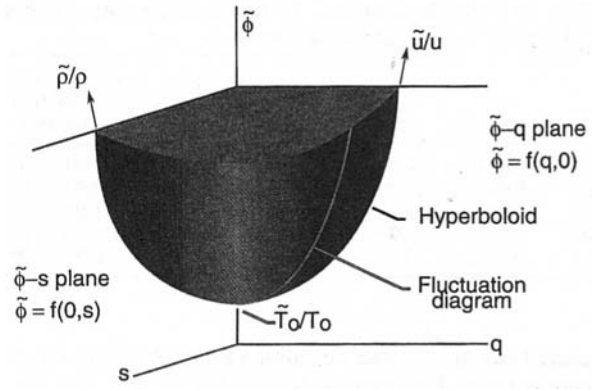

Fig. 8 General fluctuation diagram for subsonic compressible flow; $S_u \neq S_\rho$

not symmetric with respect to the ϕ-axis. If a rotation and translation of the axes are performed the hyperboloid will be symmetric with respect to the new coordinate system. The hyperboloid so obtained has an elliptic cross section that can be transformed into a circle which would result in the surface being a hyperboloid of revolution. The initial data obtained from the calibration of the heated wire and the measured mean and RMS voltage can be used to compute the fluctuations and their correlations. Using these values, the rotation, translation, and transformation of the q and s values can be performed. The values for ϕ would be unchanged. Since the surface in the new coordinate system is a hyperboloid of revolution, new values for q and s with the corresponding values of ϕ can be assumed to exist in all quadrants. Using a backward transformation, additional values for q and s can be computed and a new set of fluctuations and their correlations can be calculated. The above method can be repeated until suitable results are obtained.

As noted before, there were no fluctuating voltages given by Spangenberg. Because of this the above noted method could not be applied. However, by assuming values for the fluctuations and their correlations, a rough evaluation of the method was made. The values of q and s presented in Fig. 7 were used in this evaluation. The results indicated that the condition number for the 6×6 sensitivity matrix could be reduced from about 10^7 to $10^2 - 10^3$. Even though these latter condition numbers were obtained from an approximate analysis, the reduction of the condition numbers appeared to be encouraging enough to suggest that some effort should be expended to re-investigate the application of CCA to subsonic slip and transonic flows. Solutions obtained using the above method would require a trial and error solution, which insures that the solutions would converge.

Articles have been published (Stainback and Nagabushana, 1991, 1993, 1994; Stainback et al., 1992; Zinov'ev and Lebiga, 1988) that describe in detail the fluctuation and mode diagrams for transonic and subsonic slip flows under the assumption that there were solutions to Eq. (9). These studies revealed that the fluctuation diagram exists on the surface of a hyperboloid as illustrated in Fig. 8. The velocity fluctuation can be obtained from the intersection of hyperboloid with the $\phi - q$ plane and density fluctuation from the intersection with the $\phi - s$ plane. The total temperature fluctuation can be obtained from $s = q = 0$. Examples of mode diagrams were also presented for conditions where a single mode existed.

Concluding Remarks

From the present study of hot-wire anemometry for a constant-current anemometer applicable to subsonic compressible and subsonic slip flows, the following concluding remarks can be made:

- Based on Spangenberg's data and the data from current on going work, there appears to be a wide range of M and Kn available where a solution to the mean square equation for constant current hot-wire anemometry in subsonic flow might be possible based on the fact that $S_u \neq S_\rho$.
- It was shown that the mean square equation for CCA has possible solutions provided that the functional relationship which adequately relates s to q when substituted into the equation results in only six terms. Again Spangenberg's data were used to show that this condition can often be satisfied.
- The application of the method of least squares to the mean square equation resulted in a 6×6 matrix that was very ill-conditioned for the data used. This result indicated that near perfect data would be require to reduce large errors in the measured fluctuation.
- Several possible reasons for the large condition numbers were presented. First, it is necessary to extrapolate the data in three-dimension space to $q = s = 0$ to obtain the total temperature fluctuations. Second, the fact that q and s approach almost equal values in the vicinity of $q = s = 0$ results in a degeneracy of the system of equations. Finally, and most important, hot wire anemometry can furnish data for the evaluation of q and s in only one quadrant and attempts to define a three-dimensional surface from this limited amount of data apparently cannot result in the accurate calculation of fluctuations and their correlations.
- A method was proposed which might be used to reduce the condition number of the 6×6 sensitivity matrix, thereby permitting suitable solution to be obtained for the mean square equation.

Acknowledgment

The authors acknowledge the support of this research by National Aeronautics and Space Administration under contracts NAS1-19320 and NAS1-19672/NAS1-18585/NAG1-1552 respectively.

References

Anders, J. B., Jr., 1974, "Turbulence Measurements in Hypersonic Helium Flow," Report 1157, Gas Dynamics Laboratory, Princeton University, Princeton, NJ.

Baldwin, L. V., 1958, "Slip-Flow Heat Transfer From Cylinders in Subsonic Airstreams," NACA-TN-4369.

Demetriades, A., 1978, "Probes for Multivariant Flow Characteristics," *Proceedings of the Dynamic Flow Conference on Dynamic Measurements in Unsteady Flows,* IMST, Marseilles, France, pp. 13–44.

Jones, G. S., and Stainback, P. C., 1988, "A New Look at Wind Tunnel Flow Quality for Transonic Flows," SAE 881452 Aerospace Technology Conference and Exposition, Anaheim, CA.

Kovasznay, L. S. G., 1950, "The Hot-Wire Anemometer in Supersonic Flows," *Journal of the Aeronautical Sciences,* Vol. 17, No. 9, pp. 565–584.

Kovasznay, L. S. G., 1953, "Turbulence in Supersonic Flow," *Journal of the Aeronautical Sciences,* Vol. 20, No. 10, pp. 657–674.

Laufer, J., 1961, "Aerodynamic Noise in Supersonic Wind Tunnels," *Journal of the Aerospace Sciences,* pp. 685–692.

Morkovin, M. V., 1956, "Fluctuations and Hot-Wire Anemometry in Compressible Flows," AGARDograph 24.

Nagabushana, K. A., Stainback, P. C., and Jones, G. S., 1994, "A Rational Technique for Calibrating Hot-Wire Probes in Subsonic to Supersonic Speeds," AIAA-94-2536, AIAA 19th Aerospace Ground Test Conference, Colorado Springs, CO.

Spangenberg, W. G., 1955, "Heat Loss Characteristics of Hot-Wire Anemometers at Various Densities in Transonic and Supersonic Flows," NACA-TN-3381.

Stadler, J. R., Goodwin, G., and Creager, M. O., 1951, "A Comparison of Theory and Experiment for High-Speed Free-Molecule Flow," NACA Rep. 1032 (Supersedes NACA-TN-2244).

Stainback, P. C., and Nagabushana, K. A., 1991, "Fluctuation Diagrams for Hot Wire Anemometry in Subsonic Compressible Flows," NASA-CR-189580.

Stainback, P. C., and Nagabushana, K. A., 1993, "*Invited Paper:* Review of Hot-wire Anemometry and the Range of their Applicability," FED-Vol. 167, pp. 93–134, *Third International Symposium on Thermal Anemometry* ASME Fluids Engineering Division Summer Meeting, Washington, DC, June 20–24.

Stainback, P. C., and Nagabushana, K. A., 1994, "Hot-Wire Anemometry in Subsonic Slip and Transonic Flow Regimes," AIAA-94-2535, AIAA 19th Aerospace Ground Test Conference, Colorado Springs, CO, July 20–23.

Stainback, P. C., Nagabushana, K. A., and Bushnell, D. M., 1992, "Mode Diagrams for Hot Wire Anemometry in Subsonic Flows," International Conference on Methods of Aerophysical Research, organized by Institute of Theoretical and Applied Mechanics (ITAM) of the Siberian Division of the Russian Academy of Sciences, Novosibirsk, Russia, Aug. 31–Sept. 4.

Strang, G., 1976, *Linear Algebra and its Application,* Academic Press.

Wagner, R. D., and Weinstein, L. M., 1974, "Hot-Wire Anemometry in Hypersonic Helium Flow," NASA-TN-D-7465.

Zinov'ev, V. N., and Lebiga, V. A., 1988, *Measurements of Fluctuations For High Subsonic Velocities Using a Hot-Wire Anemometer,* Plenum Publishing, Novosibirsk, Translated from Zhurnal Prikladoni Mekhanikii Teckhnicheskoi Fiziki, No. 3, pp. 80–84.

Appendix

A Note on the Mean Square Equation for CCA

The necessary condition required to assure a solution to the hot-wire equation for the constant current anemometer can be developed as follows. The equation in terms of mean square values is:

$$\overline{\phi'^2} = q^2\overline{\left(\frac{u'}{u}\right)^2} + s^2\overline{\left(\frac{\rho'}{\rho}\right)^2} + \overline{\left(\frac{T_0'}{T_0}\right)^2} + 2qs\,\frac{\overline{u'\rho'}}{u\rho} - 2q\,\frac{\overline{u'T_0'}}{uT_0} - 2s\,\frac{\overline{\rho'T_0'}}{\rho T_0} \quad \text{(A-1)}$$

where

$$q = \frac{S_u}{S_{T_0}} \quad \text{and} \quad s = \frac{S_\rho}{S_{T_0}} \quad \text{(A-2)}$$

In Eq. (A-1) the quantities $\overline{\phi'^2}$, q, and s are functions of τ_w. Therefore, s can be considered to be function of q. Assume that solutions are sought using the method of least squares and $s = f(q)$; substitute this functional relationship into Eq. (A-1):

$$\overline{\phi'^2} = q^2\overline{\left(\frac{u'}{u}\right)^2} + [f(q)]^2\overline{\left(\frac{\rho'}{\rho}\right)^2} + \overline{\left(\frac{T_0'}{T_0}\right)^2} + 2qf(q)\,\frac{\overline{u'\rho'}}{u\rho} - 2q\,\frac{\overline{u'T_0'}}{uT_0} - 2f(q)\,\frac{\overline{\rho'T_0'}}{\rho T_0} \quad \text{(A-3)}$$

Any functional relationship which adequately relates q and s results in Eq. (A-3) having six terms that satisfies Eq. (A-1) resulting in a solution. This can be illustrated by assuming the following equation for s:

$$s = a + bq^f + cq^g + dq^h \quad \text{(A-4)}$$

Substituting Eq. (A-4) into (A-1) and collecting terms gives:

$$\begin{aligned}\overline{\phi'^2} = {} & \overline{\left(\frac{u'}{u}\right)^2}q^2 + \left[2a\,\frac{\overline{u'\rho'}}{u\rho} - 2\,\frac{\overline{u'T_0'}}{uT_0}\right]q \\ & + \left[2ab\overline{\left(\frac{\rho'}{\rho}\right)^2} - 2b\,\frac{\overline{\rho'T_0'}}{\rho T_0}\right]q^f \\ & + \left[2ac\overline{\left(\frac{\rho'}{\rho}\right)^2} - 2c\,\frac{\overline{\rho'T_0'}}{\rho T_0}\right]q^g \\ & + \left[2ad\overline{\left(\frac{\rho'}{\rho}\right)^2} - 2d\,\frac{\overline{\rho'T_0'}}{\rho T_0}\right]q^h \\ & + \left[b^2\overline{\left(\frac{\rho'}{\rho}\right)^2}\right]q^{2f} + \left[c^2\overline{\left(\frac{\rho'}{\rho}\right)^2}\right]q^{2g} \\ & + \left[d^2\overline{\left(\frac{\rho'}{\rho}\right)^2}\right]q^{2h} + \left[2bc\overline{\left(\frac{\rho'}{\rho}\right)^2}\right]q^{f+g} \\ & + \left[2bd\overline{\left(\frac{\rho'}{\rho}\right)^2}\right]q^{f+h} + \left[2cd\overline{\left(\frac{\rho'}{\rho}\right)^2}\right]q^{h+g} \\ & + \left[2b\,\frac{\overline{u'\rho'}}{u\rho}\right]q^{f+1} + \left[2c\,\frac{\overline{u'\rho'}}{u\rho}\right]q^{g+1} \\ & + \left[2d\,\frac{\overline{u'\rho'}}{u\rho}\right]q^{h+1} \\ & + \left[a^2\overline{\left(\frac{\rho'}{\rho}\right)^2} + \overline{\left(\frac{T_0'}{T_0}\right)^2} - 2a\,\frac{\overline{\rho'T_0'}}{\rho T_0}\right] \quad \text{(A-5)}\end{aligned}$$

A solution to this equation is possible for any values of f, g, and h provided that the resultant equation, after the substitution of values for f, g, and h into the equation, has six terms. Some examples of values for f, g, and h which results in an equation which has six terms are presented in Table 1. However, noninteger values cannot be used since the fluctuation diagram exist on the surface of a hyperboloid and this surface must be defined in all quadrants. This results in the values of f being restricted to the values presented in the first two rows of Table 1. The major problem in obtaining a solution to Eq. (A-1) is evaluating the powers of q in Eq. (A-4) which will give the best fit to the mean flow calibration data relating s to q. This can be done by using standard statistical techniques.

A. C. Aldo
Graduate Student.

B. M. Argrow
Assistant Professor.

Department of Aerospace Engineering Sciences, University of Colorado, Boulder, CO 80309

Dense Gas Flow in Minimum Length Nozzles

Recently, dense gases have been investigated for many engineering applications such as for turbomachinery and wind tunnels. Supersonic nozzle design can be complicated by nonclassical dense-gas behavior in the transonic flow regime. In this paper, a method of characteristics (MOC) is developed for two-dimensional (planar) and axisymmetric flow of a van der Waals gas. A minimum length nozzle design code is developed that employs the MOC procedure to generate an inviscid wall contour. The van der Waals results are compared to perfect gas results to show the real-gas effects on the flow properties and inviscid wall contours.

Introduction

A minimum length nozzle (MLN) produces a uniform supersonic flow with a minimum ratio of total nozzle length to throat height or radius. Argrow and Emanuel (1991, 1988) present a detailed discussion of MLN designs, comparisons of different types, computational flow-field analysis, and engineering applications. Before Aldo and Argrow (1993), all MLN analyses, that we are aware of, have considered only perfect gases. Cramer and Fry (1993), Kluwick (1993), Cramer and Crickenberger (1992), Chandrasekar and Prasad (1991), Schnerr and Leidner (1991), Bober and Chow (1990), and Vinokur (1990) have recently investigated nozzle flows for nonideal gases.

Aldo and Argrow (1993), Cramer and Fry (1993), Kluwick (1993), Schnerr and Leidner (1993, 1991), Cramer and Crickenberger (1992), Cramer and Tarkenton (1992), Cramer et al. (1992), Anderson (1991), Cramer (1991), Cramer and Best (1991), and Chandrasekar and Prasad (1991), have recently discussed steady flows of dense gases. Under certain conditions, some of these gases will exhibit nonclassical behavior. Such behavior includes the possibility of a local minimum of the Mach number during steady isentropic expansion, expansion shocks, an increase in the critical Mach number, and other nonclassical behaviors. With the exception of Anderson (1991), each of these references discuss the thermodynamic condition that governs the classical or nonclassical behavior of a dense gas. Thompson (1971) introduced the governing thermodynamic parameter Γ as the fundamental derivative of gas dynamics which can be written as,

$$\Gamma = 1 + \frac{\bar{\rho}}{\bar{a}}\left(\frac{\partial \bar{a}}{\partial \bar{\rho}}\right)_{\bar{s}},$$

where

$$\bar{a} = \left(\frac{\partial \bar{p}}{\partial \bar{\rho}}\right)_{\bar{s}}^{1/2}$$

is the speed of sound and $\bar{\rho}$, $\bar{p}$, and $\bar{s}$ are the density, pressure, and entropy, respectively. The overbar indicates dimensional quantities.

For most gases, $\Gamma > 0$ under normal conditions, however the nonclassical behavior occurs when $\Gamma < 0$. Gases that will attain the $\Gamma < 0$ condition typically have large polyatomic molecules with comparatively large specific heats. Cramer (1991) refers to these gases as BZT (Bethe, 1942; Zel'dovich, 1946; Thompson, 1971) fluids to recognize the individuals that first theorized their existence. The $\Gamma < 0$ region of a BZT fluid occurs in the dense-gas region near the coexistence curve in the pv-plane as shown in Fig. 1. Stagnation conditions are chosen such that the isentrope shown in this nondimensionalized diagram passes through the $\Gamma < 0$ region. These stagnation conditions are used for the sample BZT case that we will refer to as the reference case, to be discussed in more detail later.

The Mach number M variation for the reference case shown in Fig. 2 illustrates nonclassical behavior typical of a BZT fluid during an isentropic expansion. The M variation for the reference case computed from the MLN code is also shown in this figure. The nonclassical behavior occurs where M decreases as ρ decreases (M is decreasing during a portion of an isentropic, supersonic expansion). This M increase is because the local speed of sound increases at a faster rate than the flow velocity in the $\Gamma < 0$ region.

There appear to be practical uses for dense gases, such as in turbomachinery and heavy-gas wind tunnels. Cramer and Fry (1993), Kluwick (1993), Schnerr and Leidner (1993, 1991), Cramer and Tarkenton (1992), and Anderson (1991) are a sample of references that discuss applications that may capitalize on the classical and nonclassical behavior of dense gases and BZT fluids. The most obvious application of a MLN designed for dense-gas flow is in heavy-gas wind tunnels. Schnerr and Leidner (1993) show two-dimensional, finite-difference Euler solutions for the flow of a dense gas through a nozzle. The de Laval nozzle they study has constant-area subsonic and supersonic portions with a circular-arc shaped wall in the transonic section. Sulfur hexaflouride (SF_6) is an example of a gas that may be used in heavy-gas wind tunnels. Anderson (1991) investigated the feasibility of using this large-molecule gas for wind tunnel applications and shows Navier-Stokes calculations for SF_6 flow over a NACA 0012 airfoil. Cramer and Crick-

Contributed by the Fluids Engineering Division for publication in the JOURNAL OF FLUIDS ENGINEERING. Manuscript received by the Fluids Engineering Division October 18, 1993; revised manuscript received June 3, 1994. Associate Technical Editor: R. L. Panton.

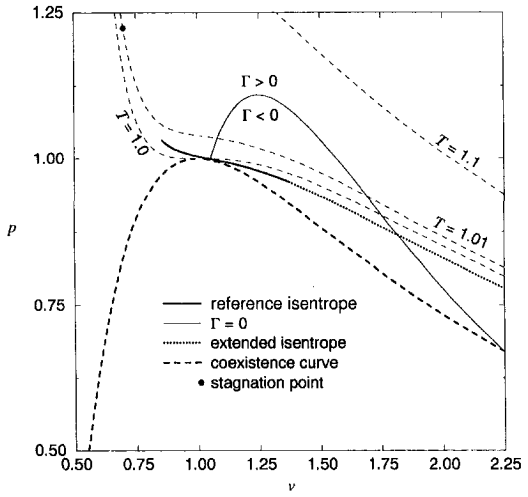

Fig. 1 *pv*-diagram with coexistence curve, isotherms, Γ regions, and the reference isentrope

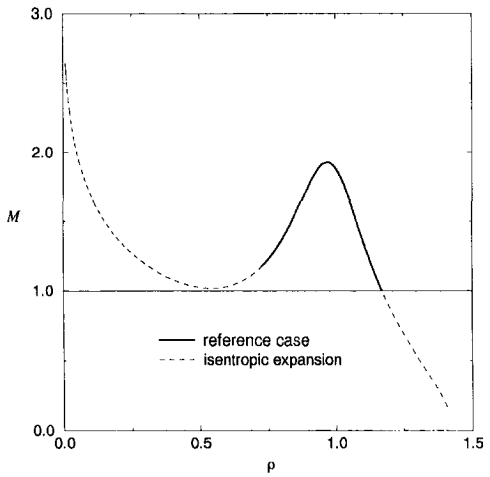

Fig. 2 Variation of Mach number *M* through an isentropic expansion, reference case

enberger (1992) investigated several gases, including SF_6, for nonclassical behavior. Thompson et al. (1986) also include SF_6 in their discussion of retrograde fluids. From the calculations of these references and the authors' own calculations, it is unclear whether SF_6 is a BZT fluid because of the dependency of the results on the equation of state used.

Many of the previous references speculate that nozzles can be designed to produce shock-free supersonic flow of a BZT fluid. With the exception of the recent two-dimensional calculations of Schnerr and Leidner (1993), the calculations have been limited to one-dimensional cases (Cramer and Fry, 1993; Kluwick, 1993; Cramer and Crickenberger, 1992; Chandrasekar and Prasad, 1991; Cramer, 1991; Schnerr and Leidner, 1991). Aldo and Argrow (1993) show what we believe to be the first instance of the use of the method of characteristics (MOC) to compute a dense-gas flow field and the first instance of nozzle contours designed to produce shock-free supersonic flows of a BZT fluid in the $\Gamma < 0$ state. This paper is a continuation of that original work.

Thermodynamic Model

The van der Waals equation of state is

$$\bar{p} = \frac{\overline{RT}}{\bar{v} - \bar{b}} - \frac{\bar{a}}{\bar{v}^2},$$

where $\bar{R}$ is the specific gas constant and

$$\bar{b} = \frac{\overline{RT}_c}{8\bar{p}_c} \quad \text{and} \quad \bar{a} = \frac{27}{64}\frac{\bar{R}^2\bar{T}_c^2}{\bar{p}_c}$$

The c subscript refers to conditions at the critical point. The temperature is represented by $\bar{T}$, and $\bar{v}$ is the specific volume, which is used instead of density because it simplifies the equations. The following thermodynamic development and nondimensionalization scheme follows that of Cramer and Best (1991). The enthalpy $\bar{h}$ and speed of sound $\bar{a}$ are given by

$$\bar{h} = \bar{e}_r + \frac{\overline{RT}}{\delta}\left(1 + \delta\frac{\bar{v}}{\bar{v} - \bar{b}}\right) - \frac{2\bar{a}}{\bar{v}},$$

$$\bar{a} = \left[\overline{RT}(1 + \delta)\left(\frac{\bar{v}}{\bar{v} - \bar{b}}\right)^2 - \frac{2\bar{a}}{\bar{v}}\right]^{1/2},$$

Here $\bar{e}_r$ is an arbitrary reference energy and

$$\delta \equiv \bar{R}/\bar{c}_v.$$

Note that in Fig. 1 the change in temperature along the reference isentrope is small. Because there is minimal temperature variation for the flows investigated, we assume a constant $\bar{c}_v = \bar{c}_{v\infty}$, where $\bar{c}_{v\infty}$ is the ideal-gas specific heat. The temperature variation for isentropic flow of a van der Waals gas is given by

$$\frac{\bar{T}}{\bar{T}_0} = \left(\frac{\bar{v}_0 - \bar{b}}{\bar{v} - \bar{b}}\right)^{\delta},$$

where the 0 subscript refers to stagnation conditions.

The nondimensional (reduced variable) form of the van der Waals equation is written as

$$p = \frac{8T}{3v - 1} - \frac{3}{v^2},$$

and the reduced variables are

$$p = \frac{\bar{p}}{p_c}, \quad T = \frac{\bar{T}}{T_c}, \quad v = \frac{\bar{v}}{v_c}.$$

Quantities without an overbar represent nondimensionalized or reduced variables. The nondimensional form of other essential relations are,

$$T = T_0\left(\frac{v_0 - b}{v - b}\right)^{\delta},$$

$$h = \frac{T}{\delta}\left(1 + \delta\frac{v}{v - b}\right) - \frac{2\alpha}{v},$$

$$h_0 = \frac{T_0}{\delta}\left(1 + \delta\frac{v_0}{v_0 - b}\right) - \frac{2\alpha}{v_0},$$

$$a = \left[T(1 + \delta)\left(\frac{v}{v - b}\right)^2 - \frac{2\alpha}{v}\right]^{1/2},$$

$$M = \frac{\sqrt{2(h_0 - h)}}{a},$$

$$V_{\max} = \sqrt{2h_0},$$

where,

$$h \equiv \frac{\bar{h} - \bar{e}_r}{\overline{RT}_c}, \quad a \equiv \frac{\bar{a}}{\sqrt{\overline{RT}_c}}, \quad b \equiv \frac{\bar{b}}{\bar{v}_c} = \frac{1}{8Z_c}, \quad \alpha \equiv \frac{\bar{a}}{\overline{RT}_c\bar{v}_c} = \frac{27}{64}\frac{1}{Z_c},$$

$V_{\max}$ is the maximum speed, and the critical compressibility is

$$Z_c = \left(\frac{pv}{RT}\right)_c = \frac{3}{8}.$$

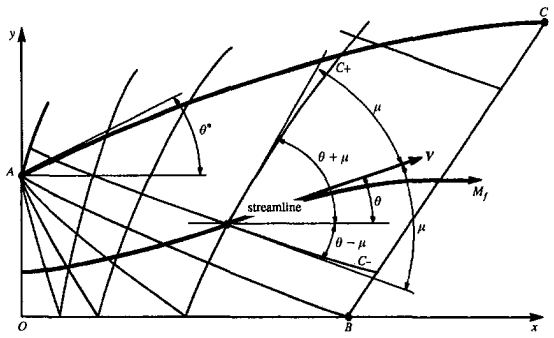

Fig. 3 MLN supersonic flow field geometry, upper half-plane

Method of Characteristics for Real Gases

The method of characteristics (MOC) used by Argrow and Emanuel (1988) assumes an isentropic, irrotational flow of a perfect gas. The governing two-dimensional partial differential equation reduces to a set of four equations, two characteristic and two compatibility equations. For the axisymmetric case, the characteristic and compatibility equations form a set of four ordinary differential equations that are solved simultaneously. Details of the solution procedures can be found in Argrow and Emanuel (1988).

A MOC for the isentropic two-dimensional or axisymmetric flow of a real gas is used for the present study (Zucrow and Hoffman, 1977). For this method, the choice of the equation of state is arbitrary and we use the van der Waals thermodynamic model, more for its simplicity than accuracy. The governing partial differential equations (PDEs) are given by the gas dynamic equation, the irrotationality condition, and the speed of sound relation,

$$(V_x^2 - a^2)\frac{\partial V_x}{\partial x} + (V_y^2 - a^2)\frac{\partial V_y}{\partial y} + 2V_xV_y\frac{\partial V_x}{\partial y} - \sigma\frac{a^2V_y}{y} = 0,$$

$$\frac{\partial V_x}{\partial y} - \frac{\partial V_y}{\partial x} = 0,$$

$$a = a(V) = a(V_x, V_y),$$

where $\sigma = 0$ or 1 for two-dimensional or axisymmetric flow, x and y are the axial and transverse (radial) coordinates nondimensionalized with respect to the throat half-height or radius, V_x and V_y are the corresponding velocity components, and V is the velocity magnitude; all velocities are nondimensionalized in the same manner as the speed of sound a. Along the characteristic lines, corresponding to Mach lines in the flow, this system of PDEs reduces to two ordinary differential equations called compatibility equations.

Figure 3 is a schematic of the supersonic flow field showing the MLN configuration and the flow geometry associated with an arbitrary point on a streamline. The angle θ^* is the initial inclination of the supersonic nozzle contour. The left and right-running characteristics designated as C_+ and C_- are Mach lines inclined at the Mach angle μ with respect to the velocity vector **V**. The corresponding characteristic and compatibility equations are

$$C_\pm \text{ characteristic equation: } \left(\frac{dy}{dx}\right)_\pm = \lambda_\pm = \tan(\theta \pm \mu), \quad (1a)$$

$C_\pm$ compatibility equation: $(V_x^2 - a^2)\,dV_{x_\pm}$

$$+ [2V_xV_y - (V_x^2 - a^2)\lambda_\pm]\,dV_{y_\pm} - \sigma\frac{a^2V_y}{y}\,dx_\pm = 0. \quad (1b)$$

The gas is assumed to enter the supersonic portion of the nozzle, along the straight sonic line OA, uniform and parallel to the axis. It is then expanded through the nozzle and exits with a uniform flow crossing the terminating C_+ characteristic BC with an exit Mach number M_f. For the two-dimensional nozzle, the centered expansion generated by the sharp throat is a Prandtl-Meyer expansion. In the axisymmetric case, the flow at the wall is locally two-dimensional, thus at the throat the expansion is locally a centered Prandtl-Meyer expansion. Gautam (1992) and Argrow and Emanuel (1991) investigated the effects of the subsonic inlet shape and the straight sonic line (SSL) assumption on the quality of the exit flow for a viscous, perfect gas. Their full Navier-Stokes calculations show that MLNs designed using the MOC with the SSL assumption will produce a very uniform exit flow if the radius of curvature of the converging subsonic section is greater than zero. The computed sonic lines for the SSL MLN are shown to be curved, however the flow along the sonic line is mostly parallel indicating that this is the dominant condition for exit flow uniformity.

Construction of the flow field begins by discretizing the centered expansion into equally-spaced speed increments. Each speed increment ΔV has an associated isentropic flow turn angle increment $\Delta\theta$. The angle increment $\Delta\theta$ is computed from the relation

$$\theta_2 - \theta_1 = \int_{V_1}^{V_2} \frac{\sqrt{M^2 - 1}}{V}\,dV. \quad (2)$$

For a perfect gas, the ΔM, associated with an angular deflection $\Delta\theta$ can be easily determined from the Prandtl-Meyer function. For a real gas, the Prandtl-Meyer computation requires the solution of a system of ordinary differential equations as shown by Cramer and Crickenberger (1992). We avoid this computation by using the angle-speed relation in Eq. (2).

With the position of the throat specified and the velocity components (V_x, V_y) computed from V and θ, the necessary flow variables are determined at the throat. Equations (1) are solved simultaneously using the second-order, average-property, Euler predictor-corrector scheme described by Zucrow and Hoffman (1977). The characteristic net of the kernel region OAB and the transition region ABC is constructed using the unit processes described by Argrow and Emanuel (1988). The wall contour corresponds to the streamline that passes through points A and C. This streamline is also determined by using the average-property. Euler predictor-corrector scheme to integrate the equation

$$\frac{dy_w}{dx} = \tan\theta_w$$

from the initial condition, $\theta_w = \theta^*$ at $x = 0$ to the exit condition $\theta_w = 0$ at $x = x_f$. The w subscript refers to quantities at the wall and the f subscript refers to the exit condition.

The accuracy of the characteristic computations and the wall contour are affected by the spacing of the characteristic nodes. The C_- characteristics that emanate from the corner at point A reflect from the axis as C_+ characteristics and bend away from the centered expansion. This may cause relatively large spacing between characteristic node points and the subsequent computed wall points just downstream of the throat where the gradients are the largest. To alleviate this situation, the characteristic net is compressed toward the sonic line by decreasing the step size of the speed increments in the centered expansion discretization. This is comparable to the procedure used by Argrow and Emanuel (1988) where the Prandtl-Meyer and turn angles are discretized and compressed in a similar manner. Figure 4 shows a typical characteristic net using a relatively coarse discretization for clarity.

In the transition region, the C_- characteristics are uniformly spaced along BC. This uniform spacing is determined by the average spacing of C_+ characteristics along AB, which bounds the kernel region, multiplied by a constant aspect ratio.

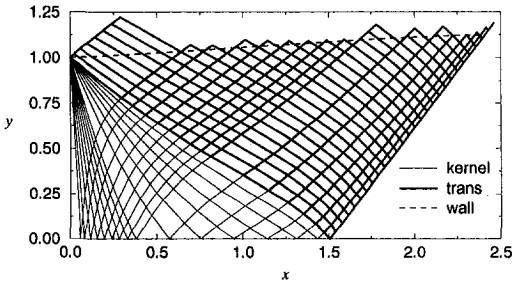

Fig. 4 Characteristic net indicating kernel and transition regions with 16 characteristics, reference conditions

Results

Stagnation conditions and the initial wall slope for the reference case are: $T_0 = 1.01$, $\nu_0 = 0.7$, $\delta = 0.015$, and $\theta^* = 2.5$ deg. For the speed discretization, $\Delta V \cong 10^{-5}$ for dV in Eq. (2). The first characteristic is chosen at ΔV, then each successive characteristic is chosen at an increasing multiple of ΔV, until about $25\Delta V$. Then a characteristic is generated at every $25\Delta V$. This allows characteristics to be compressed towards the sonic line for improved accuracy. The limits of integration for Eq. (2) are set at the sonic speed $V_1 = 0.33$ to $V_2 = 0.9V_{\max}$ with $V_{\max} = 11.5$, for the reference case. Similar discretizations are used in the other cases. For the relatively short nozzles produced in this study, the aspect ratio is set at 0.5. Argrow and Emanuel (1988) give a complete description of how the characteristic compression and transition region aspect ratio affect the overall computational accuracy.

Figure 2 shows the isentropic expansion, for the reference stagnation conditions, computed using quasi one-dimensional equations. As mentioned earlier, this set of stagnation conditions falls on an isentrope that passes through the $\Gamma < 0$ region shown in Fig. 1. The path along a streamline in the MOC nozzle calculation with the same stagnation conditions is shown overlying a portion of the quasi one-dimensional curve. As will be shown in more detail later, M_f does not vary monotonically with θ^* for a BZT fluid in the $\Gamma < 0$ region as it does in the case of a conventional gas, therefore the maximum M_f does not correspond to the maximum θ^* value, $\theta^*_{\max}$. Note that the MOC calculation begins at sonic conditions and terminates at a relatively low supersonic M after passing through a maximum. From this diagram we should expect that at $\theta^*_{\max}$, M_f is less than the maximum M, which occurs inside the nozzle. Figure 1 shows the supersonic portion of the isentrope of the reference case in the pv-plane. The stagnation point for the reference case is also shown on the $T = 1.01$ isotherm. It is apparent from this diagram that the exiting flow has $\Gamma < 0$. Note that Cramer and Best (1991) produced a plot similar to Fig. 2 for a van der Waals gas, that shows the $\Gamma < 0$ case with $T_0 = 1.01$ and $\nu_0 = 0.7$, but with $\delta = 0.02$. For this δ value, the isentrope passes through the two-phase region below the critical point. These same conditions, were also used by Aldo and Argrow (1993) and although the case presents no computational difficulties, it is physically unrealistic. With $\delta = 0.015$, the reference isentrope passes just above the critical point and remains in the single-phase region as shown in Fig. 1.

Figure 4 shows the characteristic net and nozzle contour approximately to scale. The case shown is for the reference conditions ($T_0 = 1.01$, $\nu_0 = 0.7$, $\delta = 0.015$), but with only 16 characteristics used so that the characteristic net can be easily seen. Also, because of the small number of characteristics, compression of the first few causes a noticeable gap in the overall distribution. However, this plot uses coarse discretization to clearly show the effect of compressing characteristics toward the sonic line. It is also apparent that both the kernel and transition regions are non-simple wave regions where both families of characteristics are curved. In the two dimensional case (not shown), the transition region is a simple-wave region where the C_+ characteristics are straight. The last two C_+ characteristics at the nozzle exit converge as they move from the axis. Slightly increasing θ^* will cause these two characteristics to overlap, signaling the beginning of shock formation. This is the condition that effectively defines the value for $\theta^*_{\max}$. Once a shock occurs (compression or expansion), the flow is no longer isentropic and the MOC cannot be applied without a special procedure to account for the placement of the shock. These shocks are expansion shocks in the $\Gamma < 0$ region.

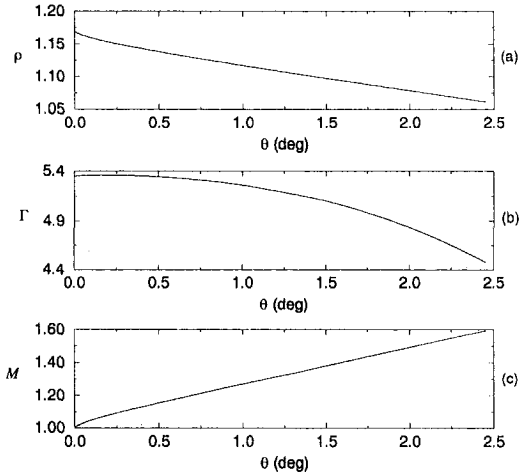

Fig. 5 Variation of density ρ, fundamental derivative Γ, and Mach number M through the centered expansion, reference case

Figures 5(a–c) show the variation of flow parameters through the centered expansion as the gas expands around the sharp corner from $\theta = 0$ deg to $\theta = \theta^*$, for the reference case. Since the gas has not yet been expanded into the $\Gamma < 0$ region, the values are similar to what would be expected for a perfect gas. The density decreases through the centered expansion, as expected, which causes Γ to drop from near 5.4 to about 4.5 where the supersonic wall contour begins. The Mach number steadily increases since the gas is still behaving classically.

Figures 6(a–d) show the wall contour and the variation of M, ρ, and Γ along the nozzle axis and wall for an axisymmetric MLN with $T_0 = 1.01$, $\delta = 0.015$, and $\nu_0 = 0.7$, 0.9. The $\nu_0 = 0.9$ case is an example of a dense gas with the isentrope never crossing into the $\Gamma < 0$ region during the supersonic portion of the expansion. Figure 6(a) indicates the increase in nozzle size required for the more dense gas. Note that for all comparisons in Figs. 6, $\theta^* = 2.5$ deg $\cong \theta^*_{\max}$. The upper limit on θ^* is determined by the production of shock waves. These shocks occur when C_+ characteristics near BC overlap (see Fig. 3).

For Figs. 6(b–d) there are two sets of curves. The curves along the nozzle axis terminate at the start of the uniform exit flow region that coincides with the termination of the kernel at point B as shown in Fig. 3. The curves for flow variables along the wall extend to the end of the contour at point C of Fig. 3. The density ρ varies smoothly along the axis and wall for both cases as shown in Fig. 6(b). Figure 6(c) shows that the gas is expanded into a $\Gamma < 0$ region that extends to the nozzle exit for the reference $\nu_0 = 0.7$ case. For this case, the Mach number reaches a maximum of about 1.92 upstream of the exit, before decreasing. This agrees with the quasi one-dimensional results obtained by Cramer and Best (1991) and Fig. 2. In contrast, for the $\nu_0 = 0.9$ case the Mach number monotonically increases.

A comparison of the wall contours at the maximum M_f for the two-dimensional and axisymmetric cases using the refer-

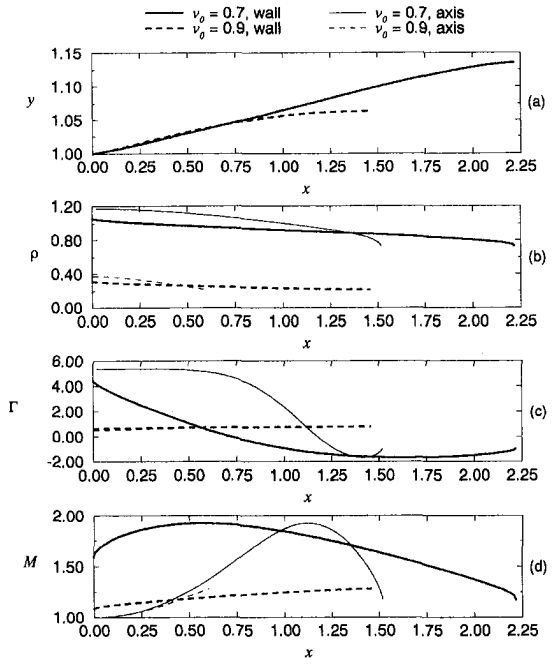

Fig. 6 Wall contour, density ρ, fundamental derivative Γ, and Mach number M distributions along the axis and wall, for the reference and ν_0 = 0.9 case

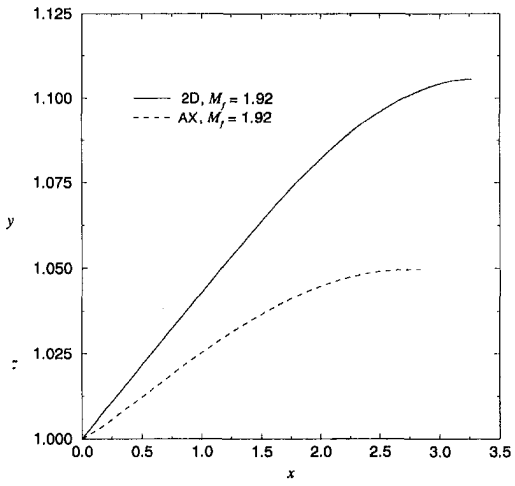

Fig. 7 Contours for two-dimensional and axisymmetric nozzles at the same exit Mach number

ence conditions is shown in Fig. 7. Note that vertical axis is substantially stretched in order to enhance the visibility of the differences in the two contours. Although difficult to discern, the axisymmetric contour contains an inflection point just downstream of the throat that is not present in the two-dimensional contour. Also, θ^* is larger for the two-dimensional case as will be shown in more detail in the following figures. The axisymmetric nozzle is shorter and smaller, showing that it is more efficient than a two-dimensional nozzle in expanding a gas to a specific Mach number. The results of this plot, including the axisymmetric inflection point, agree with the perfect-gas results of Argrow and Emanuel (1988).

Figures 8 and 9 show the θ^* versus M_f variation for the axisymmetric and two-dimensional cases, respectively. These figures show the reference case and the effect of varying ν_0, keeping other reference conditions fixed, compared to a perfect gas. The perfect gas is modeled by setting α and b to zero and Z_c = 1 in the thermodynamic equations. When a perfect gas is

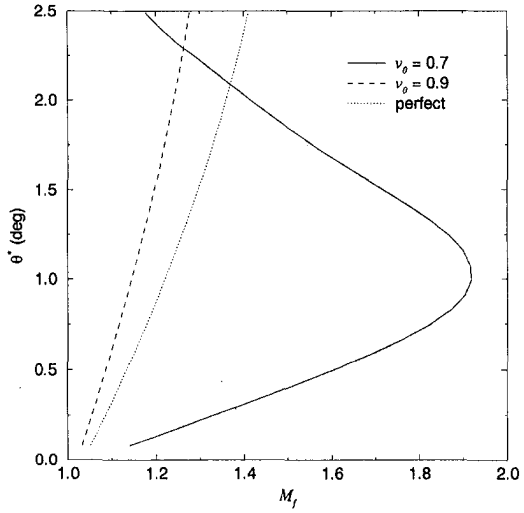

Fig. 8 Initial wall turn angle θ^* versus exit Mach number M_f, variable ν_0, axisymmetric case

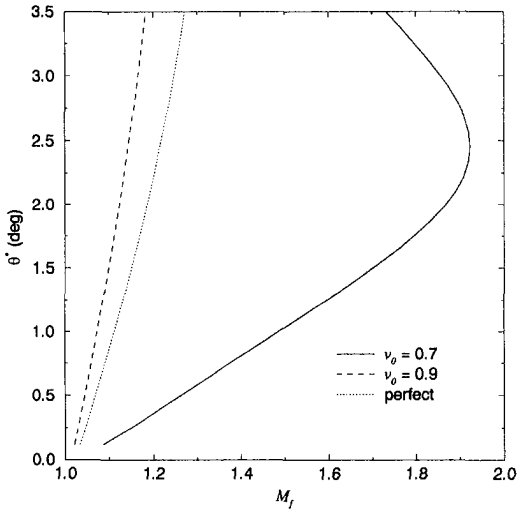

Fig. 9 Initial wall turn angle θ^* versus exit Mach number M_f, variable ν_0, two-dimensional case

modeled, changing stagnation conditions does not alter the nondimensional results. In the less dense case, $\nu_0 = 0.9$, the isentrope passes completely through the $\Gamma < 0$ region during the subsonic acceleration from stagnation to the sonic throat conditions. Thus, the supersonic portion of the isentrope, computed with the MOC, is completely in the $\Gamma > 0$ region. The $\nu_0 = 0.7$ case with $\Gamma < 0$, reaches a maximum M_f of about 1.92 for $\theta^* \cong 1$ deg for the axisymmetric case shown in Fig. 8. Then M_f decreases to about 1.18 when $\theta^*_{max} \cong 2.5$ deg. For the two-dimensional case shown in Fig. 9, the maximum $M \cong 1.92$ is reached at $\theta^* \cong 2.5$ deg, and $M_f \cong 1.73$ at $\theta^*_{max} \cong 3.5$ deg. In each of Figs. 8 and 9, increasing ν_0 beyond the value of 0.9 (decreasing the stagnation density) keeping T_0 fixed, causes the curves to move to the right toward the perfect-gas limit. Decreasing ν_0 (increasing stagnation density) from the 0.9 value moves the curves to the left until the $\Gamma < 0$ condition is reached, then the curves bow toward the right, beyond the perfect gas limit as shown. Figure 10 is an axisymmetric case that shows that the same behavior occurs by increasing T_0, keeping other conditions fixed at the reference values.

Figures 11 and 12 show the variation of the kernel length x_b and nozzle length x_f versus M_f, respectively. Here, T_0 and δ are set at the reference values ($T_0 = 1.01$, $\delta = 0.015$). The nonclassical behavior is apparent from the double-valued curves.

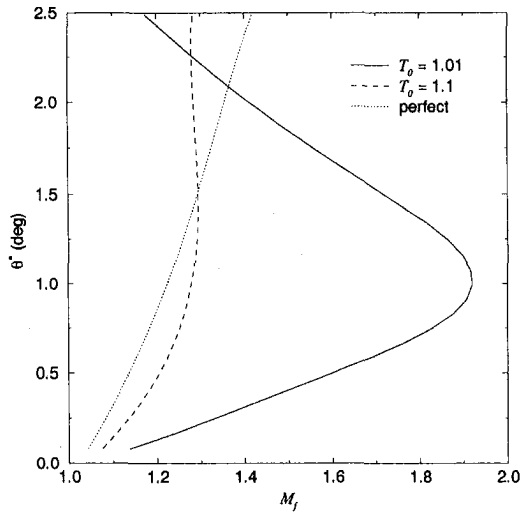

Fig. 10 Initial wall turn angle θ^* versus exit Mach number M_f, variable T_0, axisymmetric case

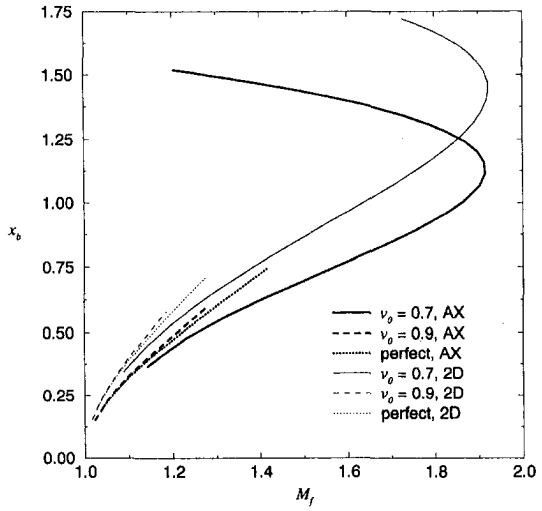

Fig. 11 Kernel length x_b versus exit Mach number M_f, variable ν_0

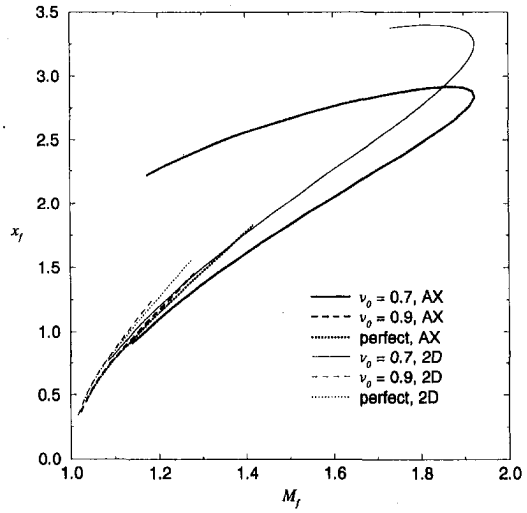

Fig. 12 Nozzle length x_f versus exit Mach number M_f, variable ν_0

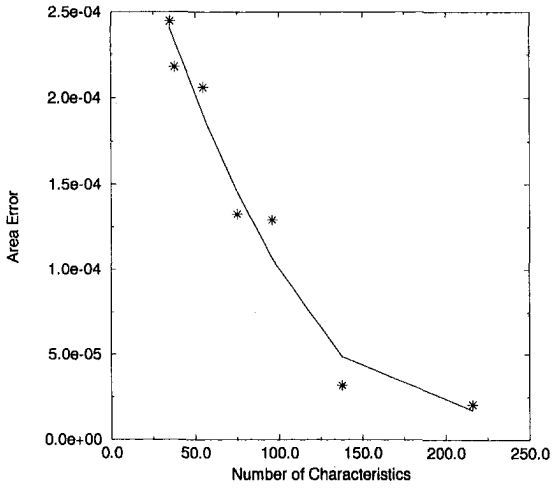

Fig. 13 Area error for varying number of characteristics, reference case

These curves indicate that for given stagnation conditions the same M_f can often be produced from nozzles with two different θ^*. In Fig. 11, the kernel length continues to increase even as M_f decreases (and θ^* increases). However, in Fig. 12, the nozzle length begins to decrease after M_f decreases somewhat. Therefore, there is a range where M_f decreases (with increasing θ^*), the kernel region expands, and the transition region contracts. The overall economy of the axisymmetric nozzle is apparent from the smaller x_f values required to produce a particular value for M_f as shown in Fig. 12. All perfect and lower-density ($\nu_0 = 0.9$) cases shown behave classically, with similar kernel and nozzle lengths. Note that as in Figs. 8–12, the perfect gas and $\nu_0 = 0.9$ curves do not extend to M_f values as high as those with the reference conditions. Again, this is because all curves only extend to the θ^* limit of the reference BZT case. The perfect gas and $\nu_0 = 0.9$ curves could be extended indefinitely if θ^* (with $T_0 = 1.01$, $\delta = 0.015$) is allowed to increase beyond $\theta^*_{max} \cong 2.5$ deg for the axisymmetric case or beyond $\theta^*_{max} \cong 3.5$ deg for the two-dimensional cases.

Figure 13 shows how increasing the number of characteristics decreases the error in the computed ratio of exit area to throat area, A_f/A^*. The error is the difference between A_f/A^* computed from the wall contour, and A_f/A^* computed from the exact quasi one-dimensional relation. The quadratic regression curve shows the trend of increasing accuracy with increased computational effort.

Conclusions

The MOC is applied to the steady isentropic flow of a single-phase dense gas. A method is presented for generating inviscid MLN contours to produce a uniform supersonic flow based on a straight sonic line assumption. The computed dense-gas MLN contours are similar in shape and size to the perfect-gas cases. The double-valued relation between θ^*, x_b, and x_f, with respect to M_f for the BZT fluid, can result in substantially greater values for x_b and x_f than for the less dense $\Gamma > 0$ and perfect gas cases. In these instances the lower of the two θ^* values will result in shorter values for x_b and x_f. Thus, for the limited M_f values investigated, there is no obvious reason to use the larger of the two θ^* values for the double-valued BZT cases.

The MLN procedure presented is limited to cases where there is only one sonic point. Inclusion of more than one sonic point will require the coupling of the present method with a subsonic contour design procedure. As shown in Fig. 2, in order to isentropically expand the BZT fluid from a stagnation state to $M \to \infty$ with the reference stagnation conditions, M must first reach a local maximum, before it decreases to a local super-

sonic minimum. An isentropic expansion to $M \rightarrow \infty$ is not possible with a single centered expansion. At best, the single centered-expansion MLN can generate an M slightly beyond the local maximum before an expansion shock is generated. A design that employs two centered expansions separated by a finite, converging wall segment may be able to accomplish the expansion beyond the low supersonic M_f values shown. Figure 1 shows that once the gas is expanded beyond the local supersonic minimum, it will behave classically with further expansion.

The method we present will produce MLN contours that account for real-gas effects of a dense gas, including the nonclassical behavior of a BZT fluid. Although the simple van der Waals model is used, more accurate state equations are easily incorporated. For existing perfect-gas codes, the primary modification is to replace the perfect-gas state equations with real-gas state equations, the procedure for construction of the characteristic net is unchanged from that used in previous work (Argrow and Emanuel, 1988, 1991). A MLN can be designed to produce a steady supersonic flow of a BZT fluid that exits the nozzle in a $\Gamma < 0$ state. This raises the possibility of interesting wind tunnel experiments to study the supersonic flow of a dense gas over airfoils and other aerodynamic shapes.

Acknowledgment

The authors gratefully acknowledge Professors Mark S. Cramer and George Emanuel for their insightful correspondence and suggestions.

References

Aldo, A. C., and Argrow, B. M., 1993, "Supersonic Minimum Length Nozzle Design for Dense Gases," Fifth Annual Thermal and Fluids Analysis Workshop, NASA CP-10122, pp. 329–341.

Anderson, W. K., 1991, "Numerical Study on Using Sulfur Hexaflouride as a Wind Tunnel Test Gas." *AIAA Journal*, Vol. 29, No. 12, pp. 2179–2180.

Argrow, B. M., and Emanuel, G., 1991, "Computational Analysis of the Transonic Flow Field of Two-Dimensional Minimum Length Nozzles," ASME JOURNAL OF FLUIDS ENGINEERING, Vol. 113, pp. 479–488.

Argrow, B. M., and Emanuel, G., 1988, "Comparison of Minimum Length Nozzles," ASME JOURNAL OF FLUIDS ENGINEERING, Vol. 110, pp. 283–288.

Bethe, H. A., 1942, "The Theory of Shock Waves for an Arbitrary Equation of State," Office of Scientific Research and Development, Report No. 545.

Bober, W., and Chow, W. L., 1990, "Nonideal Isentropic Gas Flow Through Converging-Diverging Nozzles," ASME JOURNAL OF FLUIDS ENGINEERING, Vol. 112, pp. 455–460.

Chandrasekar, D., and Prasad, P., 1991, "Transonic Flow of a Fluid with Positive and Negative Nonlinearity through a Nozzle," *Physics of Fluids A*, Vol. 3, pp. 427–438.

Cramer, M. S., 1991, "On the Mach Number Variation in Steady Flows of Dense Hydrocarbons," ASME JOURNAL OF FLUIDS ENGINEERING, Vol. 113, pp. 675–680.

Cramer, M. S., 1991, "Nonclassical Dynamics of Classical Gases." *Nonlinear Waves in Real Fluids*, Springer-Verlag, pp. 91–145.

Cramer, M. S., and Best, L. M., 1991, "Steady, Isentropic Flows of Dense Gases," *Physics of Fluids A*, Vol. 3, pp. 219–226.

Cramer, M. S., and Crickenberger, A. B., 1992, "Prandtl-Meyer Function for Dense Gases," *AIAA Journal*, Vol. 30, No. 2, pp. 561–564.

Cramer, M. S., and Fry, R. N., 1993, "Nozzle Flows of Dense Gases," *Physics of Fluids A*, Vol. 5, pp. 1246–1259.

Cramer, M. S., and Tarkenton, G. M., 1992, "Transonic Flows of Bethe-Zel'dovich-Thompson Fluids," *Journal of Fluid Mechanics*, Vol. 240, pp. 197–228.

Cramer, M. S., and Tarkenton, L. M., and Tarkenton, G. M., 1992, "Critical Mach Number Estimates for Dense Gases," *Physics of Fluids A*, Vol. 4, pp. 197–228.

Gautam, Alok S., "A Computational Analysis of the Viscous Transonic Flow Field of Axisymmetric Minimum Length Nozzles," M.S. thesis, University of Oklahoma, 1992.

Kluwick, A., 1993, "Transonic Nozzle Flow of Dense Gases," *Journal of Fluid Mechanics*, Vol. 247, pp. 661–688.

Schnerr, G. H., and Leidner, P., 1991, "Diabatic Supersonic Flows of Dense Gases," *Physics of Fluids A*, Vol. 3, pp. 2445–2458.

Thompson, P. A., Carofano, G. C., and Kim, Y.-G., 1986, "Shock Waves and Phase Changes in a Large-Heat-Capacity Fluid Emerging from a Tube," *Journal of Fluid Mechanics*, Vol. 166, pp. 57–92.

Thompson, P. A., 1971, "A Fundamental Derivative in Gasdynamics," *Physics of Fluids*, Vol. 14, pp. 1843–1849.

Vinokur, M., 1990, "Discussion of Nonideal Isentropic Gas Flow Through Converging-Diverging Nozzles," ASME JOURNAL OF FLUIDS ENGINEERING, Vol. 112, pp. 460–461.

Zel'Dovich, Ya. B., 1946, "On the Possibility of Rarefaction Shock Waves," *Zh. Eksp. Teor. Fiz.*, Vol. 4, pp. 363–364.

Zucrow, M. J., and Hoffman, J. D., 1977, *Gas Dynamics*, Vol. 2, Krieger, pp. 112–136.

A Fast, Accurate Real Gas Equation of State for Fluid Dynamic Analysis Applications

R. H. Aungier
Manager, Product Development,
Elliott Company,
Jeannette, PA 15644-1473

A modified form of the Redlich-Kwong two-parameter equation of state is presented. The modified equation employs the acentric factor and the critical point compressibility factor as additional parameters to improve its accuracy and to extend its application range to include the critical point. This modified equation is as simple as the original form, yet achieves substantially better prediction accuracy, including thermodynamic parameters such as enthalpy and entropy. Results from this equation, the original equation, and three other popular modified forms are compared with gas property data for several compounds to demonstrate its improved accuracy and increased application range. Practical application limits to the other modified forms are identified to guide current users of those methods.

Introduction

The fluid dynamic analysis of turbomachinery often requires the consideration of highly, nonideal gases or gas mixtures. The simple two-parameter equation of state is very attractive for this purpose. First, the increase in computation time for real gases over perfect gases is a minimum for this form. Second, the data required are readily available for almost all compounds of interest.

The Redlich-Kwong equation of state is generally considered the most accurate of the two-parameter equations of state. The original form (Redlich and Kwong, 1949) is

$$P = \frac{RT}{V - b} - \frac{a_0}{V(V + b)\,T_R^{0.5}} \tag{1}$$

where a_0 and b are constants related directly to the gas critical pressure and temperature. Many investigators have attempted to improve the accuracy of the Redlich-Kwong equation. A good review of many of these modifications is given by Ried et al. (1977). Many of these modified equations are not suitable for the fluid dynamic analysis application due to complex forms not easily extended to predict thermodynamic parameters such as enthalpy and entropy, without excessive computation time. The models of Soave (1972), Wilson (1966), and Barnes-King (Barnes, 1973) are quite suitable for this application. These modified equations employ the acentric factor (Pitzer, 1955) as an additional correlating parameter in a fully analytical form. The original references for the models of Wilson and Barnes-King were not available to the author, so the description by Ried et al. (1977) was used for those models. This does not provide information relative to the basis for the modifications employed. Soave employed vapor pressure data for a series of hydrocarbon compounds to develop his modified form. His method emphasizes vapor-liquid equilibrium prediction accuracy.

Results from the Redlich-Kwong equation, and the modifications by Soave, Wilson, and Barnes-King have been compared to gas property data, with the intention of selecting the best model for fluid dynamic analysis activity in turbomachinery. Each of the modified forms showed improved prediction accuracy for certain compounds and for certain ranges of reduced temperature and pressure. But, when the modified forms were used beyond their range of validity, large deviations from gas property data were observed. For these same conditions, the deviations of the original Redlich-Kwong equation were relatively modest. It was concluded that unless the validity of the modified equations for the problem of interest is well established, the safest choice is the original Redlich-Kwong equation.

These forms of the Redlich-Kwong equation can be represented by the general equation

$$P = \frac{RT}{V - b} - \frac{a(T)}{V(V + b)} \tag{2}$$

where

Redlich-Kwong: $a(T) = a_0/T_R^{0.5}$

Soave: $a(T) = a_0[1 + (0.48 + 1.57\omega - 0.17\omega^2)(1 - T_R^{0.5})]$

Wilson: $a(T) = a_0[T_R + (1.57 + 1.62\omega)(1 - T_R)]$

Barnes-King: $a(T) = a_0 T_R[1 + (0.9 + 1.21\omega)(T_R^{1.5} - 1)]$

and for all forms,

$$a_0 = 0.42747R^2T_c^2/P_c$$
$$b = 0.08664RT_c/P_c \tag{3}$$

which satisfy the thermodynamic stability criterion that the first

Contributed by the Fluids Engineering Division and presented at the Fluids Engineering Division Summer Meeting, Lake Tahoe, NV, June 19–23, 1994 of THE AMERICAN SOCIETY OF MECHANICAL ENGINEERS. Manuscript received by the Fluids Engineering Division February 22, 1994; revised manuscript received June 2, 1994. Associate Technical Editor: R. L. Panton.

and second partial derivatives of P with respect to V must equal zero at the critical point.

The Present Method

The observation that the original Redlich-Kwong equation was the most general of the four methods evaluated, suggests a modified form more closely associated with the original equation might be a promising direction for investigation. The present method employs a similar form

$$P = \frac{RT}{V - b + c} - \frac{a(T)}{V(V + b)} \tag{4}$$

where Eq. (3) apply and

$$a(T) = a_0 T_R^{-n} \tag{5}$$

The additional constant, c, is a correction to eliminate a known weakness of the Redlich-Kwong model at the critical point, where it (and the modified forms described above) predicts a compressibility factor of 1/3. This makes the equations virtually useless in the vicinity of the critical point. To remove this weakness, the constant, c, is defined by

$$c = \frac{RT_c}{P_c + \dfrac{a_0}{V_c(V_c + b)}} + b - V_c \tag{6}$$

The addition of c does compromise the thermodynamic stability condition. But, typical values of c are about two orders of magnitude smaller than b. Experience has shown that the addition of c has virtually no effect upon predictions except in the immediate vicinity of the critical point. At the critical point, Eq. (4) becomes exact.

The more significant aspect of the present modification is the use of Eq. (5), where the Redlich-Kwong equation's exponent of 0.5 is replaced by the general parameter, n. The optimum value of n was established for twelve different compounds covering a wide variation in acentric factor values. Predictions with Eq. (4) were compared to tabulated property data over a range of n to select the value of n that yields the minimum root-mean-square (rms) error in P for given values of V and T. All compounds showed a clear minimum rms error, but with an uncertainty range of about 0.05 over which the rms error showed little variation. The maximum error was also considered in selecting the optimum value of n within this range of uncertainty for each compound. Table 1 shows the results obtained and the range of temperature and pressure covered by the data sets for the compounds considered.

Data for helium were obtained from Akin (1950). Data for refrigerant R134a (1,1,1,2-tetrafluoroethane) were obtained from NIST (1991). Data for all other compounds were obtained from Canjar and Manning (1967). The data sets used for the twelve compounds typically consisted of about fifty points distributed over the temperature and pressure ranges indicated in Table 1. These ranges were chosen to insure validity of the new model for anticipated fluid dynamic applications. Due to the form of Eq. (5), values of T_R above and below unity are significant to making a valid selection of n. It was quickly noted that minor deviations can be magnified at higher values of P_R. Where practical, the data sets were selected for T_R from 0.6 to 2 and P_R up to 2. Some sets deviate from that preferred practice, due to data availability or to conform to conditions of practical interest for fluid dynamic analysis applications.

The optimum values of n are well correlated by the empirical Eq. (7) as can be seen in Fig. 1.

$$n = 0.4986 + 1.1735\omega + 0.4754\omega^2 \tag{7}$$

Table 1 Optimum values of n

Compound	ω	n	T (°K)	P (bar)
Helium	-0.464	0.03	19 - 588	1.0 - 103
Hydrogen	-0.220	0.31	89 - 366	3.5 - 172
Methane	0.0080	0.53	144 - 394	1.0 - 93
Nitrogen	0.0400	0.60	105 - 1366	1.0 - 96
Ethylene	0.0868	0.59	200 - 560	1.0 - 103
Propane	0.1520	0.63	310 - 478	1.0 - 83
I-Butane	0.1848	0.68	310 - 810	1.0 - 69
Carbon Dioxide	0.2250	0.77	222 - 589	1.0 - 138
N-Pentane	0.2539	0.76	377 - 700	1.0 - 69
Ammonia	0.2550	0.85	344 - 588	1.0 - 139
R134a	0.3254	0.96	262 - 588	0.3 - 81
Steam	0.3440	1.02	422 - 1144	1.0 - 172

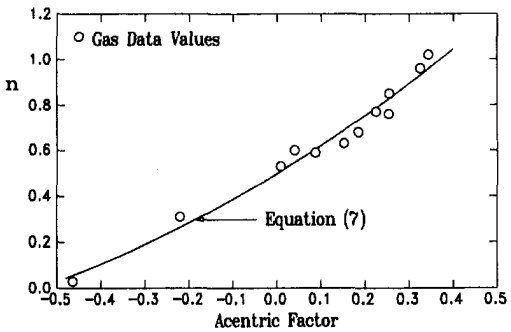

Fig. 1 Empirical equation for n

Pressure-Volume-Temperature Predictions

The evaluation of the present method is best presented by comparing results from it with the other alternate forms of the Redlich-Kwong equation of state. The five methods discussed in this paper were compared in terms of the errors in predicted pressure with respect to the gas property data sets. Table 2 lists the rms errors in the predicted pressure for the various equations. Table 3 shows a similar comparison for the maximum error.

The data sets used, necessarily include some points where real gas effects are negligible. These points serve as a control on the selection of n, to insure that the selected value does not introduce non-ideal behavior where there is none. Also, they

Nomenclature

A = Helmholtz energy, $dA = -PdV$
a = function of temperature in modified equations
a_0 = gas constant defined in Eq. (3)
b = gas constant defined in Eq. (3)
c = gas constant defined in Eq. (6)
C_p = specific heat at constant pressure
H = specific enthalpy
M = molecular weight
n = exponent in the modified equation, Eq. (4)
P = pressure
R = gas constant, R_u/M
R_u = universal gas constant
S = specific entropy
T = temperature
V = specific volume
x = mole fraction
Z = compressibility factor, $PV/(RT)$
ω = acentric factor = $-\log P_{vR} - 1$ (evaluated at $T_R = 0.7$)

Subscripts

c = value at the critical point
R = reduced parameter (normalized by its critical point value)
v = condition on vapor saturation curve

Superscripts

0 = condition at a reference pressure where the ideal gas model applies, $P^0V^0 = RT^0$

Table 2 Comparison of rms pressure errors

Compound	Present Method	Redlich -Kwong	Soave	Wilson	Barnes -King
Helium	0.43%	1.55%	3.42%	3.61%	11.5%
Hydrogen	0.53%	1.17%	0.98%	3.04%	9.99%
Methane	0.52%	0.52%	0.49%	2.00%	1.53%
Nitrogen	0.87%	0.65%	0.82%	4.69%	1.78%
Ethylene	0.39%	0.78%	1.04%	3.39%	0.71%
Propane	0.44%	0.97%	1.04%	2.43%	0.34%
I-Butane	0.58%	1.41%	1.15%	3.09%	0.51%
Carbon Dioxide	1.23%	1.73%	1.83%	3.90%	1.51%
N-Pentane	0.70%	1.61%	1.41%	3.15%	1.01%
Ammonia	1.00%	1.45%	1.36%	2.19%	1.21%
R134a	0.62%	2.09%	1.23%	3.37%	1.20%
Steam	0.74%	1.19%	1.01%	1.97%	1.05%
Average	0.65%	1.28%	1.31%	3.07%	2.69%

Table 3 Comparison of maximum pressure errors

Compound	Present Method	Redlich -Kwong	Soave	Wilson	Barnes -King
Helium	1.19%	5.26%	11.0%	10.1%	32.2%
Hydrogen	0.92%	4.08%	2.30%	6.54%	22.7%
Methane	1.33%	1.25%	1.63%	5.23%	3.66%
Nitrogen	1.36%	1.67%	2.19%	8.89%	3.43%
Ethylene	1.39%	1.46%	3.18%	7.64%	1.31%
Propane	1.51%	2.14%	3.18%	7.43%	0.92%
I-Butane	3.00%	3.41%	5.07%	8.95%	2.78%
Carbon Dioxide	4.08%	5.00%	4.54%	11.6%	4.26%
N-Pentane	2.71%	4.33%	4.68%	9.43%	3.49%
Ammonia	3.64%	4.67%	3.82%	6.17%	3.94%
R134a	1.86%	4.94%	4.90%	12.3%	4.78%
Steam	3.48%	3.71%	3.55%	5.23%	3.55%

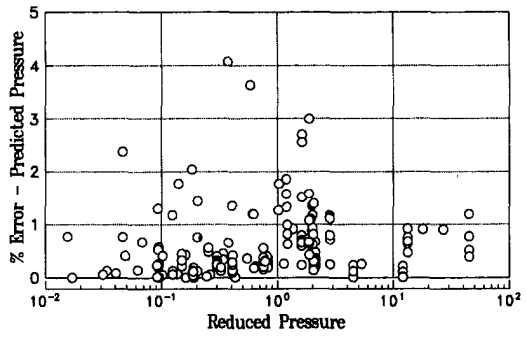

Fig. 2 Typical pressure errors—present method

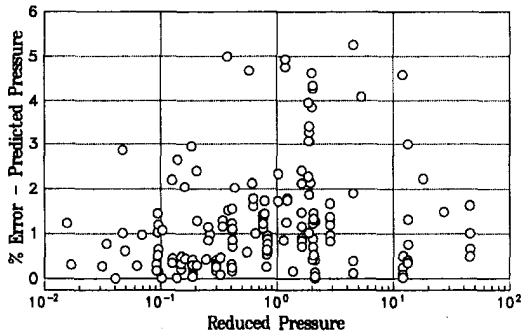

Fig. 3 Typical pressure errors—Redlich-Kwong model

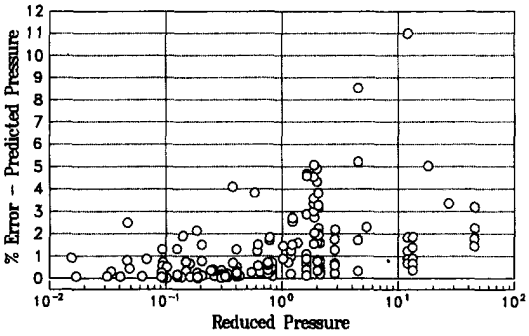

Fig. 4 Typical pressure errors—Soave's model

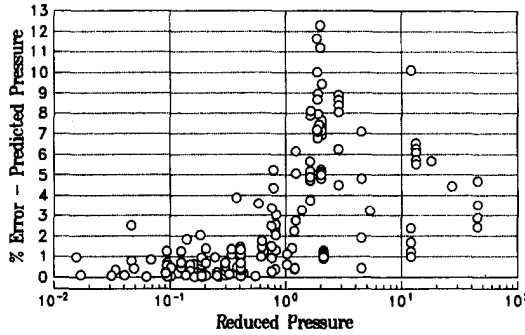

Fig. 5 Typical pressure errors—Wilson's model

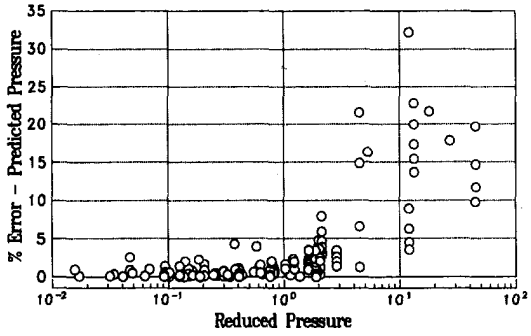

Fig. 6 Typical pressure errors—Barnes-King model

serve as base points to permit an evaluation of prediction accuracy for enthalpy and entropy. To avoid an artificially low error estimate, these points are not included in the rms errors shown in Table 2. Whenever both the specific equation of state and the gas property data showed less than 1 percent deviation from an ideal gas equation (i.e., $0.99 < Z < 1.01$), the point was dropped from the rms error calculation.

Figures 2 through 6 show a more detailed summary for about 25 percent of the data points used in the evaluation. These figures include an intermediate and a high pressure point for each temperature considered for all compounds (low pressure points are of less interest since real gas behavior is less significant).

It is clear that the present method achieves significantly better overall prediction accuracy than any of the other four models evaluated. Tables 2–3 and Figs. 2–6 also support the earlier conclusion that the classical Redlich-Kwong equation was found to be a safer choice than the modified equations of Soave, Wilson and Barnes-King. For the gas property data sets used here, only the present method consistently achieves an overall accuracy better than the original Redlich-Kwong equation, with an average rms error in pressure about 50 percent less for the twelve compounds considered. The other modified forms do show excellent prediction accuracy over a major portion of the data set points used, but also show substantial local deviations that are reflected in the rms and maximum errors. From a detailed analysis of the individual data point errors, the following observations can be made.

Table 4 Comparison of rms enthalpy errors

Compound	Present Method	Redlich -Kwong	Soave	Wilson	Barnes -King
Helium	0.45%	1.39%	1.56%	1.58%	4.46%
Hydrogen	0.15%	0.92%	0.51%	0.69%	2.54%
Methane	0.28%	0.30%	0.43%	0.77%	0.53%
Nitrogen	0.37%	0.40%	0.56%	1.25%	0.41%
Ethylene	0.49%	0.53%	0.64%	1.10%	0.52%
Propane	0.14%	0.41%	0.20%	0.53%	0.22%
I-Butane	0.16%	0.41%	0.20%	0.42%	0.21%
Carbon Dioxide	0.56%	0.99%	0.72%	1.19%	0.71%
N-Pentane	0.16%	0.42%	0.16%	0.35%	0.17%
Ammonia	1.27%	2.08%	1.36%	1.50%	1.43%
R134a	0.34%	0.74%	0.45%	0.77%	0.50%
Steam	0.72%	1.55%	0.82%	1.05%	0.87%
Average	0.42%	0.84%	0.63%	0.93%	1.05%

Table 5 Comparison of rms entropy errors

Compound	Present Method	Redlich -Kwong	Soave	Wilson	Barnes -King
Helium	0.54%	0.73%	0.94%	1.30%	5.06%
Hydrogen	1.16%	1.11%	1.04%	0.82%	4.89%
Methane	0.46%	0.48%	0.51%	1.19%	0.89%
Nitrogen	1.68%	1.70%	1.61%	2.89%	1.89%
Ethylene	0.68%	0.77%	0.87%	1.62%	0.76%
Propane	0.16%	0.42%	0.28%	0.73%	0.21%
I-Butane	0.15%	0.38%	0.25%	0.60%	0.20%
Carbon Dioxide	0.73%	1.02%	1.00%	2.01%	0.95%
N-Pentane	0.20%	0.47%	0.21%	0.46%	0.21%
Ammonia	1.07%	1.50%	1.20%	1.70%	1.20%
R134a	0.28%	0.59%	0.46%	0.96%	0.49%
Steam	0.57%	1.22%	0.69%	1.24%	0.75%
Average	0.64%	0.87%	0.75%	1.29%	1.46%

- Only the present method and the original Redlich-Kwong equation should be used for $\omega < 0$. With reference to Figs. 2–6, this includes all points with $P_R > 4$. But, even at lower reduced pressures, the other modified forms show less accuracy when $\omega < 0$.
- Soave's model yields an accuracy comparable to the present method when $P_R < 1$. This result is consistent with the model's development from vapor pressure data for vapor-liquid equilibrium prediction.
- The Barnes-King model also shows an accuracy comparable to the present method for $P_R < 1$. Presumably this model also was developed for lower reduced pressures.
- Wilson's model tends to lose accuracy for $P_R > 0.7$ and shows larger deviations near the saturation line than the other models. Even in the lower reduced pressure range, the Soave and Barnes-King models appear to be superior.
- All five equations show increased errors near the saturation line. Surprisingly, Soave's model does not appear to offer any advantage over the other models in this region.

Enthalpy-Entropy Predictions

Following Ried et al. (1977) the enthalpy and entropy departure functions are defined by

$$A - A^0 = \int_\infty^V \left(P - \frac{RT}{V}\right) dV - RT \ln \frac{V}{V^0}$$

$$S - S^0 = -\frac{\partial}{\partial T}(A - A^0)_V$$

$$H - H^0 = A - A^0 + T(S - S^0) + RT(Z - 1) \qquad (8)$$

where the superscript, 0, identifies values at a reference pressure, P^0, where the ideal gas law applies. Departure functions for all of the variants of the Redlich-Kwong model can be shown to be given by

$$H - H^0 = PV - RT + \frac{1}{b}\left(T\frac{\partial a}{\partial T} - a\right) \ln\left[\frac{V+b}{V}\right] \qquad (9)$$

$$\frac{S - S^0}{R} = \ln\left[\frac{V}{V^0}\frac{V-b+c}{V}\right] + \frac{1}{Rb}\frac{\partial a}{\partial T} \ln\left[\frac{V+b}{V}\right] \qquad (10)$$

where the proper form of a, b, and c are employed for the various forms (note that $c = 0$ for all but the present method). To avoid any bias due to inaccuracy in the ideal gas curve fits used to predict H^0 and S^0, enthalpy and entropy errors were evaluated based upon differences between the lowest pressure data point and all other data points for each temperature in each data set. The thermodynamic variable errors were expressed as

$$H \text{ error} = \frac{\Delta H}{C_p T}; \quad S \text{ error} = \frac{\Delta S}{C_p} \qquad (11)$$

Tables 4 and 5 show the rms errors expressed in this fashion. Again, the error analysis dropped all points for which both the data and the equation of state indicated that no significant nonideal gas behavior was present.

With regard to enthalpy departure, it can be seen that the present method is superior to all of the other forms of the Redlich-Kwong equation evaluated here. Indeed, it achieves the lowest rms enthalpy error for all twelve compounds considered. Except for $\omega < 0$, the Soave and Barnes-King models also yield better accuracy than the original form. Wilson's model shows less accuracy, again directly related to local deviations at reduced pressures above about 0.7.

With regard to entropy departure, the present method again achieves the best accuracy. It consistently yields the lowest rms errors (except for nitrogen, where Soave's model shows a slight advantage). Soave's model and the Barnes-King model (except for $\omega < 0$) and the original equation also offer good accuracy. Wilson's model shows the largest entropy deviations, again, due to large deviations for $P_R > 0.7$.

Conclusions

The modified Redlich-Kwong equation of state presented here offers significantly better prediction accuracy than the original form and the other modified forms evaluated. The equation has been validated over a range of acentric factor values from −0.464 to 0.344, which includes most values of practical interest. The present method also removes the large, local inaccuracy of the other Redlich-Kwong models near the critical point. The revised equation is as simple as the original form, making it very attractive for use in fluid dynamic analysis applications, where computational speed is a critical consideration. Conversion of existing Redlich-Kwong computational methods to this new form should be relatively trivial.

The present method requires two additional parameters relative to the original form—the acentric factor and the critical point compressibility factor. Both of these parameters are readily available for nearly all compounds of interest. In the rare cases where this is not true, suitable estimation methods are available (e.g., Ried et al., 1977). For gas mixtures, a direct extension of the original Redlich-Kwong mixing rules should be appropriate, i.e.,

$$T_c^{(1+n)} = \frac{[\Sigma x_i \sqrt{T_{ci}^{(2+n)}/P_{ci}}]^2}{\Sigma(x_i T_{ci}/P_{ci})} \qquad (12)$$

$$P_c = \frac{T_c}{\Sigma(x_i T_{ci}/P_{ci})} \qquad (13)$$

$$\omega = \Sigma(x_i \omega_i) \qquad (14)$$

$$Z_c = \Sigma(x_i Z_{ci}) \quad (15)$$

$$M = \Sigma(x_i M_i) \quad (16)$$

Based on the present comparison of predictions with tabulated gas property data, users of the Soave and Barnes-King models should use caution when applying those methods for $P_R > 1$. For Wilson's model, caution is recommended for $P_R > 0.7$. These three modified forms of the Redlich-Kwong equation should not be used for compounds with a negative acentric factor. Of the five models evaluated, only the original Redlich-Kwong model and the present method were found suitable for unrestricted use for the compounds and thermodynamic data ranges considered. The present method yields typical rms prediction errors approximately 50 percent lower than the original form.

References

Akin, S. W., 1950, "The Thermodynamic Properties of Helium" *Trans. ASME*, Aug., pp. 751–757.

Barnes, F. J., 1973, Ph.D. thesis, Department of Chemical Engineering, University Of California, Berkeley.

Canjar, L. N., and Manning, F. S., 1967, *Thermodynamic Properties And Reduced Correlations For Gases*, Gulf Publishing, Houston.

NIST, 1991, "NIST Thermodynamic Properties Of Refrigerants And Refrigerant Mixtures Database," National Institute of Standards and Technology, Gaithersburg, MD.

Pitzer, K. S., 1955, *Journal of the American Chemical Society*, Vol. 77, pp. 3427–3440.

Redlich, O., and Kwong, J., 1949, *Chem. Rev.*, p. 233.

Ried, R. C., Prausnitz, J. M., and Sherwood, T. K., 1977, *The Properties of Gases And Liquids*, McGraw-Hill, New York.

Soave, G., 1972, "Equilibrium Constants From a Modified Redlich-Kwong Equation Of State" *Chemical Eng. Science*, Vol. 27, pp. 1197–1203.

Wilson, G. M., 1966, "Calculation Of Enthalpy Data From A Modified Redlich-Kwong Equation Of State" *Adv. Cryogenic Eng.*, Vol. 11, p. 392.

Multidimensional In-Cylinder Flow Calculations and Flow Visualization in a Motored Engine

Bahram Khalighi
Staff Research Engineer,
Engine Research Department,
General Motors Research and Development Center,
Warren, MI 48090-9055

Multidimensional simulations of coupled intake port/valve and in-cylinder flow structures in a pancake-shape combustion chamber engine are reported. The engine calculations include moving piston, moving intake valve, and valve stem. In order to verify the calculated results, qualitative flow visualization experiments were carried out for the same intake geometry during the induction process using a transient water analog. During the intake process the results of the multidimensional simulation agreed very well with the qualitative flow visualization experiments. An important finding in this study is the generation of a well-defined tumbling flow structure at BDC in the engine. In addition, this tumbling flow is sustained and amplified by the compression process and in turn causes generation of a high turbulence level before TDC. Many interesting features of the in-cylinder flow structures such as tumble, swirl, and global turbulent kinetic energy are discussed.

Introduction

The in-cylinder fluid motion in internal combustion engines is one of the most important factors controlling the combustion process. A good understanding of fluid motion during induction and compression strokes is critical to developing engine designs with the most desirable operating and emissions characteristics (Heywood, 1987). Many experimental and computational methods have contributed to understanding the role of in-cylinder flow structures in internal combustion engines (Kyriakides and Glover, 1985; Gosman, 1985; Arcoumanis et al., 1982; Haworth et al., 1990; Khalighi, 1990; Henriot et al., 1989; Hirotomi et al., 1981; Vafidis et al., 1987).

In recent years, many multidimensional modeling programs have emerged that offer researchers and designers valuable insights that can not be gleaned from the use of test-bed analysis alone (O'Conner, 1992). Although there are common flow characteristics in all engines, the exact flow depends on the particular engine under investigation. In most cases, multidimensional models have complemented the experimental work in identifying important in-cylinder flow characteristics for a particular engine that can impact the engine performance.

The aim of the present investigation is to apply an in-house developed Computational Fluid Dynamics (CFD) code (Haworth et al., 1990) to investigate the in-cylinder flow structures generated in a pancake-shaped combustion chamber engine during both intake and compression strokes. An attempt has been made to verify the computational results using qualitative in-cylinder flow visualization. The flow visualization study was carried out for the same engine utilizing the transient water analog used in our previous studies (Khalighi, 1990 and Khalighi, 1991).

Contributed by the Fluids Engineering Division for publication in the JOURNAL OF FLUIDS ENGINEERING. Manuscript received by the Fluids Engineering Division September 21, 1993: revised manuscript received June 27, 1994. Associate Technical Editor: O. Baysal.

Engine Geometry and Configurations

The engine specifications adopted for the present study are summarized in Table I. This engine geometry is intended to represent a pancake-shape combustion chamber with one intake valve and a centrally located spark plug. The engine's intake system consists of a bell-mouth, a 90-degree circular bend, a straight pipe (intake runner), and a 90-degree circular intake port all with the same circular cross sections. The bell-mouth is installed at the entrance of the runner to ensure a uniform entry velocity distribution into the intake system. A schematic of the intake runner and port is illustrated in Fig. 1. The valve guide does not protrude into the port and thus the illustrated port-wall curvature is maintained where the valve stem passes through the port wall.

Computational Approach

In this section, a brief description of the numerical algorithm and turbulence modeling is given. Next, initial and boundary conditions are described, followed by a brief presentation of the computational mesh and grid generation.

Numerical Algorithm and Modeling. An in-house computational fluid dynamics (CFD) code is used for the present study (Haworth et al., 1990 and Haworth et al., 1993a). This code is a general finite volume based approach and is suitable for solving problems which are: one, two, or three-dimen-

Table 1 Engine specifications

Bore	92.00 mm
Stroke	86.00 mm
Con. rod length	223.50 mm
Compression ratio	8:1
Max. intake valve lift	8.90 mm at 474 degree after TDC
IVO	364 deg after TDC (lift = 0.50 mm)
IVC	590 deg after TDC (lift = 0.25 mm)
Engine speed	1300.00 r/min
MAP	46.00 kPa

Table 2 Model constants used in the k-ϵ equations

Constant	Value
C_μ	0.09
C_1	1.44
C_2	1.93
C_3	−0.34
σ_k	1.00
σ_ϵ	1.19
k	0.4187

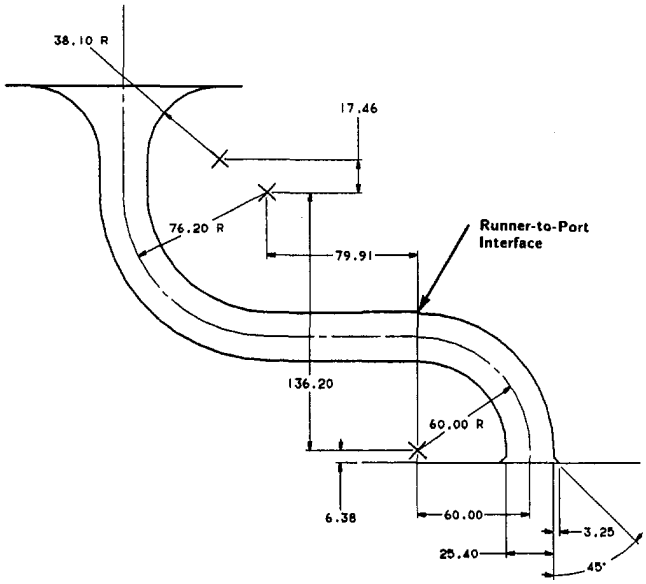

Fig. 1 The engine intake runner, port, and valve seat

sional, transient or steady, turbulent or laminar, compressible or incompressible; and which depend on heat and species transfers. The principal equations solved are the mean momentum, mean internal energy, turbulence kinetic energy (k), and viscous dissipation rate of turbulence energy (ϵ). The mean density is calculated from an equation of state. A standard two-equation $k-\epsilon$ turbulence model is used. The model constants adopted for this study are summarized in Table 2. These constants have been used for several previous engine calculations (Haworth et al., 1990) and, hence, are adequate for our application. Complete details of the derivation of the governing equations and the turbulence modeling may be found in Haworth et al., 1990.

The governing partial differential equations are discretized on an unstructured finite element-like mesh of arbitrary hexahedral cells (Haworth et al., 1990 and Haworth et al., 1993a). This approach provides maximum geometric flexibility, which is particularly important for generating grids in engine applications. All computed variables (velocities, turbulence, densities, etc.) are located at cell centers. Blended differencing has been implemented for the approximation of spatial derivatives in the mean momentum equations. This includes the standard (first-order) upwind differencing and the central differencing (second-order) numerical schemes. Blending is controlled by a parameter γ as described by Haworth et al. (1990). This parameter varies between $\gamma = 0$ for pure upwind differencing and $\gamma = 1$ for pure central differencing. For our study, the value of $\gamma = 0.5$ was used. Another important parameter is the computational time-step which was varied from 1/4 crank-angle at intake valve opening (IVO) and intake valve closing (IVC) to one crank-angle during the computation.

To account for the motion of the intake valve and the piston in an unstructured grid environment, a general grid motion treatment was employed. This algorithm allows three-dimensional deformation of the computational mesh in response to arbitrary motion of the boundaries (Haworth et al., 1990). In addition, a nonaligned-interface (shearing grid) capability is utilized which allows for surfaces inside the computational mesh whose cell faces need not match across common surfaces. This allows simpler or optimum mesh topologies to be selected.

In a recent article, Demirdzic and Peric (1988) have presented a volume conservation constraints applicable to numerical solutions of fluid flow problems in moving coordinates. The algorithm used in the present study satisfies this constraint exactly, since grid point, and not cell face, velocities are being solved for.

Initial and Boundary Conditions. The calculations are started at intake valve opening (IVO) with the piston and the intake valve assigned their appropriate position and speeds. The in-cylinder axial mean velocity is assumed to vary linearly between the piston velocity and the velocity at the port outlet. The in-cylinder radial and tangential (x and y) velocity components as well as mean velocity in the port, are set to be zero. The initial fluid temperature, mean density, pressure and species concentrations are assumed to be uniform inside the cylinder as well as inside the intake port. Initial turbulence kinetic energy and its dissipation rate are scaled to the mean piston speed as described by Haworth et al., 1990.

Boundary conditions are specified at all moving (piston and valve) and stationary walls (cylinder and port walls) as well as the intake port entrance (orifice). This includes mean velocities, temperatures, turbulent kinetic energy (k) and turbulence dissipation rate (ϵ). At the port-orifice entrance, constant and uniform mean static pressure and temperature are specified. Turbulence kinetic energy at the orifice is scaled to the mean velocity, while the dissipation term is tied to the port diameter. A detailed description of boundary treatments may be found in Haworth et al., 1990.

Grid Generation. Figure 2 outlines the computational mesh at 540 deg crank angle (BDC) used in this investigation. TDC at the start of intake is defined as 360 deg crank angle throughout this paper. The computational model reflects the geometry of the hardware used in the experimental studies. The total number of computational cells is approximately 60,000 for this model. The model includes the intake port, intake valve, valve stem, runner, and the intake bell-mouth as shown in Figs. 1

Nomenclature

BDC = bottom dead center
IVC = intake valve closure
IVO = intake valve opening
TDC = top dead center
TR_x = x component of tumble ratio
TR_y = y component of tumble ratio
SR_z = swirl ratio
U_p = mean piston speed
k = turbulent kinetic energy
u' = turbulence fluctuation
ϵ = dissipation rate

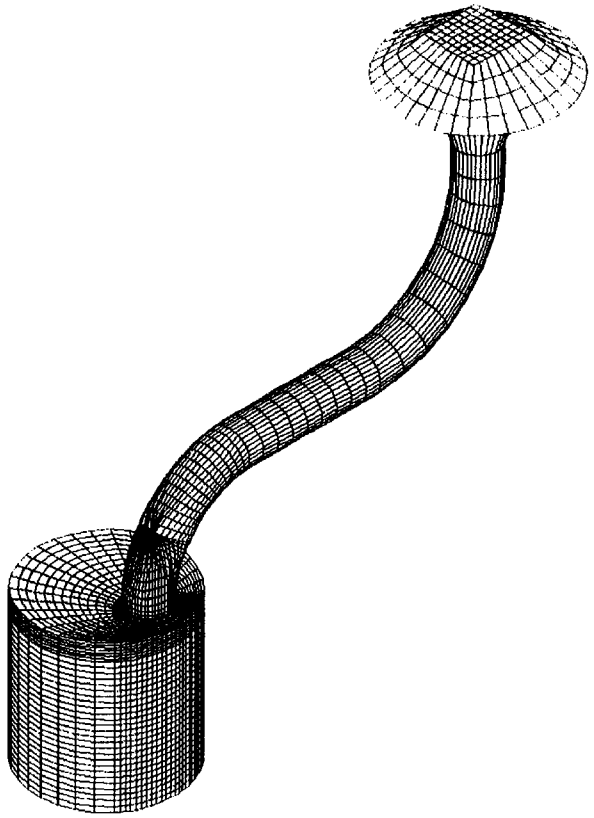

Fig. 2 Outline of the computational mesh at BDC

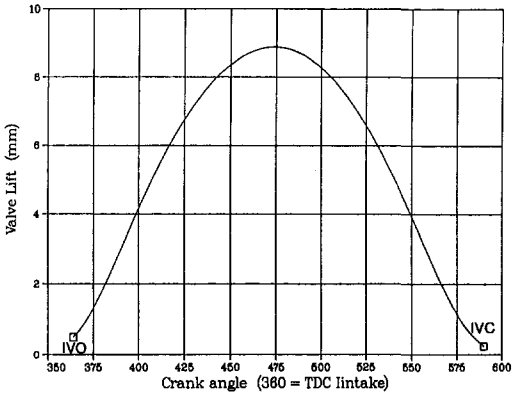

Fig. 3 Intake valve lift profile

and 2. The exhaust valve and port are not modeled for this study. The intake valve lift profile used for the calculations is shown in Fig. 3. In order to carry out the computations, the valve lift profile had to be truncated at both ends (opening and closing). This compromise was made to ensure that the minimum valve lift was limited to a nonzero value so that computational cells in the valve seat region remain of nonzero volume. In all the calculations, the intake valve opening (IVO) and intake valve closing (IVC) are set at 364 and 590 deg, respectively (see Fig. 3).

Numerical Accuracy. Numerical accuracy remains an issue in multidimensional computational fluid dynamics for in-cylinder flows. The degree of spatial accuracy of the numerical solution is known to have a strong influence on computed in-cylinder angular momentum, turbulence level, and mixing between fresh charge and residual gas, in particular.

The conventional approach to assessing numerical accuracy in multidimensional fluid flow calculations has been to per-

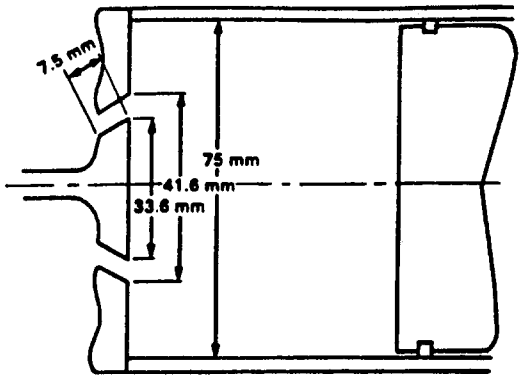

Fig. 4 Axisymmetric piston-cylinder assembly (Vafidis and Whitlaw, 1984)

form grid refinement tests. Our present calculations with two different grid sizes 60,000 and 120,000, showed insignificant changes in the levels of tumble (TR_x and TR_y) and swirl (SR_z) inside the engine. Based on our calculations an order-of-magnitude increase in the number of cells are required for substantial benefits in accuracy. On the other hand, higher-order schemes have been seen to yield substantial improvement in results.

It is well known that standard linear-upwind differencing yields excessive artificial dissipation. Higher-order numerical schemes offer a computationally efficient route to the accurate representation of three-dimensional time-dependent internal flows on practical computational meshes. There is a substantial benefit to using values of γ as small as 0.5 (for the present study), even though the formal accuracy of the convective differencing remains first order in space. To illustrate the importance of numerics, the computed BDC tumble ratio (TR_x) in the present computation is $TR_x = -1.5$ using the 50/50 percent blend, while pure linear upwind differencing ($\gamma = 0$) yields $TR_x = -1.3$. The higher tumble ratio magnitude results from improved conservation of angular momentum with higher-order scheme. Furthermore, the computed turbulence kinetic energy increased markedly (20 percent) with improved numerics.

To address the issue of accuracy in more details we present calculations for an axisymmetric piston-cylinder assembly shown in Fig. 4. This flow has been the subject of numerous modeling and experimental studies (Gosman et al., 1980, Diwaker and El Tahry, 1983, Vafidis and Whitelaw, 1984, Haworth and El Tahry, 1991, Haworth et al., 1993b), and the reader is referred to these studies for details of the flow and for comparison between computations and measurements. Example comparisons between computed and measured mean axial velocities at 36 deg after top-dead-center (TDC) is shown in Fig. 5 (Haworth et al., 1993b). It can be seen that agreement is good except at the second measurement station, where computed profile undershoots the measured one.

Local convergence is shown in Fig. 6. In this figure, the computed peak mean axial velocity at the measurement location closest to the head plane at 36 deg after TDC (Fig. 5) has been plotted as a function of mesh spacing n_r and of differencing parameter γ. It can be seen that increasing the spatial accuracy of the convective differencing scheme is an effective approach to improved accuracy: an order-of-magnitude increase in the number of computational cells with $\gamma = 0$ gives the same improvement as increasing γ from 0.0 to 0.7 with $n_r = 28$ (Haworth et al., 1993b). These results are typical of our experience with in-cylinder and other internal flows.

Experimental Procedures

In order to validate the computational results obtained from our calculations, an experimental flow investigation was car-

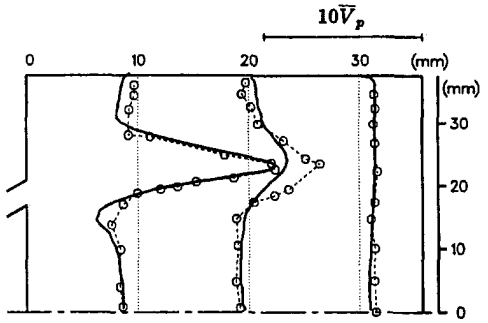

Fig. 5 Computed (bold solid lines) and Measured (symbols, light dashed lines) mean axial velocity profiles at 36 deg after TDC normalized by the mean piston speed. Computations are for a 50 × 50 mesh with γ = 0.9 (Haworth et al., 1993b)

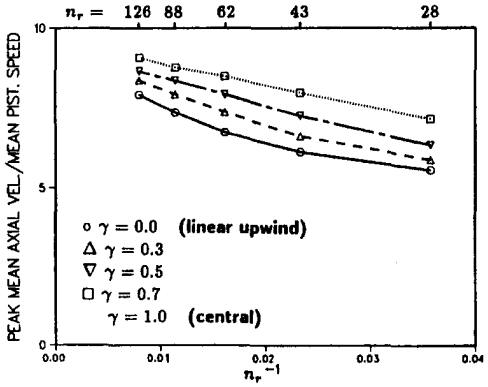

Fig. 6 Peak mean axial velocity at 10 mm from the head versus grid spacing n_r^{-1} and differencing scheme γ, axisymmetric configuration (Haworth et al., 1993b)

ried out. The experimental study involved in-cylinder flow visualization during the induction stroke.

A flow box model of the engine head was fabricated and mounted on the transient water analog (Khalighi, 1990 and Khalighi, 1991). The working fluid was water which was seeded with a small amount of neutral density particles. Particles used for the flow visualization were Pliolite spheres with sizes of 250–300 μm. For these experiments, the field of interest was illuminated by a continuous laser light sheet, and a Panasonic video system (S-VHS system) was used to record the in-cylinder flow development during the induction process. For this study the transient water analog was operated at 65 r/min, which corresponds to an equivalent engine speed of 1300 r/min. Details of the operation and similarity discussion for the transient water analog are given in Khalighi, 1991. It should be mentioned that the water analog experiment is used only to validate the intake process and can not be used for validation of the compression stroke.

Results

The coupled port-and-cylinder modeling (computation) study for the engine is carried through the induction and compression strokes starting shortly after TDC intake (TDC intake is 360 deg). Computational results presented in this report are for the in-cylinder flow simulating a single part-load, low-speed engine operating condition (46 kPa manifold pressure, 1300 r/min) under motored conditions (no combustion).

Results are presented in two sections. First, detailed in-cylinder spatial mean velocity fields are discussed. The corresponding in-cylinder flow visualization (experimental) result is presented and compared with the computed one. The second set of results (computed) are global quantities of interest such as tumble and swirl ratios, and the mass-averaged turbulence kinetic energy (k).

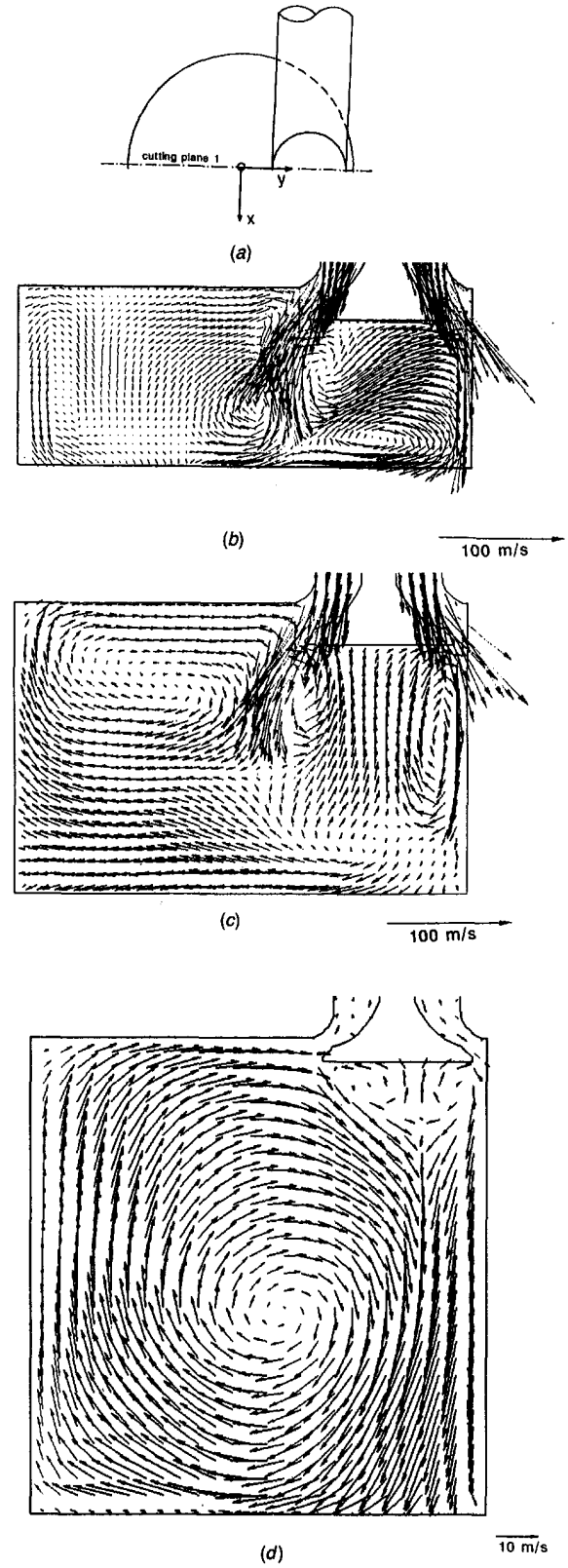

Fig. 7 Computed velocity field on cutting plane 1: (*a*) position of the cutting plane; (*b*) 420 deg; (*c*) 450 deg; (*d*) BDC

Spatial In-Cylinder Flow Structures

Induction Process (Intake Stroke). Figure 7 illustrates the calculated in-cylinder flow structures on an axial cutting plane.

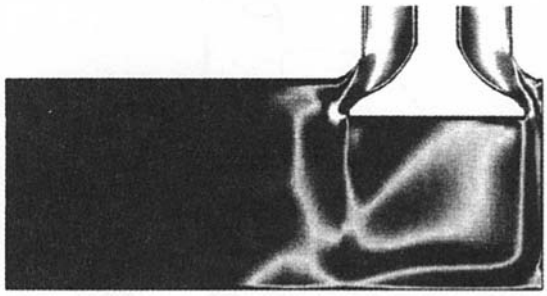

Fig. 8 Velocity contours on cutting plane 1 at 420 deg. Dark color (around the intake valve) represents the jet penetration inside the cylinder.

The cutting plane, the location of the intake valve, and the coordinate system are also depicted in the figure. This figure shows the development of the intake process during an engine cycle at three different crank angles. Velocity fields are presented with vectors (arrows) whose lengths are proportional to the local velocities at the corresponding locations in the flow field. The directions of the velocities are specified by the direction of the arrows.

These velocity fields indicate the presence of a structured flow comprised of two pairs of counter-rotating vortices under the intake valve during the early induction (420 deg in Fig. 7(*b*)). These flow structures are visible for most of the intake flow process. As the piston moves towards BDC, a coherent tumbling motion is being developed in this cutting plane. At BDC the in-cylinder flow field is clearly dominated by this single large scale flow structure (Fig. 7(*d*)) with its axis of rotation in the $-x$ direction (clockwise rotation in the figure). The $+x$ direction defines the axis of a counter clockwise vortical motion on this plane.

To see how the tumbling flow is generated in this engine configuration, it is useful to re-examine Fig. 7; this time using contour plots as shown in Fig. 8 to represent velocities. Different gray levels in this figure correspond to instantaneous spatial velocities, and it is suitable to observe the jet flow penetrations inside the cylinder. As can be observed from this figure, the in-cylinder flow is characterized by the presence of two distinct jet-like flows emerging from the valve curtain area during early induction (dark area on the right and left sides inside the valve). It should be noted that these two distinct jet flows are parts of a single annular (conical) jet produced by the intake valve opening. However, for convenience it is treated as two separate jets on a two-dimensional cutting plane. As the piston moves downward, the jet flow on the right side (see Fig. 8) maintains its relatively high momentum and attaches to the cylinder walls while the jet flow on the left side goes down the cylinder axis. During the induction stroke the strong jet (right side) is redirected by the piston face which produces the tumbling flow later at BDC.

It was rather surprising that such a well defined tumbling flow structure (Fig. 7(*d*)) existed for this engine configuration (with standard intake valve) since in most previously reported works, shrouds were used to produce such a well defined tumble in pancake-shape geometry engines (Kyriakides and Glover, 1985; Gosman et al., 1985). Therefore, it was necessary to verify the in-cylinder flow structure obtained from these calculations. As mentioned earlier, this was accomplished by conducting flow visualization experiments using a transient water analog.

In making comparisons between the flow structures observed in the water rig and the calculated flow, one must remain aware of different natures of the quantities involved, i.e., cycle-resolved flow field for the former versus phase-averaged velocities for the latter. In cases where flow structures are repeatable from cycle to cycle, these comparisons are justified.

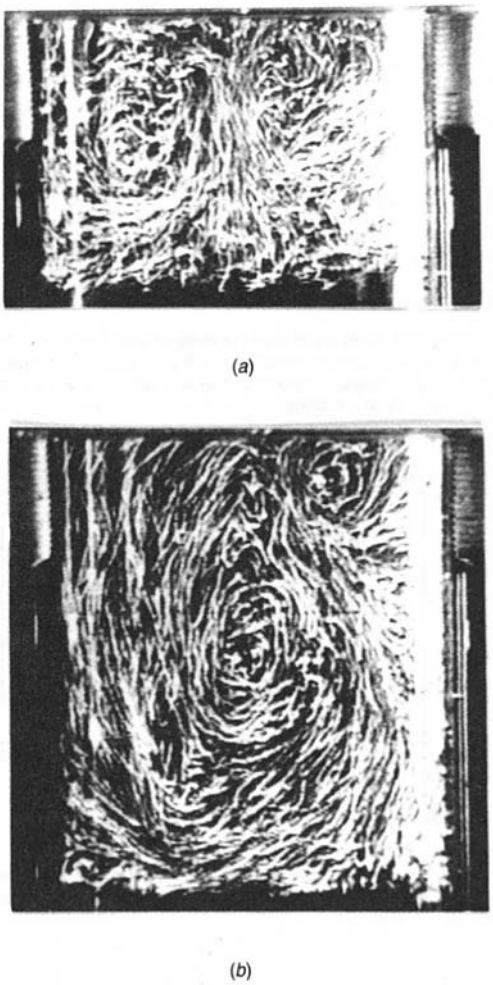

(*a*)

(*b*)

Fig. 9 Flow visualization pictures of the flow field on cutting plane 1: (*a*) 450 deg; (*b*) BDC

Our flow visualization experiments for the present engine configuration showed that the in-cylinder flow structure was repeatable from cycle to cycle except during early induction (to about 480 deg).

Figure 9 presents video images showing the in-cylinder flow structures for two different crank angles during intake for the same intake configuration. These pictures were taken on the same plane (cutting plane 1). As can be seen from these images, this intake configuration generates a well defined tumble at BDC, and the calculations (Fig. 7) have captured the qualitative features of in-cylinder flow structures very well. In particular, one can observe the generation of the counter rotating vortices under the valve during mid-induction and the well-defined tumbling flow at BDC (Fig. 9 (*b*)). In the water rig, it was also observed that a coherent tumbling motion is not established until near BDC intake; this is consistent with the computational results of Fig. 7.

Compression Process. Development of the in-cylinder flow structures during the compression stroke is shown in Figure 10 on the same cutting plane. This figure contains a sequence of velocity fields at three different crank angles, namely 630, 690, and 720 deg. As evident in this figure, the dominant feature of the mean flow field continues to be the main tumbling flow which becomes considerably compressed and weaker during the compression stroke. As the piston moves toward TDC, the vortex is confined under the intake valve near the cylinder wall (right-side wall in Fig. 10(*a*)). At TDC, however, the tumbling vortex is clearly dissipated and a pair of very weak vortices

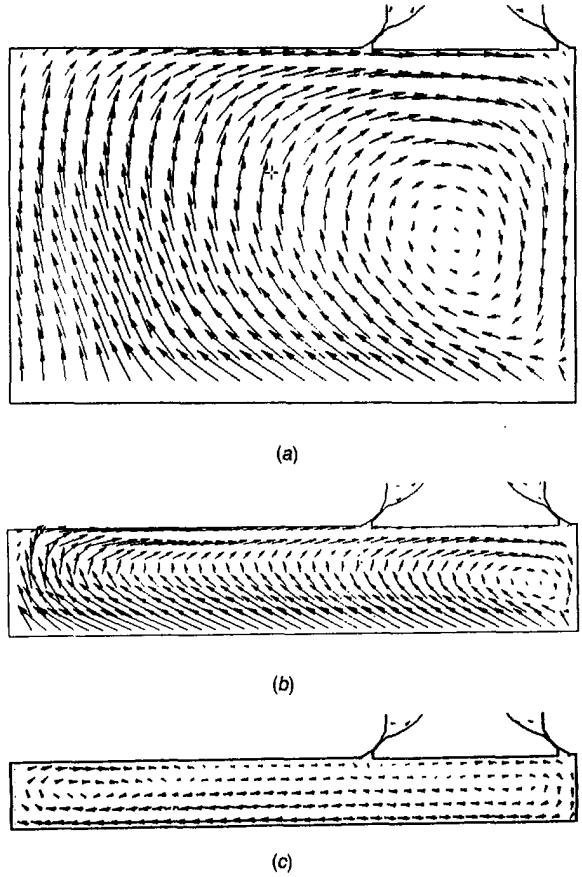

Fig. 10 Development of the in-cylinder flow during compression on cutting plane 1: (a) 630 deg; (b) 690 deg; (c) 720 deg

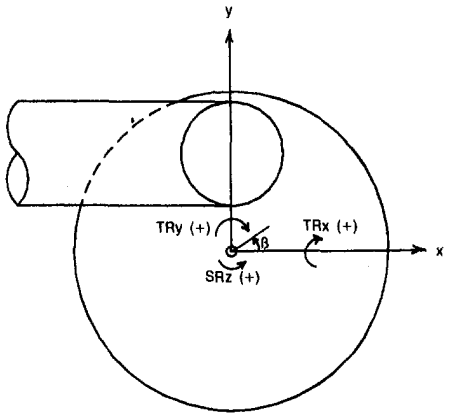

Fig. 11 Schematic of the tumble and swirl components and their corresponding axes of rotations

are apparent (with mean velocity of less than 1.5 m/s, Fig. 10(*c*)).

Evolution of Global Quantities. In this section we discuss the evolution of the computed global in-cylinder quantities during intake and compression strokes. These quantities are: tumble, swirl, and turbulence kinetic energy ($k = u'/U_p$). U_p is the mean piston speed.

Tumble and swirl ratios are the total angular momentum of the in-cylinder fluid about the respective axis, divided by the moment of inertia about that axis, and normalized by the crankshaft angular speed. Tumble and swirl ratios are calculated with respect to the instantaneous fluid center of mass as described in Haworth et al., 1990. Figure 11 illustrates the

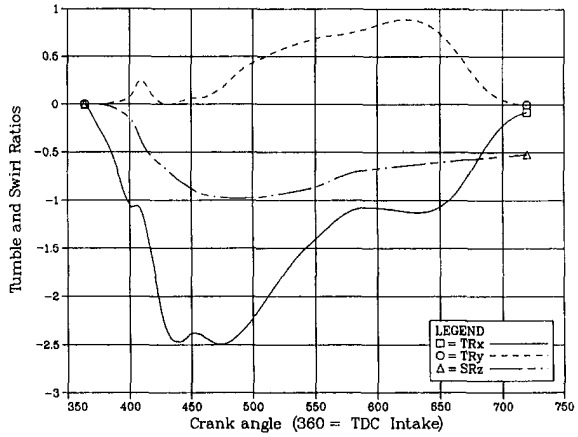

Fig. 12 Tumble and swirl ratios about the instantaneous center-of-mass

schematic of the various tumble and swirl components (TR_x, TR_y, and SR_z) and their corresponding axes of rotation.

Tumble and Swirl Ratios. Figure 12 shows the evolution with crank angle of the tumble (TR_x and TR_y) and swirl (SR_z) ratios for this engine. Looking at angular momentum as an equivalent rotation rate in this engine, we observe some interesting features of the global behavior of the in-cylinder tumble. First, in general the dominant tumble components TR_x (Fig. 12) increases (absolute value) during the early induction, reaches its peak, and then significant decay occurs, particularly during late compression to a level of almost zero at TDC. Second, TR_y increases (absolute value) somewhat during part of the compression stroke as the piston moves upward. This is usually referred to as "spinning-up" during compression. Similar observations have been reported by Gosman et al., 1985 and Haworth et al., 1990. This "spin-up" process is due to decreasing moment of inertia of the in-cylinder fluid as the piston rises while the fluid tends to maintain its angular momentum (Gosman et al., 1985; Haworth et al., 1990). Both the rapid destruction of the tumble motion and the "spin-up" are linked to turbulence generation at TDC and will be discussed later.

As seen in Fig. 12, swirl ratio (SR_z) increases (absolute value) during the intake stroke and reaches its maximum level (swirl ratio of 1) at approximately 480 deg. From this crank angle on, swirl magnitude decreases (absolute value) through the rest of the engine cycle (i.e., intake and compression). This reduction is due to the dissipation of angular momentum in the cylinder (physical), and also some artificial dissipation introduced by the numerical scheme. Therefore, the actual dissipation rate in the swirling process is most likely somewhat smaller than the one computed here.

The computed and measured intake-valve-closure (IVC) swirl ratios for this engine configuration are 0.65 (at 590 deg) and 0.70, respectively. The agreement between the calculated and measured swirl is excellent. The measured swirl value was obtained from steady-flow measurements of torque at fixed valve lifts; these data are processed by an engine simulation program to yield equivalent swirl ratio. The result from such an experiment is generally regarded as the swirl value at IVC. The momentum summation done by the engine simulation program does not account for dissipation and, hence, is expected to be somewhat higher.

Global Turbulence Kinetic Energy. A very interesting aspect of this study is the relative behavior of the turbulence kinetic energy during compression. The evolution of the turbulent kinetic energy with crank angle for this engine configuration is shown in Fig. 13. This figure clearly illustrate the expected trend of higher turbulence energy during the intake process. There is a peak around 450 deg (maximum valve annulus flow velocities).

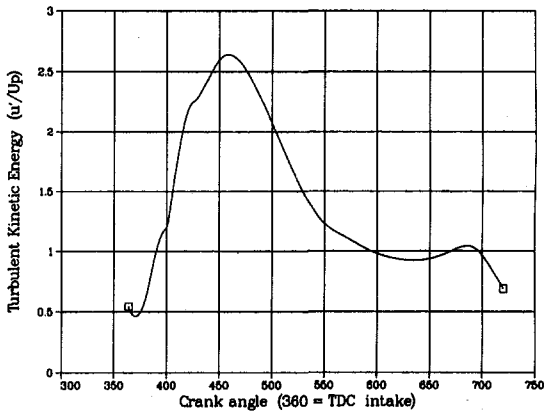

Fig. 13 Global in-cylinder turbulence kinetic energy as a function of crank angle

Looking at Fig. 13 it can be observed that a significant decay of the global turbulent kinetic energy occurs between 460 and 630 deg. It is after this point (630 deg) that the global turbulent energy is amplified rather than decayed. This additional turbulence produced just before TDC can significantly enhance flame propagation. The increase in the turbulence level is mostly attributed to generation of the well-defined tumble motion during the intake process which persists long enough into the compression stroke to be destroyed and enhanced by the compression process (Gosman et al., 1985 and Haworth et al., 1990). Therefore, this reiterates the fact that tumble is the major source of turbulence production inside the engine cylinder during compression while the effect of swirl on turbulence generation is minimal particularly during early combustion.

It should be noted that the initial phase of combustion is controlled by both flow and spark plug characteristics. From then on, flame propagation tends to become independent of ignition conditions and very sensitive to the remaining mean flow velocity field. This suggests that the role of swirl may in fact be important during late combustion, particularly for cyclic variability, since the tumbling flow clearly vanishes at TDC as discussed earlier. However, it is still not clear what conditions near TDC of compression are optimum from the point of view of enhanced burning and reduced cyclic variability.

Summary and Conclusions

Multidimensional in-cylinder flow calculations and flow visualization experiments were performed for a pancake-shape combustion chamber engine. Comparisons of the in-cylinder flow structures between computations and flow visualization experiments during the intake stroke revealed that our calculations have captured the general in-cylinder flow features very well.

It was rather surprising to see that this engine configuration produced a well-defined cylinder-size tumbling flow structure. The reason is, of course, the behavior of the intake jet flows emerging from the valve curtain area as seen in both the calculations and experiments. This engine configuration generated a jet flow which attached to the cylinder wall was then directed across the cylinder by the piston face.

Principal findings are as follows:

- The engine with standard intake valve generates a well-defined tumbling flow structure at BDC which is sustained and amplified by the compression process and in turn causes generation of a high level of turbulence before TDC.
- Computed flow fields during intake agreed fairly well with the flow visualization experiments.
- In order to generate a well-defined in-cylinder tumble it is essential for the jet flow emerging from the intake valve curtain area to attach to the cylinder wall and be redirected by the piston face.
- Computed swirl ratio at IVC (Intake Valve Closure) was in excellent agreement with the measured one under steady flow condition.

Acknowledgments

The author would like to thank D. C. Haworth and M. S. Huebler for their support and contributions during the course of this study.

References

Arcoumanis, C., Bicen, A. F., and Whitelaw, J. H., "Effect of Inlet Parameters on the Flow Characteristics in a Four-Stroke Engine," SAE Paper No. 820750, 1982.

Demirdzic, I., and Peric, M., 1988, "Space Conservation Law in Finite Volume Calculations of Fluid Flow," *International Journal for Numerical Methods in Fluids*, Vol. 8, pp. 1037–1050.

Diwaker, R., and El Tahry, S. H., 1983, "Comparison of Computed Flowfields and Wall Heat Fluxes with Measurements from Motored Reciprocating Engine-Like Geometries," *Computational Engineering*, Vol. 1, pp. 175–188.

El Tahry, S. H., 1982 "A Numerical Study on the Effect of Fluid Motion at Inlet-Valve Clousure on Subsequent Fluid Motion in a Motored Engine," SAE Paper No. 820035.

Glover, A. R., Hundleby, G. E., and Hadded O., 1988, "An Investigation into Turbulence in Engine Using Scanning LDA," SAE Paper No. 880379.

Gosman, A. D., Johns, R. J. R., and Watkins, A. P., 1980, "Development of Prediction Methods for In-Cylinder Process in Reciprocating Engines," Mattavi, J. N., and Amann, C. A., eds, *Combustion Modeling in Reciprocating Engines*, Plenum, New York, pp. 69–129.

Gosman, A. D., 1985, "Multidimensional Modeling of Cold Flows and Turbulence in Reciprocating Engines," SAE Paper No. 850344.

Gosman, A. D., Tsui, Y. Y., and Vafidis, C., 1985, "Flow in a Model Engine with a Shroud Valve—a Combined Experimental and Computational Study," SAE Paper No. 850498.

Haworth, D. C., El Tahry, S. H., Huebler, M. S., and Chang S., 1990, "Multidimensional Port-and-Cylinder-Flow Calculations for Two-and Four-Valve-per-Cylinder Engines: Influence of Intake Configuration on Flow Structure," SAE Paper No. 900257.

Haworth, D. C., and El Tahry, S. H., 1991, "A pdf Approach for Multidimensional Turbulent Flow Calculations with Application to In-Cylinder Flows in Reciprocating Engines," *AIAA Journal*, Vol. 29, pp. 208–218.

Haworth, D. C., Huebler, M. S., El Tahry, S. H., and Matthes W. R., 1993a, "Multidimensional Calculations for a Two-Stroke Cycle Engine: A Detailed Scavenging Model Variation," SAE Paper No. 932712.

Haworth, D. C., El Tahry, S. H., and Huebler, M. S., 1993b, "A Global Approach to Error Estimation and Physical Diagnostics in Multidimensional Computational Fluid Dynamics," *International Journal for Numerical Methods in Fluids*, Vol. 17, pp. 75–97.

Henriot, S., Coz, J. F., and Pinchon, P., 1989, "Three-Dimensional Modeling of Flow and Turbulence in a Four-Valve Spark Ignition Engine-Comparison with LDV Measurements," SAE Paper No. 890843.

Heywood, J. B., 1987, "Fluid Motion within the Cylinder of Internal Combustion Engines-The 1986 Freeman Scholar Lecture," ASME JOURNAL OF FLUIDS ENGINEERING, Vol. 109/3, Mar.

Hirotomi, T. et al., 1981, "Study of Induction Swirl in a Spark Ignition Engine," SAE Paper No. 810496.

Khalighi, B., 1990, "Intake-Generated Swirl and Tumble Motion in a 4-Valve Engine with Various Intake Configurations-Flow Visualization and Particle Tracking Velocimetry," SAE Paper No. 900059.

Khalighi, B., 1991, "Intake Swirl Process Generated by an Engine Head: a Flow Visualization Study," ASME *Journal of Engineering for Gas Turbines and Power*, Vol. 113, No. 3, pp. 433–439.

Kyriakides, S. C. and Glover, A. R., 1985, "A Study of the Correlation Between In-Cylinder Air Motion and Combustion in Gasoline Engines," IMechE.

O'Conner, L., 1992, "Computational Fluid Dynamics: Giving A Boost to Engine Design," *Mechanical Engineering*, Vol. 114, No. 5, pp. 44–50, May.

Vafidis, C., and Whitelaw, J. H., 1984, "Intake Valve and In-Cylinder Flow Development in a Reciprocating Model Engine," Report FS/84/32, Imperial College, Department of Mechanical Engineering, London, UK.

Vafidis, C., Vorropoulos, G., and Whitelaw, J. H., 1987, "Effect of Intake Port and Combustion Chamber Geometry on In-Cylinder Turbulence in a Motored Reciprocating Engine," ASME Winter Annual Meeting.

Mathematical Modeling of Swirling Flames of Pulverized Coal: What Can Combustion Engineers Expect From Modeling?

R. Weber

A. A. F. Peters

P. P. Breithaupt

International Flame Research Foundation,
IJmuiden, The Netherlands

B. M. Visser
Gasunie Research,
Groningen, The Netherlands

The present study is concerned with mathematical modeling of swirling pulverized coal flames. The attention is focused on the near burner zone properties of high- and low-NO_x flames issued from an Aerodynamically Air Staged Burner of 3.4 MW thermal input. The swirling combusting flows are calculated using the k-ϵ model and second-order models of turbulence. The Eulerian balance equations for enthalpy and mass fractions of oxygen, volatiles, carbon monoxide and final combustion products (CO_2 + H_2O) are solved. The Lagrangian particle tracking is accompanied by appropriate models of coal devolatilization and char combustion. Nitric oxide emissions are calculated using a NO_x post-processor for thermal-, prompt- and fuel-NO. The objective of this paper is to examine whether the engineering information required for designing industrial burners is obtainable through the mathematical modeling. To this end, the flame computations, including NO emissions, are compared with the measured in-flame data. The guidelines as to the combination of physical submodels and model parameters needed for quality predictions of different flame types are given. The paper is a shorter version of our recent ASME publication (Weber et al., 1993).

Introduction

Manufacturers and users of coal combustion equipment are making significant efforts to design efficient and reliable combustion systems which would meet the present emission standards or even more stringent forthcoming regulations. Modifications to and retrofitting of the existing equipment need to be carried out without reduction in overall process efficiency and reliability. Both tasks require careful considerations of the combustion chamber, burners, heat extraction unit and flue gas cleaning equipment. An integral part of the combustion system is either a single flame or more frequently a row of flames. Engineering information required for designing flames suitable for a particular process can be classified into:

First-order information:

—knowledge of flame shape and length, and an estimate of flame temperatures with accuracy of around 200°C,
—estimate of heat fluxes to the heat extraction unit with accuracy of around 30–40 percent,
—location of regions of high- and low-mixing intensities;

Second-order information:

—knowledge of temperature distribution (accuracy within 100°C), oxygen concentration (acc. 0.3 percent) and unburned fuel (acc. 0.3 percent),
—identification of furnace and burner zones of slagging potential;

Third-order information:

—knowledge of flue emissions of nitrogen oxides, carbon monoxide, sulphur oxides, soot, Polycyclic Aromatic Hydrocarbons (PAH) and char burnout,
—knowledge of in-flame temperatures (acc. 50°C) and detailed chemistry including identification of regions of high pollutant formation rate.

The objective of this paper is to examine whether the three-level engineering information listed above, is obtainable through mathematical modeling. To this end, the flame computations are compared with in-flame data gathered in swirling flames of thermal input in the range 0.9–3.4 MW (Smart et al., 1989; Dugué et al., 1991).

General Classification of Swirling Flames

A range of well-defined flame types relevant to pulverized coal burner design can be identified. Figure 1 shows the var-

Contributed by the Fluids Engineering Division for publication in the JOURNAL OF FLUIDS ENGINEERING. Manuscript received by the Fluids Engineering Division August 24, 1993; revised manuscript received May 3, 1994. Associate Technical Editor: A. F. Ghoniem.

ious characteristic mixing patterns that result in the flame classification system (see Smart and Weber, 1989). Each of these basic flame types produces significantly different NO_x emission levels when firing the same coal.

A type-0 flame, produced without or with low inlet swirl, is a long jet-flame stabilized at the fuel injector or downstream. It is used in corner-fired boilers and cement-kilns. When a single, 2 MW type-0 flame of a highly volatile (34 percent daf) Scotts Brench coal containing 1.63 percent N (daf) is fired in the IFRF furnace, typical NO_x emissions are in the range 470–520 ppm (0 percent O_2) with burnout of circa 98 percent (Weber et al., 1987).

When a sufficiently high degree of swirl is imparted on the combustion air, an internal recirculation zone (IRZ) is formed. The pulverized fuel is rapidly entrained into swirling combustion air resulting in a short, intense, type-2 flame which ignites in the close vicinity of the coal injector. Coal devolatilization takes place on the IRZ boundary, in an oxygen-rich zone, and the NO_x emissions for Scotts Brench coal are high, being in the range 900–1000 ppm (0 percent O_2) with char burnout above 99.6 percent (Weber et al., 1987). Type-2 flames are encountered in wall-fired boilers equipped with conventional (high NO_x) burners.

A type-1 flame is a combination of type-2 and type-0 flame; the fuel jet penetrates either partially or fully through the internal recirculation zone. By promoting the coal devolatilization inside the oxygen depleted IRZ, a substantial reduction of nitrogen oxides emission can be achieved. A typical 2 MW, type-1 flame of Scotts Brench coal produces 200–400 ppm NO_x (0 percent O_2) with char burnout above 99.5 percent (Weber et al., 1987; Smart and Weber, 1987). A number of industrial low-NO_x burners designed to retrofit existing boilers utilize the principle of internal air staging to produce type-1 flames.

Fluid Flow in the Near Burner Zone

In our previous publications (Weber et al., 1987, Smart et al., 1988) and more recently in a study of Abbas et al. (1992), the paramount influence of quarl zone aerodynamics on emission of nitrogen oxides was demonstrated. It is essential that computations of near-field aerodynamics of swirl burners provide a good knowledge of not only the size and shape of the IRZ, but also the velocity profiles. These are required to describe the interaction between nonswirling particle-laden jet stream, the swirling combustion-air, and the IRZ. The flow-field resulting from such a complex interaction determines the trajectories of coal particles.

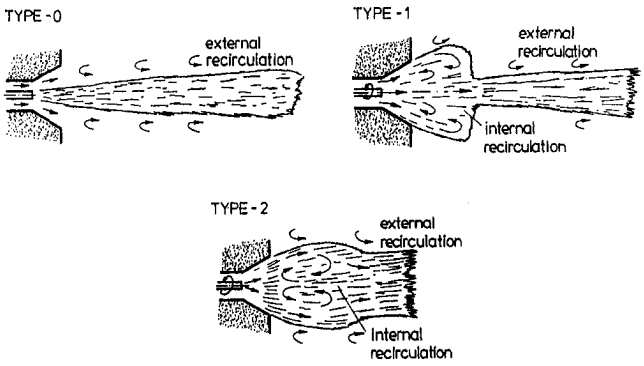

Fig. 1 Flame classification system

The importance of the interaction between a coal-laden primary air jet and the swirl induced IRZ is demonstrated in this article using the Aerodynamically Air Staged Burner (AASB) shown in Fig. 2 (Smart and Weber, 1989). The burner is equipped with a movable-block swirler producing a constant tangential velocity vortex of around 20 percent turbulence intensity. The near burner zone properties and consequently NO_x emissions can be reduced by optimizing trajectories of coal particles (Smart et al., 1988). Figure 2 shows a range of coal-particle trajectories within the AASB. The near burner flow field, momentum of the primary air and position of the fuel injector can be optimized to promote trajectories 3 and 4. By far, the simplest way of achieving this is by inserting the coal injector into the burner quarl.

Nomenclature

a = parameter of B_{pdf}
A_c = pre-exponential factor
b = parameter of B_{pdf}
B_{pdf} = Beta probability density function
D_p = particle diameter
ET = expectation of the fluctuating temperature
h = enthalpy
H_{CO} = lower calorific value of CO
H_{vol} = lower calorific value of volatiles
k_c = pseudo-reaction rate
k_d = oxygen diffusion rate to coal particle
$K_{e,NO}$ = equilibrium constant of reaction (R4)
M_{NO} = molecular weight of NO
p = static pressure
P_{O2} = bulk oxygen partial pressure
q = overall char combustion rate
s = variance coefficient
S_c = Schmidt number
S_j = source/sink term due to gaseous combustion and generation of gaseous species (volatiles, CO) from the coal phase
$\overline{s_{k-NO}}$, $k = t$, p, f = the time-averaged NO sources for thermal-, prompt- and fuel-NO
S_{part}, $S_{part,j}$ = source terms representing interactions between the solid and gaseous phase
T_b = burnt temperature
T_p = particle temperature
T_u = unburnt temperature
U_i, u_i = time-mean and fluctuating velocities
var T = variance of the fluctuating temperature
VM_{max} = high temperature volatile yield
[ ] = concentrations of chemical species
μ_{eff} = effective viscosity
ρ = fluid density
$\rho\overline{u_i u_j}$ = Reynolds stress
T_g = temperature of gas surrounding the coal particle

Subscripts

b = burnt
CO = carbon monoxide
d = diffusion
e = equilibrium
eff = effective
g = gas
i = co-ordinate direction or initial
j = coordinate direction or individual species number
p = coal/char particle
pdf = probability density function
p-NO = promt NO
t-NO = thermal NO
u = unburnt
vol = volatiles

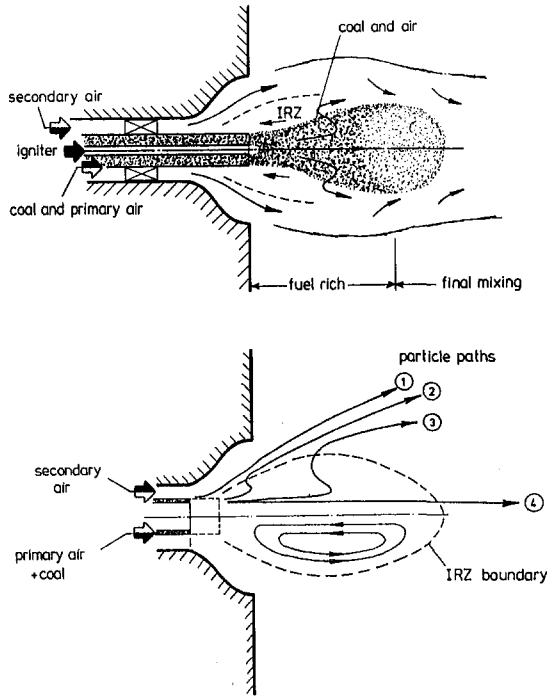

Fig. 2 The aerodynamically air staged burner (top) and particle trajectories in the near burner zone (bottom)

The Mathematical Model

Fluid Flow Equations. The computation of two-phase turbulent flows requires that the continuity equation,

$$\frac{\partial}{\partial x_i}(\rho U_i) = S_{\text{part}} \tag{1}$$

and the momentum balance equation,

$$\frac{\partial}{\partial x_i}(\rho U_i U_j) = -\frac{\partial p}{\partial x_j} + \frac{\partial}{\partial x_i}\left(\mu\left(\frac{\partial U_i}{\partial x_j} + \frac{\partial U_j}{\partial x_i}\right) - \rho\overline{u_i u_j}\right) + S_{\text{part},j} \tag{2}$$

be accompanied by a model of turbulence that relates the Reynolds stresses $\rho\overline{u_i u_j}$ to known or calculable quantities. In the above equations S_{part} and $S_{\text{part},j}$ are source terms representing interactions between the solid and gaseous phase. Three turbulence models are used in this study, the Reynolds Stress Model (RSM), the Algebraic Stress Model (ASM) and the k-ϵ model. Their formulation and constants are given in Weber et al. (1990).

Chemically Reactive Gaseous Species. Four gaseous species are considered: oxygen, volatile matter, carbon monoxide and final combustion products consisting of carbon dioxide and water vapor. The mass balance equation for species J is as follows:

$$\frac{\partial}{\partial x_i}(\rho U_i m_j) = \frac{\partial}{\partial x_i}\left(\frac{\mu_{\text{eff}}}{Sc}\frac{\partial m_j}{\partial x_i}\right) + S_j \tag{3}$$

where S_j is a source/sink term due to gaseous combustion and generation of gaseous species (volatiles, CO) from the coal phase. Details of the global combustion model, the eddy break-up turbulent combustion submodel and radiation can be found in the full paper (Weber et al., 1993).

Solid Phase. In utilities, coals are pulverized typically to 75 percent < 75 micron with the largest particles being around 150 micron. When injected into the flame, the particles are rapidly heated at a rate up to 10^5–10^6 K/s depending on the particle size. The volatiles are given off after heating up the coal to around 500 °C. The devolatilization process is fast and in typical swirling large-scale flames is completed within 30 ms. Combustion of char particles may take several seconds. Here again for details on the particle trajectories subroutine and its turbulent dispersion part the reader is referred to Weber et al. (1993).

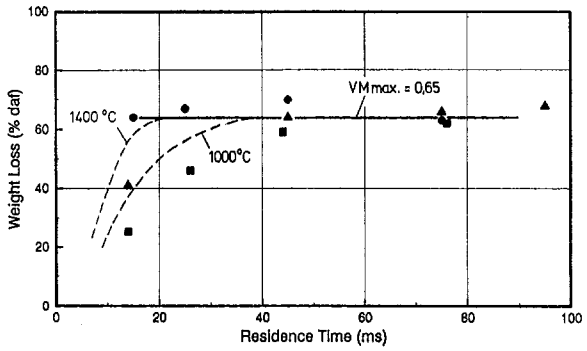

Fig. 3 Devolatilization data for HVB Coal Valley coal; ●—1400 °C, ▲—1200 °C, ■—1000 °C, --- Eq. (4)

Devolatilization. It has been recognized that coal devolatilization has a major impact on the flame properties in the burner vicinity (see Brewster et al., 1988; Truelove and Jamalludin, 1986; Görner, 1991). The devolatilization rates of similar coals range over several orders of magnitude (Wall, 1987), depending on the heating rate and final temperature of particles. Under rapid heating conditions (>10^4 K/s), substantially more volatiles are given off than under low heating rates (1 K/s). Thus, the proximate volatile matter content cannot be used in the modeling but instead high temperature volatile yield ($VM_{\max}$) is used.

For high-volatile bituminous coals, Knill et al. (1989), have proposed the following formulae to calculate the particle temperature dependent volatile yield VM:

$$T_p < 773\ \text{K} \quad VM = 0$$
$$773 < T_p < 1273\ \text{K} \quad VM = (0.5 + (T_p - 773)/1000)\, VM_{\max}$$
$$1273 < T_p \quad VM = VM_{\max} \tag{4}$$

It has been assumed that the release of volatiles is fast compared to the time required to heat-up a particle. When T_p is reached, the particle gives off its volatiles in amount determined by the above formulas. The maximum volatile yield $VM_{\max}$ is dependent on the specific coal and it should be established experimentally. Figure 3 shows the devolatilization data for HVB Coal Valley coal together with the approximation provided by Eq. (4).

Char Combustion. The combustion of char occurs predominantly after volatiles are given off. Char produced from rapid pyrolysis are microporous solids whose properties can be described by their size, true and apparent density, porosity, pore volume distribution and surface area distribution (see for example Smith 1982; Wall, 1987). Although the process of carbon combustion is relatively well understood, there has been little success in predicting the char combustion rates using the knowledge of the coal. At present, modeling of the char combustion rates requires that these rates have to be measured for each type of char, under conditions representative of the flame.

It is assumed that char consists of pure carbon and carbon monoxide is the product of char oxidation. The char reaction submodel takes into account the bulk diffusion of oxygen to the particle external surface, the chemical reaction and pore

diffusion. The overall reaction rate (q) is:

$$q = k_c\left(P_{O_2} - \frac{q}{k_d}\right)^{0.5} \tag{5}$$

where k_d is the oxygen diffusion rate to a spherical particle which is calculated as follows:

$$k_d = 5 \times 10^{-12}\left(\frac{T_p + T_g}{2}\right)^{0.75}\frac{1}{D_p} \tag{6}$$

In Eq. (5) k_c is an Arrhenius type expression representing the pseudo-reaction rate (k_c) which incorporates the chemical reaction and pore-diffusion:

$$k_c = A_c \exp(-E_c/RT_p) \tag{7}$$

Emissions of Nitric Oxide (NO_x Post-Processor). The stationary, time-mean balance equation for the total-NO mass fraction (m_{NO}) reads:

$$\frac{\partial}{\partial x_i}(\rho U_i m_{NO}) - \frac{\partial}{\partial x_i}\left(\frac{\mu_{eff}}{Sc}\frac{\partial m_{NO}}{\partial x_i}\right) = \sum_{k=t,p,f}\overline{s_{k-NO}} - \sum \overline{s_{NO-red}} \tag{8}$$

where $\overline{s_{k-NO}}$, $k = t, p, f$ are the time-averaged NO sources for thermal-, prompt- and fuel-NO, and $\overline{s_{NO-red}}$ are the time-averaged NO sinks due to NO reduction reactions. The sections below describe the basis of the NO_x post-processor while details are given in Peters and Weber (1991).

Thermal-NO. In combustion of lean and near stoichiometric fuel-air mixtures, the principal reactions governing thermal-NO are known as Zeldovich mechanism:

$$O + N_2 \Leftrightarrow NO + N \tag{R1}$$

$$N + O_2 \Leftrightarrow NO + O \tag{R2}$$

The above mechanism is often complemented by the reaction

$$N + OH \Leftrightarrow NO + H \tag{R3}$$

which is neglected in the calculations presented in this paper.

Under the assumption that the N-radicals concentration can be calculated using a steady-state approximation, the rate of thermal-NO formation is (in gmole/cm^3 s):

$$r_{t-NO} = 2k_1[O]\frac{[O_2][N_2] - (K_{e,NO})^{-2}[NO]^2}{[O_2] + (k_{-1}/k_2)[NO]} \tag{9}$$

where [ ] indicates concentrations of chemical species in gmole/cm^3 and $K_{e,NO}$ denotes the equilibrium constant of the overall reaction

$$0.5\ O_2 + 0.5\ N_2 \Leftrightarrow NO \tag{R4}$$

The forward and backward rate constants appearing in Eq. (9) are taken from Bowman (1975). Furthermore, the O-radical concentration is assumed to be in equilibrium with molecular oxygen and is calculated following Westenberg (1975).

Equation (9) is applicable to pre-mixed laminar combustion and shows the strong dependence of thermal-NO formation on the combustion gas temperature and the lesser dependence on the oxygen concentration. In order to obtain the time-mean NO formation rate appropriate for turbulent combustion, a presumed single-variable *pdf* approach of Hand et al. (1989) is used with the gas temperature being the only fluctuating variable:

$$\overline{s_{t-NO}} = 10^3 M_{NO}\int_{T_u}^{T_b} r_{t-NO}(T)B_{pdf}(T; a, b)\frac{dT}{T_b - T_u} \tag{10}$$

where a and b are parameters of the Beta-pdf function. The expectation $E\underline{T}$ of the fluctuating temperature is set to its time-average value calculated from the enthalpy equation,

$$E\underline{T} = \int_{T_u}^{T_b} TB_{pdf}(T; a, b)\frac{dT}{T_b - T_u} = T_u + \frac{a}{a+b}(T_b - T_u) = \bar{T} \tag{11}$$

and the variance (var T) of the temperature is assumed to be approximately equal to a fraction of the maximum possible variance,

$$\text{var}\,\underline{T} = E\underline{T}^2 - (E\underline{T})^2 = \frac{ab}{(a+b)^2(a+b+1)}(T_b - T_u)^2 = s(\bar{T} - T_u)(T_b - \bar{T}), \quad 0.5 \le s < 1.0 \tag{12}$$

Here, the fraction s is called the variance coefficient. From the above two equations the following expressions for the B_{pdf} parameters a and b can be found:

$$a = \frac{1-s}{s}\frac{\bar{T} - T_u}{T_b - T_u}, \quad b = \frac{1-s}{s}\frac{T_b - \bar{T}}{T_b - T_u} \tag{13}$$

The variance coefficient s is an important parameter of the NO-submodel and from a statistical point of view, its value can vary between zero and one. In Eq. (12), however, s can only vary from 0.5 to 1.0. The reason is twofold. A value of 0.6 has been recommended (Missaghi, 1987) on the basis of both experimental and theoretical results. If s is allowed to take values in the range 0.5 to 1 then, both parameters a and b can vary only between zero and one. Consequently, all the possible *B-pdf*'s have a U-shape. For s-values near 1.0, the largest fluctuations have a very high probability to occur while the intermediate fluctuations have a negligible small probability. Thus, for s-values near 1.0, the pdf-model calculates relatively high statistical averages. On the other hand, for s-values near 0.5, all fluctuations have a significant probability to occur and the model calculates lower statistical averages.

The other important parameters of the NO-submodel are the lowest possible value (T_u) and the highest possible value (T_b) of the fluctuating temperature. The choice of the unburned temperature (T_u) value is rather straightforward; it is the combustion air temperature. Unfortunately there is no such an obvious choice for the burnt temperature (T_b). It is typically assumed to be either equal to the maximum value of the in-flame time-mean temperature field of the flame computed or equal to the adiabatic flame temperature. In the authors' opinion both alternatives are inappropriate for diffusion flames. First, there is an overwhelming experimental evidence that the temperature fluctuations may exceed the maximum value of the time-mean temperature field. Secondly, in large-scale diffusion flames, where radiation losses are significant, the maximum fluctuating temperature may be substantially lower than the adiabatic flame temperature.

In the modeling work presented in this paper, the T_b values are calculated throughout the flame/furnace. For this purpose, use has been made of the local stoichiometry λ. An enthalpy increase Δh which would occur if all the combustibles were burnt, can be calculated as:

$$\Delta h = H_{vol}\, m_{vol} + H_{CO}\, m_{CO}, \quad \text{if } \lambda \ge 1, \tag{14}$$

and

$$\Delta h = H_{vol}\frac{m_{O_2}}{s_{vol}}, \quad \text{if } \lambda < 1$$

The corresponding temperature increase ΔT is the solution of the algebraic equation

$$\Delta T = \frac{h + \Delta h}{C_p(\bar{T} + \Delta T)} - \bar{T} \tag{15}$$

Now, the unburnt and the burnt temperatures, T_u and T_b are set to

$$T_u = \min(T_{cai}, \bar{T}) - 0.5$$

and

$$T_b = \tilde{T} + \max(\Delta T, 0.5) \quad (16)$$

where T_{cai} is the combustion air inlet temperature. In order to make sure that T_u is always less than T and that T_b is always larger than T, the value of 0.5 K appears in the above equations.

Prompt-NO. The prompt-NO mechanism is complex and involves a number of radical reactions (Bowman, 1975). Considerable efforts have been recently allocated to reduce the mechanism to a few key reactions only but so far without success. A roughly estimated prompt-NO formation rate for methane combustion was given by De Soete (1990) and in terms of concentration it reads (in gmole/cm^3 s):

$$r_{p-NO} = C \frac{M^{1+b}}{\rho^{1+b}} [O_2]^b [N_2][\text{fuel}] \exp\left(-\frac{E_a}{RT}\right) \quad (17)$$

The constants, C, b and E_a take the following values: $C = 6.4 \times 10^6$ s^{-1}, $b = 0.5$, $E_a = 72.5 \times 10^3$ cal/gmole.

In the calculations of natural gas flames presented later on, Eq. (17) is used to calculate prompt-NO formation rates. The effect of fluctuating temperature is accounted for by the Beta-*pdf* function in the same way as for thermal-NO (see Eq. [10]). In calculations of NO emissions from pulverized coal combustion, the prompt-NO is omitted.

Fuel-NO. The coal-bound nitrogen is released from the pulverized coal either via devolatilization or direct char combustion. In the case of devolatilization, the coal-bound nitrogen enters the gaseous phase mainly in the form of hydrocyanic acid (HCN) or ammonia (NH_3). These are the main nitrogen-containing species of the volatile matter, in short, MN_x-species. Due to very fast reactions with oxygen-containing (O_x-) species (O, OH, O_2, . . .) and H-radicals, the MN_x are transformed into mainly NCO-, NH_i, and N-radicals which are called intermediate nitrogen-containing species, in short, IN_x-species. The whole of MN_x-species and IN_x-species is called the cyanide/amine-pool (De Soete, 1990). In the case of direct char combustion, the assumption is made that the coal-bound nitrogen is released into the cyanide/amine-pool in the form of IN_x-species directly. Depending on the conditions in the flame, a fraction of the IN_x-species reacts with O_x-species to finally form fuel-NO.

There are two routes to reduce the NO formed. In the first route, the remaining IN_x-species, those which do not react with the O_x-species to form NO are available to react with N-containing species (mainly NO) to form molecular nitrogen. In the second route, the NO formed can, under fuel-rich conditions react with CH_x-radicals to form MN_x species. The former route is frequently named the air staging mechanism while the latter the fuel staging mechanism. Details of the fuel-NO submodel can be found in Peters and Weber (1991) and Weber et al. (1993).

Numerical Solution. The effects of numerical diffusion, associated with the first-order numerical schemes caused great concern with respect to their applicability to multi-dimensional flows. Therefore, the computational results presented in this paper are obtained with the quadratic upstream differencing (QUICK) scheme of Leonard (1987). It has been demonstrated (Weber et al., 1990) that the differences between second-order QUICK predictions and first-order hybrid predictions can be as large as the differences stemming from the use of different turbulence models.

Figure 4 demonstrates the necessity of applying fine numerical grids even when using the QUICK scheme. The time-mean velocities and turbulence of an ambient air flow, of 0.7 inlet swirl, were measured using laser velocimetry (Hagiwara et al., 1986). In Fig. 4, the measured and computed contours of zero-axial velocity are shown. The two-dimensional com-

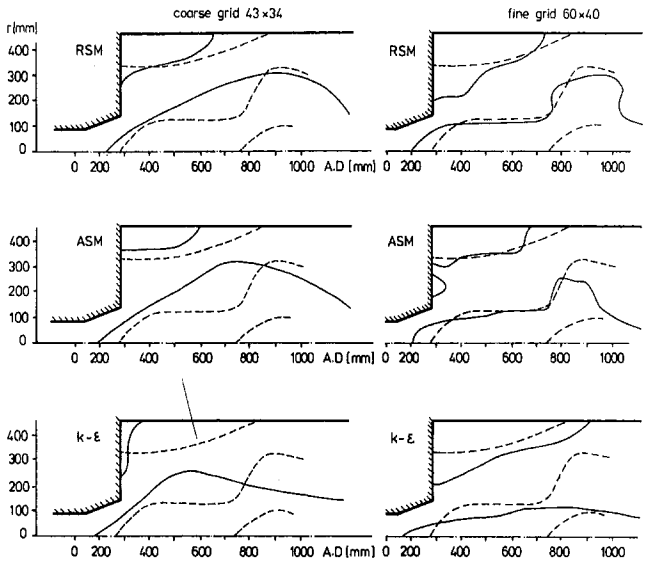

Fig. 4 Predicted contours of $U = 0$ for two grid sizes and three turbulence models (---- measured; —— computed)

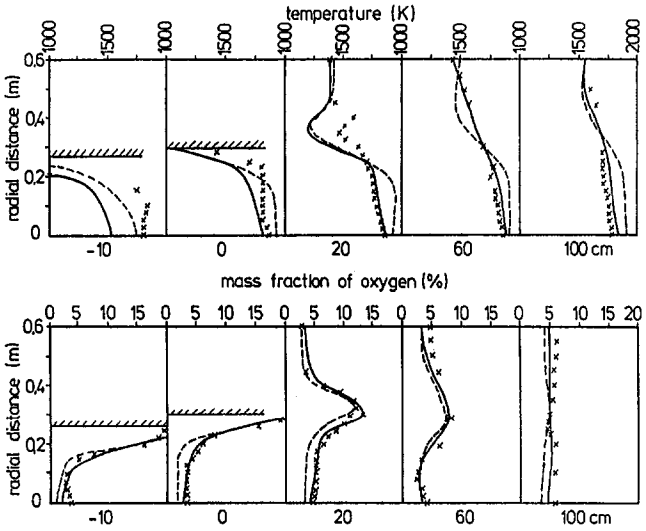

Fig. 5 Type-2 flame; computed and measured temperature and oxygen inside the AAS burner; —— ASM computed, ---- k-ϵ computed (−10 cm, 0 cm, . . ., 100 cm—distance from the furnace front wall)

putations were carried out using the three turbulence models and two numerical grids; a course grid containing 43 × 43 nodes, and a finer 60 × 40 grid. Figure 4 demonstrates, that the numerical related errors can be so large, that they eliminate the benefits expected from the second-order turbulence modeling. Only when the imperfections of the numerical tool are minimized, the turbulence models can be properly assessed.

A detailed assessment of the numerical diffusion effects, grid independence and convergence for the swirling flows shown in Figs. 4 and 6 is given in Weber et al. (1990). The flame predictions shown in Figs. 5 and 7 are obtained using 76 × 56 grid nodes with 20 × 33 nodes located inside the burner quarl. In order to determine the grid sensitivity the calculations are repeated with a double number of grid nodes (148 × 110). The flow patterns, temperature and chemistry fields are almost identical for both computer runs, see Visser (1991).

Flow-Field Predictions in the Near-Burner Zone

Type-0 Flames and Corresponding Isothermal Flows. Numerous computations of (cold) isothermal, non-

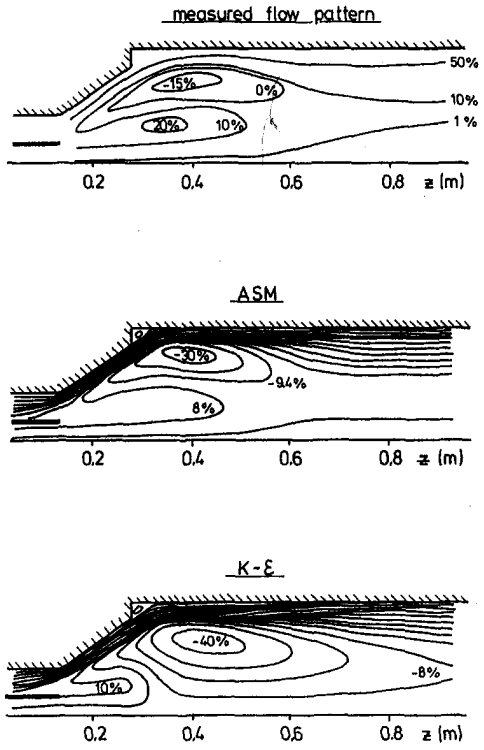

Fig. 6 Measurements and predictions of isothermal swirling flow with a central nonswirling jet, S_0 = 1.5

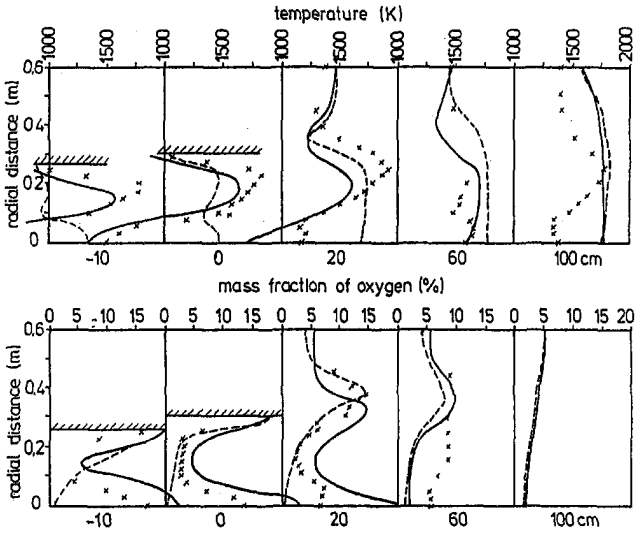

Fig. 7 Type-1 flame; computed and measured temperature and oxygen inside the AAS burner; —— ASM computed, --- k-ε computed; x—measured values (−10 cm, 0 cm, . . ., 100 cm-distance from the furnace front wall)

swirling and weakly swirling jets have indicated that good quality predictions of both velocities and turbulence within the jet are obtainable using the k-ϵ model, provided that the numerical related errors are minimized. It is generally accepted that a little improvement can be gained by application of a second-order turbulence models to such flows. This is also valid for predictions of non-swirling, pulverized coal flames. A number of researchers (Lockwood and Salooja (1983), Zinzer (1987), Görner (1991), have performed simulations of the long, non-swirling flames of pulverized coal which were measured by Michel and Payne (1980). These calculations have demonstrated that good flame predictions can be obtained when applying the k-ϵ model.

Type-2 Flames and Corresponding Isothermal Flows. Over the last two decades, substantial efforts were allocated to the development of second-order turbulence models for predicting complex, highly-swirling flows (see Launder, 1988). Both the RSM and ASM predictions were rigorously tested against the velocity and turbulence measurements of fourteen highly-swirling flows, see Weber et al. (1986, 1990) and Visser (1991). It was concluded that reliable engineering predictions of the swirling flows can be made if fine numerical grids are used in conjunction with the numerical QUICK method and either RSM or ASM is applied. The k-ϵ computations failed already in the burner quarl where flow expansion is inviscid (see Fig. 4). Neither the (anisotropic) generation of turbulence nor the distribution of the tangential momentum in the downstream flow could be correctly predicted by the k-ϵ model. Now, the question arises whether second-order turbulence modeling is also required for computing type-2 flames of pulverized coal.

Rigorous assessment of performance of the k-ϵ, ASM, and RSM in the near burner zone of pulverized coal flames is not possible for the absence of measured data containing velocity and turbulence. Thus, it is usually assumed that the predicted flow patterns are in agreement with the existing velocities when the predicted and measured distributions of temperature and chemical composition agree. It has been experienced that the oxygen distribution in a flame provides a reliable indication of the accuracy of the predicted flow pattern since small changes in the predicted flow patterns have generally a very significant effect on the predicted oxygen distribution.

Figure 5 shows the computed temperature and oxygen fields inside and just downstream of the quarl of the AAS Burner. Only small differences can be observed between the k-ϵ and the ASM predictions. Both turbulence models perform very well. The computed flame of 3.4 MW thermal input is a typical type-2 flame of 0.96 inlet swirl (see Smart et al., 1989). The ignition front is located in the close vicinity of the fuel injector and the flow pattern is very similar to the flows of type-2 flames of coke-oven gas which were considered by Weber and Dugué (1992). Thus, the effects of combustion on the swirling flows must be similar in both cases. The detailed laser velocimetry and flow-field analysis of the coke-oven gas flames have proven that in type-2 flames the basic effect of combustion on swirling flows is to reduce the importance of the centrifugal forces with respect to the inertia forces by increasing the latter substantially. Despite 0.7 or 1.4 inlet swirl level, the effective swirl number of the type-2 coke-oven gas flames is low being in the range 0.1 to 0.2. Thus, the flow pattern inside the AAS Burner resembles strongly a swirling ambient air flow of 0.15–0.2 inlet swirl and therefore the k-ϵ predictions are of the same quality as the ASM results in the type-2 pulverized coal flame.

The work of Weber and Dugué (1992) has demonstrated that the combustion induced effects on swirling flows depend on the combustion front location. When the original cold vortex is combustion accelerated in the vicinity of the quarl inlet, the IRZ strength and size are substantially reduced. When the same vortex is combustion accelerated downstream of the burner quarl, the IRZ is increased in size and strength. The above observations have important implications for mathematical modeling of pulverized coal flames. In the 3.4 MW pulverized coal flame, the volatiles are given off rapidly and in large quantities. This results in the ignition front located at the coal injector. Combustion of an anthracite coal in the same AAS Burner would result in the ignition front located downstream of the burner quarl. The flow field inside the burner would not be so drastically affected by combustion and it is expected that the RSM (or ASM) calculations would offer improvements over the k-ϵ predictions.

Type-1 Flames and Corresponding Isothermal Flows. When considering type-1 flames the interaction be-

tween a nonswirling, particle-laden stream and the swirling combustion air stream is an important phenomenon. Capabilities of the turbulence models to predict this interaction are examined here using an ambient-air flow measured by Hagiwara et al. (1986).

Figure 6 shows a comparison between the measured, k-ϵ computed and ASM-computed flow patterns. A primary nonswirling jet of $U_p = 5$ m/s inlet velocity interacts with a swirling annular flow of the same axial velocity but of 1.5 inlet swirl. The measured full penetration of the primary air through the IRZ is not predicted when the k-ϵ model is used (detailed comparison of the measured and computed velocities and turbulence can be found in Visser, 1991.) The discrepancies between the k-ϵ flow predictions and the measured flow may have large consequences for the predicted characteristics of the solid phase in swirling pulverized coal flames. A simulation with the k-ϵ model would indicate that most of the coal particles, injected with the primary air, do not penetrate the IRZ. A simulation with the ASM would indicate substantial penetration.

Figure 7 shows the measured and predicted temperature and oxygen fields in the burner zone of a type-1 pulverized coal flame of 430 ppm flue NO_x. Generally, the agreement between the measurements and predictions is worse than for the type-2 flame. Clearly, the ASM results being far from perfect, simulate the primary jet penetration better than the k-ϵ predictions. Examining Figures 6 and 7 may lead to a conclusion that a second-order turbulence model is required for predicting type-1 flames. That would certainly be suggested if it had not been experienced that for the type-1 flame considered another ASM mathematical solution, different to that presented in Fig. 7, could be found. These two fully converged ASM-predictions are obtained with identical inlet and boundary conditions. Moreover, it is possible to transform the two solutions into each other by applying a "little" disturbance to the flame region located in the close vicinity of the fuel injector as demonstrated by Visser et al. (1990). Needless to say, the alternative solution (Fig. 10 in Weber et al., 1993) which was obtained with the ASM applied, is very similar to the k-ϵ results shown in Fig. 7.

The above discussion clearly indicates that designing a burner which would produce type-1 flames, cannot be based entirely on the mathematical model predictions. This is because the degree of IRZ penetration by the primary air jet is not only a function of the burner setup but is also strongly dependent on the hysteresis effect present. In general, the flow field of type-1 flames is very difficult to compute with the necessary confidence.

Temperature and Oxygen

Predictability of temperature, oxygen, and carbon monoxide fields are examined using flames of hvBb coal of the following ultimate analysis (daf): C 0.754, H 0.045, N 0.009, S 0.003, O 0.189, LCV 28.46 MJ/kg; proximate analysis (as fired) fixed carbon 0.518, volatiles 0.356, ash 0.106 and moisture 0.02. Prior to the flame computing, the hvBb coal was characterized in a vertical furnace. The devolatilization data are shown in Fig. 3 while the experimentally derived char combustion model parameters take values $k_c = 1.8$ kg m^{-2} s^{-1} Pa$^{-0.5}$ and $E_c = 92.1$ kJ/gmole.

Type-2 Flames of Pulverized Coal. A comparison between computed and measured temperature and oxygen fields is given in Fig. 5. An important quantity to verify is the oxygen concentration in the flame. The path of the air through the flame can be followed via a sequence of maxima in the radial profiles of the oxygen concentration. The agreement between measured and predicted locations of these maxima is very good. This indicates that the path of the air in the near burner zone

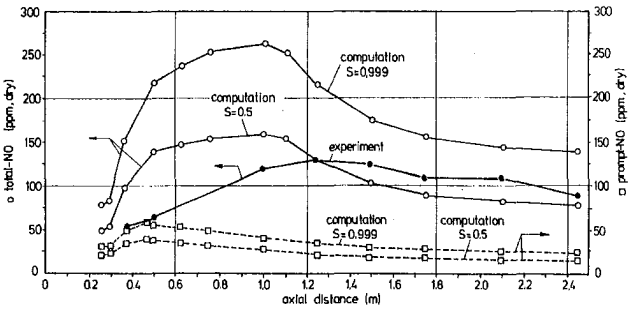

Fig. 8 Measured and computed nitric oxide concentrations in 2 MW natural gas flame

is correctly predicted and hence, that the predicted IRZ size is in agreement with the actual one. There is also good agreement between the measured and predicted values of the oxygen mass fraction in the combustion gases. This is a strong indication that the axial consumption rate of oxygen and hence the combustion rate is correctly predicted by the model. The predicted temperatures agree well with those measured; only in the secondary air stream the measured values are higher than the predicted ones.

Type-1 Flames of Pulverized Coal. The comparison between the measured and computed temperature and oxygen fields of the type-1 flame is shown in Fig. 7. Clearly, the differences between the predicted and measured properties are substantial. The type-1 flame and the type-2 flame considered previously, were computed with an identical set of model parameters determining the devolatilization rate, the rate of volatile matter and char combustion. However, the quality of predictions for the type-1 flame is worse than that for the type-2 flame. It is believed that the imperfections in fluid flow calculations, in particular with respect to the depth of primary jet penetration are responsible for the lesser quality. A detailed sensitivity study of the predictions to a number of model parameters for type-1 flames of 0.9, 2.2 and 3.4 MW thermal inputs can be found in Visser (1991), and Weber et al. (1993).

Predictions of Nitric Oxide

Nitric Oxide in a Natural Gas Flame. The NO_x postprocessor has been first tested for predictability of thermal and prompt NO. To this end a swirling natural gas flame of 2 MW thermal input has been selected (flame 258 in the experiments of Dugué et al. (1991)) for which the inlet conditions to the burner and thermal boundary conditions in the furnace have been measured. The flame is a high-NO_x flame of 134 ppm (at 3 percent O_2) flue emissions; neither air staging nor fuel gas staging is applied to reduce NO_x. The in-flame measurements of velocities, temperature, oxygen, carbon oxides, and NO_x allow for validation of the thermal- and prompt-NO models.

Figure 8 shows the thermal-, prompt- and total-NO calculated along the furnace axis using two values of the s parameter, 0.5 and 0.999. The figure demonstrates a strong sensitivity of the calculated flue NO emissions to the s parameter influencing the temperature fluctuations. The predicted total-NO emissions range, depending on the variance coefficient s, from 60 percent up to 104 percent of the measured total-NO emissions. The model calculates that 20–23 percent of the NO-emissions is prompt-NO. The thermal-NO source is only significant in the region bounded by the 1600 K-isoline of the mean temperature. The thermal-NO and prompt-NO sources reach their maximum values in positions very near stoichiometric conditions. The prompt-NO source reaches its maximum inside the burner quarl while the thermal-NO source just downstream of the burner quarl; i.e., prompt-NO is produced somewhat earlier than thermal-NO. This should be the case

Table 1 Measured and predicted flue concentrations of NO in 3.4 MW flames of pulverized coal (concentrations in ppm, dry, at 0 percent O_2)

NO emissions	Type-1 flame	Type-2 flame
Measured	470	1074
Fuel-NO predictions	482	1053
Total NO predictions		
$s = 0.5$	638	1189
$s = 0.999$	846	1352

indeed, because at temperatures less than 1200 K, prompt-NO is produced much faster than thermal.

The above NO calculations are performed with the maximum value of the fluctuating temperature (T_b) calculated from Eq. (16). Similar calculations with T_b value set to the adiabatic flame temperature result in NO emissions around eight times higher than the measured NO flue emissions. It was experienced that when the time-mean temperatures are increased by 10 percent throughout the natural gas flame considered, the predicted NO emissions increase from 93 to 770 ppm (for $s = 0.6$). A similar 10 percent alteration to the oxygen concentration field increases the predicted NO emissions from 93 to 126 ppm (for $s = 0.6$).

The above considerations on the sensitivity, call for a high accuracy on temperature and oxygen predictions. The higher the flame and process temperature, the more accurately the in-flame temperatures have to be calculated in order to secure good NO predictions. Thus, all the factors influencing the accuracy of the temperature predictions beginning with the rate of combustion, radiation, dissociation of combustion products and ending with the formulae for specific heat are of importance.

Nitric Oxide In Pulverized Coal Flames. Capabilities of the NO_x post-processor for predictions of thermal-, fuel- and total-NO are shown herewith using both the type-2 flame shown in Fig. 5, and type-1 flame shown in Fig. 7. For pulverized coal combustion, the prompt NO mechanism is omitted at this stage of NO modeling. Three computations are performed for each of the two flames considered. The first run is to calculate exclusively the fuel-NO while the second ($s = 0.5$) and third ($s = 0.999$) runs to obtain total-NO. While calculating the fuel-NO only, the thermal-NO source is switched off. In the two total-NO runs, both fuel- and thermal-NO mechanisms are activated and some of the NO formed via Zeldovich mechanism is reduced by reactions with CH radicals. The results summarized in Table 1 show that the total-NO emissions for the low-NO_x flame are overpredicted by either 35 or 80 percent depending on the s value, despite omitting prompt-NO. For the high-NO_x type-2 flame the discrepancies are smaller being in the range 10 to 25 percent. For both flames the major part of the predicted flue emissions is the fuel-NO contributing up to 90 percent in the type-2, high NO_x flame and up to 76 percent in the type-1, low-NO_x flame ($s = 0.5$).

A clear difference between emissions of the high and low NO_x flames has been correctly identified by the model. A comparison between the in-flame measured and predicted NO concentrations leads to an observation (see Peters and Weber, 1991) that the computed total-NO values are underpredicted in fuel rich regions and over-predicted in oxygen rich regions. The NO post-processor has distinguished the high NO_x flame from the low NO_x one mainly because the flame model has correctly identified the large differences in the size of the fuel rich region of the two flames (Weber et al., 1993). The NO_x post-processor is bound to fail if the fuel rich zone is wrongly predicted.

Conclusions

The mathematical modeling technique for simulating pulverized coal flames including the NO predictions has been scrutinized. The objective is to analyze whether the mathematical modeling can provide engineers with the three-level technical information (see Introduction) required for designing large scale burners and flames. The following has been concluded:

The first-order information containing the knowledge of the flame shape, length, and a global estimate of flame temperatures with accuracy around 200 °C is generally obtainable from the modeling. Here the modeler can use as a starting point the proximate and ultimate coal analyses and estimate the devolatilization rate, high temperature volatile yield and char combustion rate. Such computations can be performed using the k-ϵ turbulence model, but coarse numerical grids and first-order numerical schemes should be avoided. Neither predictions of char burnout nor emissions of NO_x or CO are reliable.

The second-order information containing detailed knowledge of temperature distribution, oxygen and unburned fuel can be obtained if both the inlet conditions to the burner are precisely known and the coal combusted has been characterized e.g. its pyrolysis rate, the high temperature volatile yield and char combustion rate are measured prior to the modeling. The computations should be performed using a second-order numerical scheme and a fine numerical grid. Reliable flow field predictions of non-swirling jet-flames and type-2 swirling flames (see Fig. 1) of high- or medium-volatile coals can be obtained using the k-ϵ model of turbulence. In the case of type-2 flames, when the inlet swirling flow is combustion accelerated in the vicinity of the fuel injector, the swirl induced effects are rapidly reduced and the k-ϵ turbulence model works satisfactory. For type-2 flames of low volatile or anthracite coals better predictions of the flow field inside the burner quarl can be obtained if a second-order turbulence model is applied.

Obtaining the second-order information by computing type-1, low-NO_x flames which are typical for internal air staged burners, is very difficult. It has been demonstrated that the quality of the near burner zone predictions of type-1 flames is substantially worse than for type-2 flames. This has been attributed to difficulties in computing correctly the penetration depth of the fuel jet inside the swirl induced reverse flow. Both full penetration and partial penetration flames can be generated in such burners. Similarly, the computations may lead to more than one mathematical solutions (see text).

At this stage of the modeling the third-order information is obtainable only in very special circumstances when the modeler "extrapolates gently" from rigorously verified predictions. First, a confidence in the predictions must be gained by comparing them with in-flame measurements of temperature and chemical species including NO. If a good agreement is obtained, then a subsequent computer run, with either slightly altered burner geometry or with different inlet or boundary conditions can provide the desired third-level information.

Acknowledgment

The authors gratefully acknowledge the financial support of the IEA Coal Combustion Science Program, Annex 2, sponsored by organizations within Canada, Germany, the Netherlands, and the United Kingdom. We thank the Joint Committee of the IFRF for permission to publish this paper.

References

Abbas, T., Costen, P., and Lockwood, F. C., 1992, "The Influence of Near Burner Region Aerodynamics on the Formation and Emission of Nitrogen Oxides in a Pulverized Coal-Fired Furnace," *Combustion and Flame*, pp. 346–363.

Bowman, C. T., 1975, "Kinetics of Pollutant Formation and Destruction in Combustion," *Progress in Energy and Combustion Science*, Vol. 1, pp. 33–47.

Brewster, B. S., Baxter, L. L., and Smoot, L. D., 1988, "Treatment of Coal Devolatilization in Comprehensive Combustion Modeling," *Energy and Fuels*, Vol. 2, No. 4, pp. 362–370.

Dugué, J., A. Saponaro, and Weber, R., 1991, "Development of Multy-Fuel Low NO_x Burner Technology. Phase 1: Natural Gas Burner," IFRF Doc. No. F 010/y/02.

Görner, K., 1991, *Technische Verbrennungssysteme, Grundlagen, Modellbildung, Simulation*, Springer-Verlag, Berlin.

Hagiwara, A., Bortz, S., and Weber, R., 1986, "Theoretical and Experimental Studies on Isothermal, Expanding Swirling Flows with Application to Swirl Burner Design," IFRF Doc No F 259/a/3.

Hand, G., Missaghi, M., Pourkashanian, M., and Williams, A., 1989, "Experimental Studies and Computer Modeling of Nitrogen Oxides in a Cylindrical Natural Gas Fired Furnace," *9th Members Conference of the IFRF*, Vol. 2, Noordwijkerhoud, Netherlands.

Knill, K. J., Maalman, T. F. J., and Morgan, M. E., 1989, "Development of Combustion Characterization Technique for High Volatile Bituminous Coals," IFRF Doc No F 88/a/10.

Launder, B. E., 1988, "Turbulence Modeling of Three-Dimensional Shear Flows," *AGARD 63rd FDP Symposium on Fluid Dynamics of 3D Turbulent Shear Flows and Transition*, Cesme, Turkey.

Leonard, B. P., 1987, "Locally Modified QUICK Scheme for Highly Convective 2D and 3D Flows," *Ffth International Conference on Numerical Methods in Laminar and Turbulent Flows* C. Taylor, W. G. Habashi, M. M. Hafez, eds. Vol. 5, Part 1, Montreal, Canada.

Lockwood, F. C., and Salooja, A. P., 1983, "The Prediction of Some Pulverized Bituminous Coal Flames in a Furnace" *Combustion and Flame*, Vol. 54, pp. 23–32.

Michel, J. B., and Payne, R., 1980, "Detailed Measurements of Long Pulverized Coal Flames for the Characterization of Pollutant Formation," IFRF Doc No F 09/a/23.

Missaghi, M., 1987, "Mathematical Modeling of Chemical Sources in Turbulent Combustion," Ph.D. thesis, University of Leeds, England.

Peters, A. A. F., and Weber, R., 1991, "The Development of a NO_x Post-processor," IFRF Doc No F 36/y/17.

Smart, J. P., and Weber, R., 1987, "NO_x Reduction and Burnout Optimisation Using Aerodynamic Air-Staging and Air-Staged Procombustors," IFRF Doc. No. F 037/a/18.

Smart, J. P., Knill, K. J., Visser, B. M., and Weber, R., 1988, "Reduction of NO_x Emissions in a Swirled Coal Flame by Particle Injection into the Internal Recirculation Zone," *Twenty-Second Symposium (International) on Combustion*, The Combustion Institute, pp. 1117–1125.

Smart, J. P., and Weber, R., 1989, "Reduction of NO_x and Optimisation of Burnout with an Aerodynamically Air-Staged Burner and an Air-Staged Precombustor Burner," *Journal of the Institute of Energy*, Vol. LXII, No. 453, pp. 237–245.

Smart, J. P., van de Kamp, W. L., and Morgan, M. E., 1989, "The Effect of Scale on the Performance of the Aerodynamically Air Staged Burner," IFRF Doc No F 37/a/19.

Smith, I. W., 1982, "The Combustion Rates of Coal Chars: A Review," *Nineteenth Symposium (International) on Combustion*, pp. 1045–1065.

Smoot, L. D., 1993, *Fundamentals of Coal Combustion*, Elsevier, New York.

De Soete, G. G., 1990, "Fundamental Chemistry of NO_x and N_2O Formation and Destruction," The IFRF Third Flame Research Cource on Fuel Utilization and Environment, Noordwijkerhout, The Netherlands.

Truelove, J. S., and Jamalludin, A. S., 1986, "Models for Rapid Devolatilization of Pulverized Coal," *Combustion and Flame*, Vol. 64, pp. 369–372.

Visser, B. M., Smart, J. P., Van de Kamp, W. L., and Weber, R., 1990, "Measurements and Predictions of Quarl Zone Properties of Swirling Pulverized Coal Flames," *Twenty-Third Symposium (International) on Combustion*, The Combustion Institute, pp. 949–955.

Visser, B. M., 1991, "Mathematical Modeling of Swirling Pulverized Coal Flames," Ph.D. thesis, the University of Delft, The Netherlands.

Wall, T. F., 1987, "The Combustion of Coal as Pulverized Fuel through Swirl Burners," *Principles of Combustion Engineering for Boilers*, C. J. Lawn, ed., Academic Press, London.

Weber, R., Boysan, F., Swithenbank, J., and Roberts, P. A., 1986, "Computations of Near Field Aerodynamics of Swirling Expanding Flows," *Twenty-First Symposium (International) on Combustion*, The Combustion Institute, pp. 1435–1443.

Weber, R., Smart, J. P., and Phelan, W. J., 1987, "NO_x Reduction and Burnout Optimisation Using Aerodynamic Air-Staging and Air-Staged Precombustors," IFRF Doc. No. F 037/a/16.

Weber, R., Visser, B. M., and Boysan, F., 1990, "Assessment of Turbulence Modeling for Engineering Prediction of Swirling Vortices in the Near Burner Zone," *International Journal of Heat and Fluid Flow*, Vol. II, No. 3, pp. 225–235.

Weber, R., and Dugué, J., 1972, "Combustion Accelerated Swirling Flows in High Confinements," *Progress in Energy and Combustion Science*, Vol. 18, pp. 349–367.

Weber, R., Peters, A. A. F., Breithaupt, P. P., and Visser, M. B., 1993, "Mathematical Modeling of Swirling Pulverized Coal Flames: What Can Combustion Engineers Expect from Modeling," ASME, FACT Vol. 17, Combustion Modeling, Co-firing and NO_x Control, pp. 71–86.

Westenberg, A. A., 1975, "Kinetics of NO and CO in Lean, Premixed, Hydrocarbon-Air Flames," *Combustion Science and Technology.*, Vol. 4, pp. 59–64.

Zinzer, W., 1987, "Prediction of NO_x from Pulverized Coal Flames," *Erdöl und Kohle-Erdgas*, Bd. 40, Heft 7, pp. 312–314.

Sizing of an Aircraft Fuel Pump

U. S. Rohatgi
Brookhaven National Laboratory,
Department of Advanced Technology,
Building 475B,
Upton, NY 11973

A need to pump a mixture of two-phase fluid appears naturally in many situations. One example of this situation is aircraft fuel systems, where the pump inlet may have two-phase mixture due to the desorption of the dissolved gases at low pressures at higher altitudes. A simple procedure of selecting proper design conditions for the inlet inducer and a method of sizing the inducer, impeller and volute to meet all the design requirements has been described. This procedure has also been applied to a typical fighter plane boost pump design.

Introduction

Two-phase flow appears naturally in many situations and pumps are needed to pump the mixture. One example of this situation is the boost pump for aircraft fuel systems. The fuel has many types of dissolved gases and as the pressure reduces, the gases come out of the fuel creating two-phase conditions at the pump inlet. The aircraft has to operate at various altitudes and speeds. This will lead to different pressures resulting in different V/L (vapor to liquid volume ratio) at the pump inlet. The pump is required to handle all these situations.

The other requirement on the pump is that the fluid temperature rise due to friction, and secondary losses should be small. Furthermore, the weights of aircraft components are critical and so the pumps are designed for very high speed, which may result in severe cavitation problems. In general, a combination of inducer and centrifugal pumps (as shown in Fig. 1) are used. The inducer is designed to raise the pressure sufficiently to maintain proper inlet conditions for the centrifugal pump where most of the energy transfer to fluid takes place. A volute (Fig. 2) is attached at the exit of the pump to recover the pressure.

Selection for Design Conditions. The aircraft engine manufacturer supplies a set of requirements which specify the inlet fluid conditions, pump speed, flow rate, and expected pressure rise. These conditions vary with altitude. The inducer should be able to increase the pressure in such a way that the following conditions (Stepanoff, 1957; Dixon, 1978; Sabersky et al., 1971) are met at the exit of inducer or inlet of centrifugal impeller for all conditions:

$$\text{V/L} = 0.0, \quad \text{and} \quad s \leq 3.0 \text{ rad.} \tag{1}$$

First eliminate the conditions for which the inducer suction specific speed is less than 3.0 rad as no inducer will be needed for these. For the remaining specified conditions, the head rise required by the inducer is estimated for supplying proper impeller inlet conditions. The inducer is sized for the worst conditions. In situations where it is not straightforward to select the worst situation, the inducer is sized for one and checked for the other. The inducer inlet pressure will depend upon V/L

$$(\text{V/L})_1 = \theta\left(\frac{p_0 - p_1}{p_1 - p_{v,1}}\right) \tag{2}$$

$$p_1 = (\theta p_0 + (\text{V/L})_1 p_{v,1})/(\theta + (\text{V/L})_1) \tag{3}$$

The pressure rise required to dissolve all the gases in this case is $(p_0 - p_1)$.

The two phase mixture is compressible and the head rise corresponding to the pressure rise of $(p_2 - p_1)$ will be

$$gH = \frac{c_2^2 - c_1^2}{2} + \frac{p_2 - p_1}{\rho_l} + \frac{\theta}{\rho_l}(p_0 - p_v)\log\left(\frac{p_2 - p_v}{p_1 - p_v}\right) \tag{4}$$

The centrifugal or mixed flow impeller is sized to generate the remaining head for the above case. However, the total pump when sized for one set of conditions should be verified for all the other specified conditions.

Inducer Sizing. Inducer is an axial flow pump with gradual blade loading. It is designed to handle values of V/L of up to 0.45 which corresponds to void fraction of 0.30 at the inlets. The void fraction of 0.30, is the limit of bubbly flow regime (Ishii et al., 1980). As the critical Weber number is generally of order of 10, the bubble sizes are expected to be less than 0.3 cm. Therefore, it is assumed that the two phases are well mixed at the inlet and behave as pseudo single phase. The inlet of the inducer is sized on the basis of the following conditions:

(*a*) compute specific speed for the inducer and use a table (Stepanoff, 1957) for estimating the coefficient k_{cm}

$$C_{m,1} = k_{cm}\sqrt{2gH_{\text{IND}}} \tag{5}$$

(*b*) The optimum flow coefficient is computed from cavitation number, K (Cooper, 1963 and Jacobsen and Keller, 1971)

$$\phi_{\text{opt}} = \sqrt{K/2(K+1)};$$

$$\text{where} \quad K = (p_1 - p_{\text{sat}})/(\rho_f w_{1,t}^2/2) \tag{6}$$

The value of K varies for inducer inlet conditions and blade design and a minimum value of K which can be safely used has been suggested by many researchers (Jacobsen and Keller, 1971; Stripling and Acosta, 1962; and Wade and Acosta, 1966).

$$K_{\min} = \tan^2(\beta_1'/2) \tag{7}$$

The hub size is based on strength consideration. The lowest inlet velocity is selected for inlet sizing from these two approaches. The other inducer inlet parameters are as follows:

$$A_1 = Q_1 B_1/c_{m,1} = \pi(r_{1,t}^2 - r_{1,h}^2),$$

$$\text{where} \quad B_1 = 1/(1 - n_b t/2\pi r_1 \sin\beta_1') \tag{8}$$

$$r_{1,t} = \left(\frac{Q}{2\pi^2 \phi_{\text{opt}} \Omega(1 - \Sigma_1^2)}\right), \quad \text{where} \quad \Sigma_1 = \frac{r_{1,t}}{r_{1,h}} \tag{9}$$

The inducer solidity and number of blades are selected from empirical considerations. The normal practice is to have 3 blades and solidity of 2.0,

$$\text{Solidity} = \sigma = C/S \simeq l_{ax}/\Lambda \tag{10}$$

The inducer exit size is based on head requirement for the inducer. The fluid is assumed to be a homogeneous-equilibrium two-phase mixture. As the inducer gradually increases the pres-

Contributed by the Fluids Engineering Division for publication in the JOURNAL OF FLUIDS ENGINEERING. Manuscript received by the Fluids Engineering Division March 19, 1993; revised manuscript received June 6, 1994. Associate Technical Editor: L. Nelik.

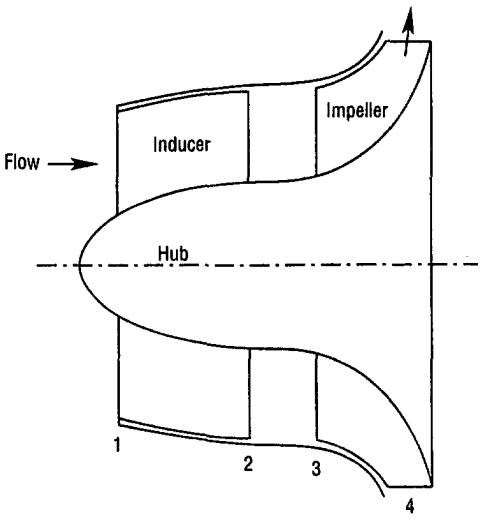

Fig. 1 Schematic diagram of inducer and impeller

sure, the fluid particles are expected to have sufficient time to absorb the gases and achieve equilibrium. The exit fluid slip is considered in the design. The set of equations which govern the exit flow are:

$$H_{th,\infty} = u_2 c'_{u2}, \quad Q_2 = \pi(r_{t,2}^2 - r_{h,2}^2) c_{m2} \eta_{\text{vol}} B_2, \qquad (11)$$

where

$$B_2 = 1/(1 - n_{\text{IND}} t/2\pi r_2 \sin(\beta'_2)),$$

$$\text{and} \quad r_2^2 = (r_{t,2}^2 + r_{h,2}^2)/2 \qquad (12)$$

$$c_{m2} = (\Omega r_2 - c'_{u2}) \tan \beta'_2 \qquad (13)$$

The remaining relationships will come from assumptions about the type of inducer, or a shaft strength consideration. The general practice is to specify r_{h2} and either have a constant pitch or constant axial velocity inducer. This will result in two additional equations:

$$r_{h,2} = \text{specified}, \quad \text{and} \quad r_2 \tan \beta'_1 = \text{constant}, \quad \text{or},$$

$$c_{m,2} = c_{m,1} \qquad (14)$$

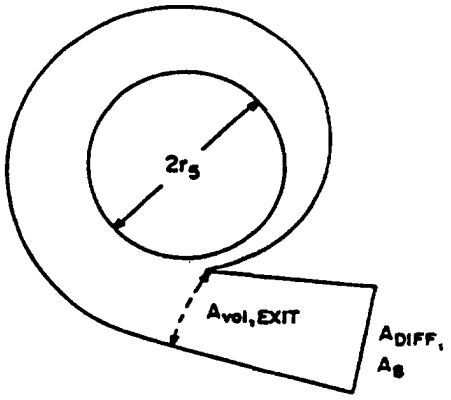

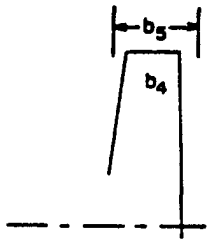

Fig. 2 Schematic diagram of a volute

Nomenclature

A_s = volute surface area
B = blockage factor
b = blade height
C = specific heat
c = absolute fluid velocity
c_f = friction coefficient
c_m = meridional velocity
C_P = Pleiderer constant
c_u = component of fluid velocity in the direction of blade velocity
D = hydraulic diameter
H = head
H_{th} = theoretical head with slip but no loss
$H_{th\infty}$ = theoretical head with no slip, no loss, $H_{th\infty} = U_2 C'_{u2}$
ΔH = volute losses
K = cavitation number
k_{cm} = flow constant, inlet flow
k_v = flow constant for volute flow
l = length
N = rotor speed, rad/s
n = number of blades
P_{disk} = loss due to disk friction
p = pressure
p_v = vapor pressure
p_0 = tank pressure
Q = volume flow rate, m^3/s
r = radius
Re = Reynolds number
S = blade spacing
s = suction specific speed,

$$s = N\sqrt{Q}/\left[\frac{p - p_{\text{sat}}}{\rho_l} + \frac{c^2}{2}\right]^{0.75}, \text{ rad}$$

ΔT = temperature rise
t = blade thickness
u_i = blade velocity, $u_i = \Omega r_i$
V/L = vapor volume to liquid volume ratio
w = relative velocity
W = mass flow rate
α = vapor volume fraction, (V/L)/(1 + (V/L))
α_v = volute angle
β = relative velocity angle
β' = blade angle
Φ = Flow coefficient
Λ = blade lead
η = efficiency
ω = angular velocity
μ = viscosity
ρ = density
θ = Ostwald coefficient in V/L equation

Subscripts

ax = axial
d = diffuser
e = expansion
f = friction
g = gas
IMP = impeller
IND = inducer
l = liquid
m = mixture
ref = reference
st = straight pipe
sat = saturation
v = volute
vol = volumetric
1 = inducer inlet
2 = inducer exit
3 = impeller inlet
4 = impeller exit
5 = volute

Superscript

$'$ = ideal no-slip conditions

Symbols

$\langle\,\rangle$ = average between inlet and exit

Table 1 Performance requirement for boost pump

Parameter	Conditions I	II	III
Altitude	10,000 ft	Sea Level	Sea Level
Fuel Temperature Boost Stage Inlet	57.2°C	57.2°C	57.2°C
Boost Stage Inlet (V/L)	0.45	0.45	0
Pump Speed (Ω/Ω_{ref})	1.14	1.14	1.0 to 1.11
Fuel Flow ($W_4/W_{4,ref}$) Boost Stage	0.57	0.66	0.25 to 1.0
Pressure Rise for Pump	--	--	Between 4.69 bar to 8.27 bar

The constant lead (or pitch) inducer is easier to manufacture and, therefore, is preferred.

The $H_{th\infty}$ is related to actual head through Pfleiderer's correlation (Lazarkiewicz and Troskolanski, 1965) and losses through the blade channel.

$$H_{th\infty,\mathrm{IND}} = (1 + C_p)H_{th,\mathrm{IND}},$$

$$\text{where} \quad C_p = 0.175(1 + \sin \beta_2')/\sigma \sin\left(\frac{\beta_2' + \beta_1'}{2}\right) \tag{15}$$

$$H_{th},\ \mathrm{IND} = H_{\mathrm{IND}} + \text{Losses},$$

$$\text{where} \quad \text{Losses} = \frac{fl}{2D}\langle\rho_m\rangle_{\mathrm{IND}}\langle w\rangle^2_{\mathrm{IND}} \tag{16}$$

The channel average quantities can be assumed as a linear average of inducer inlet and exit quantities. Among many approaches available in the literature for estimating friction factor for two phase flow (Wallis, 1969) the homogeneous model is the easiest to use and is within the uncertainty of other correlations. The homogeneous model implies that the gas and the liquid have the same velocities. The friction factor is assumed to be a function of Reynolds number based on mean quantities. The mixture viscosity (Wallis, 1969) is estimated at the inlet and exit, and an average viscosity is computed from them.

$$\mathrm{Re} = \frac{\langle\rho_m\rangle\langle w\rangle D}{\langle\mu_m\rangle}, \quad \text{where} \quad \rho_m = \alpha\rho_g + (1 - \alpha)\rho_l$$

$$\text{and} \quad \frac{1}{\mu_m} = \frac{\alpha}{\mu_g} + \frac{(1 - \alpha)}{\mu_l} \tag{17}$$

$$\alpha = \mathrm{V/L}/(1 + \mathrm{V/L})$$

The V/L at the inducer exit is estimated from exit pressure, which is obtained from Bernoulli type equations connecting exit pressure to inlet and exit absolute velocities, actual head and inlet pressure. This completes the system of non-linear equations which can be solved for inducer dimensions and fluid conditions. It is assumed that gas will be re-dissolved as the pressure increases in the channels.

Impeller Sizing. The fluid at the exit of the inducer should be single phase as the inducer is sized to not only dissolve any gas in the fuel but also to raise the pressure such that the suction specified speed is less than 3.0 rad. The impeller is sized for the remainder of the head.

The inlet conditions are the same as the exit of the inducer. The flow will have whirl. The number of blades should be some multiple of inducer blades and is estimated as follows:

$$n_{\mathrm{IMP}} = 6.5\frac{r_3 + r_4}{r_4 - r_3}\sin((\beta_3 + \beta_4)/2) \tag{18}$$

The other impeller inlet conditions are,

$$c_{u3} = c_{u2}, \quad \text{and} \quad u_3 = u_2 \tag{19}$$

An impeller with 6 blades will be a good choice as any increase in the number of blades will increase the flow blockage and friction loss. The procedure of sizing is quite similar to the previous method (Lazarkiewicz and Troskolanski, 1965). The set of equations governing the flow are:

$$H_{th\infty,\mathrm{IMP}} = (u_4 c_{u4}' - u_3 c_{u3}),$$

$$\text{where} \quad c_{u4}' = u_4 - c_{m4}/\tan\beta_4' \tag{20}$$

$$c_{m4} = Q_4/(2\pi r_4 b_4 \eta_v B_4), \quad \text{and} \quad C_{\mathrm{ecm3}} = k_{cm,4}\sqrt{2gH_{\mathrm{IMP}}}, \tag{21}$$

$$H_{th\infty,\mathrm{IMP}} = (1 + C_{p,\mathrm{IMP}})H_{\mathrm{IMP}}/\eta_{\mathrm{hyd}},$$

$$\text{where} \quad C_{P,\mathrm{IMP}} = \frac{2.2(1 + 1\sin\beta_4)(r_3/r_4)}{n_{\mathrm{IMP}}(1 - r_4^2/r_3^2)} \tag{22}$$

$$B_4 = 1/(1 - n_{\mathrm{IMP}}t_4/2\pi r_4 \sin\beta_4'), \quad \text{and} \quad u_4 = \Omega r_4 \tag{23}$$

The hydraulic efficiency, η_{hyd} will be estimated on the basis of losses in the blade channel. The system of equations is not closed. There is one more unknown variable than the equations. The additional assumption is to choose conditions from the following constraints:

$$\frac{w_4}{w_3} > 0.63, \quad \text{and} \quad 20° < \beta_4' < 35° \tag{24}$$

β_4' is generally chosen to minimize losses in the scroll and blade channel.

The hydraulic losses in the blade channel are estimated from the following procedure (Takagi et al., 1980).

(*a*) Incidence losses

$$(w_2 - w_3)^2/2 \tag{25}$$

(*b*) Skin friction loss (Cooper, 1963)

$$\frac{fl}{2D}\rho\langle w\rangle^2_{\mathrm{IMP}}, \tag{26}$$

where,

$$f = 0.00714 + 0.6104/\mathrm{Re}^{0.35},$$

$$\text{where} \quad \mathrm{Re} = \rho\langle w\rangle_{\mathrm{IMP}}D/\mu \tag{27}$$

(*c*) Secondary losses

$$\frac{f_s l}{2D}\rho\langle w\rangle^2_{\mathrm{IMP}} \tag{28}$$

Here f_s is the friction factor for rotating pipe (Ito and Nanbu, 1971).

$$f_s = f(0.924R_t^{1/20}), \quad \text{where} \quad R_t = \rho\Omega^2 D^3/w\mu \tag{29}$$

Table 2 Pump fuel temperature rise requirements

Case	Design Point	Pump Speed Ω/Ω_{ref}	Flow W/W_{ref}	Boost Pump Temp rise, $\Delta T°c$
I	Sea Level Idle	0.775	0.014	12.0 MAX
II	Sub Sonic Cruise	0.90	0.014	12.0 MAX
III	Alt. Int. Power	1.01	0.017	12.0 MAX
IV	Idle Descent	0.79	0.01	12.0 MAX

Table 3 Summary of design

INDUCER				
Constant Pitch				
	INLET		EXIT	
Hub	1.25 cm	31.0°	2.0 cm	20.58°
Tip	3.57 cm	11.88°	4.1 cm	10.38°
IMPELLER				
Hub	2.0 cm	19.8°	5.24 cm	30°
Tip	4.1 cm	11.38°	5.25°	30°
VOLUTE				
REGULAR VOLUTE				
Volute width at impeller exit = 1.4 cm				
Volute exit area = 11.00 cm^2				
Volute base diameter = 12.26 cm				
SMALLER VOLUTE				
Half the flow area				

Volute Sizing. The last component of this pump is the volute which collects the fluid and an exit diffuser. The volute is sized on the basis of standard procedure (Stepanoff, 1957). The fluid velocity in the volute is;

$$c_{m,v} = c_{m5} = k_v\sqrt{2gH} \tag{30}$$

The constant k_v and volute angle a_v are functions of specific speed (Kovats, 1979). The volute exit area is given as

$A_{v,\text{exit}} = 2\pi r_5 b_5 \sin(\alpha_v)$ where,

$$r_5 - r_4 \simeq 0.17r_4, \quad \text{and} \quad b_5 \simeq 1.4b_4 \tag{31}$$

The volute is generally sized for constant velocity so the cross-sectional area at any location is

$$A_v(\theta) = A_{v,\text{exit}}\left(\frac{\theta}{2\pi}\right) \tag{32}$$

There are three types of losses in the volute, i.e., expansion, skin friction and diffusion in volute exit.

(*a*) Expansion loss

$$\Delta H_{v,e} = \frac{(c_{n4} - c_{m5})^2 + c_{m4}^2}{2} \tag{33}$$

(*b*) Skin friction loss

$$\Delta H_{v,f} = 0.5\,\frac{C_f A_s c_{m,5}^2}{A_{v,\text{exit}}} \tag{34}$$

$A_s = \pi^2 D_v(r_4 + D_v/3)$, where, $D_v = \sqrt{4A_{v,\text{exit}}/\pi}$,

$$\text{and} \quad C_f = C_{f,\text{st}}\left[\text{Re}\left(\frac{D_v}{2\sqrt{2}r_4}\right)^2\right]^{1/20} \tag{35}$$

where A_s and uc_f are surface area and friction coefficients, respectively. Furthermore,

$$C_{f,\text{st}} = 0.316/\text{Re}^{0.25} \tag{36}$$

here c_f and $c_{f,\text{st}}$ are the friction coefficients for curved pipe and straight pipe (Ito, 1959).

(*c*) Diffusion loss

The fluid leaving the volute also goes through a diffuser

$$\Delta H_{v,d} = 0.1\left(1 - \frac{A_{v,\text{exit}}}{A_d}\right)^2 c_{m5}^2 \tag{37}$$

so the total loss in the volute

$$\Delta H_v = \Delta H_{v,e} + \Delta H_{v,f} + \Delta H_{v,d} \tag{38}$$

The volute size is important as smaller volute will reduce the expansion losses, while increasing the other two losses. In general, smaller volute will imply smaller losses at partial capacity. In some aircraft pump applications the temperature rise, which is a measure of friction and secondary losses, is important and at low flow it may become critical. One solution is to reduce the size of the volute.

Application. This simple approach can be used for sizing aircraft boost pump. The crucial element of this pump is the inducer which should be able to feed proper inlet conditions to the impeller for all situations. The aircraft fuel is generally JP-4 which has dissolved gases and various petroleum components which vaporize at different temperatures and pressures.

Some of the specifications for a typical fighter aircraft fuel pump are shown in Tables 1 and 2. The reference flow rate and pump speed for this pump is 10 kg/s and 730 rad/s, respectively.

The three worst conditions from this set of requirements were all from Table 1. The first two conditions in Table 1 have inducer inlet V/L of 0.45 and the inducer should dissolve all the gases back into the liquid. The static pressure at the inlet of the inducer to support V/L of 0.45 for case 1 was 0.445 bar and for case 2 it is 0.543 bar. The inducer would have to increase the pressure above the corresponding tank pressure to dissolve all the gas at the impeller inlet. The head requirement for two cases were 3.02 m and 7.34 m. The head requirement based on the criterion of suction specific speed to be less than 3.0 rad at the impeller inlet were, 5.23 m and 6.1 m for two cases.

The third case in Table 1 is for large liquid flow at the inducer inlet. The inlet suction specific speed for this case was 4.61 rad which is more than 3.0 rad, so an inducer was needed. The head rise requirement for inducer for this case was 4.1 m. However, the flow rate is very high and at low flow rate the head will be higher to meet the requirements of cases 1 and 2. Among these three cases, case 3 of Table 1 was selected for sizing the inducer as it provided the most limiting conditions.

The impeller was also sized to meet the worst requirement, which in this case was the third case of Table 1. The flow rate was the highest. The inducer head produced for this case was subtracted from the total head required, and the impeller was then sized for the remaining head. The dimensions of a typical pump are given in Table 3. The temperature rise at the low flow is difficult to predict with simple analysis. The approach used here is to compute the shut-off power for inducer and impeller along with disk friction loss to compute the temperature rise.

$$\text{Shut-off power} = g(H_{th,\text{IND}}W)\left(\frac{\Omega}{\Omega_{\text{ref}}}\right)^3 + g(H_{\text{IMP},th}W)\left(\frac{\Omega}{\Omega_{\text{ref}}}\right)^2(0.5) + P_{\text{disk}}(\Omega/\Omega_{\text{ref}})^3 \tag{39}$$

$$P_{\text{disk}} = \frac{0.15}{\text{Re}_d^{0.2}}\frac{1}{2}\rho r_4^5\Omega^3, \quad \text{where} \quad \text{Re}_d = \frac{\rho\Omega r_4^2}{\mu} \tag{40}$$

All this power is assumed to increase the temperature of the fluid at the flows shown in Table 2.

$$\Delta T = \text{shut-off power/CW} \tag{41}$$

Table 4 Temperature rise predicted

Case	Shutoff Power Watts	ΔT IND °C	ΔT IMP °C	ΔT disk °C	ΔT TOTAL °C
I	2518	1.65	5.21	0.63	7.83
II	4049	2.58	8.47	1.03	12.09
III	5875	3.07	9.70	1.18	13.96
IV	2736	2.48	7.84	0.96	11.29

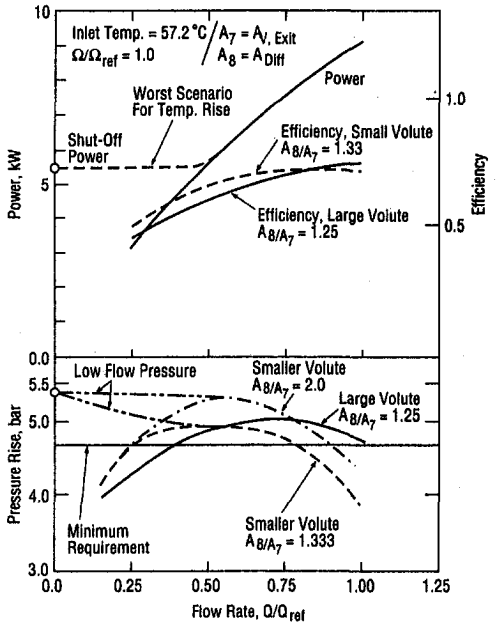

Fig. 3 Predicted performance of a typical fighter plane boost pump

Table 4 shows the temperature rise predicted for the boost pump. The pump met the criteria for all conditions except for case III. However, it was quite close and there was some flow through the pump so the friction losses would be smaller than shut off power.

This design was also checked for the third case of Table 1 and the results are shown in Fig. 3 for two different size volutes and exit diffuser. The design meets the requirement, except at low flow rate where the method may not be applicable. The smaller volute (50 percent area) provided better head and efficiency. It may help in reducing the shut-off power, as there will be less fluid circulating.

Conclusion

A simple approach of designing the boost pump has been described. The crucial steps in this application are setting up the design conditions from the many specified requirements and sizing the inducer to provide single phase fluid with sufficiently low suction specific speed to the impeller.

This approach is not very accurate for low flow conditions as the losses, due to secondary flows at inlet and in the volute, are not well understood. An empirical approach is needed to develop the model for them. However, using shut-off power as the heat addition to the fluid is a conservative way of estimating the temperature rise.

Acknowledgments

The author is grateful for the valuable advice provided by Dr. Paul Cooper of Ingersoll-Rand Research Inc. and Mr. G. Bennett of Colt Industries in this task.

References

Cooper, P., 1963, "Advanced Inducer Study," NAS 8-4005, ER-5288, TRW Electromechanical Division, May.

Dixon, S. L., 1978, *Fluid Mechanics, Thermodynamics of Turbomachinery,* 3rd Edition, Pergamon Press.

Ishii, M., and Mishima, K., 1980, "Two-fluid Model and Analysis of Interfacial Area," ANL/RAS/LWR 80-3, May 31.

Ito, H., and Nanbu, K., 1971, "Flow in Rotating Straight Pipes of Circular Cross Section," ASME *Journal of Basic Engineering,* Sept., pp. 383–394.

Ito, H., 1959, "Friction Factors for Turbulent Flow in Curved Pipes," ASME *Journal of Basic Engineering,* Jan., pp. 123–134.

Jacobsen, J. K., and Keller, R. B., 1971, "Liquid Rocket Engine Turbopump Inducers," NASA SP-8052, May.

Kovats, A., 1979, "Effect of Non-Rotating Passages on Performance of Centrifugal Pumps and Compressors," ASME Symposium *Flow in Primary, Non-Rotating Passages in Turbomachines,* Herring, Solar and Steltz, eds.

Lazarkiewicz, S., and Troskolanski, A., 1965, *Impeller Pumps,* Pergamon Press, First Edition.

Sabersky, R. H., Acosta, A. J., and Hauptmann, E. G., 1971, *Fluid Flow,* Second Edition, Macmillan Company, New York.

Stepanoff, A. J., 1957, *Centrifugal and Axial Flow Pumps, Theory, Design and Application,* John Wiley, Second Edition.

Stripling, L. B., and Acosta, A. J., 1962, "Cavitation in Turbopumps—Part 1," ASME *Journal of Basic Engineering,* Sept., pp. 326–338.

Takagi, T., Kobayashi, J., Miyashero, H., and Morimoto, H., 1980, "Performance Prediction of Single Suction Centrifugal Pumps of Different Specific Speed, Mar., ASME Symposium, *Performance Prediction of Centrifugal Pumps and Compressors,* Gopalakrishnan et al., eds.

Wade, R. B., and Acosta, A. J., 1966, "Experimental Observation on the Flow Past a Plano-Convex Hydrofoil," ASME *Journal of Basic Engineering,* Mar.

Wallis, G. B., 1969, "*One-Dimensional Two-Phase Flow,*" McGraw-Hill.

Kenji Katoh
Associate Professor,
Department of Mechanical Engineering,
Osaka City University,
Sugimoto, Sumiyoshiku, Osaka 558, Japan

Hideomi Fujita
Professor,
Department of Mechanical Engineering,
Nagoya University,
Furocho, Chikusaku, Nagoya 464-01, Japan

Hideharu Sasaki
Ishikawajima System Technology Co., Ltd.,
Kudanminami 4-6-15, Chiyodaku,
Tokyo 102, Japan

Macroscopic Wetting Behavior of a Two-Dimensional Meniscus Under a Horizontal Plate

The purpose of this study is to investigate macroscopic wetting behavior and to verify the validity of the assumption made in the analysis of the preceding report that the complicated effects of the microscopic structures of the solid surface such as roughness or heterogeneity on the macroscopic wetting behavior are simply represented by the values of the apparent contact angles. The unstable phenomenon of a two-dimensional meniscus under a horizontal plate, in which the meniscus falls spontaneously at a certain height of the plate, is considered theoretically from a thermodynamic viewpoint. The results of the analysis based on the above assumption agree with those by an analysis in which the effect of microscopic structures of the solid surface, such as roughness and heterogeneity, are taken into consideration. Therefore, the validity of the assumption made in the preceding report is verified.

1 Introduction

The purpose of this study is to investigate macroscopic wetting behavior. In the preceding report (Katoh et al., 1990), the wetting behavior of an axisymmetric meniscus under a cone surface was theoretically considered from a thermodynamic viewpoint. Usually, it is known that the macroscopic wetting behavior is strongly influenced by small roughness or heterogeneity on the solid surface. The authors assumed that the complicated influences of these microscopic structures on the solid surface are wholly represented by the values of apparent solid-liquid contact angles observed macroscopically. Based on this assumption, the energy difference between solid surface and solid-liquid interface can be calculated by modified Young's equation in which the apparent advancing and receding contact angles are used instead of Young's contact angle. The assumption serves to simplify the analysis of the macroscopic wetting phenomena because it is thus unnecessary to consider the complicated effect of the microscopic characteristics of the solid surface. The theoretical results in the preceding report by use of the above assumption described well the practical wetting behavior observed macroscopically (Katoh et al., 1992).

In this report, the purpose is to investigate further the macroscopic wetting behavior as a continuation of the preceding report and to verify the validity of the above assumption analytically. The phenomena in which the meniscus falls spontaneously at a certain height of the solid plate are analyzed by two methods, one of which is based on the assumption regarding the Young's equation and the other based on an analysis from a microscopic viewpoint; namely, the effect of small roughness and heterogeneity on the solid surface is taken into consideration. For the purpose of simplicity of the analysis as the first step, we use a simple model for the microscopic effect (Defazio and Dyson, 1990a; Defazio and Dyson, 1990b; Johnson and Dettre, 1964; Neumann and Good, 1972). The results from both methods are compared and the validity of the assumption in the preceding report is discussed.

Contributed by the Fluids Engineering Division for publication in the JOURNAL OF FLUIDS ENGINEERING. Manuscript received by the Fluids Engineering Division November 30, 1993; revised manuscript received September 7, 1994. Associate Technical Editor: J. A. C. Humphrey.

2 Wetting Behavior of Two-Dimensional Meniscus Under a Horizontal Plate (Analysis Based on an Assumption Regarding Young's Equation)

2.1 System Energy of Two-Dimensional Meniscus Attached to an Inclined Plate. First, we calculate the system energy for the general case; namely, the meniscus attached to an inclined plate as shown in Fig. 1. In the figure, S, L, and V indicate solid, liquid, and gas phase, respectively. The x and z indicate the horizontal and the vertical direction, respectively. The infinitesimal system energy change ΔE is estimated when the attaching point of the meniscus to the plate shifts from D to D_1 by Δs as shown in Fig. 1. The details of ΔE are (i) the energy change ΔE_{SV-SL} caused by the conversion of a solid-gas interface into a solid-liquid one when the solid plate is wetted by the liquid and (ii) the energy increase by the change of the meniscus shape ΔE_M. Both energy changes are calculated as follows.

(i) The surface free energy change caused when the solid-gas interface is converted into the solid-liquid one by area Δs can be estimated by the following expression, since the surface tension can be considered as the free energy per unit area (Neumann, 1974).

$$\Delta E_{SV-SL} = (\sigma_{SL} - \sigma_{SV})\Delta s \tag{1}$$

where σ_{SL} and σ_{SV} indicate the solid-liquid interfacial tension and the solid surface tension, respectively. Using Young's equation,

$$\sigma_{SV} - \sigma_{SL} = \sigma_{LV} \cos \alpha_Y \tag{2}$$

Eq. (1) is rewritten as

$$\Delta E_{SV-SL} = -\sigma_{LV} \cos \alpha_Y \cdot \Delta s \tag{3}$$

where σ_{LV} and α_Y are liquid surface tension and Young's contact angle, respectively. The Young's contact angle in the above equation is uniquely determined for an ideally smooth and homogeneous solid surface. In practice, however, the apparent contact angle observed macroscopically is not uniquely determined because of the hysteresis phenomena caused by the surface roughness or heterogeneity and the advancing and receding contact angles, θ_{YA} and θ_{YR} are observed. In the preceding report (Katoh et al., 1990), we assumed that the surface energy change between the solid-gas and the solid-liquid interfaces per appar-

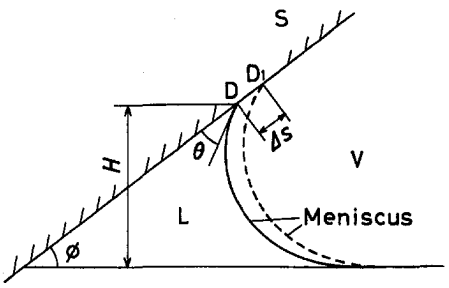

Fig. 1 Two-dimensional meniscus under an inclined plate

ent unit area can be estimated by using θ_{YA} and θ_{YR} instead of α_Y in Eq. (3). Hence the surface energy change is different whether the liquid advances or recedes on the solid surface. The authors consider that this is the remarkable characteristics of the contact angle hysteresis phenomena. This energy difference is considered to be caused by the fact that the irreversible movement such as contact line jump occurs in a different manner on the solid surface for the advance and the recession of the meniscus (Defazio and Dyson, 1990b). Equation (3), for the surface energy change ΔE_{SV-SL}, is rewritten for the macroscopic system as follows;

$$\Delta E_{SV-SL} = -\sigma_{LV} \cos \theta_{YA} \cdot \Delta s \quad \text{(for advance)} \qquad (4a)$$

$$\Delta E_{SV-SL} = -\sigma_{LV} \cos \theta_{YR} \cdot \Delta s \quad \text{(for receding)} \qquad (4b)$$

From the macroscopic viewpoint, Δs in Eqs. (4*a*) and (4*b*) indicates the infinitesimal displacement on the apparent flat surface in which there practically exist microscopic roughness or heterogeneity. The above assumption means that the effect of the infinitesimal roughness or impurities of the solid surface on the wetting behavior is wholly included in the apparent contact angle values and the energy change ΔE_{SV-SL} can be simply calculated by modified Young's Eq. (4).

(ii) When the meniscus shifts from D to D_1 on the plate as shown in Fig. 1, the meniscus shape described by the solid line changes to that by the dotted line. The meniscus energy increases by ΔE_M because of the change of its configuration. The details of ΔE_M are the energy change by the increase of the liquid area and the increase of the potential energy of the liquid. ΔE_M can be obtained by geometrical consideration. Referring to Neumann (1974) and Defazio and Dyson (1990a), ΔE_M is written as follows;

$$\Delta E_M = \sigma_{LV} \cos \theta \cdot \Delta s \qquad (5)$$

where θ indicates the apparently observed angle between the meniscus profile and the plate at the contact point as shown in Fig. 1 and a is the capillary constant defined as

$$a = \sqrt{\sigma_{LV}/\Delta\rho g}$$

($\Delta\rho$: density difference between liquid and gas,
g: gravitational acceleration)

In the derivation of Eq. (5), we neglect the energy increase caused by the small change of the meniscus configuration due to the infinitesimal roughness.

The energy change of the system ΔE is obtained by the sum of Eqs. (4) and (5). The following two expressions are written for both the advance and the receding of the meniscus.

$$\Delta E = \sigma_{LV}(\cos \theta - \cos \theta_{YA})\Delta s \quad \text{(for advance)}$$

$$\Delta E = \sigma_{LV}(\cos \theta - \cos \theta_{YR})\Delta s \quad \text{(for receding)}$$

Therefore, the derivative dE/ds is written as

$$\frac{dE}{ds} = \sigma_{LV}(\cos \theta - \cos \theta_{YA}) \quad \text{(for advance)} \qquad (6a)$$

$$\frac{dE}{ds} = \sigma_{LV}(\cos \theta - \cos \theta_{YR}) \quad \text{(for receding)} \qquad (6b)$$

It is noted that the derivative dE/ds indicates average energy change rate while the meniscus moves apparent distance Δs on the solid plate. The second-order derivative of E is obtained as

$$\frac{d^2E}{ds^2} = -\sigma_{LV} \sin \theta \frac{d\theta}{ds} \qquad (7)$$

Since $d\theta/ds < 0$ for the two-dimensional meniscus, d^2E/ds^2 is positive. Hence the system energy becomes minimum and is stable when the liquid contacts the plate at θ_{YA} for advance of the meniscus and at θ_{YR} for receding as seen from Eqs. (6*a*) and (6*b*). Although the fact that the system is stable at the contact angle is well known for the wetting behavior on the solid plate, it is noted that the analysis in this study shows two different stable conditions for the advance and receding of the meniscus.

2.2 Wetting Behavior of the Meniscus Under a Horizontal Plate. In a particular case of the inclined plate, the meniscus under a horizontal plate shown in Fig. 2 is considered in this report. It is easy to show that $d^2E/ds^2 = 0$ in Eq. (7) because $d\theta/ds = 0$ for the horizontal plate. Hence the system energy curve does not take extreme value. This result is quite different from that for the inclined plate and is interesting.

Now the wetting mechanism of the system is considered. The meniscus height H, which is equal to the horizontal plate height as shown in Fig. 2, is obtained as follows (Chappius, 1982);

$$H = a\sqrt{2(1 + \cos \theta)} \qquad (8)$$

When the height H is $H < a\sqrt{2(1 + \cos \theta_{YA})}$; namely, when

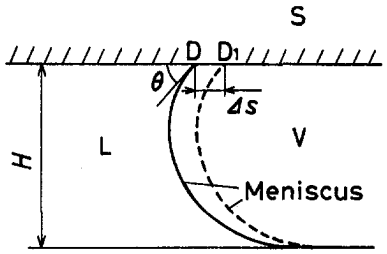

Fig. 2 Two-dimensional meniscus under a horizontal plate

Nomenclature

a = capillary constant ($=\sqrt{\sigma_{LV}/\Delta\rho g}$)
E = free energy of system
E_{SV-SL} = free energy difference between solid-gas interface and solid-liquid one
E_M = free energy of meniscus
g = gravitational acceleration
H = height of meniscus at point of attachment to solid plate
s = distance along solid surface
α_Y = Young's contact angle
β = angle at which meniscus curve contacts solid surface
θ = apparent angle at which meniscus curve contacts solid surface
θ_{YA} = advancing contact angle
θ_{YR} = receding contact angle
$\Delta\rho$ = density difference between liquid and gas
σ_{LV} = liquid-gas surface tension
σ_{SL} = solid-liquid interfacial tension
σ_{SV} = solid-gas surface tension
ϕ = inclination angle of solid plate

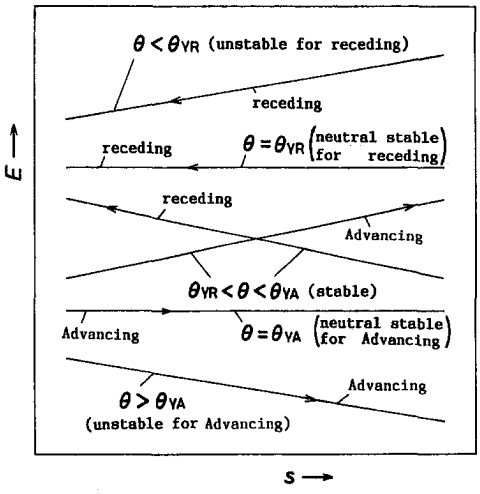

Fig. 3 Behavior of system energy E in relation to s

$\theta > \theta_{YA}$, the following relation holds from Eq. (6a) for the energy change rate dE/ds caused when the meniscus advances on the plate;

$$\frac{dE}{ds} < 0 \quad \text{(for advance)}$$

In this case, the system is unstable because the energy decreases monotonously in the direction of the advance of the meniscus. Therefore, it is considered that the meniscus spreads and wets the solid surface spontaneously.

On the other hand, when $H > a\sqrt{2(1 + \cos\theta_{YR})}$ (i.e., when $\theta < \theta_{YR}$), dE/ds caused when the meniscus recedes on the surface is written from Eq. (6b) as

$$\frac{dE}{ds} > 0 \quad \text{(for receding)}$$

Because the energy decreases in the direction of the receding of the meniscus, the meniscus dries the surface and detaches from the plate spontaneously.

Next, we consider the case in which the plate height is in the region $a\sqrt{2(1 + \cos\theta_{YA})} < H < a\sqrt{2(1 + \cos\theta_{YR})}$ and the apparently observed angle θ at which the meniscus contacts the plate is $\theta_{YR} < \theta < \theta_{YA}$. When the meniscus advances on the solid surface, the energy change rate is described by Eq. (6a). The following relation holds for $\theta < \theta_{YA}$.

$$\frac{dE}{ds} > 0 \quad \text{(for advance)}$$

From the above equation, because the energy increases for the advancing of the meniscus, the meniscus does not spread spontaneously. Similarly, the energy change rate for the receding of the meniscus is described by Eq. (6b) and for $\theta_{YR} < \theta$,

$$\frac{dE}{ds} < 0 \quad \text{(for receding)}$$

Therefore, the meniscus does not recede spontaneously on the plate. From the above results, when the angle θ is in the region $\theta_{YR} < \theta < \theta_{YA}$, the system is stable and the meniscus does not move spontaneously.

In conclusion, when $\theta < \theta_{YR}$ or $\theta > \theta_{YA}$, (i.e., when the plate height H is

$$H < a\sqrt{2(1 + \cos\theta_{YA})} \quad \text{or} \quad H > a\sqrt{2(1 + \cos\theta_{YR})},$$

the meniscus is unstable. On the other hand, when $\theta_{YR} < \theta < \theta_{YA}$ (i.e., the height of the horizontal plate is

$$a\sqrt{2(1 + \cos\theta_{YA})} < H < a\sqrt{2(1 + \cos\theta_{YR})},$$

the stable and stationary meniscus is formed. The above results are summarized as shown in Fig. 3. The ordinate and the abscissa indicate the system energy E and the distance along on the horizontal plate s, respectively. The figure shows the system energy behavior for various θ's. The energy changes are described by straight lines because $d^2E/ds^2 = 0$. It is noted that the system shows a neutral stable state when the meniscus contacts the solid plate at the advancing contact angle θ_{YA} or the reeding contact angle θ_{YR}. This is quite different from the conventional view that the system becomes stable when the meniscus contacts the solid at the contact angle.

In the above discussion, we could clarify the macroscopic wetting behavior of the system by using only the apparent contact angles θ_{YA} and θ_{YR}, and without considering the complicated effects of the microscopic structures on the solid surface.

3 Macroscopic Wetting Behavior of the Meniscus Under a Horizontal Plate (Analysis Considering the Effect of Microscopic Structures on Solid Surface)

In this section, in order to verify the assumption regarding Young's equation in the preceding section, the same problem is analyzed from the manner in which the microscopic structures on the solid surface are taken into consideration. There have been no reports in which the effect of the microscopic structures on the wetting behavior is completely clarified for general random and three-dimensional roughness or heterogeneity. Hence, in order to verify the validity of our assumption, we use the model discussed by Defazio and Dyson (1990b), Eick et al. (1975), Johnson and Dettre (1964), and Neumann and Good (1972); namely, the effect of regular two-dimensional roughness of triangular shape and of the surface heterogeneity made up of two-dimensional stripes endowed alternately with two different wetting characteristics.

3.1 Rough Surface

3.1.1 System Energy. For the system of the two-dimensional meniscus under the rough plate as shown in Fig. 4, we consider the energy change of the system when the meniscus moves by Δs on the surface. It is noted that Δs indicates the infinitesimal displacement exactly along on the rough surface and is different from that based on the macroscopic viewpoint in Section 2. The energy change rate dE/ds can be calculated in the same way as for the meniscus attached to an inclined smooth plate (Neumann, 1974) and is obtained as,

$$\frac{dE}{ds} = \sigma_{LV}(\cos\beta - \cos\alpha_Y) \qquad (9)$$

where β is the microscopically observed angle at which the meniscus contacts the solid surface as shown in Fig. 4. β is different from the angle θ between the meniscus curve and the horizontal line, which corresponds to the apparent angle observed macroscopically. In the above equation, Young's contact

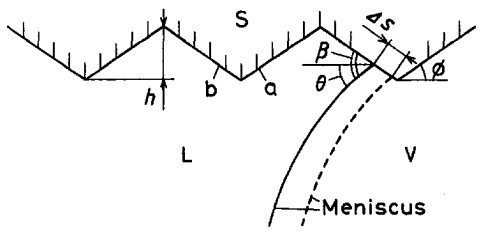

Fig. 4 Two-dimensional meniscus

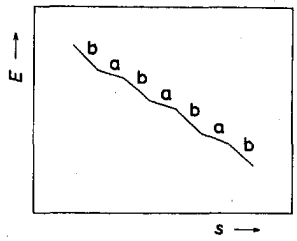

Fig. 5 Change of E with s (for $\beta > \alpha_Y + \phi$)

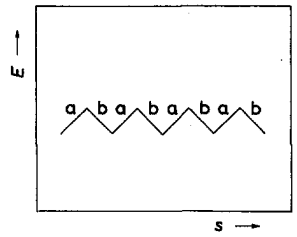

Fig. 7 Change of E with s (for $\alpha_Y - \phi < \beta < \alpha_Y + \phi$)

angle α_Y is used instead of θ_{YA} or θ_{YR} for the calculation of the energy change ΔE_{SV-SL} (Eq. (3)) between solid-gas interface and solid-liquid one, because each infinitesimal triangular side constituting the rough solid surface as shown in Fig. 4 is individually smooth and homogeneous as opposed to the apparent solid surface in Section 2.

3.1.2 Wetting Behavior of the Meniscus. Referring to Eq. (9), we consider the wetting behavior of the meniscus under the rough horizontal plate. In the following, it is assumed that the infinitesimal roughness height h, as shown in Fig. 4, is much smaller than H and hence θ is constant for any contact point of the meniscus on the rough surface. Now, considering the relation $\theta = \beta + \phi$ (ϕ: inclination angle of the roughness), the energy change rate dE/ds for the right-hand side a of the roughness as shown in the figure can be rewritten from Eq. (9) as

$$\left(\frac{dE}{ds}\right)_a = \sigma_{LV}\{\cos(\theta - \phi) - \cos\alpha_Y\} \tag{10}$$

Also dE/ds for the left-hand part b of the roughness shown in Fig. 4 can be rewritten by using the relation $\theta = \beta - \phi$ as;

$$\left(\frac{dE}{ds}\right)_b = \sigma_{LV}\{\cos(\theta + \phi) - \cos\alpha_Y\} \tag{11}$$

From Eqs. (10) and (11), it is found that the sign of dE/ds changes at $\theta = \alpha_Y + \phi$ and $\theta = \alpha_Y - \phi$. Referring to the relation, the stability and instability of the system are considered for the various conditions of θ or H in the following discussion.

(i) In the case of $\theta > \alpha_Y + \phi$ and $H < a\sqrt{2\{1 + \cos(\alpha_Y + \phi)\}}$

Substituting the condition $\theta > \alpha_Y + \phi$ into Eqs. (10) and (11), the following relation holds for dE/ds of the portion a and b.

$$\left(\frac{dE}{ds}\right)_b < \left(\frac{dE}{ds}\right)_a < 0 \tag{12}$$

From Eq. (12), the behavior of the system energy in relation to the displacement s along on the rough surface can be described qualitatively, as shown in Fig. 5. The figure shows that the system energy decreases monotonously for the advancing of the meniscus. Referring to the theoretical analysis of Eick et al. (1975), in which the hysteresis phenomena of the contact angle were investigated for the meniscus on the vertical plate with the same two-dimensional regular roughness as treated in this study, the advancing contact angle observed macroscopically θ_{YA} is expected as follows;

$$\theta_{YA} = \alpha_Y + \phi \tag{13}$$

If we consider that the above relation holds for the horizontal plate, the results of Fig. 5 shows that when the plate height H is small and the apparent angle θ becomes larger than the advancing contact angle θ_{YA}, the system becomes unstable and the meniscus wets the solid surface spontaneously.

(ii) In the case of $\theta < \alpha_Y - \phi$ and $H > a\sqrt{2\{1 + \cos(\alpha_Y - \phi)\}}$

In the same way as in the above discussion, dE/ds for the right-hand and the left-hand portion of the rough surface can be obtained by substituting the condition $0 < \theta < \alpha_Y - \phi$ into Eqs. (10) and (11).

$$\left(\frac{dE}{ds}\right)_a > \left(\frac{dE}{ds}\right)_b > 0 \tag{14}$$

Figure 6 shows the qualitative behavior of the system energy with s. Contrary to the case (i), however, the system is unstable for the receding of the meniscus. Just as with Eq. (13), for the advancing contact angle θ_{YA}, the receding contact angle θ_{YR} for the two-dimensional roughness is described as;

$$\theta_{YR} = \alpha_Y - \phi \tag{15}$$

Hence, it is found that when the plate height H increases and the apparent angle θ becomes smaller than the receding contact angle θ_{YR}, the system becomes unstable. As seen from Fig. 6, the meniscus spontaneously recedes and falls from the solid surface.

(iii) In the case of $\alpha_Y - \phi < \theta < \alpha_Y + \phi$ and $a\sqrt{2\{1 + \cos(\alpha_Y + \phi)\}} < H < a\sqrt{2\{1 + \cos(\alpha_Y - \phi)\}}$

dE/ds for this condition can be obtained in the same way as

$$\left(\frac{dE}{ds}\right)_a > 0, \quad \left(\frac{dE}{ds}\right)_b < 0 \tag{16}$$

The behavior of the system energy corresponding to the above relation is shown in Fig. 7. The figure shows that there exist many quasi-stable conditions corresponding to the local minimum of the energy on the curve. Hence the meniscus does not move spontaneously on the surface. The system is stable when

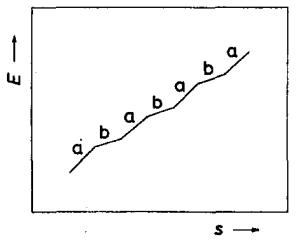

Fig. 6 Change of E with s (for $\beta < \alpha_Y - \phi$)

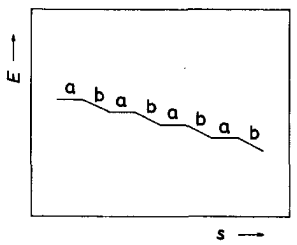

Fig. 8 Change of E with s (for $\beta = \alpha_Y + \phi$)

Table 1 Wetting behavior of two-dimensional meniscus under a horizontal plate

θ	H	Advance of Meniscus	Receding of Meniscus
$\theta > \theta_{YA}$	$H < a\sqrt{2(1+\cos\theta_{YA})}$	Unstable	Stable
$\theta = \theta_{YA}$	$H = a\sqrt{2(1+\cos\theta_{YA})}$	Neutral Stable	Stable
$\theta_{YR} < \theta < \theta_{YA}$	$a\sqrt{2(1+\cos\theta_{YA})} < H < a\sqrt{2(1+\cos\theta_{YR})}$	Stable	Stable
$\theta = \theta_{YR}$	$H = a\sqrt{2(1+\cos\theta_{YR})}$	Stable	Neutral Stable
$\theta < \theta_{YR}$	$H > a\sqrt{2(1+\cos\theta_{YR})}$	Stable	Unstable

the angle θ is in the range between the advancing contact angle $\theta_{YA} = \alpha_Y + \phi$ and the receding one $\theta_{YR} = \alpha_Y - \phi$.

(iv) In the case of $\theta_{YA} = \alpha_Y + \phi$ and $H = a\sqrt{2\{1 + \cos(\alpha_Y + \phi)\}}$

dE/ds for this condition can be written by using Eqs. (10) and (11) as

$$\left(\frac{dE}{ds}\right)_a = 0, \quad \left(\frac{dE}{ds}\right)_b < 0 \tag{17}$$

(v) In the case of $\theta = \alpha_Y - \phi$ and $H = a\sqrt{2\{1 + \cos(\alpha_Y - \phi)\}}$

In the same way, the following expression is obtained;

$$\left(\frac{dE}{ds}\right)_a > 0, \quad \left(\frac{dE}{ds}\right)_b = 0 \tag{18}$$

The conditions (iv) and (v) represent the neutral stability states of the system. For example, Fig. 8 shows that when $\theta = \alpha_Y + \phi$, (i.e., θ is equal to the advancing contact angle θ_{YA}), the system is neutral stable for the advance of the meniscus. In the same way, when $\theta = \alpha_Y - \phi$, (i.e., θ is equal to the receding contact angle), the system is neutral stable to the receding of the meniscus. As mentioned in Section 2, the advancing or receding contact angles indicate the boundary between the stable and unstable states of the meniscus under the horizontal plate.

The results of the above consideration can be summarized in Table 1. The contents of the table completely correspond to the results shown in Fig. 3 of Section 2.

3.2 Heterogeneous Surface. Next, the wetting behavior of the meniscus under a heterogeneous surface is discussed. As shown in Fig. 9, we consider the smooth heterogeneous surface consisting of two-dimensional stripes in which there are two kinds of surfaces with different characteristics; namely, portion a with Young's contact angle α_{YA} and portion b with α_{YB}. Such a surface was treated by Neumann and Good (1972), in order to investigate the effect of surface heterogeneity on the contact angle hysteresis.

The energy change rate dE/ds for the portion a and b is obtained as follows;

$$\left(\frac{dE}{ds}\right)_a = \sigma_{LV}(\cos\theta - \cos\alpha_{YA}) \tag{19}$$

$$\left(\frac{dE}{ds}\right)_b = \sigma_{LV}(\cos\theta - \cos\alpha_{YB}) \tag{20}$$

In the following discussion, we assume that α_{YA} is larger than α_{YB}. The analysis of the wetting behavior of the system is almost similar to that of Section 3.1 except that the sign of dE/ds changes at $\theta = \alpha_{YA}$ and $\theta = \alpha_{YB}$. Using Eqs. (19) and (20), the similar results corresponding to those for the conditions of (i) to (v) in the preceding section is obtained as stated in the following.

(i) In the case of $\theta > \alpha_{YA}$ and $H < a\sqrt{2(1 + \cos\alpha_{YA})}$

Substituting the relation $\theta > \alpha_{YA}$ into Eqs. (19) and (20), the same results as Eq. (12) are obtained. The behavior of the system energy can be described by Fig. 5 and the system is unstable for the advance of the meniscus.

(ii) In the case of $\theta < \alpha_{YB}$ and $H > a\sqrt{2(1 + \cos\alpha_{YB})}$

In the same manner, Eq. (14) in the preceding section is obtained. As shown in Fig. 6, the system is unstable for the receding of the meniscus.

(iii) In the case of $\alpha_{YB} < \theta < \alpha_{YA}$ and $a\sqrt{2(1 + \cos\alpha_{YA})} < H < a\sqrt{2(1 + \cos\alpha_{YB})}$

This condition corresponds to Eq. (16) and the system is stable for both advance and receding of the meniscus as shown in Fig. 7.

(iv) In the case of $H = a\sqrt{2(1 + \cos\alpha_{YA})}$

(v) In the case of $H = a\sqrt{2(1 + \cos\alpha_{YB})}$

These two conditions correspond to the neutral stability of the system as seen from Eqs. (17) and (18). The condition (iv) is represented by Fig. 8.

For the system of the heterogeneous solid surface as shown in Fig. 9, the theoretical results of Neumann and Good (1972) show that the advancing contact angle θ_{YA} is equal to the larger contact angle of the stripes and the receding contact angle θ_{YR} to the smaller one. Therefore the following expressions can be written;

$$\theta_{YA} = \alpha_{YA} \tag{21}$$

$$\theta_{YB} = \alpha_{YB} \tag{22}$$

Considering Eqs. (21) and (22), the above results for the conditions (i) to (v) can also be described by Table 1 in the preceding section for the rough surface.

The theoretical results of Sections 3.1 and 3.2, in which the microscopic effects such as surface roughness and heterogeneity are taken into consideration, agree with those in Section 2 based on the assumption that Young's equation can be applied to the apparent macroscopic system. Therefore, we can verify the validity of the assumption. In this report, only the surface roughness and heterogeneity with the ideally regular configuration are considered for the effect of the microscopic structures on the wetting behavior. For more general surface configuration, the analysis of the wetting behavior by the method, as stated in Section 3, should be more complicated. Although the microscopic viewpoint is necessary to discuss the mechanism of the hysteresis of the apparent contact angles, the macroscopic wet-

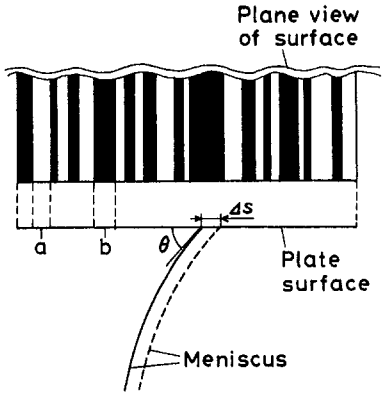

Fig. 9 Two-dimensional meniscus under a heterogeneous solid plate

ting behavior can be analyzed more simply by using the assumption as stated in Section 2.

4 Conclusion

The macroscopic wetting behavior of the two-dimensional meniscus under a horizontal plate was investigated theoretically, based on the assumption that the effects of the microscopic structure of the solid surface are wholly represented by the values of the apparent contact angles. The wetting behavior is quite different from that of the meniscus attached to an usual inclined plate. When the horizontal plate is raised or lowered to the critical height at which the meniscus attaches to the plate at the receding or the advancing contact angles, the system becomes unstable and the meniscus spontaneously breaks down.

The same problem was analyzed by the different manner in which the effect of microscopic structures of the solid surface; namely, two-dimensional roughness and heterogeneity is taken into consideration. The results obtained agree with those stated above. Therefore, the validity and the usefulness of the assumption in the preceding report was verified.

References

Chappius, J. (Edited by Hewitt, G. F., Delhaye, J. M., and Zuber, N.), 1982, "Contact Angles," *Multiphase Science and Technology,* Vol. 1, pp. 404–412.

Defazio, J. A., and Dyson, D. C., 1990a, "Stability of Rectilinear Contact Lines I, Single Contact Line Theory," *Journal of Colloid and Interface Science,* Vol. 135, pp. 45–57.

Defazio, J. A., and Dyson, D. C., 1990b, "Stability of Rectilinear Contact Lines II, Single Contact Line Examples," *Journal of Colloid and Interface Science,* Vol. 135, pp. 58–78.

Eick, J. D., Good, R. J., and Neumann, A. W., 1975, "Thermodynamics of contact Angles II, Rough Solid Surfaces," *Journal of Colloid and Interface Science,* Vol. 53, pp. 235–248.

Katoh, K., Fujita, H., and Sasaki, H., 1990, "Macroscopic Wetting Behavior and a Method for Measuring Contact Angles," ASME JOURNAL OF FLUIDS ENGINEERING, Vol. 112, pp. 289–295.

Katoh, K., Fujita, H., and Sasaki, H., 1992, "The Measurement of Solid-liquid Contact Angles," ASME JOURNAL OF FLUIDS ENGINEERING, Vol. 114, pp. 460–463.

Johnson, R. E., and Dettre, R. H., 1964, "Contact Angle Hysteresis 1, Study of an Idealized Rough Surface," *Advances in Chemistry Series,* No. 43, pp. 112–135.

Neumann, A. W., and Good, R. J., 1972, "Thermodynamics of Contact Angles I, Heterogeneous Solid Surfaces," *Journal of Colloid and Interface Science,* Vol. 38, pp. 341–358.

Neumann, A. W., 1974, "Contact Angles and Their Temperature Dependence: Thermodynamic Status, Measurement, Interpretation and Application," *Advances in Colloid and Interface Science,* Vol. 4, pp. 109–130.

Liquid Jet Pumps for Two-Phase Flows

R. G. Cunningham
Consultant,
Research Corporation Technologies, Inc.,
101 North Wilmot Road,
Tucson, AZ 85711
Fellow ASME

Isothermal compression of a bubbly secondary fluid in a mixing-throat and diffuser is described by a one-dimensional flow model of a liquid-jet pump. Friction-loss coefficients used in the four equations may be determined experimentally, or taken from the literature. The model reduces to the liquid-jet gas compressor case if the secondary liquid is zero. Conversely, a zero secondary-gas flow reduces the liquid-jet gas and liquid (LJGL) model to that of the familiar liquid-jet liquid pump. A "jet loss" occurs in liquid-jet pumps if the nozzle tip is withdrawn from the entrance plane of the throat, and jet loss is included in the efficiency equations. Comparisons are made with published test data for liquid-jet liquid pumps and for liquid-jet gas compressors. The LJGL model is used to explore jet pump responses to two-phase secondary flows, nozzle-to-throat area ratio, and primary-jet velocity. The results are shown in terms of performance curves versus flow ratios. Predicted peak efficiencies are approximately 50 percent. Under severe operating conditions, LJGL pump performance curves exhibit maximum-flow ratios or cut-offs. Cut-off occurs when two-phase secondary-flow streams attain sonic values at the entry of the mixing throat. A dimensionless number correlates flow-ratio cut-offs with pump geometry and operating conditions. Throat-entry choking of the secondary flow can be predicted, hence avoided, in designing jet pumps to handle two-phase fluids.

Introduction

The jet pump transfers momentum and energy from a high-velocity jet to a secondary fluid. Jet pumps are widely used because of their high reliability, particularly in remote or inaccessible locations. The liquid-jet liquid-secondary pump (LJL) is the most common application (Gosline and O'Brien, 1934; Cunningham, 1975). The success of one-dimensional modeling is well established. Cavitation may cause departure from the LJL theoretical performance, but cavitation is predictable using a NPSH type relationship. Close to the subject of this paper is the liquid-jet gas compressor (LJG) which has been reported theoretically, and with experimental confirmation (Cunningham, 1974; Cunningham and Dopkin, 1974; Witte, 1962). Again, in this case one-dimensional theory accurately predicted test results. Departure from theory occurs in the LJG case if the mixing of the jet and entrained gas is allowed to extend beyond the mixing throat into the diffuser.

This paper develops a one-dimensional model for a liquid jet pump handling two-phase gas-in-liquid bubbly mixtures, and examines the characteristics of this "LJGL" pump. The LJGL model also encompasses the secondary-flow extremes of a liquid (LJL pump) and a gas (the LJG compressor), i.e., the LJGL model bridges and links two established jet pumps.

Applications. In addition to pumping/compressing two-phase fluids, the LJGL pump is a compact mixer and reactor for the gas and two liquid streams. Appropriate uses: (1) Promotion of chemical or biological reactions through intimate mixing of finely dispersed gas into a liquid or mixed liquids; aeration and bulk mixing of sewage, for example. (2) Dispersing fine gas bubbles in a liquid(s) through intense shearing of a bubbly two-phase stream by a power jet. For example, generation of liquid foam in separation processing. (3) Promoting gas solution in a liquid medium.

Contributed by the Fluids Engineering Division for publication in the JOURNAL OF FLUIDS ENGINEERING. Manuscript received by the Fluids Engineering Division December 20, 1993; revised manuscript received September 7, 1994. Associate Technical Editor: J. H. Kim.

The LJGL Pump Model

Four one-dimensional flow equations are developed below to describe the LJGL pump. The LJL (liquid-liquid) pump and the LJG gas compressor can also be described by four one-dimensional flow equations; the nozzle equation is the same in all three cases. The LJG and the LJGL pumps both involve two-phase flows at the throat exit and in the diffuser. The LJGL jet pump alone involves two-phase secondary flows from the suction port to the mixing-throat entry.

The LJGL model is based on conservation equations for energy, momentum and mass. One-dimensional relations are used, and real-fluid losses are accounted for by friction-loss coefficients (K). Assumptions are: (1) The gas phase undergoes ideal-gas isothermal compression. (2) All two-phase flows (secondary flow at the throat entry, and total flows in the throat exit and diffuser) consist of homogeneous bubbly mixtures of a gas in a continuous liquid. (3) Heat transfer from the gas to the liquid is too small to raise the liquid temperature. (4) Change in solubility of the gas in the liquid between pressures P_s and P_d is negligible. (5) Vapor evolution from and condensation to the liquid are negligibly small.

Nozzle Equation

With reference to Fig. 1,

$$P_i + \rho_1 \frac{V_i^2}{2} = P_0 + \rho_1 \frac{V_n^2}{2} + K_n \rho_1 \frac{V_n^2}{2}$$

With $P_i \doteq \bar{P}_i$, the nozzle equation is

$$P_i - P_0 = Z(1 + K_n) \tag{1}$$

Throat-Entry Equation

The two-phase secondary flow is described by

$$\frac{dP}{\rho} + VdV + d\left(K_{en} \frac{V^2}{2}\right) = 0 \tag{2}$$

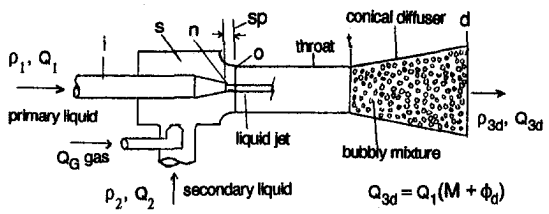

Fig. 1 Liquid-jet gas and liquid (LJGL) pump, and nomenclature

Density as a function of static pressure and flow ratios M and ϕ is

$$\rho_{2G} = \frac{m_2 + m_G}{Q_2 + Q_G} = \frac{m_1\left[\frac{m_2}{m_1} + \frac{m_G}{m_1}\right]}{Q_1(M + \phi)} = \rho_1\left[\frac{SM + \gamma\phi_s}{M + \phi}\right] \quad (3)$$

where $\phi = P_s\phi_s/P$, for isothermal flow. Inserting these relations and integrating Eq. (2) from s to 0:

$$\frac{M(P_0 - P_s) + P_s\phi_s \ln P_0/P_s}{\rho_1(SM + \gamma\phi_s)} + \frac{V_{2g0}^2}{2}(1 + K_{en}) = 0$$

Substituting from the continuity relation, $V_{2G0} = V_n(M + \phi_0)/c$, the throat-entry equation is

$$M(P_s - P_0) + P_s\phi_s \ln \frac{P_s}{P_0} = Z\frac{(SM + \gamma\phi_s)}{c^2}(1 + K_{en})(M + \phi_0)^2 \quad (4)$$

Mixing Throat Momentum Equation

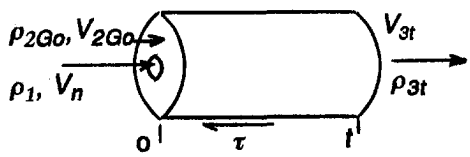

Equating control volume forces and fluid momentum changes

$$(P_0 - P_t)A_{th} - \tau A_w = (m_1 + m_2 + m_G)V_{3t} - m_1V_n - (m_2 + m_G)V_{2G0} \quad (5)$$

where

$$\frac{\tau A_w}{A_{th}} = \frac{K_{th}\rho_{3t}V_{3t}^2}{2},$$

$$\rho_{3t} = \frac{m_1 + m_2 + m_G}{Q_1 + Q_2 + Q_{Gt}} = \rho_1\left[\frac{1 + SM + \gamma\phi_s}{1 + M + \phi_t}\right], \quad \text{and}$$

$$\rho_{2G0} = \rho_1\left[\frac{SM + \gamma\phi_s}{M + \phi_0}\right]$$

From continuity

V_{2G0} see above

$$V_{3t} = Q_1\frac{(1 + M + \phi_t)}{A_{th}} = V_nb(1 + M + \phi_t)$$

Substituting these relations in Eq. (5), and dividing by A_{th} produces a quadratic equation in P_t. The throat momentum equation becomes:

Nomenclature

A = area, ft^2 (m^2)
A_w = throat wall area, ft^2 (m^2)
C = velocity of sound, ft/sec (m/s)
D = diameter, ft (m)
E = energy rate, ft lb/sec (joule/s)
K = friction loss coefficient
°K = absolute temperature, Kelvin
LJL = liquid-jet liquid pump
LJG = liquid-jet gas compressor
LJGL = liquid-jet gas and liquid pump
M = liquid/liquid flow ratio, Q_2/Q_1
MN = Mach number
NPSH = net positive suction head
P, $\bar{P}$ = pressure: static, total, psia (kPa abs.)
P_v = vapor pressure, psia (kPa abs.)
Q = volumetric rate, ft^3/sec (m^3/s)
R = gas constant, ft lbs/slug °R (joules/kg °K)
°R = absolute temperature, Rankine
S = density ratio, ρ_2/ρ_1
T = temperature, °R (°K)
V = velocity, ft/sec (m/sec)
W = work rate, ft lbs/sec (joules/s)
Z = jet dynamic pressure, psi (kPa)
a = diffuser area ratio, A_t/A_d
b = jet pump area ratio A_n/A_t
c = $A_{2G0}/A_n = (A_t - A_n)/A_n = (1 - b)/b$
m = mass flow rate, slugs/sec (kg/s)
psi = pounds per square inch
psia = pounds per square inch, absolute
r_v = gas/liquid vol. flow rate ratio Q_G/Q_2
r_{v0} = gas/liquid vol. flow rate ratio at 0: Q_{G0}/Q_2
r_m = gas/liquid mass flow-rate ratio
sp = nozzle-to-throat spacing, ft (m)
sp/D_{th} = spacing, throat diameters
η = efficiency
γ = gas density ratio at s, ρ_{Gs}/ρ_1
$\gamma\phi_s$ = m_{Gs}/m_1
ρ = density, slugs/ft^3 (kg/m^3)
τ = shear stress, psi (kPa)
ϕ = gas flow ratio Q_G/Q_1
ϕ_s = gas flow ratio Q_{Gs}/Q_1 at s

Subscripts

1 = liquid primary flow
2 = liquid secondary flow
G = gas secondary flow
$2G$ = bubbly secondary flow
$2G0$ = bubbly sec. flow at 0
L = liquid
lim = limit for cavitating flow
3 = combined fluids 1, 2, and G
i, s, n, = locations, see Fig. 1
0, t, d = locations, see Fig. 1
$c0$ = flow-ratio cut-off
f = friction loss
n = nozzle
en = throat entry
th = mixing throat
di = diffuser

Subscript Examples

Q_2 = secondary liquid vol. flow rate
Q_{G0} = secondary gas flow rate, at 0
Q_{2G0} = flow rate of bubbly mixture of gas in the secondary liquid, at 0

Exponents

* = critical flow conditions at Mach one

$$P_t^2 - Z\Big[2b - b^2(2 + K_{th})(1 + SM + \gamma\phi_s)(1 + M) + 2(SM + \gamma\phi_s)(M + \phi_0)\frac{b^2}{(1 - b)} + \frac{P_0}{Z}\Big]P_t + Z[b^2(2 + K_{th})(1 + SM + \gamma\phi_s)P_s\phi_s] = 0 \quad (6)$$

Diffuser Equations

A bubbly mixture flows from t to d:

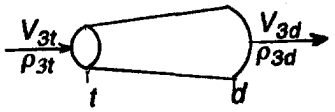

(The area ratio $a = A_t/A_d$)

$$\int_t^d \frac{dP}{\rho} + \int_t^d VdV + \int_t^d \frac{\Delta P_f}{\rho_{3t}} = 0 \quad (7)$$

The mixture density is:

$$\rho_3 = \frac{m_1 + m_2 + m_G}{Q_1 + Q_2 + Q_G} = \rho_1\left[\frac{1 + SM + \gamma\phi_s}{1 + M + \phi}\right],$$

where $\phi = \dfrac{P_s\phi_s}{P}$

From continuity,

$$V_{3t} = V_n b(1 + M + \phi_t)$$

$$V_{3d} = V_n ab(1 + M + \phi_d)$$

The friction loss term is

$$\Delta P_f = K_{di}\rho_{3t}\frac{V_{3t}^2}{2} = K_{di}\rho_1\frac{V_n^2}{2}b^2(1 + SM + \gamma\phi_s)(1 + M + \phi_t)$$

Integrating Eq. (8) and substituting, the diffuser equation becomes:

$$(P_d - P_t) + \frac{P_s\phi_s}{1 + M}\ln\frac{P_d}{P_t} = Zb^2\left[\frac{1 + SM + \gamma\phi_s}{1 + M}\right] \times [(1 + M + \phi_t)^2 - a^2(1 + M + \phi_d)^2 - K_{di}(1 + M + \phi_t)(1 + M)] \quad (8)$$

A by-definition friction loss term is used in Eq. (8) to account for energy losses in the diffuser. This approach is dictated by two considerations. (1) It results in similar definitions for the throat and diffuser losses, consistent with previous treatments of LJL and LJG friction losses. (2) Friction loss data for bubbly flow in LJG throats and diffusers (Cunningham and Dopkin, 1974) were measured using this definition. K_{th} and K_{di} data versus gas flow ratio formed flat lines independent of the gas ratio, provided only that mixing was completed in the throat. Since the LJGL diffuser and throat-exit flows in this paper are identical to the earlier LJG pump experiments, it is reasonable to assume that these K_{th} and K_{di} values are applicable to the present LJGL case. Eqs. (1), (4), (6), and (8) describe the LJGL pump in terms of the flow processes in the four components. The term $\gamma\phi_s = \rho_{Gs}Q_{Gs}/\rho_1Q_1$. For isothermal flow $\gamma\phi_s = 144P_s\phi_s/\mathbf{R}T_s\rho_1$. For air, with $\mathbf{R}$ = 1716 ft lbs/slug °R, and water, ρ_1 = 1.94 slugs/ft^3, $\gamma\phi_s = .0432P_s\phi_s/T_s$. In SI, $\mathbf{R}$ = 286.92 mN/kg °K, ρ_1 = 1000 kg/m^3, and $\gamma\phi_s = .00348P_s\phi_s/T_s$, with P_s in kN/m^2, and T_s in °K. For fluids other than water and air, the $\mathbf{R}$ and/or ρ_1 values must of course be replaced.

Two-Phase Flow Mach Numbers at Throat Entry and Exit.

$C = \sqrt{\dfrac{dP}{d\rho}}$. With $r_m = \dfrac{m_G}{m_L}$ and $r_v = \dfrac{Q_G}{Q_L}$,

(Eddington, 1967)

$$C = (1 + r_v)\sqrt{\frac{P}{\rho_1 r_v(1 + r_m)}}$$

For the LJGL pump the secondary fluid velocity at the throat entry is

$$V_{2G0} = \frac{Q_{2G0}}{A_{2G0}} = \frac{Q_1(M + \phi_0)}{A_n c} = V_n\frac{(M + \phi_0)}{c} = \sqrt{\frac{2Z}{\rho_1}}\frac{(M + \phi_0)}{c}$$

The r ratios in LJGL terminology are:

$$r_{m0} = \frac{\rho_{G0}Q_{G0}}{\rho_2Q_2} = \frac{\rho_{G0}Q_{G0}}{S\rho_1MQ_1} = \frac{\gamma_0\phi_0}{SM} = \frac{\gamma\phi_s}{SM}. \quad r_{v0} = \frac{Q_1\phi_0}{Q_1M} = \frac{\phi_0}{M}$$

Thus

$$\mathbf{MN}_{2G0} = \frac{V_{2G0}}{C_{2G0}} = \frac{\phi_0}{c}\sqrt{\frac{2Z}{P_s\phi_s}(SM + \gamma\phi_s)} \quad (9)$$

At the throat exit:

$$V_{3t} = \sqrt{\frac{2Z}{\rho_1}}b(1 + M + \phi_t)$$

$$r_{mt} = \frac{m_G}{m_1 + m_2} = \frac{\gamma\phi_s}{1 + SM}; \quad r_{vt} = \frac{Q_{Gt}}{Q_1 + Q_2} = \frac{\phi_t}{1 + M}$$

So that:

$$\mathbf{MN}_{3t} = \phi_t b\sqrt{\frac{2ZS(1 + M)}{P_s\phi_s(1 + SM)}(1 + SM + \gamma\phi_s)} \quad (10)$$

Pump Efficiencies. The LJGL pump produces two useful-work results: (1) isothermal compression of the gas component, and (2) static pressure increase of the liquid component of the secondary flow stream. With W as the work rate, ft lbs/s (power) the two work rates are

$W_G = \rho_{Gs}Q_{Gs}\mathbf{R}T_s\ln(P_d/P_s)$ the work rate on the gas component, and

$W_L = Q_2(P_d - P_s)$ the work rate on the liquid component.

The energy rate input is

$$E_{in} = Q_1(P_i - P_d)$$

The LJGL pump mechanical efficiency is the total work rate out divided by the energy rate in:

$$\eta = \frac{P_s\phi_s\ln(P_d/P_s) + M(P_d - P_s)}{P_i - P_d} = \eta_G + \eta_L \quad (11)$$

The Jet Loss. Jet pumps in practical applications have nozzle-to-throat spacings sp/D_{th} of one or more throat diameters. In this case the power jet traverses from a static pressure at or near P_s down to P_0, with no useful work recognized in the one-dimensional theory. Thus a "jet loss" occurs, which is in addition to the friction and mixing losses (Cunningham, 1975). In two-phase flow LJGL pumps jet losses will be significant because $(P_s - P_0)$ magnitudes approach those in LJL pumps.

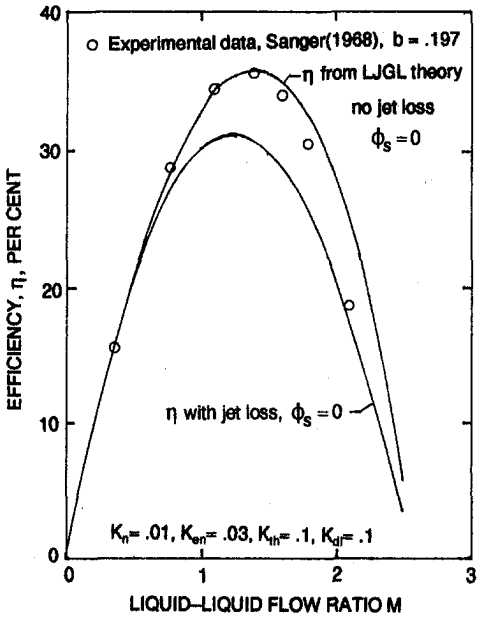

Fig. 2 LJL test data compared with LJGL model. No gas injected at the secondary inlet, hence $\phi_s = 0$ applies. Sanger's nozzle spacing zero, eliminating the jet loss.

Pump Efficiency, Incorporating Jet Loss. In Eq. (11) $(P_i - P_d)$ is expanded: $(P_i - P_d) = (P_i - P_s) - (P_d - P_s)$; and $(P_i - P_s) = (P_i - P_0) - (P_s - P_0) = Z(1 + K_n) - j(P_s - P_0)$, where $j = 1$ for a fully-inserted nozzle, *no jet loss;* and $j = 0$ for the usual case of the retracted nozzle, which produces *full jet loss.*

Eq. (11) now becomes

$$\eta = \frac{P_s\phi_s \ln (P_d/P_s) + M(P_d - P_s)}{Z(1 + K_n) - j(P_s - P_0) - (P_d - P_s)} = \eta_G + \eta_L \quad (12)$$

Equation (12) is recommended for liquid-jet pumps as follows: use $j = 1$ for no-jet-loss pumps (thin-wall nozzle fully inserted, $sp = 0$); use $j = 0$ for the full jet-loss case, which obtains for pumps with normally retracted nozzle configurations.

Computer Program. Solutions for the LJGL model equations were generated using a computer spreadsheet program. Values for Z, b, P_s, T_s, $\mathbf{R}$, ρ_1, S and the four K coefficients were fixed/assumed for each pump and operating condition. Eqs. (4), (6), and (8) were then solved for each step increase in flow ratio M, with ϕ_s held constant. Alternatively, M was held constant and the equations were solved for step increases in ϕ_s. Both types of performance curves are useful. Equations (4), (6), and (8) are interdependent: solution of Eq. (6) requires P_0 values from Eq. (4) and solution of Eq. (8) requires P_t values from Eq. (6). The program outputs at each flow-ratio step were static pressures P_0, P_t, and P_d, and the three pump efficiencies defined by Eq. (12).

LJGL Model: Comparisons With Test Data

To validate the model, comparison with published test data is possible at the two ends of the LJGL model span. Figure 2 shows LJL data from Sanger (1968, 1970) versus the LJGL theory (using $\phi_s = 0$). Sanger used nozzles fully inserted to place the tip in the throat-inlet plane; consequently there was no jet loss. Sanger's data agree with the no-jet-loss LJGL curve ($j = 1$). The poorer match at high M values is probably due to incipient cavitation, a condition which is encouraged by zero nozzle spacing sp. Fig. 2 also shows the jet-loss efficiency curve. If the pump nozzle is retracted from the throat entry, *which is the usual case in practice,* jet loss will occur, i.e., $j = 0$.

In Fig. 3, liquid-jet gas compressor data (Dopkin, 1973) are compared with LJGL theory (using $M = 0$). The K values listed in Fig. 3 are relatively large, and match those measured in the lab experiments, which used small-size pumps ($D_{th} < .5$ in.). Theory-experiment agreement is evident. The divergence at $\phi_s > 2.5$ results from the mixing process extending into the diffuser. Longer mixing throats are required for the LJG gas compressor, particularly at small b values, compared to the LJL pump. For the latter, lengths of only four to six throat diameters are adequate. Cunningham and Dopkin (1974) reported an empirical relation for the LJG pump: optimum throat-length/jet diameter = $15c$. This relation predicts a length of 43 mixing-throat diameters for a pump with $b = .1$. LJGL throat lengths will be less than for the LJG pump, approaching the LJL pump configuration, but laboratory testing may be needed to establish design guidelines.

Based on these two "end-point" matches of the LJGL theory with test data, it is reasonable to conclude that the model will also predict the performance of LJGL jet pumps, when operated under well-mixed bubbly secondary-flow conditions.

Two-Phase Flow Effects on the Liquid Jet Pump

The LJGL model was used in exploring pump-performance effects of two-phase secondary flows. One set of K values was assumed: $K_n = .05$, $K_{en} = 0$, $K_{th} = .10$, $K_{di} = .10$. These values apply to low-friction pumps similar to those used by Sanger (1970). For small-size pumps ($D_{th} < .5$ in.), larger K values would apply, e.g., see Fig. 3. Other conditions were: $Z = 40$ psi (275.8 kPa), $b = .07$, $S = 1$, $a = 0.235$, $T_s = 540$°R (300°K), and $P_s = 14.7$ psia (101.35 kPa).

The effects of gas mixed into the secondary liquid flow are shown in Fig. 4. For the $\phi_s = 0$ (LJL) case there is one efficiency $\eta = \eta_L$ curve. For $\phi_s = 2$, three curves apply: η_G, η_L, and η. The η_L curve for $\phi_s = 2$ lies below $\eta_L = \eta$ for the $\phi_s = 0$ case. The secondary-flow gas ($\phi_s = 2$) also results in a flow ratio "cut-off" of $M_{c0} = 3.59$. With $\phi_s = 2$, the gas compres-

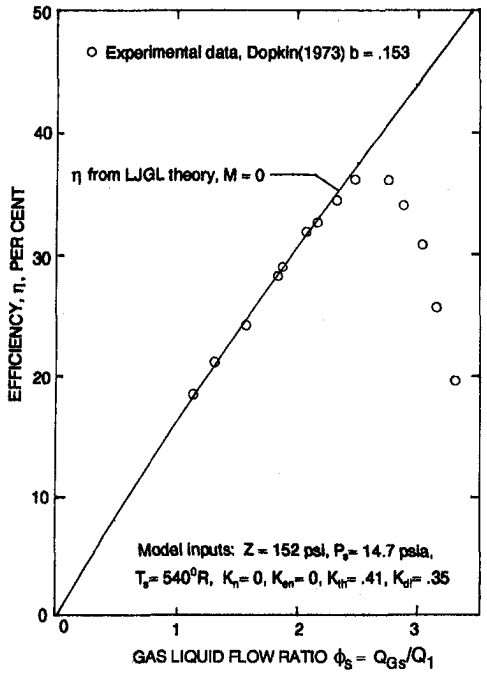

Fig. 3 Liquid-jet gas compressor test data versus LJGL model, using $M = 0$

sion efficiency η_G declines with increase in M. But the total efficiency η increases and peaks at 38 versus 27 percent for the corresponding LJL pump. *The isothermal compression work on the gas more than compensates for the loss in liquid-liquid pumping efficiency.* At the bottom of Fig. 4 note that P_0 (throat-entry pressure) is significantly depressed by a two-phase secondary flow.

LJGL performance curves were also examined as functions of the gas flow ratio ϕ_s, with M held constant. In this case the η_L liquid pumping efficiency declines as ϕ_s increases. The gas efficiency η_G increases with ϕ_s, but falls below the gas-compressor LJG case. But the LJGL two-phase total efficiency η exceeds η for the LJG gas compressor, over most of the ϕ_s range. Again, two-phase flows caused flow ratio cut-offs. For example, with $M = 2$ and 3, cut-offs occurred at $\phi_{sc0} = 5.13$ and 2.82, respectively.

Examination of Flow Ratio Cut-Off. In solving the LJGL theoretical model, cut-off was determined as the highest M liquid ratio (or highest gas ratio if ϕ_s was the independent parameter) which permitted solution of the throat-entry Eq. (4), by means of successive-approximations for the unknown, P_0. Flow ratio cut-off was found in every computer pump model in which the theoretical pump was subjected to severe operating conditions. In Fig. 4 the severe condition was the gas load of ϕ_s = 2, which caused an M_{c0} of 3.59. At this cut-off (Fig. 4) the Mach number was $\mathbf{MN}_{2G0} = .97$, at the throat entry. Performance curves vs. the gas ratio ϕ_s also exhibited throat-entry Mach numbers at or near unity value at cut-off. These Mach numbers point to compressible choked flow at the throat inlet. This is quite possible: the velocity of sound in a two-phase fluid is very low, e.g., about 70 ft/s for a 50/50 mixture of air in water.

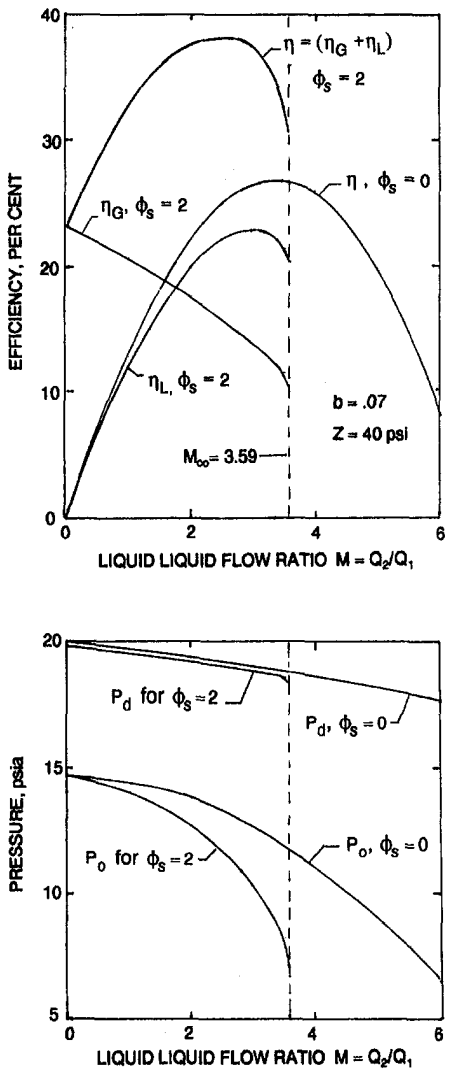

Fig. 4 Performance curves for LJL pump ($\phi_s = 0$) compared with LJGL pump with $\phi_s = 2$. The vertical dashed line indicates the cut-off flow ratio.

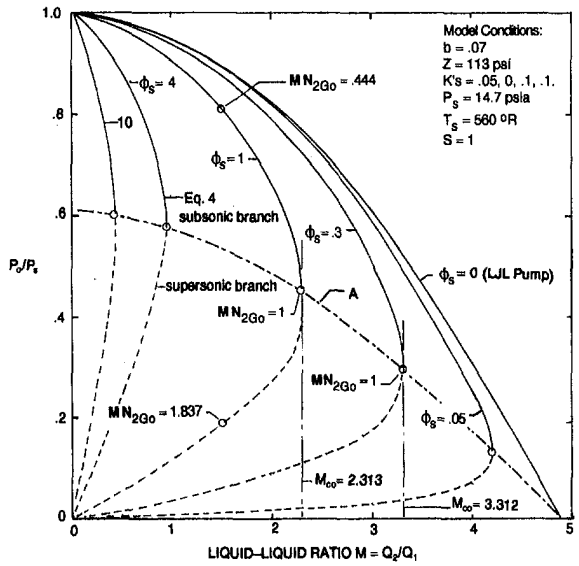

Fig. 5 Throat-entry pressure ratios versus flow ratio $M = Q_1/Q_2$. MN is Mach number.

Confirmation of choked flow at the throat entry is provided in Fig. 5. Curves of P_0/P_s versus M are *double-valued.* Equation (4) produces both subsonic- and supersonic-flow values of P_0 at each M level, up to the M_{c0} cut-off point, where $\mathbf{MN}_{2G0} = 1$ is the only solution. At each apex, $P_0/P_s = P^*/P_s = r^*$, the critical pressure ratio. The upper/solid line represents subsonic flow. On the $\phi_s = 1$ curve, one point is identified: $\mathbf{MN}_{2G0} = .444$. Subsonic Mach numbers increase as P_0 is reduced, until the apex is reached, where $\mathbf{MN}_{2G0} = 1$. The lower/dashed line represents the supersonic solutions (impossible in practice because the s-0 flow path is converging).

To the right of each of the M_{c0} points in Fig. 5 there are no solutions to the Eq. 4 descriptions of throat-entry flow. This explains the cut-off phenomenon: Eq. (4)—and hence the LJGL model—fails for any M greater than M_{c0}. Throat-entry flow curves for six ϕ_s levels from 10 down to 0 are included in Fig. 5. The uppermost curve is for $\phi_s = 0$, the LJL jet pump. It intersects the abscissa at $M = 4.79$. Line A connects this $M = 4.79$ point and the apexes of the five LJGL double valued curves. From $r^* = 0$ at the right end, r^* increases to the left, in the direction of increased gas content. In the limit, line A approaches the LJG gas compressor case ($M = 0$) and $r = .607$, the critical pressure ratio r^* for isothermal flow of an ideal gas. Figure 5 also explains how M_{c0} is reduced by increased secondary-flow gas content ϕ_s.

A different family of double valued curves results from plotting P_0/P_s versus the gas flow ratio ϕ_s, at constant M levels. (Not shown here.) These P_0/P_s curves are also double-valued, albeit of different shape. Each M-level curve peaks at a ϕ_{sc0} gas flow ratio cut-off, where $\mathbf{MN}_{2G0} = 1$.

Effects of Pump Area Ratio and Jet Velocity

Using the same operating conditions and K values listed above for Fig. 4, the effects of area ratio b and jet velocity were examined. Figure 6 shows LJGL pump efficiencies as functions

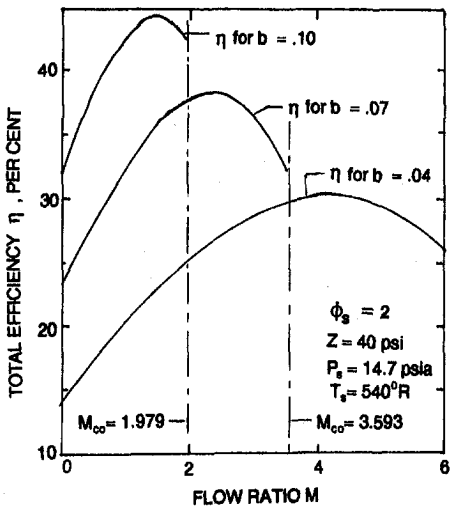

Fig. 6 Total efficiency curves for three pump area ratios $b = A_n/A_{th}$

of flow ratio M, for b = .04, .07 and .10 pumps operating at $\phi_s = 2$. Increasing the design area ratio b improves total efficiency η, but causes earlier flow-ratio cut-offs.

The jet dynamic pressure Z was raised in two stages above the "standard" 40 psi, as shown in the Fig. 7 (top) efficiency curves. Higher Z levels reduce total efficiency slightly because gas compression efficiency η_G is depressed. Of greater significance, high jet velocities cause large reductions in cut-off flow ratios.

Figure 7 (center) shows the P_d responses. High Z levels will produce high P_d discharge pressures with this low b-value pump (.07), but with penalties both in efficiency and early cut-off. Fig. 7 (lower) shows throat inlet pressures. Each P_0 curve peaks at the M_{c0} values indicated, and simultaneously the secondary-flow Mach number is 1 at the throat entry. These P_0 curves are double valued (as in Fig. 5), but only the subsonic or "real" branches are shown here.

Theoretical Prediction of Flow Cut-Off

Solving Eq. (4) by successive approximations is difficult at the peak of the double valued curves, where the curves are tangent to the vertical lines marking the cut-off flow ratios M_{c0} or ϕ_{sc0}. A better method for finding flow ratios at these peaks is the simultaneous solution of Eqs. 4 and 9 for M_{c0}, with $\mathbf{MN}_{2G0} = 1$. Table 1 contains these simultaneous solutions for M_{c0} and the corresponding values of P_0, for five b-value pumps each operating at three Z levels, and at three ϕ_s gas ratios. The values of $r^* = P^*/P_s$ are listed. ($P_0 = P^*$ for all points in Table 1). Mach numbers of the two-phase flows at the throat exit t were also calculated, using Eq. (10). $\mathbf{MN}_{3t}$ was always subsonic. In other words, throat mixing produces a subsonic flow at the throat-exit/diffuser-entry, even when the throat-entry secondary-flow velocity is maximum, i.e., sonic.

Table 1 also includes the secondary-stream gas/liquid volumetric rate ratios $r_{v0} = \phi_0/M_{c0} = Q_{G0}/Q_2$ at cut-off. Eddington (1967) observed that two-phase flows with ratios r_v from 0.1 to about 1.0 are homogeneous or bubbly mixtures of gas in a continuous liquid phase. At the other extreme, say $r_v > 10$, it may be assumed that gas is the continuous medium, i.e., droplets are suspended in the gas. Table 1 shows that $r_{v0} < 1$ for all ϕ_s = .3 calculations, and for b = .04 and .07 of the $\phi_s = 1$ series. These r_{v0} comparisons support the flow-model assumption in this paper of bubbly flow in the secondary stream, particularly for the small b ratios (.04, .07, .10), which are the most appropriate area ratios for two-phase secondary-flow jet-pumps.

In Fig. 8, M_{c0} values from Table 1 plotted versus the dimensionless parameter $c\sqrt{(P_s - P_0)/Z}$ (also listed in Table 1). Three separate curves are formed for the ϕ_s = .3, 1 and 2 gas ratios. (Area ratio c increases as b decreases). Although these data are from computer runs at one P_s value (14.7 psia), M_{c0} values from P_s-varied runs also fall on the appropriate ϕ_s-level curve. The pressure-difference ratio $(P_s - P_0)/Z$ controls the severity of the operating condition, not the individual pressure terms. In Eq. (4), note that at $\phi_s = 0$ and with $K_{en} = 0$, $M = c\sqrt{(P_s - P_0)/Z}$. Thus in Fig. 8 the 45° straight line labeled $\phi_s = 0$ represents liquid-liquid flow. In this special case M and the abscissa parameter are numerically identical.

Figure 8 shows that flow ratio cut-off behavior (M_{c0}) is dependent on four operating and geometric factors: M_{c0} can be improved by reducing ϕ_s, Z, or b (reducing b increases c), or by increasing $(P_s - P_0)$.

It is interesting to note that cavitation in LJL pumps can be correlated by a NPSH type expression: $M_{\text{lim}} = c\sqrt{(P_s - P_v)/Z\sigma}$, where M_{lim} is the cavitation-limited flow ratio, P_v is the liquid vapor pressure and σ is a cavitation coefficient, about 1.35 in magnitude. (Cunningham et al., 1970). The two limiting flow ratios M_{c0} and M_{lim} are thus similar in structure.

Figure 9 shows the profound effect of $r_{v0} = \phi_0/M_{c0}$ on the critical pressure ratio $r^* = P^*/P_s$. (Curve represents r_{v0} and r^* values in Table 1.) As the gas/liquid volumetric rate ratio becomes very large (toward the LJG case), r^* approaches .607, the isothermal critical pressure ratio. As r_{v0} moves toward zero, (toward the LJL case) r^* approaches zero. Fig. 9 confirms the limits shown in Fig. 5.

A Comparison of Phenomena Affecting Liquid-Jet Pumps

Performances of the three liquid-jet pumps, LJL, LJG, and LJGL can be described by one-dimensional models. The LJGL

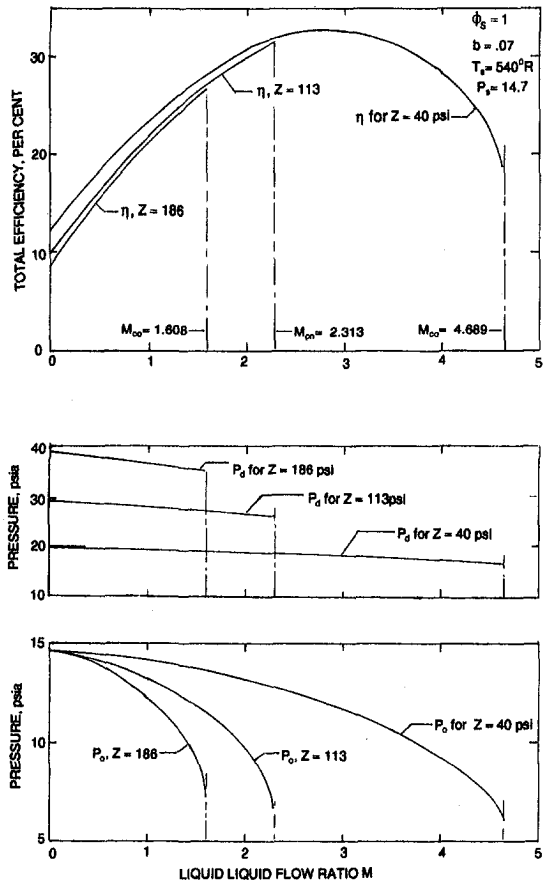

Fig. 7 Effects of jet dynamic pressure (Z) on LJGL pump performance

Table 1 Cut-off flow ratios M_{c0} versus jet dynamic pressures and area ratios for gas/liquid ratios ϕ_s = .3, 1, and 2

	ϕ_s = .3					ϕ_s = 1					ϕ_s = 2				
z	M_{c0}	P_0	r_{v0}	r^*	$c\sqrt{(P_s-P_0)/Z}$	M_{c0}	P_0	r_{v0}	r^*	$c\sqrt{(P_s-P_0)/Z}$	M_{c0}	P_0	r_{v0}	r^*	$c\sqrt{(P_s-P_0)/Z}$
	b =.04					b =.04					b =.04				
40	11.853	2.6944	0.1361	0.1833	13.1464	9.8588	4.4667	0.3323	0.3052	12.1273	8.2019	5.7879	0.6193	0.3937	11.3264
112.9	6.6167	3.3822	0.1971	0.2301	7.5988	5.1526	5.4497	0.5235	0.3707	6.8698	3.9955	6.7879	1.0840	0.4618	6.3535
185.8	4.9645	3.7584	0.2364	0.2557	5.8241	3.7116	5.9338	0.6675	0.4037	5.2131	2.7579	7.2355	1.4733	0.4922	4.8105
	b =.07					b =.07					b =.07				
40	6.0889	3.4687	0.2078	0.2373	7.0337	4.6890	5.5900	0.5606	0.3803	6.3404	3.5933	6.9218	1.1821	0.4709	5.8586
112.9	3.3122	4.3229	0.3080	0.2941	4.0279	2.3127	6.5963	0.9636	0.4487	3.5594	1.6056	7.7764	2.3547	0.5290	3.2901
185.8	2.4459	4.7656	0.3763	0.3242	3.0721	1.6060	7.0569	1.2954	0.4801	2.6946	1.0573	8.0981	3.4338	0.5509	2.5043
	b =.10					b =.10					b =.10				
40	3.8653	4.1033	0.2781	0.2791	4.6323	2.7748	6.3482	0.8346	0.4319	4.1125	1.9786	7.5842	1.9592	0.5159	3.7960
112.9	2.0539	5.0253	0.4273	0.3419	2.6346	1.2998	7.3013	1.5490	0.4967	2.3039	0.8281	8.2496	4.3035	0.5612	2.1512
185.8	1.4947	5.4998	0.5365	0.3741	2.0027	0.8774	7.6972	2.1766	0.5236	1.7472	0.5291	8.4661	6.5630	0.5759	1.6485
	b =.13					b =.13					b =.13				
40	2.7056	4.6169	0.3530	0.3141	3.3600	1.8164	6.9082	1.1715	0.4699	2.9537	1.2162	7.9994	3.0219	0.5442	2.7391
112.9	1.4057	5.5911	0.5611	0.3803	1.9009	0.8126	7.7658	2.3294	0.5283	1.6585	0.4852	8.4999	7.1294	0.5782	1.5683
185.8	1.0088	6.0785	0.7194	0.4134	1.4418	0.5354	8.0695	3.3940	0.5503	1.2623	0.3041	8.6455	11.181	0.5881	1.2081
	b =.16					b =.16					b =.16				
40	2.0024	5.0631	0.4350	0.3444	2.5769	1.2600	7.3354	1.5905	0.4990	2.2527	0.7991	8.2696	4.4468	0.5626	2.1050
112.9	1.0175	6.0641	0.7147	0.4125	1.4520	0.5413	8.0821	3.3603	0.5498	1.2711	0.3078	8.6425	11.051	0.5879	1.2161
185.8	0.7204	6.5460	0.9352	0.4453	1.0998	0.3498	8.3398	5.0388	0.5673	0.9713	0.1905	8.7425	17.649	0.5947	0.9401

Model Conditions: P_s = 14.7 psia, T_s = 560 °R, S = 1, K_n = .05, K_{en} = 0, K_{th} = .1, K_{di} = .1.

model covers all three cases. But models are valid only as long as the actual flow regimes match the assumptions used in deriving the theoretical equations. These three liquid-jet pumps are reviewed for possible actual-flow departures from theory, as follows:

(*a*) LJGL pumps may exhibit flow cut-off, as a result of compressible-flow choking of the secondary stream. The flow ratio M_{c0} or ϕ_{sc0} at which this will occur can be predicted from simultaneous solution of Eqs. (4) and (9), with $\mathbf{MN}_{2G0} = 1$. Secondary flow Eq. (4) cannot be solved at any flow ratio greater than the cut-off. In terms of practical pump operation this means that, at the cut-off, further reduction of the discharge pressure P_d will not increase the flow ratio, and efficiency will drop abruptly toward zero.

(*b*) LJL pumps may exhibit cavitation-limited flow, in which a reduction of discharge pressure no longer increases the secondary flow rate. (The pump efficiency drops in a vertical line toward zero, hence efficiency curves for the cavitating LJL pump could resemble those of a choked LJGL jet pump.) LJL pump cavitation occurs *within the mixing throat,* not in the liquid secondary flow-stream at the throat entry.

(*c*) Performance of the LJG gas compressor is predictable via one-dimensional theory *provided* mixing is completed in the throat, before diffuser entry. If the discharge pressure is too low, i.e., below design level, mixing will extend into the diffuser and performance will then deteriorate. LJG gas compressor pumps are not subject to cavitation or choked flow.

Commonalities for all three liquid-jet pumps are noted: friction coefficients K, the nozzle-to-throat spacing sp, and the mixing-throat length cannot be predicted from one-dimensional theory. The LJL and LJG literatures contain recommendations for the two longitudinal dimensions, and for measured K friction coefficients as well. Friction coefficients may also be found as

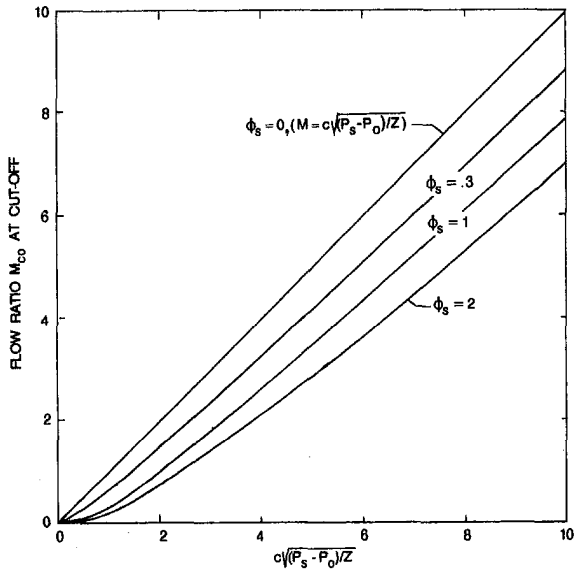

Fig. 8 Liquid flow ratio cut-off M_{c0} (Table 1) versus parameter $c\sqrt{(P_s - P_0)Z}$

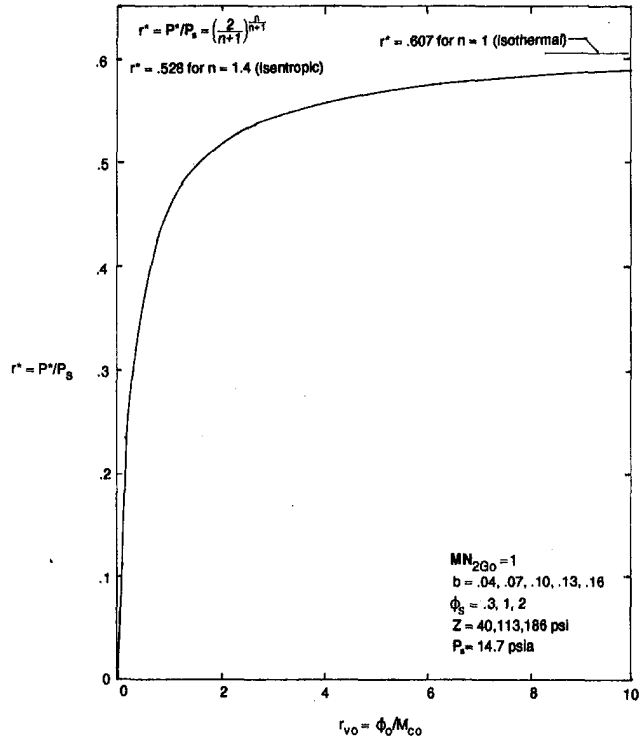

Fig. 9 Critical pressure ratio r^* versus the gas flow ratio $f_{v0} = \phi_0/M_{c0}$, from Table 1

published K values for nozzles, short tubes and diffusers. The alternative is laboratory testing of liquid-jet pumps or components to measure the K values.

Conclusions and Summary

A one-dimensional model describes the LJGL pump, a device which can operate with liquid, gas or two-phase secondary flows. Losses which occur in actual pumps are accounted for by friction loss coefficients. Five assumptions or restrictions are listed above in the derivation. The LJGL equations reduce to models for the well-known liquid-liquid (LJL) jet pump, or for the gas compressor (LJG) jet pump, upon removal of the terms for gas flow ratio ϕ_s, or the M terms, respectively.

Comparisons with published experimental data for the LJL and LJG jet pumps validate the LJGL pump model as applicable to these "end" conditions. Because of these theory-experiment agreements, it is logical to expect similar success in predicting two-phase secondary-flow jet pumps. No experimental data are known to be available at this time for comparison with the gas-in-liquid two-phase secondary-flow predictions.

The addition of gas to a secondary liquid stream reduces the liquid pumping efficiency. Conversely, adding liquid to the gas stream of the gas compressor reduces gas compression efficiency. But LJGL total efficiencies usually exceed the efficiencies of the corresponding single-phase secondary-flow pumps, i.e., the LJL and LJG jet pumps.

The effects of design area ratio $b = A_n/A_t$, and the primary-jet velocity are treated in terms of performance curves vs. both liquid and gas flow ratios.

Flow-ratio cut-off is identified as a phenomenon which will affect two-phase secondary-flow jet pumps under extreme conditions. This study shows that flow-ratio cut-offs result from choking of two-phase secondary flows, at the throat entry. Maximum flow ratios M_{c0} or ϕ_{sc0} can be predicted from the LJGL pump model equations.

The effects of operating conditions and design area-ratio on cut-off flow ratio are correlated as M_{c0} versus $c\sqrt{(P_s - P_0)/Z}$, where each ϕ_s flow ratio (gas load) forms one curve. This study indicates that the design and application of two-phase secondary-flow pumps are quite feasible. Throat-entry choking of the secondary flow can be predicted, hence avoided.

References

Cunningham, R. G., Hansen, A. G., and Na, T. Y., 1970, "Jet Pump Cavitation," ASME *Journal of Basic Engineering,* Vol. 92, 1, pp. 483–494.

Cunningham, R. G., 1974, "Gas Compression with the Liquid Jet Pump," ASME JOURNAL OF FLUIDS ENGINEERING, Vol. 96, No. 3, Series 1, pp. 203–215.

Cunningham, R. G., and Dopkin, R. J., 1974, "Jet Breakup and Mixing Throat Length for the Liquid Jet Gas Pump," ASME JOURNAL OF FLUIDS ENGINEERING, Vol. 96, 3, Series 1, pp. 216–226.

Cunningham, R. G., 1975, "Liquid Jet Pump Modeling: Effects of Axial Dimensions on Theory-Experiment Agreement," *2nd Symposium on Jet Pumps and Ejectors,* BHRA Fluid Engineering, Cranfield, Bedford, England, March 24.

Dopkin, R. J., 1973, "The Liquid-Jet Gas Pump: A Study of Jet Breakup and Required Throat Length," M. S. thesis, The Pennsylvania State University.

Eddington, R. B., 1967, "Investigation of Supersonic Shock Phenomena in a Two-Phase (Liquid-Gas) Tunnel," NASA TR 32-1096, Mar. 15.

Gosline, J. E., and O'Brien, M. P., 1934, "The Water Jet Pump," *University of California Publications in Engineering,* Vol. 3, pp. 167–190.

Sanger, N. L., 1968, "Noncavitating Performance of Two Low-Area Ratio Water Jet Pumps Having Throat Lengths of 7.25 Diameters," NASA TN D-4445.

Sanger, N. L., 1970, "An Experimental Investigation of Several Low-Area-Ratio Water Jet Pumps," ASME *Journal of Basic Engineering,* Vol. 92, 1, pp. 11–20.

Witte, J. H., 1962, "Mixing Shocks and Their Influence on the Design of Liquid-Gas Ejectors," Ph.D. dissertation, Delft.

Journal of Fluids Engineering

Technical Briefs

Planar Ultrasonic Imaging of a Two-Phase Mixture

A. Shekarriz[1] and B. B. Brenden[1]

Introduction

Flows of solid-liquid mixtures, fiber suspensions, polymer melts, and colloidal dispersions are commonly encountered in chemical, petroleum, pulp and paper, and food industries. In most cases, the dynamics of the flow field can impact the rheology of the mixture and the morphology of the final products. Studying and understanding the dynamics is limited due to the fact that these mixtures are optically opaque, heterogeneous in properties, and dynamic in behavior. The use of optical diagnostics tools, and other non-ultrasonic techniques are limited due to various reasons as pointed out in detail in a comprehensive review by Cheremisinoff (1986), Kytömaa and Corrington (1993), and Shekarriz et al. (1994).

The system used in this study is a real-time ultrasonic imaging system (RTUIS). It has unique characteristics with a usable degree of spatial resolution and with a temporal resolution much higher than other (non-optical) planar techniques. The objectives of this study are to demonstrate the feasibility of using RTUIS for non-intrusive planar velocity measurement on the basis of the motion of visible texture caused by the scattering particles. A simple two-phase channel flow is utilized for demonstration of the current technique.

Experimental Apparatus

A schematic drawing of RTUIS is given in Fig. 1. Ultrasonic tone bursts of about 50 μs duration and a frequency of 5 MHz,[2] generated by a 127 mm diameter quartz crystal, propagate through water to the test section. The ultrasound is scattered by particles carried in the fluid stream within the test section. This scattered field, or the object beam, is focused by a pair of acoustic lenses and an ultrasonic reflector onto the liquid surface shown. Interference between the object beam and a reference beam deforms the interface into a grating. The amplitude of the surface deformation varies in accordance with the amplitude of the ultrasound in the object plane and it is usually less than 0.13 μm. This grating is the analog of an optical hologram that can be reconstructed to form an image of the scatterers. Coherent light reflected from this grating is focused to form separate domains of light for each diffracted order. A 400 μm diameter pinhole is used in the focal plane to reject all but the light in the first-order diffracted beam. The first-order diffracted light passes to a video camera which is focused on the liquid surface. In this manner, the ultrasonic image is converted to an image on a video monitor. (The reader is referred to Brenden, 1993, for further detail on the principles of operation of RTUIS.)

The response and decay time of the liquid film deformation amplitude to a value of $1/e$ is less than 2 ms, as determined from experimental measurement of free surface response to a tone burst. Although the ultrasonic imager is capable of creating more than 300 images per second, it operates in synchronism with a closed circuit video system at a 60 field/s rate. Limits on the velocity of flow which can be studied are imposed by the frame rate of the video camera and the resolution of the sound field.

Each video frame includes a field-of-view of at least 63.5 mm in diameter. In the case of the experiments reported here, the field was restricted to 25 mm $\times$ 50 mm. The depth-of-field is 6 mm, within which velocity measurements are not affected by blurring of the image.

The flow system consisted of a small centrifugal pump, a test section having a 25 mm square cross-section, a reservoir, and a valve. The test section has optically-opaque, stainless steel windows on two sides for transmission of the 5 MHz ultrasound beam. Windows were made of 13 μm thick shim stock. We believe that plane parallel stainless windows of thicknesses up to at least 20 mm can be used under specific conditions.

The fluid used was water and the solid particles were made of polystyrene with a specific gravity slightly higher than water ($\sim$1.04). The particles ranged between 500 mm to 700 mm in diameter. These particles exhibit monopolar resonance at 5 MHz, which was deemed beneficial in ensuring their visibility. Consequently, the upper limit of the volume fraction of the solid particles was found by trial and error to be 1 percent.

Results and Discussion

Figure 2 is a sample image of the flow field obtained using RTUIS. The dark regions are the regions of high particle density. Note that individual particles cannot as easily be identified as in optical techniques. The images were recorded on an optical disk in order and separate fields within each frame were digitized for several consecutive frames. The images were grabbed and digitized at a resolution of approximately 5.5 pixels/mm in real space dimensions. After enhancement of the images using a standard image processing routine, the velocity distribution for each frame was obtained by determining the average shift or displacement of the particles from the first to the second field in that frame. This approach is known as the spatial cross-correlation technique and it is commonly used in digital signal

[1] Fluid Dynamics Laboratory and Electro-Optics Groups, respectively, Pacific Northwest Laboratory, Richland, WA 99352.

Pacific Northwest Laboratory is operated for the U.S. Department of Energy by Battelle Memorial Institute under Contract DE-AC06-76RL01830.

[2] The system can operate at 1 MHz, 3 MHz, and 5 MHz.

Contributed by the Fluids Engineering Division of THE AMERICAN SOCIETY OF MECHANICAL ENGINEERS. Manuscript received by the Fluids Engineering Division March 17, 1994; revised manuscript received February 14, 1995. Associate Technical Editor: O. C. Jones.

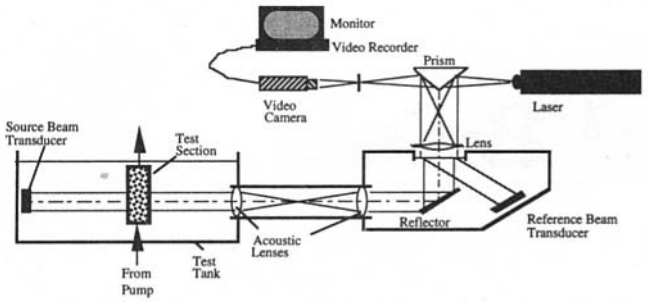

Fig. 1 Schematic diagram of the real time ultrasound imaging system (RTUIS)

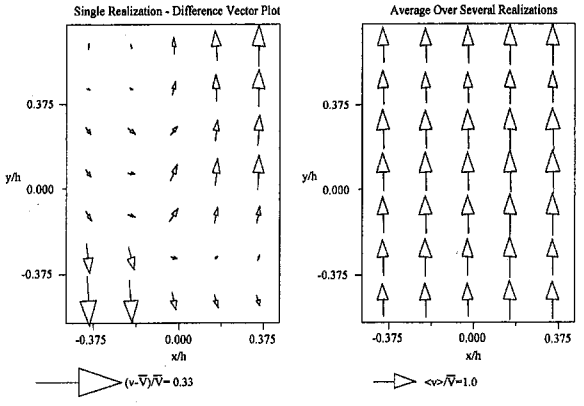

Fig. 3 A typical instantaneous velocity vector plot for a pipe flow at Re = 800. The map on the right is the average over several realizations for the same flow conditions.

processing and specifically in Digital Particle Image Velocimetry (DPIV) technique. For more information the reader is referred to Shekarriz et al. (1994).

An instantaneous velocity map for a single realization and an average velocity map over several realizations are shown in Fig. 3. Note that the left figure is obtained by removing the measured average velocity and the right figure is the ensemble average between four different maps. These results are for the flow of water with 1 percent solids content at $Re_D = 800$ (based on the hydraulic diameter, D_h).[3] The vectors shown in these figures represent the distribution of velocity in a "plane" along the direction of flow. Since the depth of field within the imaging plane is approximately 6 mm, then each vector is an average over a 12 mm × 12 mm × 6 mm volume in real space dimensions. In dimensionless format, normalized by the hydraulic diameter, D_h, the size of the sampling volume becomes 0.47 × 0.47 × 0.24. The presence of secondary flow and lateral velocity in the channel is quite evident in the single realization instantaneous map.

At the first glance, it may appear that continuity is not satisfied in the flow field since the average velocity at each cross-section changes from one streamwise location to the next. Also one may ask why the velocity profile in the channel does not have a parabolic profile as would be the case for steady laminar fully developed channel flow. For a laminar channel flow, $L_e/D_h = 0.06\ Re_D$. Thus, the flow should become fully-developed beyond 48 diameters downstream of the entrance to the channel. In our experiments, due to the limitations in the size of the imaging setup, we visualized a section of the flow field between 3 and 5 diameters downstream of the entrance. Thus, the results are for flow within the entrance length. The boundary layers have not grown and the flow in the channel is developing. It is also expected that some secondary flow would exist within this entrance length caused by separation and recirculation at the entrance of the pipe into the channel (the pipe diameter was smaller than h and the entrance was abrupt).[4]

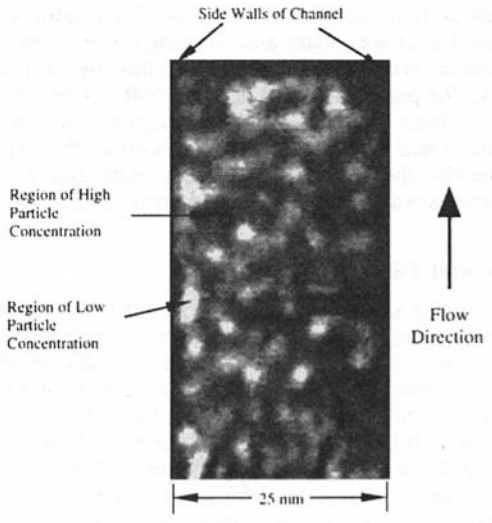

Fig. 2 A sample image of the particulate flow using RTUIS

The average velocities of the particles determined from four different maps (averaging all the vectors in each map), when normalized by the measured fluid velocity,[5] are 0.99, 0.84, 0.80, and 0.75, respectively. The average of all the values shown above is 0.85. It is expected that the velocity of the particles would lag the fluid velocity, since the particles are approximately 4 percent more dense than the fluid. The slip velocity between the particles and the fluid can be estimated using the Stoke's drag approximation. The slip velocity, when normalized by the measured fluid velocity, is found to be 0.24. Thus, the estimated fluid velocity, which is the sum of the measured particle velocity and the estimated particle slip velocity, is 1.09. If the particles achieve a terminal settling velocity in this portion of the pipe, this would imply a measurement error of 9 percent. Some lack of precision is anticipated for these proof of concept experiments for the following reasons: the error could be the result of insufficient number of samples for averaging as well as biasing the average velocity toward the center of the channel by not including data point from the region near the side walls.

One should bear in mind that the scope of this study has been to determine how feasible it is to use the ultrasound imaging technique for planar measurement of the velocity. We have established that this method can be successfully implemented for measuring the velocity. We have also identified some of the limiting parameters such as the frame rate and flow velocity. No attempt has been made throughout this study to utilize this technique for understanding the physics of flow. Some of the target problems for the future are study of pulp and paper flows, polymer flows, and dense slurry flows, where studies of flow regime and phase separation are of interest.

References

Brenden, B. B., 1993, "Ultrasonic Holography Using a Liquid Surface Sensor," to appear in *International Advances in Nondestructive Testing*, W. J. McGonnagle, ed., Gordon and Breach Science Publishers, New York.

[3] The hydraulic diameter is defined as 4 × cross-sectional area/wetted perimeter. It is equal to h for a square channel.

[4] The very small velocities near the walls of the channel are not measurable in the current system due to the limited resolution of the system as well as limited field of view, which does not cover the region close to the walls, as mentioned in the analysis section.)

[5] The measured fluid velocity is the average velocity found from measuring the flow rate in the channel.

Cheremisinoff, N. P., 1986, "Measurement Techniques for Multiphase Flows," *Encyclopedia of Fluid Mechanics,* N. P. Cheremisinoff, ed., Gulf Publishing Co., Houston, Texas, Vol. 1, Chapter 38, pp. 1280–1338.

Kytömaa, H. K., and Corrington, S. W., 1993, "Ultrasonic Imaging Velocimetry of Transient Liquefaction of Cohesionless Particulate Media," To appear in *International Journal of Multiphase Flow.*

Shekarriz, A., Brenden, B. B., and Nakamura, G., 1994, "Planar Velocity Measurement of a Two-Phase Mixture Using Ultrasonic Imaging," ASME-FED 1994, *Liquid-Solid Flows,* Vol. 189, pp. 83–89.

Analysis of Throughflow Velocity in Two-Dimensional Fluidized Bed Bubbles

Dinesh Gera[1] and Mridul Gautam[1]

The formation of gas bubbles is one of the most characteristic phenomena of fluidized beds. Many unique properties of fluidized beds can be related directly to the presence of bubbles and are dominated by their behavior. Therefore, accurate prediction of parameters such as bubble shape and size, voidage variation and throughflow are practically important. In the present analysis, an approximate model, based on a strongly idealized picture of the bubble formation has been presented. The bubbling gas fluidized bed has regions of low solids density comprised of gas pockets or voids. The observed voids exhibited a variety of shapes (Halow and Nicoletti, 1992), depending upon the material and fluidization velocity. In the low-velocity experiments with the finer materials, rounded voids are observed. However, with coarser materials, voids were typically large and blunt-nosed. In the image analyses work, reported by Gautam (1989), in a bed operating slightly above the incipient fluidization, elongated bubbles ($a > b$, as shown in Figure 1) were observed for glass beads (sp. gravity = 2.5) of mean diameter 500 μm and flattened bubbles ($a < b$) were seen for mean particle diameter of 350 μm. Also, he noticed the dependence of throughflow velocity on the elongation of the bubble as it traverses up the bed. Additionally, throughflow velocity was found to be independent of the excess gas flow rate through the bed. The digitized image of a typical bubble (refer Gautam et al., 1994) which shows that the bubble were elongated in the vertical direction and were more elliptical than circular. Therefore, description of a bubble on the basis of just one diameter, either the horizontal or the vertical or an equivalent diameter, as has been done by many researchers in the past, is rather incomplete. It is inferred from the present work that the bubble aspect ratio plays an important role in predicting an accurate gas flow through the bubble.

1 Theoretical Formulation

There exist three distinct classical theories on fluidized bed bubble phenomenon, given by Davidson (1961), Jackson (1963), and Murray (1965), which differ in the treatment of the voidage fraction of the particulate phase. Davidson (1961) assumes it to be constant and equal to the voidage at incipient fluidization; Jackson (1963) makes voidage a dependent variable and predicts voidages greater than the voidage at the incipient fluidization, ϵ_0, near a rising bubble; Murray (1965) also assumes a variable voidage, but confines changes in voidage to a thin "boundary layer" around a bubble. Lockett and Harrison's (1967) experimental results do not support Murray's (1965) assumption that for theoretical purposes it is reasonable to confine all voidage changes to a thin "boundary layer" region close to the bubble. Collins (1965) treatment of the problem in two-dimensional beds also utilized a set of assumptions similar to Davidson's (1963) except that he includes a transformation of the bubble shape in his analysis which mapped a kidney shape (actual shape of the bubble) of the bubble on x-y plane to a circular shape on s (complex) plane. It was inferred from his analysis that the distortion introduced by employing a mapping has little effect on fluid flow. That is the reason for choosing Jackson's theory for computing voidage distribution in this paper.

Consider an elliptical gas bubble embedded in a two-dimensional aggregative fluidized bed. Assuming that there are no particles inside the bubble, the fluid pressure therefore must be uniform (at least to the present approximation in which the fluid density is neglected). The problem is therefore of the "free-stream line" type. We require a solution which satisfies the condition of incipient fluidization at points well ahead of the bubble and for which the bubble surface is both a stream line surface of the particle motion and a surface of constant fluid pressure.

The equations of steady motion of the solid particles and gas viewed as a mixture of two interpenetrating interacting continuum media may be written as:

$$\text{div } \epsilon\mathbf{u} = 0 \tag{1.1a}$$

$$\text{div } (1-\epsilon)\mathbf{v} = 0 \tag{1.2a}$$

$$n_0 m(\mathbf{v}.\text{grad } \mathbf{v} + n_0 mg\mathbf{i} - \beta(\mathbf{u}-\mathbf{v}) = 0 \tag{1.3a}$$

$$\text{grad } p + \beta(\mathbf{u}-\mathbf{v}) = 0 \tag{1.4a}$$

where ϵ is the voidage fraction, $\mathbf{u}$ and $\mathbf{v}$ are interstitial gas velocity and particle velocity respectively; p is the gas pressure, n_0 is the number of particles per unit bed volume and $\beta = \beta(\epsilon)$ is the fluid/particle drag coefficient. Equations (1.1a) and (1.2a) represent the continuity equations for the gas and particulate phases respectively. The changes in momentum associated with the rapid changes of fluid velocity on a scale comparable with the particle size is given by Eq. (1.3a). The relative velocity between the fluid and solid particles is given by Darcy's law (Eq. 1.4a).

It is important to realize that there are two mathematically distinct processes of successive approximations which would be involved in obtaining a solution of high accuracy to the problem of bubble motion. First, one would take an elliptical bubble surface and calculate successive approximations to a solution which made the pressure approximately constant on the upper part of this surface. It would then be necessary to adjust slightly the shape of the surface on which the constant pressure condition would be satisfied more accurately and over a larger region. This process could, in principle, be continued, making successive adjustments to the shape of the surface and, at each stage, obtaining an approximate solution of the equations of motion by the iterative procedure as suggested by Jackson (1963). That is, on the first iteration we take $\epsilon = \epsilon_0$ everywhere in the conservation equations except where it enters in the drag coefficient $\beta(\epsilon)$. The independent variable then becomes β, and the solution for β determines the new estimate of ϵ, which can be used in further iterations. In this study we limit the analysis to the first iteration, and with these assumptions the equations of continuity and momentum become (Jackson, 1963):

$$\text{div } \mathbf{u} = 0 \tag{1.1}$$

$$\text{div } \mathbf{v} = 0 \tag{1.2}$$

[1] Department of Mechanical & Aerospace Engineering, West Virginia University, Morgantown, WV 26506.

Contributed by the Fluids Engineering Division of THE AMERICAN SOCIETY OF MECHANICAL ENGINEERING. Manuscript received by the Fluids Enzymes Division March 15, 1994; revised manuscript received October 31, 1994. Associate Technical Editor: M. W. Reeks.

Cheremisinoff, N. P., 1986, "Measurement Techniques for Multiphase Flows," *Encyclopedia of Fluid Mechanics,* N. P. Cheremisinoff, ed., Gulf Publishing Co., Houston, Texas, Vol. 1, Chapter 38, pp. 1280–1338.

Kytömaa, H. K., and Corrington, S. W., 1993, "Ultrasonic Imaging Velocimetry of Transient Liquefaction of Cohesionless Particulate Media," To appear in *International Journal of Multiphase Flow.*

Shekarriz, A., Brenden, B. B., and Nakamura, G., 1994, "Planar Velocity Measurement of a Two-Phase Mixture Using Ultrasonic Imaging," ASME-FED 1994, *Liquid-Solid Flows,* Vol. 189, pp. 83–89.

Analysis of Throughflow Velocity in Two-Dimensional Fluidized Bed Bubbles

Dinesh Gera[1] and Mridul Gautam[1]

The formation of gas bubbles is one of the most characteristic phenomena of fluidized beds. Many unique properties of fluidized beds can be related directly to the presence of bubbles and are dominated by their behavior. Therefore, accurate prediction of parameters such as bubble shape and size, voidage variation and throughflow are practically important. In the present analysis, an approximate model, based on a strongly idealized picture of the bubble formation has been presented. The bubbling gas fluidized bed has regions of low solids density comprised of gas pockets or voids. The observed voids exhibited a variety of shapes (Halow and Nicoletti, 1992), depending upon the material and fluidization velocity. In the low-velocity experiments with the finer materials, rounded voids are observed. However, with coarser materials, voids were typically large and blunt-nosed. In the image analyses work, reported by Gautam (1989), in a bed operating slightly above the incipient fluidization, elongated bubbles ($a > b$, as shown in Figure 1) were observed for glass beads (sp. gravity = 2.5) of mean diameter 500 μm and flattened bubbles ($a < b$) were seen for mean particle diameter of 350 μm. Also, he noticed the dependence of throughflow velocity on the elongation of the bubble as it traverses up the bed. Additionally, throughflow velocity was found to be independent of the excess gas flow rate through the bed. The digitized image of a typical bubble (refer Gautam et al., 1994) which shows that the bubble were elongated in the vertical direction and were more elliptical than circular. Therefore, description of a bubble on the basis of just one diameter, either the horizontal or the vertical or an equivalent diameter, as has been done by many researchers in the past, is rather incomplete. It is inferred from the present work that the bubble aspect ratio plays an important role in predicting an accurate gas flow through the bubble.

1 Theoretical Formulation

There exist three distinct classical theories on fluidized bed bubble phenomenon, given by Davidson (1961), Jackson (1963), and Murray (1965), which differ in the treatment of the voidage fraction of the particulate phase. Davidson (1961) assumes it to be constant and equal to the voidage at incipient fluidization; Jackson (1963) makes voidage a dependent variable and predicts voidages greater than the voidage at the incipient fluidization, ϵ_0, near a rising bubble; Murray (1965) also assumes a variable voidage, but confines changes in voidage to a thin "boundary layer" around a bubble. Lockett and Harrison's (1967) experimental results do not support Murray's (1965) assumption that for theoretical purposes it is reasonable to confine all voidage changes to a thin "boundary layer" region close to the bubble. Collins (1965) treatment of the problem in two-dimensional beds also utilized a set of assumptions similar to Davidson's (1963) except that he includes a transformation of the bubble shape in his analysis which mapped a kidney shape (actual shape of the bubble) of the bubble on x-y plane to a circular shape on s (complex) plane. It was inferred from his analysis that the distortion introduced by employing a mapping has little effect on fluid flow. That is the reason for choosing Jackson's theory for computing voidage distribution in this paper.

Consider an elliptical gas bubble embedded in a two-dimensional aggregative fluidized bed. Assuming that there are no particles inside the bubble, the fluid pressure therefore must be uniform (at least to the present approximation in which the fluid density is neglected). The problem is therefore of the "free-stream line" type. We require a solution which satisfies the condition of incipient fluidization at points well ahead of the bubble and for which the bubble surface is both a stream line surface of the particle motion and a surface of constant fluid pressure.

The equations of steady motion of the solid particles and gas viewed as a mixture of two interpenetrating interacting continuum media may be written as:

$$\text{div } \epsilon\mathbf{u} = 0 \tag{1.1a}$$

$$\text{div } (1-\epsilon)\mathbf{v} = 0 \tag{1.2a}$$

$$n_0 m(\mathbf{v}.\text{grad } \mathbf{v} + n_0 mg\mathbf{i} - \beta(\mathbf{u}-\mathbf{v}) = 0 \tag{1.3a}$$

$$\text{grad } p + \beta(\mathbf{u}-\mathbf{v}) = 0 \tag{1.4a}$$

where ϵ is the voidage fraction, $\mathbf{u}$ and $\mathbf{v}$ are interstitial gas velocity and particle velocity respectively; p is the gas pressure, n_0 is the number of particles per unit bed volume and $\beta = \beta(\epsilon)$ is the fluid/particle drag coefficient. Equations (1.1a) and (1.2a) represent the continuity equations for the gas and particulate phases respectively. The changes in momentum associated with the rapid changes of fluid velocity on a scale comparable with the particle size is given by Eq. (1.3a). The relative velocity between the fluid and solid particles is given by Darcy's law (Eq. 1.4a).

It is important to realize that there are two mathematically distinct processes of successive approximations which would be involved in obtaining a solution of high accuracy to the problem of bubble motion. First, one would take an elliptical bubble surface and calculate successive approximations to a solution which made the pressure approximately constant on the upper part of this surface. It would then be necessary to adjust slightly the shape of the surface on which the constant pressure condition would be satisfied more accurately and over a larger region. This process could, in principle, be continued, making successive adjustments to the shape of the surface and, at each stage, obtaining an approximate solution of the equations of motion by the iterative procedure as suggested by Jackson (1963). That is, on the first iteration we take $\epsilon = \epsilon_0$ everywhere in the conservation equations except where it enters in the drag coefficient $\beta(\epsilon)$. The independent variable then becomes β, and the solution for β determines the new estimate of ϵ, which can be used in further iterations. In this study we limit the analysis to the first iteration, and with these assumptions the equations of continuity and momentum become (Jackson, 1963):

$$\text{div } \mathbf{u} = 0 \tag{1.1}$$

$$\text{div } \mathbf{v} = 0 \tag{1.2}$$

[1] Department of Mechanical & Aerospace Engineering, West Virginia University, Morgantown, WV 26506.

Contributed by the Fluids Engineering Division of THE AMERICAN SOCIETY OF MECHANICAL ENGINEERING. Manuscript received by the Fluids Enzymes Division March 15, 1994; revised manuscript received October 31, 1994. Associate Technical Editor: M. W. Reeks.

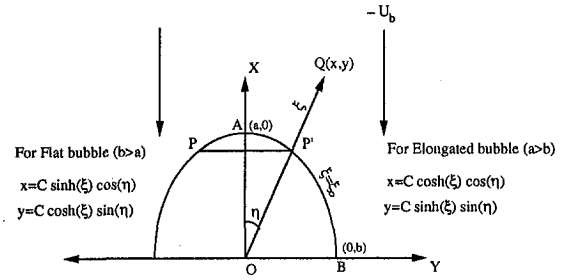

Fig. 1 Coordinate system

$$\text{grad } p = -n_0 m(\mathbf{v}.\text{grad})\mathbf{v} - n_0 mg\mathbf{i} \tag{1.3}$$

$$\beta(\mathbf{u} - \mathbf{v}) = -\text{grad } p \tag{1.4}$$

Rewriting Eq. (1.4):

$$\mathbf{u} = \mathbf{v} - (\gamma/\beta_0)\ \text{grad } p \tag{1.5}$$

where β_0 is the value in the undisturbed bed remote from the bubble and $\gamma = \beta_0/\beta$. More explicitly:

$$\gamma = \left(\frac{1-\epsilon_0}{1-\epsilon}\right)^2 \left(\frac{\epsilon}{\epsilon_0}\right)^2$$

and ϵ_0 is the voidage at incipient fluidization. Using continuity for gas and particle phase, Eq. (1.4) reduces to:

$$\text{div } (\gamma\ \text{grad } p) = 0 \tag{1.6}$$

Rewriting Eq. (1.6):

$$\text{grad } \gamma.\text{grad } p + \gamma \nabla^2 p = 0 \tag{1.7}$$

In the present analysis, Eq. (1.7) has been numerically integrated with the boundary condition $\gamma = 1$ at a distance far away from the bubble to compute the variation of voidage in the vicinity of an elliptical bubble.

As a first step, a curvilinear coordinate system is defined with the origin at the center, and where ξ = constant, represents an elliptical contour (as shown in Fig. 1). Now, neglecting wake effects, the particle velocity field vector $\mathbf{v}$ may be taken simply as a solution of equations corresponding to a potential flow around an ellipse with the velocity $-U_b$ at a large distance upstream. It was suggested by Martin-Gautier and Pyle (1975) that a region very close to the bubble, with a width of about $\frac{1}{4}$ of the bubble radius, where convective terms are more important than viscous effects, potential flow solution is a very good approximation to the particulate velocity field.

Mathematically,

$$\mathbf{v} = -\nabla\phi \tag{1.8}$$

and ϕ, the velocity potential for a flow around an ellipse, may be written as (Milne-Thomson, 1962):

$$\phi = U_b(a+b)\cosh(\xi - \xi_0)\cos(\eta) \tag{1.9}$$

where U_b, the bubble rise velocity, may be expressed as (Grace and Harrison, 1969):

$$U_b = \frac{\sqrt{(1-e^2)}}{1+\sqrt{(1-e^2)}}\, g^{1/2} a^{1/2} \tag{1.10}$$

where e, the eccentricity (c/a) is defined as a ratio of the focal distance (c) to the semi-axis of an ellipse (a) in the vertical direction, and g is the acceleration due to gravity.

The pressure distribution then follows from integration of Eq. (1.3):

$$\frac{p}{\rho g} = -c\cosh(\xi)\cos(\eta) + \frac{1}{2g}U_b^2 \times \left[1 - \frac{a+b}{a-b}\left(\frac{\sinh^2(\xi-\xi_0)+\sin^2(\eta)}{\sinh^2(\xi)+\sin^2(\eta)}\right)\right] \tag{1.11}$$

It is observed that p remains almost constant for all the different values of aspect ratios (b/a) up to $\eta = 30$ deg, and does not vary much upto $\eta = 50$ deg (Gera and Gautam, 1994). Therefore, the approximation of actual bubble by an elliptical cap is justified up to this value of η.

By the proper parameterization (selection of the paths of integration), the governing equation (Eq. (1.7)) in two independent variables can be reduced approximately to a set of first order simultaneous ordinary differential equations.

2 Computational Analysis

Following the analysis of Jackson (1963), consider a small displacement $\mathbf{h}$ of length h in the direction of grad p, from some starting point $Q(\xi, \eta)$. The radial and angular components of this displacement are:

$$h_\xi = \frac{hp_\xi}{h_1|\nabla p|}; \quad h_\eta = \frac{hp_\eta}{h_2|\nabla p|} \tag{2.1}$$

where h_1 and h_2 are the scaling factors (for details refer Gera, 1994).

The vector grad p has no component perpendicular to this displacement $\mathbf{h}$; therefore,

$$\text{grad } \gamma.\text{grad } p = \frac{d\gamma}{dh}\,|\text{grad } p| \tag{2.2}$$

where, $d\gamma/dh$ denotes the rate of change of γ with displacement in the direction of $\mathbf{h}$. Substituting this into Eq. (1.7), yields:

$$\frac{d\gamma}{dh} = -\frac{\nabla^2 p}{|\nabla p|}\gamma \tag{2.3}$$

where

$$|\nabla p| = \sqrt{\frac{1}{h_1^2}p_\xi^2 + \frac{1}{h_2^2}p_\eta^2}$$

The changes in coordinates ξ and η which accompany the displacement $\mathbf{h}$ are similarly given by:

$$\frac{d\xi}{dh} = \frac{1}{h_1^2}\frac{p_\xi}{|\nabla p|} \tag{2.4}$$

$$\frac{d\eta}{dh} = \frac{1}{h_2^2}\frac{p_\eta}{|\nabla p|} \tag{2.5}$$

The three simultaneous first order differential equations of γ (Eq. 2.3), ξ (Eq. 2.4), and η (Eq. 2.5) can be integrated using a fourth order Runge-Kutta method from any set of initial values; since the functions p_ξ, p_η, and $\nabla^2 p$, which appear on their right-hand side can be calculated from the known form (Eq. (1.11)) of the pressure field (Gera, 1994). Considering the voidage at incipient fluidization, $\epsilon_0 = 0.4$ to be constant (Lockett and Harrison, 1967), the variation of voidage at the surface of an ellipse for different η can be calculated. One approach to estimate the absolute errors in computations is to assume that the local truncation errors have the form $K(\Delta h)^{m+1}$ with K constant (Carnahan et al., 1972), (Δh is the step size, m is the order of accuracy, in our case, $\Delta h = 0.0001$ and $m = 4$), and K normally depends on upon the function itself and its higher order partial derivatives. In the present analysis, truncation error was estimated to be less than 5.0E-06 for each variable (Gera, 1994).

The outflow across PAP′ (Fig. 1) can be derived as:

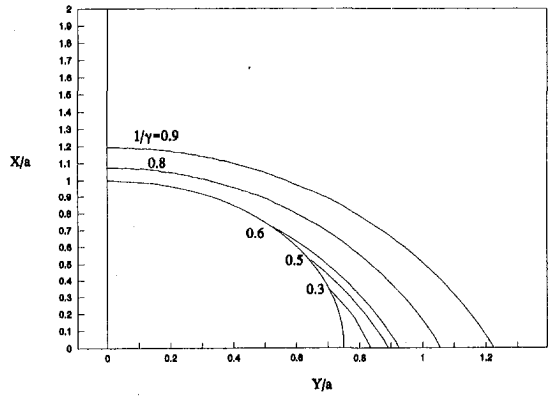

Fig. 2(a)

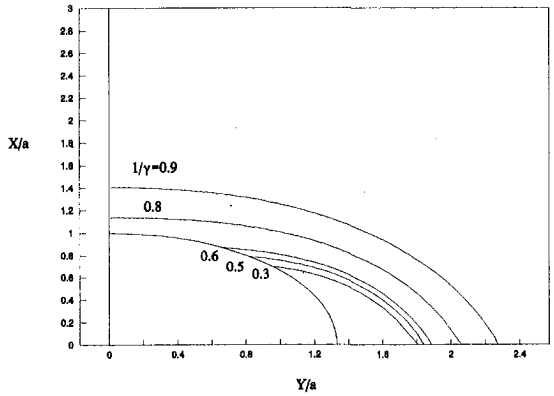

Fig. 2(b)

Fig. 2 Variation of $1/\gamma$ in the neighborhood of the bubble with aspect ratio (a) a/b = 1.33, (b) a/b = 0.75

$$q_{PP'} = \int_0^{\eta} 2\epsilon\xi_0 u_{\xi 0} d\eta \tag{2.6}$$

Following the analysis of Lockett et al. (1967) the throughflow velocity (U_{th}) component relative to bubble across a plane normal to its vertical axis (PP') may be written as:

$$U_{th} = \frac{\int_0^{\eta} 2\epsilon u_{\xi 0}\xi_0 d\eta}{2\xi_0 \sin \eta} \tag{2.7}$$

where $\xi = \xi_0$, represents the surface of an ellipse and $u_{\xi 0}$, the component of interstitial fluid velocity at $\xi = \xi_0$, can be derived from the velocity field (Jackson, 1963):

$$\mathbf{u} = \mathbf{v} - \frac{1}{\beta}\nabla p \tag{2.8}$$

Simplifying;

$$\mathbf{u}_{\xi=\xi_0} = -\frac{1}{h_1}\frac{\partial \phi}{\partial \xi}\bigg|_{\xi=\xi_0} - \frac{\gamma U_0}{\epsilon_0}\left(\frac{1}{h_1}\frac{\partial p}{\partial \xi}\right)\bigg|_{\xi=\xi_0} \tag{2.9}$$

3 Results and Discussion

The predicted voidages have their best accuracy on the line through the vertical axis of the bubble. Ideally, the fluid pressure is not constant over the surface of the bubble. Hence, the shape of the bubble needs to be adjusted to achieve a constant pressure over the bubble surface. It is observed experimentally (Halow and Nicoletti, 1992) that smaller changes in voidage are found near bubbles in a system of particles of uniform size than in systems with wide size distributions; and thus, as the size distribution is increased, voidages near the bubble cloud increase enough to make it difficult to define a real boundary between the bubble and particulate phases. In such a situation, there could be a tendency for the particles to rain through the bubble rather than to take the path of potential flow around it. However, in the present analyses, a sharp interface between the bubble phase and emulsion phase was assumed.

Table 1 Comparison of throughflow velocities at the bubble nose

Aspect ratio (a/b)	Present work	Gautam et al. (1994) experimental data	Leung[1] (1970)
0.83	1.49 U_0	1.46 U_0	Not applicable
0.98	1.53 U_0	1.56 U_0	Not applicalbe
1.0	1.54 U_0	Not reported	1.6 U_0

[1] Assuming constant voidage at the surface of the bubble.

It is evident from the numerical solution of Eq. (1.7) that γ does not depend on the value of $\epsilon_0 U_0/U_b$; and hence, it may be inferred that the distribution of particle density in the neighborhood of the bubble is independent of the rise velocity. The function γ is, therefore, the same for all bubbles of all sizes and is plotted in the form of contours plots in Fig. 2. Using these contours, the values of ϵ are calculated at the surface of the bubble, which are in turn used for computing throughflow velocities of elliptical bubbles with different aspect ratios. It is observed from Fig. 2 that the upper surface of the bubble is surrounded by a fairly thin mantle in which the particle density is lower than in the bulk of the bed. The voidage at the nose of an elongated bubble is higher than that of a flattened bubble which is a result of higher throughflow velocity component in the former case.

Comparison of computed values of throughflow velocities with the data observed by Gautam et al. (1994) shows a fairly good agreement (refer to Table 1). Direct experimental evidence indicated that the present analysis comes closer to predicting the throughflow velocity than the earlier theory of Leung et al. (1970). It may be seen that at least a part of discrepancy between Leung's (1970) theory and current analysis could be accounted for by considering the effects of modifications in bubble shapes.

It may be inferred from Table 2 that the mean throughflow velocity increases with the bubble aspect ratio (a/b). It decreases when the bubble becomes more flat, this is due to the increase in the frontal area of the bubble. It may also be noted that bubble throughflow velocity at the nose of the bubble (η = 0 deg) decreases with the decrease in the aspect ratio (a/b). Previously the throughflow velocity was calculated using Davidson's modeling as $(1 + a/b)U_0$ (Grace and Harrison, 1969). It could be verified easily from Grace and Harrison's analysis that the throughflow velocity would vary from $1.75U_0$ to $2.33U_0$ for aspect ratio changing from 0.75 to 1.33, which is very inconsistent from the experimental data. However, it is interesting to note that the present analysis predicts the throughflow component more accurately than that of Grace and Harrison (1969).

Table 2 Comparison of mean throughflow velocities

$\bar{U}_{th\|\eta=\eta}$	Elongated bubble a/b = 1.33	Flattened bubble a/b = 0.75
η = 0°	1.62 U_0	1.47 U_0
η = 15°	1.63 U_0	1.56 U_0
η = 30°	1.52 U_0	1.58 U_0
η = 40°	1.43 U_0	1.59 U_0

4 Conclusions

Direct experimental evidence indicates that the current analysis comes closer to predicting the throughflow velocity than the existing theories. This may be accounted for by considering the effects of modifications in bubble shape. Throughflow velocity component at the nose of an elongated bubble is higher than that in a flattened bubble.

References

Carnahan, B., Luther, H. A., and Wilkes, J. O., 1972, *Applied Numerical Methods,* Wiley, New York.

Collins, R., 1965, "An Extension of Davidson's Theory of Bubbles in Fluidized Beds," *Chemical Engineering Science,* Vol. 20, pp. 747–754.

Davidson, J. F., 1961, "Symposium On Fluidization-Discussion," *Transactions, Institution of Chemical Engineers,* Vol. 39, pp. 230–232.

Gautam, M., Jurewicz, J. T., and Kale, S. R., 1994, "An Experimental Investigation of Throughflow Velocities in Two-Dimensional Fluidized Bed Bubbles: Laser Doppler Anemometers Measurements," ASME JOURNAL OF FLUIDS ENGINEERING, Vol. 116(3), pp. 605–612.

Gera, D., 1994, "Analysis and Prediction of Throughflow Velocity in Two-Dimensional Fluidized Beds," Ph.D. dissertation, West Virginia University, Morgantown, WV.

Gera, D., and Gautam, M., 1994, "Effect Of Voidage Variation and Bubble Aspect Ratio on Throughflow in 2-D Elliptical Bubbles," *Powder Technology,* Vol. 79(2), pp. 159–65.

Grace, J. R., and Harrison, D., 1969, "The Behavior Of Freely Bubbling Fluidized Beds," *Chemical Engineering Science,* Vol. 24, pp. 497–508.

Hailu, L., Plaka, F., Clift, R., and Davidson, J. F., 1993, "Measurement of Gas Flow Through a Two-Dimensional Bubble in a Fluidized Bed," *Institution of Chemical Engineers, Transactions,* Vol. 71, Part-A, pp. 382–89.

Halow, J. S., and Nicoletti, P., 1992, "Observations Of Fluidized Bed Coalescence Using Capacitance Imaging," *Powder Technology,* Vol. 69, pp. 255–277.

Jackson, R., 1963, "The Mechanics Of Fluidized Beds: Part-I and Part-II," *Transactions, Institution of Chemical Engineers,* Vol. 41, pp. 13–28.

Leung, L. S., Sandford, I. C., and Mak, F. K., 1970, "Effects Of Voidage on Throughflow in Bubbles In A Fluidized Beds," *Chemical Engineering Sci.,* Vol. 25, pp. 220–221.

Lockett, M. J., Davidson, J. F., and Harrison, D., 1967, "On The Two Phase Theory Of Fluidization," *Chemical Engineering Science,* Vol. 22, pp. 1059–66.

Martin-Gautier, A. L. F., and Pyle, D. L., 1975, "The Fluid Mechanics of Single Bubbles," *Fluidization Technology,* D. Kearns, ed., Hemisphere Publishing Corp., Washington, pp. 21–41.

Milne-Thomson, L. M., 1962, *Theoretical Hydrodynamics,* 4th edition, Macmillan.

Murray, J. D., 1965, "On The Mathematics Of Fluidization Part 2," *Journal of Fluid Mechanics,* Vol. 22, pp. 57–80.